



NON-INVASIVE ALCOHOL AND GLUCOSE DETECTION USING MICROWAVE RESONATORS

LIONEL WENDLING

A thesis submitted in partial fulfilment of the requirements
of Liverpool John Moores University
for the degree of Doctor of Philosophy

General Engineering Research Institute

December, 2009

Dedicated to my parents Michele and Jean-Luc, and my brothers Mathieu, Olivier and Herve.

ACKNOWLEDGEMENTS

I would like to thank my supervisors Prof A.I. Al-Shamma'a and Dr A. Shaw for their continued support and encouragement throughout my PhD studies. Additionally I would like to thank Dr J.D Cullen, Dr S.R. Wylie and Dr A. Mason who alongside my supervisors afforded me much wisdom and patience. I would particularly like to thank Eric Bader, a good friend of mine, for his help in producing the printed circuit board. I would also like to show appreciation for all of the members of the RF and Microwave Laboratory, the General Engineering Research Institute and the many workshop technicians who made this work possible.

I also would like to show my gratitude to my family, especially my mum, dad and brothers, for their constant support during my stay in England and for giving me incredible strength when my confidence was down.

I also would like to thank my girlfriend Leanne who always thought that I would get there, my flatmates Nick and Martin for their support, as well as the many friends I have made who made me feel welcome in their country.

LIST OF SYMBOLS

D	electric flux density
ρ	(free) charge density
E	electric field intensity
B	the magnetic flux density
H	magnetic field intensity
c	speed of light
J	free current density
k	wavenumber
λ	wavelength
Z	the intrinsic impedance
C_g	the capacitance of the ring resonator gap
C_f	capacitance of the ring resonator feed line
C_r	equivalent capacitance of the ring resonator
L_r	equivalent inductance of the ring resonator
ω	angular frequency
ω_0	resonant angular frequency
Z_0	characteristic impedance
w	width of the ring resonator track
R_m	average radius of the ring resonator
S	coupling gap

TABLE OF CONTENTS

1. INTRODUCTION	1
1.1 AIM OF THE PROJECT	1
1.2 FURTHER GOALS	6
1.3 DEFINED PROJECT TARGETS.....	9
2. ALCOHOL AND COMPOUND DETECTION	10
2.1 AIM OF THE PROJECT	10
2.1.1 WHAT IS ALCOHOL?	10
2.1.2 HOW ALCOHOL ENTERS THE BODY?.....	12
2.1.3 HOW ALCOHOL LEAVES THE BODY?.....	13
2.1.4 THE EFFECT OF ALCOHOL.....	15
2.2 DETECTION TECHNIQUES AND TECHNOLOGIES.....	17
2.2.1 INFRARED AND NEAR INFRARED SPECTROSCOPY	19
2.2.2 INFRARED AND NEAR INFRARED SPECTROSCOPY APPLICATIONS.....	22
2.2.3 FUEL CELLS.....	29
2.2.4 FUEL CELLS APPLICATIONS	31
2.2.5 OTHER METHODS FOR ALCOHOL DETECTION	33
3. ELECTROMAGNETIC WAVES IN THE MICROWAVE REGION	36
3.1 PROPERTIES OF ELECTROMAGNETIC WAVES.....	36
3.1.1 THE ELECTRIC FIELD.....	40

3.1.2	THE MAGNETIC FIELD	43
3.1.3	TRANSMISSION SYSTEM PROPERTIES	44
3.1.4	STRUCTURE TRANSITIONS	47
3.2	REFLECTION, TRANSMISSION AND STANDING WAVES.....	48
3.2.1	WAVE NORMALLY INCIDENT ON A CONDUCTOR	49
3.2.2	WAVE OBLIQUELY INCIDENT ON A CONDUCTOR	53
3.2.3	REFLECTION AND TRANSMISSION BETWEEN TWO DIELECTRICS.....	59
3.2.4	STANDING WAVES	67
3.3	MICROWAVE AND MATERIAL CHARACTERISATION	70
3.3.1	MATERIAL PROPERTIES IN THE MICROWAVE REGION	70
3.3.2	DIELECTRIC MATERIALS	74
3.3.3	RESONANT AND NON-RESONANT MEASUREMENTS.....	76
3.3.4	ONE PORT AND TWO PORTS MEASUREMENT METHODS	78
3.3.5	SCATTERING PARAMETERS (S-PARAMETERS)	79
3.3.6	QUALITY FACTOR (Q-FACTOR).....	82
3.3.7	EXPECTED RESPONSE OF A SAMPLE.....	84
4.	CAVITY RESONATORS DESIGN AND SIMULATIONS	88
4.1	CAVITY RESONATOR PROPERTIES	88
4.1.1	CAVITY RESONATOR DEFINITION	88
4.1.2	CAVITY COUPLING.....	89
4.1.3	CAVITY PROPAGATION MODES	91
4.2	CAVITY RESONATOR DESIGN.....	97
4.2.1	CAVITY RESONATOR CONSTRUCTION	97
4.2.2	THE TUNING SECTION.....	99
4.3	CAVITY RESONATOR SIMULATIONS.....	100

4.3.1 HFSS MODEL SIMULATIONS	100
4.3.2 PARAMETRIC SIMULATIONS.....	106
5. CAVITY RESONATORS EXPERIMENT RESULTS	113
5.1 SYSTEM SETUP	113
5.1.1 HARDWARE	113
5.1.2 SOFTWARE	114
5.2 CAVITY RESONATOR ETHANOL EXPERIMENT.....	118
5.2.1 SAMPLE PREPARATION.....	118
5.2.2 ETHANOL RESULTS FROM WATER (0%) TO ETHANOL (100%) BY 5% INCREMENTS.....	121
5.2.3 ETHANOL RESULTS FROM WATER (0%) TO 5% BY 1% INCREMENTS	126
5.2.4 ETHANOL RESULTS FROM WATER (0%) TO 1% BY 0.2% INCREMENTS	130
5.2.5 ETHANOL EXTRACTED DATA	131
5.3 CAVITY RESONATOR GLUCOSE EXPERIMENT.....	137
5.3.1 SAMPLE PREPARATION.....	137
5.3.2 GLUCOSE RESULTS - 0MOL/L OF GLUCOSE TO 1MOL/L BY 0.1MOL/L INCREMENTS.....	141
5.3.3 GLUCOSE EXTRACTED RESULTS	143
6. SUSPENDED RING RESONATOR DESIGN AND SIMULATIONS	148
6.1 MICROSTRIP RING RESONATOR BACKGROUND.....	148
6.2 MICROSTRIP RING RESONATOR DESIGN PROPERTIES	149
6.2.1 GENERAL PROPERTIES.....	149
6.2.2 COUPLING GAP	153
6.2.3 RING WIDTH	156
6.2.4 RING PROPAGATION MODE AND DIELECTRIC DETERMINATION	157

6.3	HFSS DESIGN AND SIMULATIONS	159
6.3.1	HFSS MODEL OF THE MICROSTRIP RING RESONATOR.....	159
6.3.2	HFSS MODEL OF THE SUSPENDED RING RESONATOR	162
6.3.3	PARAMETRIC SIMULATIONS.....	167
7.	MICROSTRIP RING RESONATOR EXPERIMENT RESULTS.....	180
7.1	MICROSTRIP RING RESONATOR CONSTRUCTION	180
7.2	SUSPENDED RING RESONATOR ETHANOL EXPERIMENTS	183
7.2.1	EXPERIMENTAL SETUP.....	183
7.2.2	ETHANOL RESULTS FROM WATER (0%) TO ETHANOL (100%) BY 5% INCREMENTS.....	184
7.2.3	ETHANOL RESULTS FROM WATER (0%) TO 5% BY 1% INCREMENTS	188
7.2.4	ETHANOL RESULTS FROM WATER (0%) TO 1% BY 0.2% INCREMENTS	190
7.2.5	ETHANOL EXTRACTED DATA	191
7.2.6	TEMPERATURE EFFECT	193
7.3	SUSPENDED RING RESONATOR GLUCOSE MEASUREMENTS	197
7.3.1	SAMPLE PREPARATION.....	197
7.3.2	GLUCOSE RESULTS - 0MOL/L OF GLUCOSE TO 1MOL/L BY 0.1MOL/L INCREMENTS	197
7.3.3	GLUCOSE EXTRACTED DATA	199
8.	ELECTRONIC CIRCUIT FOR MICROWAVE MEASUREMENTS	201
8.1	MINI-CIRCUITS MODULES.....	201
8.1.1	S-PARAMETERS AND PHASE MEASUREMENTS	202
8.1.2	MEASUREMENTS OF S-PARAMETERS ONLY.....	205
8.1.3	EXPERIMENTAL SETUP.....	206
8.1.4	POWER SUPPLY ISSUES.....	207
8.1.5	VCO CALIBRATION.....	208

8.1.6	POWER DETECTOR CALIBRATION.....	211
8.2	SURFACE MOUNTED COMPONENTS	213
8.2.1	DESIGN REQUIREMENTS.....	213
8.2.2	DESIGN 1-TEST BOARDS.....	214
8.2.3	DESIGN 2-TEST BOARDS.....	215
8.2.4	DESIGN 3-SINGLE BOARD	216
8.2.5	EXPERIMENTAL SETUP.....	217
8.2.6	CALIBRATIONS AND EXPERIMENTAL RESULTS	218
9.	CONCLUSION AND FURTHER WORK.....	221
9.1	CONCLUSION	221
9.1.1	CAVITY RESONATOR	222
9.1.2	MICROSTRIP RING RESONATOR.....	222
9.1.3	SUSPENDED MICROSTRIP RING RESONATOR	223
9.1.4	GLUCOSE TESTING.....	224
9.1.5	HANDHELD DEVICE DESIGN.....	224
9.2	FURTHER WORK	225
9.2.1	SUSPENDED RING RESONATOR	225
9.2.2	GLUCOSE TESTING	226
9.2.4	HUMAN TISSUES CHARACTERISATION.....	226
	TABLE OF ABBREVIATIONS.....	228
	REFERENCES	230

ABSTRACT

Road safety is one of the priorities for every government in Europe and including in the UK. One of the major concerns for road safety is the consumption of alcohol by drivers which seriously increases the risk of an accident. According to the department of transport in 2007, there were over 17,000 drink-drive casualties including 530 fatalities in England alone. For this reason, the police force needs a fast and easy way to assess the alcohol level of drivers. We propose a new method of detection, using microwaves, which would detect the alcohol-blood ratio from the finger/wrist of the driver. We also study the possibility of blood sugar detection for diabetes using microwave resonators.

The system is based on microwave resonators using very low power sources (1mW). This PhD project explores the limits and feasibility of a rectangular cavity resonator and a microstrip suspended ring resonator for use with water/ethanol samples and water/glucose samples. Samples of water/ethanol are tested in three parts for each sensor, 0% (water) to 100% (ethanol) in 5% increments, 1% to 5% in 1% increments and samples less than to 1% in 0.2% increments. Samples of water/glucose are tested from 0mol of glucose to 1mol per litre of water in 0.1mol/l increments. Both systems are studied, designed, simulated and tested for the full ranges of both mixtures. The data acquisition software has been written in C# in order to allow ease of data extraction and manipulation during the tests. Using variables such as the Q-factor, the resonant frequency and the reflection coefficient, the resonators can detect permittivity changes in the samples. The rectangular cavity is able to detect a lower limit of 1% of ethanol, and a tenth of a mole for water/glucose mixtures. The suspended ring resonator can detect down to 1% of ethanol using the Q-factor, the resonant frequency and the magnitude and down to 0.2% using the transmission magnitude at a fixed frequency. This method can also detect a lower limit of 0.1mol/l for glucose/water mixtures.

1 INTRODUCTION

1.1 Aim of the Project

This project started with the idea of investigating the possibility of a non-invasive system capable of measuring and quantifying ethanol molecules in the blood stream. The police are continuously seeking a passive technology capable of detecting drunk drivers on the road. Current methods of detection require the cooperation of the driver and a breath sample or a blood sample is required for analysis and measurement of alcohol. Despite a slight decrease in drink driving casualties over the years, the figures could be made lower by controlling drink drivers more efficiently. Figure 1.1 represents the estimated number of KSI (Killed or Seriously Injured) drink drive casualties in GB (Great-Britain) over the past 10 years. Figure 1.2, shows the total number of breath tests carried out and the number of positive/refused breath tests during the same period. These statistics have been published by the Department of Transport [1] for the year 2007. In that year there were a total of 247,780 casualties of all severities, 4% lower than in 2006. 2,946 people were killed, 7% lower than in 2006, 27,774 were seriously injured (down 3% on 2006) and 217,060 were slightly injured (down 4% on 2006).

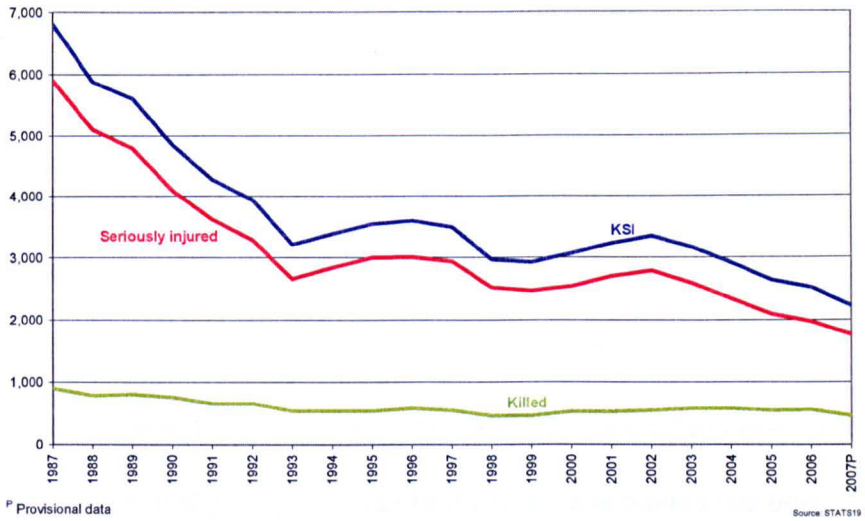


Figure 1.1. Estimated number of killed or seriously injured drink drive casualties, GB 1987-2007 [1].

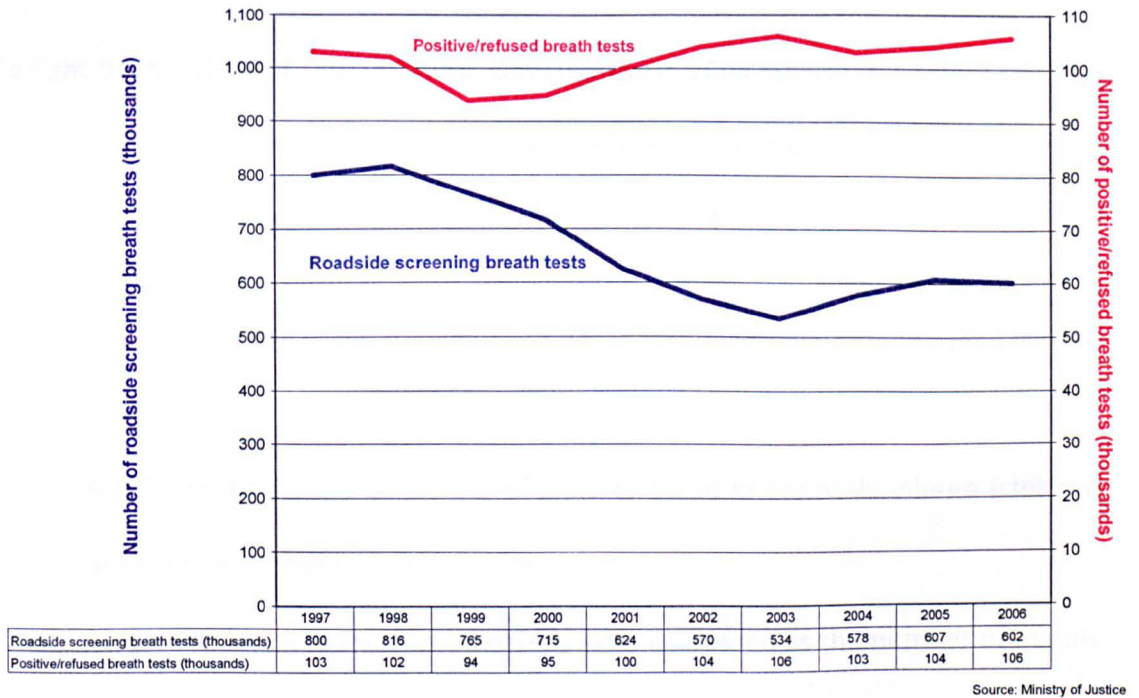


Figure 1.2. Roadside screening breath tests and breath test failures, England and Wales 1994-2006, [1].

Concerning drink driving, in 2007:

- It was estimated that 14,480 casualties (6% of all road casualties) occurred when someone was driving whilst over the legal limit for alcohol. The number of deaths was 460 (16% of all road deaths).
- The provisional number of killed or seriously injured casualties in 2007 was 2,220, approximately a quarter of the 1980 level and 12% below the 2006 level.
- The numbers of slight injuries due to drink drive accidents has been falling since 2002, but the provisional figures for 2007 suggests a rise of 3.5% compared to 2006.

To fight the numbers of casualties, the Government in 2000 published a safety strategy called 'Tomorrow's Roads Safer for Everyone' [2]. By 2010, the aim is to achieve, the following reductions compared with the average for 1994-98:

- A 40% reduction in the number of people killed or seriously injured (KSI) in road accidents;
- A 50% reduction in the number of children killed or seriously injured (children are defined as those aged under 16);
- A 10% reduction in the slight casualty rate, expressed as the number of people slightly injured per 100 million vehicle kilometres.

If the Government wants to reach its objectives, a new way of controlling and monitoring drink drivers must be rapidly developed. Therefore, the aim of this project consists of creating a system that could detect and quantify alcohol concentrations in test tube samples and to improve it in order to be able to control drink drivers using a passive reading, or at least prove the feasibility of such a complex task.

The possibility of measuring the amount of alcohol will be tested using microwave sensors (cavities, ring resonators and coplanar waveguides). Like all electromagnetic waves, microwaves have an electrical component as well as a magnetic component. When subject to microwave radiation, polar, semi-polar and non-polar materials will absorb part of the energy and their molecules will rotate according to the electric field.

Microwaves have the advantage (over other techniques) of being able to penetrate through bulk material in a non-invasive manner and thus provide a passive way of measuring or characterising a material. The energy used for a measurement is very small, in this case less than 1mW and therefore absolutely harmless to human body tissue.

For many years, this property of microwaves has been mainly used for cooking. The water, fat, and sugar molecules in food absorb energy from the microwaves in a process called dielectric heating. Many molecules (such as those of water) are electric dipoles, meaning that they have a positive charge at one end and a negative charge at the other, and therefore rotate as they try to align themselves with the alternating

electric field induced by the microwaves. This molecular movement creates heat as the rotating molecules hit other molecules and put them into motion.

At much lower power, the effect of microwaves on molecules has found a particular application in chemistry in a process called microwave spectroscopy (or rotational spectroscopy). A sample can be characterised by the attenuation and phase shift of a microwave field.

Microwave spectroscopy has been used principally on matter in the gas phase where the rotational motion of molecules can be calculated [3]. However, in solids or liquids, the rotational motion of molecules is much more complex. The rotational motion of molecules depends on two main parameters: the permittivity and the loss factor [4] which are also a function of the temperature and the pressure [5]. For this reason it is not possible to calculate the exact response of solids and liquids to microwave radiation. However, it is possible to interpolate the concentration of components by using multivariable calibration.

In this project multivariable calibration and microwave spectroscopy will be used to obtain a quantitative analysis of the alcohol present in a driver's blood. The method will be based on the response of a cavity resonator and a suspended ring resonator, into which a driver's finger is inserted. Microwaves are sent through the sensor and are affected by the properties of the finger tested. This type of approach has been used successfully in different applications. Based on the properties of electromagnetic wave, it has been possible to monitor the changes in the permittivity

of a fluid in a pipeline [6], to monitor the constituents of an oil pipeline [7] and to detect moisture present in food [8]. All these applications have shown the viability of compound detection using microwaves in solid and liquid media. The design of the cavity will influence the response of the media under test and will determine the accuracy of detection [9].

The in-vivo detection of chemical components, in this case alcohol, in the human body using this technique has not been researched before and offers a great opportunity. This research project presents for the first time, a novel technique for measuring the alcohol content in the blood stream using a suspended ring resonator.

1.2 Further Goals

Another application of the system is to detect blood-sugar levels. Over 2 million people in England are living with diabetes. Many more have the condition but do not know it. There are two types of diabetes, called type 1 and type 2. The causes of both types are different, but both result in poor regulation of glucose (sugar) in the blood stream.

Type 1 diabetes is caused by the body's failure to produce insulin. Insulin is a hormone released by the pancreas to help control levels of sugar in the blood. It is sometimes called juvenile diabetes or early-onset diabetes because it usually appears before the age of 40.

Type 2 diabetes is caused by the body not producing enough insulin or not using what it produces effectively. It is the most common form and accounts for around 90% of all diabetes.

Diabetes can increase the risk of developing other conditions, such as heart disease, kidney failure, eye damage, loss of feeling in the extremities (due to nerve damages) and sometimes lead to amputations. It can be managed effectively and many people with diabetes lead a healthy, active life. Diabetes can also occur in pregnancy. This is known as gestational diabetes. Some pregnant women have high levels of glucose in their blood because their bodies do not produce enough insulin to meet the extra demands of pregnancy. It affects less than one in 20 pregnant women and usually disappears after birth. However, women with gestational diabetes are more at risk of developing type 2 diabetes later in life [10]. Before home blood glucose testing became common, the only lancing device available was a sharp piece of stamped steel that made a painful and fairly deep cut in the fingertip. In parallel with the development of blood glucose meters, lancing devices also evolved.

Both small, disposable units and reusable “pens” with replaceable tips became commercially available, and these had the added advantage that the sharp point was hidden from view. They were also spring-loaded, so pushing a button replaced one’s own “stabbing” motion that was previously required to pierce the skin. Modern lancing devices have improved further, and most now feature adjustments to control depth of penetration of the needle. Needles are smaller and sharper, and recent devices have

been approved for “alternate site testing,” (obtaining blood from the forearm, upper arm, back of the hand, thigh or calf) but anybody who test their blood glucose would say that it still hurts sometimes and can cause bruising. Add the natural dislike of needles to the actual pain produced, to the social unacceptability of droplets of blood and bloody test strips and meters (and concerns about blood-borne diseases), and it is easy to understand why people have long looked for a measurement that does not involve taking blood. Also diabetics often have thicker hardened skin on the fingers and it is more difficult and painful to draw blood.

In the blood glucose monitoring industry, it is well accepted that there are three “C” terms that drive people’s willingness to test: Cost, Comfort and Convenience. The comfort advantage of a non-invasive less pain technology is easily understood, and since very few proposed non-invasive approaches need a test strip that is consumed every time a test is performed, there should be a clear cost advantage to both customers and insurance companies alike. The cost of meters, however, would most likely increase with a successful non-invasive approach—the projected cost for common non-invasive approaches varies from several hundred to several thousand dollars. Convenience includes such issues as how long a test takes, how obtrusive or visible the apparatus is, and whether a visible drop of blood is required to perform the test. This issue is more subjective and deals with the comfort level of people have to test in public, letting everyone know they have diabetes, as well as concerns about the sight of blood [11].

1.3 Defined Project Targets

The bullet points below define the project targets.

- Design an On-line NDT microwave sensor for alcohol (or glucose) detection/prediction in the blood stream using low power.
- Investigate the system's key features and their suitability, limits and feasibility.
- Support experimental results by theory/simulations.
- Develop data acquisition software, acquiring measurements from the sensor.
- The accuracy of the system should be capable of detecting the lower limit of the BAC (Blood Alcohol Concentration ratio) or as close as technically possible (BAC =0.8g/l in the UK).
- Test the system using water/ethanol sample before blood testing.
- Consider commercialisation concerns, cost and production options.
- Explore the achievability of the sensor for diabetes monitoring.

Summary

This chapter has discussed the need for a passive and non-invasive technique for alcohol detection and presented the novel aim of this work, which is to design such a sensor using microwave technology. It has also discussed the possible use of this sensor for detecting the blood-sugar concentration of diabetics.

2 ALCOHOL AND COMPOUND DETECTION

2.1 Alcohol and Human Metabolism

2.1.1 What is Alcohol?

Alcohol is a general term denoting a family of organic chemicals with common properties. From a chemical point of view, an alcohol is any organic compound in which a hydroxyl group (-OH) is bound to a carbon atom of an alkyl or substituted alkyl group. Members of this family include ethanol, methanol, isopropanol, and others.

In general usage, “alcohol” refers specifically to ethanol, also known as grain alcohol, formed by the fermentation of sugars. It also often refers to any beverage that contains ethanol.

As a result, what we call the alcohol percentage of a drink corresponds actually to its concentration in ethanol. The molecular formula of the ethanol is C_2H_6O , variously represented as EtOH or C_2H_5OH . For this report, we will always be referring to ethanol when mentioning alcohol. Table 2.1 below presents the main characteristics of ethanol [12].

Ethanol	
General	
Systematic name	Ethanol
Other names	Ethyl alcohol, grain alcohol, hydroxyethane, EtOH
Molecular formula	C ₂ H ₆ O
Dielectric constant, ϵ_r	24.3 ϵ_0 at 20 °C
Molar mass	46.06844(232) g/mol
Appearance	clear liquid
Index of refraction, n_{25}	1.361
Properties	
Density and phase	0.789 g/cm ³ , liquid
Solubility in water	Fully miscible
Melting point	-114.3 °C (158.8 K)
Boiling point	78.4 °C (351.6 K)
Acidity (pK_a)	15.9 (H ⁺ from OH group)
Viscosity	1.200 cP at 20 °C
Dipole moment	1.69 D (gas)

Table 2.1. Characteristics of Ethanol.

2.1.2 How Alcohol Enters the Body?

When a person drinks an alcoholic beverage, the alcohol begins to be absorbed into the body through the linings of the mouth and oesophagus. However, alcohol is mainly absorbed into the blood through the walls of the stomach (about 20%) and the intestines (about 80%). The alcohol is then distributed throughout the body via the bloodstream: it is dissolved in the blood and, as the blood circulates around the body, it enters and dissolves into the liquid of every tissue of the body. Major organs such as the liver, kidneys, lungs and brain absorb more alcohol. Organs such as the brain have special sensitivity to alcohol and its related compounds and therefore can be adversely affected [13].

The absorption and distribution of alcohol throughout the body happens quickly, within a few minutes of taking a drink, alcohol reaches the body's organs. How fast the alcohol is absorbed depends upon several factors:

- The concentration of alcohol in the beverage - the greater the concentration, the faster the absorption.
- The type of drink - carbonated beverages tend to speed up the absorption of alcohol.
- Whether the stomach is full or empty - food slows down alcohol absorption.

Once inside the tissues, alcohol exerts its effects on the body. The observed effects depend directly on the blood alcohol concentration (BAC), which is related to the

amount of alcohol consumed. The BAC can rise significantly within 20 minutes after having a drink [14].

2.1.3 How Alcohol Leaves the Body?

Once absorbed into the bloodstream, the alcohol leaves the body in three ways:

- The kidneys eliminate 5 percent of alcohol in the urine. To do this, the kidneys filter the blood – the blood is normally filtered about 20 times a day. Then, proteins and amino acids are reabsorbed into the blood. Waste and excess products do not get reabsorbed – they are excreted into the urine and then eliminated from the body. The kidneys also work to keep the volume of water in your body constant. Alcohol is a diuretic. If too much alcohol is consumed, the body eliminates more water than it absorbs – resulting in a dehydration, with dizziness and a headache.
- The lungs exhale 5 percent of alcohol, which can be detected by breathalyzer devices. The lungs take in air to bring oxygen to the body and get rid of waste carbon dioxide. When the alcohol in the bloodstream reaches the lungs, some of it passes into the lungs' air sacs and is evaporated into the air. It is then

exhaled and eliminated from the body. This is how alcohol is detected by breathalysers and why it can be smelled on the breath.

- The liver chemically breaks down the remaining alcohol (90%) into acetic acid. The breakdown, or oxidation, of ethanol occurs in the liver. An enzyme in the liver called alcohol dehydrogenase strips electrons from ethanol to form acetaldehyde. Another enzyme, called aldehyde dehydrogenase, converts the acetaldehyde, in the presence of oxygen, to acetic acid, the main component in vinegar. When ethanol is oxidized to acetic acid, two protons and two electrons are also produced. The acetic acid can be used to form fatty acids or can be further broken down into carbon dioxide and water.

The liver can only deal with a limited amount of alcohol at a time. If too much alcohol is taken into the body, the liver's store of glutathione runs out, leaving the toxic acetaldehyde to build up in the body. This can cause headache and nausea. It can take three hours or more to remove the alcohol from just one drink from your system – the rate depending on factors such as size and gender [13]. The concentration of alcohol in the body depends on the amount of water contained in that body. The more water present in the body, the more diluted the alcohol will become as it is absorbed into the system. As a result, for the same quantity of alcohol consumed, the Blood Alcohol Concentration (BAC) will vary according to the percentage of water in the body.

The maximum concentration of ethanol within the body tissues is achieved somewhere between 30 minutes and 90 minutes following consumption. The BAC increases when the body absorbs alcohol faster than it can eliminate it. The body can only eliminate about one unit of alcohol per hour, so consuming several drinks in an hour will increase your BAC much more than having one drink over a period of an hour or more.

As a rule of thumb, an average person can eliminate 15 ml of alcohol per hour. So, it would take approximately one hour to eliminate the alcohol from a 330ml can of beer [14].

2.1.4 The Effect of Alcohol

Drinking excessive amounts of alcohol will affect a person's performance and behaviour. The body responds to alcohol in stages, which correspond to an increase in BAC. Table 2.2 shows the different effects depending on the BAC.

BAC	Effect	
0.03-0.12	<i>Euphoria</i>	Become more self-confident or daring.
		Attention span shortens.
		May look flushed.
		Judgement is not as good
		Have trouble with fine movements, such as writing or signing their name.
0.09-0.25	<i>Excitement</i>	Become sleepy.
		Have trouble understanding or remembering things (even recent events).
		Do not react to situations as quickly.
		Body movements are uncoordinated.
		Begin to lose their balance easily.
		Their vision becomes blurry.
		May have trouble sensing things (hearing, tasting, feeling, etc.).
0.18-0.30	<i>Confusion</i>	Confused
		Dizzy and may stagger.
		Be highly emotional -- aggressive, withdrawn or overly affectionate.
		Cannot see clearly.
		Sleepy.
		Slurred speech.
		Uncoordinated movements (trouble catching an object thrown to them).
		May not feel pain as readily as a sober person.
0.25-0.40	<i>Stupor</i>	Can barely move at all.
		Cannot respond to stimuli.
		Cannot stand or walk.
		May vomit.
		May lapse in and out of consciousness.
0.35-0.50	<i>Coma</i>	Unconscious.
		Reflexes are depressed.
		Feel cool (lower-than-normal body temperature).
		Breathing is slower and more shallow.
		Heart rate may slow.
		May die.
> 0.50	<i>Death</i>	The person usually stops breathing and dies.

Table 2.2. BAC Concentration and its Effect [14].

2.2 Detection Techniques and Technologies

On the spot detection of a driver's alcohol level is now common place. The method used by the police is called breath analysis. The principle of this technique relies on the driver breathing into a probe usually via a mouthpiece, this probe will then give information on the presence of alcohol in the driver's blood. Some detectors do not require a mouthpiece. They are mainly used at police roadblocks or in high intensity testing (such as in factories). In this kind of test, most subjects who have not consumed alcohol will have a zero alcohol level. The important factor is therefore to test as many subjects as quickly as possible and with minimum cost per test, in order to pick out those subjects who do have alcohol in their system and who may therefore be required to undergo further testing. It is important to consider two possible results of a breath test:

- The first is a quantitative measurement of the subject's (i.e. driver) body alcohol concentration by analysis of deep lung or alveolar breath. This form of testing is generally carried out to determine if the level of alcohol is in excess of a non-zero limit.

- The second is a qualitative determination of alcohol to see if the subject has any alcohol at all in his or her body - but with no particular concern for how much. This form of test would be carried out in any country where it is forbidden to drive with alcohol in the body. It is also common in industry and the military.

The choice between these two types of measurement will depend mainly on the legislation in the country of use. In 1995, Breakspere and Williams [15], compared and studied the different aspects of breath analysers.

In the area of breath analysers, there exist many technologies dedicated to the detection of alcohol. It is important to review all of them. At the moment, the most widely used technique in breath analysis is infrared spectrometry. These analysers operate on the principle that organic substances absorb infrared light at different wavelengths depending on their molecular structure. The quantity of radiation absorbed depends on the concentration of the absorbing substance present in the sample, and is thus a measure of it.

The second most widely used technique for breath analysers is the fuel cell. Fuel cells are electrochemical devices that operate on the principle of oxidizing the sample. The alcohol undergoes a chemical oxidation reaction at a catalytic electrode surface to generate a quantitative electrical response. Since the volume of breath introduced into the fuel cell is constant, the electron flow is fully proportional to the amount of alcohol in the sample, and the electron flow generated, after passing through the instrument's measuring electronics, is displayed in terms of the concentration of alcohol present in the breath sample.

The last technique uses colorimeters to show the presence of alcohol. This method is purely chemical. The technique is based on the oxidation of alcohol by an acidified solution of potassium dichromate, resulting in a quantitative yellow to green

colour change. The analytical principle is also still employed in disposable alcohol detector tubes (the bag and tube) used essentially for screening purposes.

All those methods are “active” breath detection methods because the subject has to cooperate and blow properly into the mouthpiece. A true passive instrument, as the name suggests, requires the subject to do nothing. This is what the police want as it would allow them to test a lot of drivers, without any of the inconvenience of the “active” technique.

2.2.1 Infrared and Near Infrared Spectroscopy

Spectroscopy is the study of matter using light, sound, or particles that are emitted, absorbed or scattered by the matter under investigation. There are three possible interactions: absorption, emission and scattering [16]. Absorption is a highly significant interaction between electromagnetic radiation and matter. All matter absorbs electromagnetic waves to a certain degree and the absorption is frequency (or wavelength) dependent.

The spectroscopy methods based on absorption are analytical tools used to determine the concentration of a particular compound, and to study the structure of a substance. The spectroscopy method based on absorption uses electromagnetic frequencies that the substance absorbs. Electromagnetic waves at a particular

frequency travel through the matter. After calibration, the amount of absorption can be related to the concentrations of the material.

Ultraviolet/visible (UV/ Vis) absorption spectroscopy is usually performed on liquid samples whereas infrared (IR) spectroscopy is performed on liquid, semi-liquid (paste or grease), dried, solid samples or gases. Typically, X-rays are used to reveal chemical composition, and near ultraviolet to near infrared wavelengths are used to distinguish the configurations of various isomers.

At wavelengths corresponding to the resonant energy levels of the sample, some of the incident photons are absorbed, resulting in a drop in the measured transmission intensity and a corresponding dip in the spectrum. The absorption spectrum can be measured using a spectrometer and by knowing the shape of the spectrum, the optical path length and the amount of radiation absorbed, one can determine the structure and concentration of the compound [17].

Another possible interaction between electromagnetic waves and matter is the emission of a new electromagnetic wave. Emission spectroscopy uses the range of electromagnetic frequencies in which a substance radiates best. The substance first absorbs energy and then re-radiates this energy as electromagnetic waves with a different frequency. This energy can be from a variety of sources, including collision (either due to high temperatures or otherwise), and chemical reactions. Emission spectroscopy is mainly used to examine the discrete photon emissions radiated by a given element. The element first absorbs energy, elevating electrons to higher energy

levels, and then radiates this energy as characteristic emissions of light that are directly related to the decrease in electron energy as it drops back to the ground state.

The last effect that can occur is scattering. Scattering spectroscopy can determine certain physical properties by measuring the amount of light that a substance scatters at certain wavelengths, incident angles, and polarization angles [18].

Raman spectroscopy is a spectroscopic technique used in matter physics and chemistry to study vibrational, rotational, and other low-frequency modes in a system. It relies on inelastic scattering, or Raman scattering of monochromatic light, usually from a laser in the visible, near infrared, or near ultraviolet range. Phonons or other physical excitations in the system are absorbed or emitted by the laser light, resulting in the energy of the laser photons being shifted up or down. The shift in energy gives information about the phonon modes in the system.

Infrared spectroscopy yields similar, but complementary information. Light from the illuminated spot is collected with a lens and sent through a monochromator. Wavelengths close to the laser (due to elastic Rayleigh scattering) are filtered out and those in a certain spectral window away from the laser line are dispersed onto a detector. Spontaneous Raman scattering is typically very weak, and as a result the main difficulty of Raman spectroscopy is separating the weak inelastically scattered light from the intense Rayleigh scattered laser light. Raman spectrometers typically use holographic diffraction gratings and multiple dispersion stages to achieve a high degree

of laser rejection. A photon-counting photomultiplier tube (PMT) or, more commonly, a CCD camera is used to detect the Raman scattered light (frequency shift of a medium).

2.2.2 Infrared and Near Infrared Spectroscopy Applications

The different kinds of interaction between matter and electromagnetic waves has lead to thousands of applications but just a few of these relate to the human body. Human in-vivo compound detection is still a very large challenge. However, some techniques already exist and most of them are based on near infrared or infrared spectroscopy.

Near-infrared spectroscopy (NIRS) utilises the region of the electromagnetic spectrum between about 800 nm and 2500 nm. The typical applications of the near infrared spectroscopy include pharmaceutical, medical diagnostics, food and agrochemical quality control. One of its medical application is the process called pulse oximetry. Pulse oximetry is a non invasive method of measuring a person's oxygenation level by monitoring the percentage of haemoglobin which is saturated with oxygen (oxyhaemoglobin). A probe is attached to the patient's finger (Figure 2.1). This probe contains a pair of small light-emitting diodes facing a photodiode. One LED emits red light, with a wavelength of 660 nm, and the other emits infrared, 910 nm. Absorption at these wavelengths differs significantly between oxyhaemoglobin and its

deoxygenated form [20] as shown in figure 2.2, the oxy/deoxyhaemoglobin ratio can be calculated.

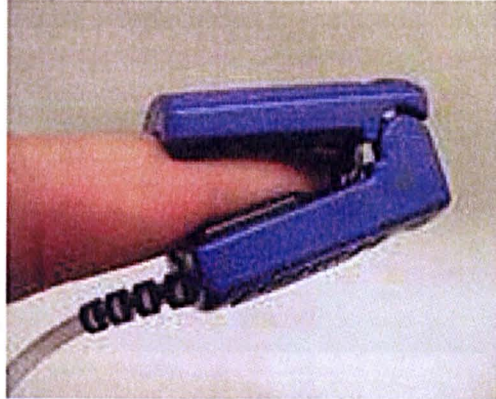


Figure 2.1. The Pulse Oxymetry Device [20].

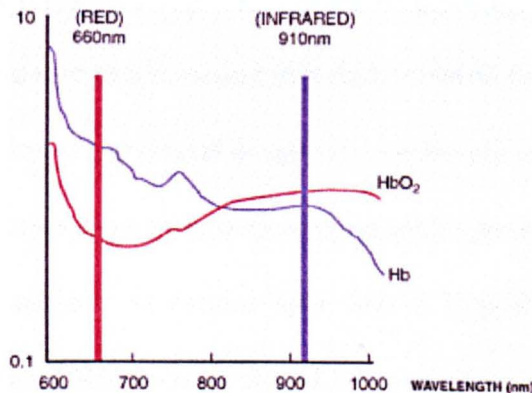


Figure 2.2. Oxygenated and Deoxygenated Haemoglobin Absorption Wavelength.

As the light from the two LEDs pass through the body tissues to the photo-detector, it is absorbed by blood and soft tissue (Figure 2.3). At the measuring site there are constant light absorbers that are always present. They are skin, tissue, venous blood, and arterial blood. However, with each heart beat the heart contracts and there is a surge of arterial blood, which momentarily increases arterial blood

volume across the measuring site (Figure 2.4). By examining only the varying part of the absorption spectrum, absorption due to tissues or nail polish [21] are ignored and only the absorption caused by arterial blood is analysed.

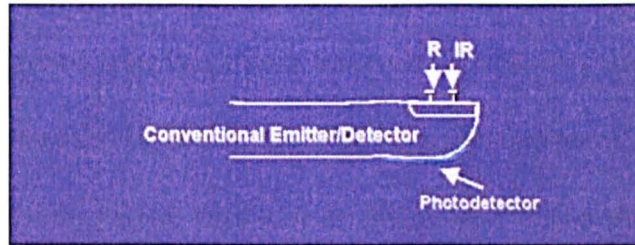


Figure 2.3. Principle of IR Absorption Spectroscopy [21].

The ratio of the transmitted red (R) and infrared (IR) signals are received by the photo-detector, is compared to a look-up table that converts the ratio to a SpO_2 value. The SpO_2 is the saturation of peripheral oxygen is an estimate of the oxygen saturation levels. Most manufacturers have their own look-up tables based on calibration curves derived from healthy subjects at various SpO_2 levels. Typically an R/IR ratio of 0.5 equates to approximately 100% SpO_2 , a ratio of 1.0 to approximately 82% SpO_2 , while a ratio of 2.0 equates to 0% SpO_2 .

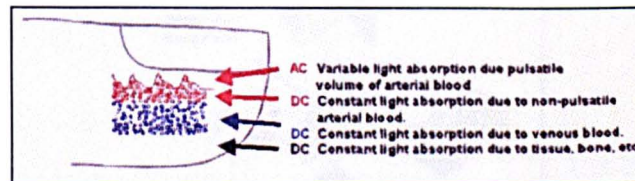


Figure 2.4. IR Absorption in a Finger [21].

If the light absorption at the trough (which should include all the constant absorbers) is subtracted from the light absorption at the peak then, in theory, the resultants are the absorption characteristics due to added volume of blood only; which is arterial. Since peaks occur with each heartbeat or pulse, the term "pulse oxymetry" was coined. This solved many problems inherent to oxymetry measurements in the past and is the method used today in conventional pulse oxymetry. It was important to present this application as the final aim of the project is the determination of the alcohol in the blood by monitoring a finger. As a result, this application is related to our project. This explanation was also necessary to introduce the existing non-invasive method of alcohol detection using infrared [22]. The system is named TruTouch and it has been designed by the company TruTouch Technology Inc. [23]. This technology is also based on near infrared spectroscopy and the method they used is based on the detection of alcohol through NIFTS (Near Infrared Fourier's Transform Spectrometer). The Fourier transform spectrometer (FTS) [24] is based on a Michelson configuration [25] (Figure 2.5).

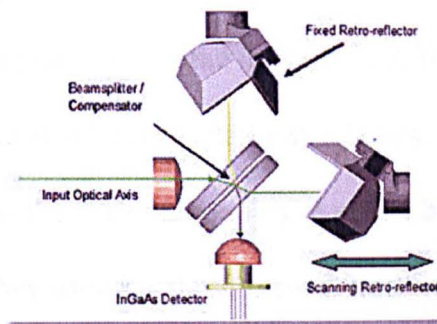


Figure 2.5. The Fourier Transform Spectrometer [25].

Moving the scanning retro-reflector alters the phase shift between the two beams producing sinusoidal intensity variations at the detector that have frequencies proportional to the wavelengths of the incoming light. The system is shown in use in figure 2.6.



Figure 2.6. The TruTouch Device [23].

The method of detection used is based on the detection of alcohol in the capillary blood of a thin layer of the skin [26]. It is currently very hard to find any technical information about their system as the technology is very well protected by commercial secrecy. However, the results presented are relevant to this study (Figure 2.7). As we can see in the graph presented in Figure 2.7, their results show an overall linearity in the detection of alcohol through the skin layers. Moreover, their technology shows a better result than the breath analysers. It would be interesting to know what kind of breath analyser they used for these results, however this information was not available.

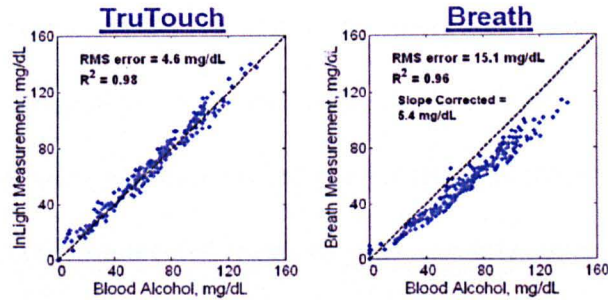


Figure 2.7. The TruTouch Measurement Results [22].

However, in this project, it was decided to use the microwave region, not the infrared. Microwaves are applied to a cavity resonator to monitor the alcohol. At the moment, this technology has already been used in the food industry. It is therefore essential to review this process [27].

The method used is called Guided Microwave Spectrometry (GMS). It can detect non-polar, semi-polar and polar components in a solid, semi-solid or fluid mixture flowing in a process stream [27]. It transmits milliwatts of microwaves through the sample to a sensor. Microwaves are directed through a waveguide in a confined area of the material under test.

Microwaves operate at a frequency range which is sufficiently low to be very sensitive to the presence of polar molecules (such as water) as well as DC conductivity changes (such as ion/salt concentrations). Microwaves also have the advantage of penetrating the entire mixture and not just the surface. The technique is being commercially used in food processing facilities [27].

As the microwaves penetrate through the material, the waves rotate molecules into or out of polar alignment. This spectroscopic technique is also called rotational spectroscopy as the spectrum depends of the rotation of the molecules. The energy needed to rotate the molecules reduces the velocity and wavelength of the microwaves as a function of the molecules' average dipole moment. Molecule responses change with frequency, thus a range of frequency is used (e.g. 0.2 GHz to 3.2 GHz).

The material under test is placed in a measurement chamber that mimics a section of RF waveguide. The GMS spectrometer applies a sinusoidal microwave signal to the material that passes through the sample in the chamber providing a representative measurement of the bulk product. The scalar response is measured over a wide bandwidth at wavelengths long enough to mitigate errors that can be introduced by reflections due to the particular dimensions. Due to the unique shape of the cavity, the electromagnetic energy is held within the waveguide thereby minimizing upstream and downstream turbulence effects.

In the presence of microwave energy, the polar molecules in the sample rotate and align themselves with the electromagnetic field, similar to aligning the poles on a magnet. The movement of the molecules causes the microwave signal to be attenuated and the velocity of the wave decreases as it passes through the sample.

Some of the most recent research conducted on the Guided Microwave Spectroscopy has been the detection of ethanol in different water-ethanol mixes.

This research was conducted in 2001 by Anthony D. Walmsley and Victoria C. Loades [28] from the Department of Chemistry of the University of Hull in England. Their research paper entitled "*Determination of acetonitrile and ethanol in water by guided microwave spectroscopy with multivariate calibration*" demonstrates the possibility of the detection of ethanol in different concentrations.

During their research, they used a GMS from Epsilon Industrial Inc. (the company which created the GMS process) which has a cavity resonator of 10.0 x 4.7 x 11.5 cm. They researched the possibility of detecting ethanol with an accuracy of 1.1%. They obtained those results using a combination of Partial least squares (PLS) and weighted ridge regression (WRR) to model the system.

2.2.3 Fuel Cells

Sir William Grove invented the first fuel cell in 1839. Grove knew that water could be split into hydrogen and oxygen by sending an electric current through it (a process called electrolysis). He hypothesized that by reversing the procedure it would be possible to produce electricity and water. He created a primitive fuel cell and called it a gas voltaic battery. After experimenting with his new invention, Grove proved his hypothesis. Fifty years later, scientists Ludwig Mond and Charles Langer coined the term fuel cell while attempting to build a practical model to produce electricity [29]. In principle, a fuel cell operates like a battery. Unlike a battery, a fuel cell does not run

down or require recharging. It will produce energy in the form of electricity and heat as long as fuel and electrodes are supplied.

Fuel cells generate electricity by a chemical reaction. Every fuel cell has two electrodes the anode and cathode (see Figure 2.8). The reactions that produce electricity take place at the electrodes. Every fuel cell also has an electrolyte, which carries electrically charged particles from one electrode to the other, and a catalyst, which speeds the reactions at the electrodes.

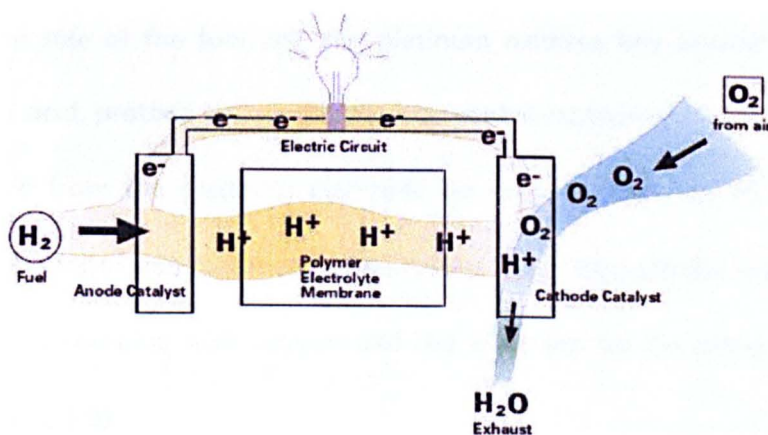


Figure 2.8. Principle of a fuel cell [29].

Hydrogen atoms enter a fuel cell at the anode where a chemical reaction strips them of their electrons. The hydrogen atoms are now ionized, and carry a positive electrical charge. The negatively charged electrons provide the current through wires to do work (i.e. provide electrical energy) [30]. Hydrogen is the basic fuel, but fuel cells also require oxygen. One great appeal of fuel cells is that they generate electricity with

very little pollution—much of the hydrogen and oxygen used in generating electricity ultimately combines to form water. A single fuel cell generates a small amount of direct current (typically 0.6V-0.7V). In practice, many fuel cells are usually assembled into a stack.

2.2.4 Fuel Cell Applications

Fuel cell breathalysers have two platinum electrodes with a porous acid-electrolyte material sandwiched between them. As the exhaled air from the subject flows past one side of the fuel cell, the platinum oxidizes any alcohol in the air to produce acetic acid, protons and electrons. A current is measured as the electrons flow through a wire from the platinum electrode on one side (anode) to the platinum electrode on the other side (cathode). The protons move through the lower portion of the fuel cell and combine with oxygen and the electrons on the other side to form water (See Figure 2.9).

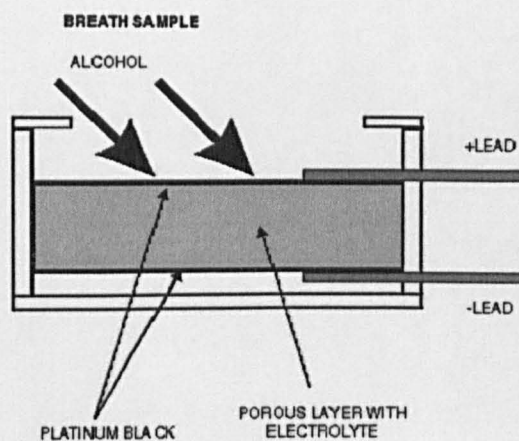


Figure 2.9. Fuel Cell used for breath alcohol detection [31].

When introducing a precise volume of breath sample into a fuel cell quickly, the output current from the cell rises from zero to a peak, and then ultimately decays back to zero. The rate at which this happens is highly dependent on the load resistor across the output terminals of the sensor. Traditionally, measurement instruments used fuel cells with load resistors of several hundred to one thousand ohms and used the amplitude of the voltage peak across the resistor as the measure of alcohol content in the sample. The Intoximeters, including the AlcoSensor's range uses a peak measurement technique. Although this technique produces good linearity, the time to complete the conversion of alcohol to electric current increases because of the load resistance of the measurement circuit. The more alcohol there is oxidize, the greater the electrical current. A microprocessor then measures the electrical current and calculates the BrAC (BReath Alcohol Concentration) [31].

Another example of fuel cell application is the Secure Continuous Remote Alcohol Monitor (SCRAM) Bracelet. The system is a tamper-proof ankle tag that allows police and probation authorities to constantly monitor criminals' alcohol consumption while they are on probation or bail (is being introduced in states across the US). If a person is convicted of crimes such as drink driving, or being drunk and disorderly, courts can use the system to impose a drinking ban as an alternative to prison. It weighs 227g and consists of two modules that are held on opposite sides of the subject's ankle by a strap and a tamper clip, resembling an electronic ankle tag. The

right side contains the ethanol sensing circuits (fuel cells) that measure the TAC (Transdermal Alcohol Concentration). The left side electronics are for security (obstructing, interfering), tamper detection, temperature sensing and removal detection. It incorporates technology using the science of transdermal testing to determine a person's TAC level. The device measures insensible perspiration (gaseous), which is the constant, imperceptible excretion of sweat through the skin using a fuel cell. The average person emits approximately one litre of insensible perspiration each day. SCRAM measures the ethanol gas in this insensible perspiration, which is a predictable result of alcohol consumption. Figure 2.10 shows how the bracelet is worn.



Figure 2.10. The SCRAM bracelet [32].

2.2.5 Other Methods for Alcohol Detection

The earliest technique for alcohol screening is colorimetry. The first Alco test device was developed in 1953 and found early broad application in police practice. The first devices were blowing tubes and bags, which indicated the content of alcohol in

the breath sample by a colour change, using a chemical reaction (Figure 2.11). Today these tubes are still being produced but mainly for private use self-check and police screening. The original function mode of the early Alco-test appears today with the name of Alco-check test tube.



Figure 2.11. The Alco-Check Device (left picture); (right picture) from left to right: unused tube, below the limit, reached the limit, above the limit [34].

The approximate content of alcohol in the exhaled air is indicated by means of a reaction of ethanol with the chemicals contained in the tube which cause a colour change. The tubes contain silicagel and a mixture of potassium dichromate and sulphuric acid. If ethanol is present in the breath sample, then the yellow potassium dichromate is reduced to green chrome. The colorimeter therefore uses the oxidation properties of ethanol. The content of ethanol is indicated by the length of the colour change. A line serves as a marker for the drink driving limit. The size of the breath sample has to be the same for each measurement as the system has been calibrated for a certain amount of breath; this is why a bag is used. Tests are only usable once [34].

Another colorimetric device (Figure 2.12) uses saliva to detect the Saliva Alcohol Concentration (SAC). Alco-Screen produces a colour change in the presence of saliva alcohol ranging from a light green-gray colour at 0.02% blood alcohol concentration to a dark blue-gray colour near 0.30% blood alcohol concentration. It consists of a plastic strip with a reactive pad situated at one end.



Figure 2.12. The Alco Screen Device [33].

The strip's tip will turn shades of green to blue depending on the amount of alcohol using alcohol oxidase and peroxidase chemistry. Colour blocks are provided within this range to allow an approximation of blood alcohol concentration to be made [33].

Summary

This chapter explains how the human body excretes consumed alcohol and discusses the various techniques currently used for alcohol detection and the use of electromagnetic waves for the detection and characterisation of materials.

3 ELECTROMAGNETIC WAVES IN THE MICROWAVE REGION

3.1 Properties of Electromagnetic Waves

The existence of electromagnetic waves (including microwaves) was predicted by James Clerk Maxwell in 1864, using the equations that are now named after him. In 1888, Heinrich Hertz was the first to demonstrate the existence of electromagnetic waves by building an apparatus that produced and detected waves in the UHF region. For time varying fields in the presence of a dielectric, the Maxwell equations take on the following forms:

$$\nabla \cdot D = \rho \tag{3.1}$$

$$\nabla \times E = -\frac{\partial B}{\partial t} \tag{3.2}$$

$$\nabla \cdot B = 0 \tag{3.3}$$

$$\nabla \times H = J + \frac{\partial D}{\partial t} \tag{3.4}$$

Where D is the electric flux density, ρ is the (free) charge density, E is the electric field intensity, B is the magnetic flux density, H is the magnetic field intensity, c is the speed of light and J is the free current density [35].

The microwave range includes ultra high frequency (UHF) (0.3-3 GHz), super high frequency (SHF) (3-30 GHz), and extremely high frequency (EHF) (30-300 GHz) signals. Microwave is a term loosely applied to identify electromagnetic waves above 300 megahertz in frequency because of the short physical wavelengths of these frequencies. Short wavelength energy offers distinct advantages in many applications. For instance, excellent directivity can be obtained using relatively small antennas and low-power transmitters. These features are ideal for use in both military and civilian radar and communication applications. On the other hand, microwave frequencies present special problems in transmission, generation, and circuit design that are not encountered at lower frequencies. The concept of electromagnetic field interaction is not entirely new, since electromagnetic fields form the basis of all antenna theory [36].

An electromagnetic wave consists of two fields, an electric field and a magnetic field, which are perpendicular to each other and to the direction of propagation of the wave front. Figure 3.1 shows a representation of a propagating electromagnetic wave [37]. The fields quantities, units and symbols related to the electromagnetic wave are presented in table 3.1.

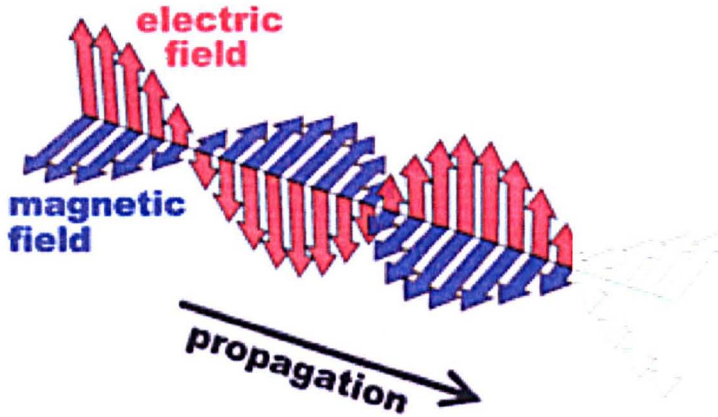


Figure 3.1. Schematic view of an electromagnetic wave [37].

	Field Quantity	Symbol	Unit
Electric	Field Intensity	E	V/m
	Flux density	D	C/m ²
Magnetic	Field Intensity	H	A/m
	Flux density	B	T

Table 3.1. Electric and magnetic field quantities. [38]

The electric field results from the charge distribution of the voltage, and the magnetic field results from the flow of current. The electric and magnetic fields that radiate from an antenna form the electromagnetic field. This field is responsible for the transmission and reception of electromagnetic energy through free space. An antenna, however, is also part of the electrical circuit of a transmitter or a receiver and is equivalent to a circuit containing inductance, capacitance, and resistance. Therefore, the antenna can be expected to display definite voltage and current relationships with

respect to a given input. A current through the antenna produces a magnetic field, and a charge distribution on the antenna produces an electric field. These two fields combine to form the induction field [39]. However, the induction field refers to the stored energy around an antenna rather than the transmitted energy.

Electromagnetic waves exist at different wavelengths and frequencies but include groups such as radio waves, microwaves, infrared radiation, visible light, ultraviolet radiation, X-rays, and gamma rays. Collectively, these wavelengths and frequencies make up the electromagnetic spectrum, as shown in figure 3.2. Microwaves are electromagnetic waves with wavelengths longer than those of Terahertz (THz) wavelengths, but relatively short for radio waves. Microwaves have wavelengths approximately in the range of 30 cm (frequency = 1 GHz) to 1 mm (300 GHz). However, the boundaries between far infrared light, Terahertz radiation, microwaves, and ultra-high-frequency radio waves are fairly arbitrary [40].

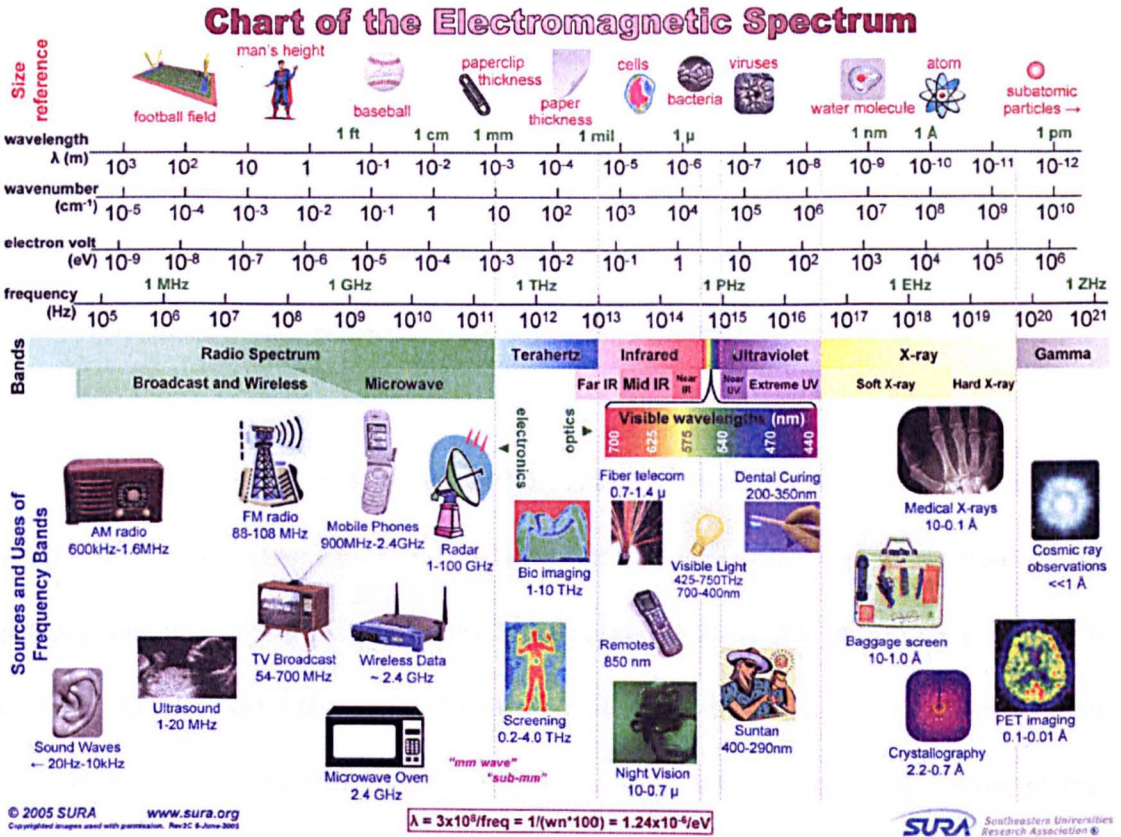


Figure 3.2. Representation of the electromagnetic spectrum [41].

3.1.1 The Electric Field

Around every electrically charged object is a force field that can be detected and measured. This force field can cause electric charges to move in the field. When an object is charged electrically, there is either a greater or a smaller concentration of electrons than normal. Thus, a difference of potential exists between a charged object and an uncharged object. An electric field is, therefore, associated with a difference of potential, or a voltage.

This invisible field of force is commonly represented by lines that are drawn to show the paths along which the force acts. The lines (flux) representing the electric field are drawn in the direction that a single positive charge would normally move under the influence of that field. A large electric force is shown by a large concentration of lines; a weak force is indicated by a few lines.

When a capacitor is connected across a DC voltage source it will begin to accumulate charge (See Figure 3.3) Because of the EMF (electromotive force) of the battery, negative charges flow to the lower plate, leaving the upper plate positively charged. As the stored charge increases, the electric field also builds up. The flux lines are directed from the positive to the negative charges and at right angles to the plates. When the capacitor is fully charged, the voltage of the capacitor is equal to the voltage of the source. The charged capacitor stores the energy in the form of an electric field. It can be said, therefore, that the presence of an electric field indicates voltage or potential difference.

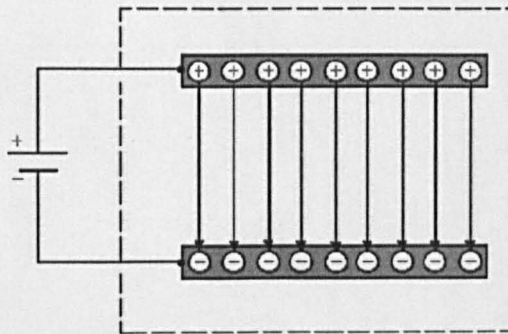


Figure 3.3. Capacitor charged by a DC battery, creating electrical fields [38].

If changed to an AC voltage source, the direction of the polarity of the electric field will change periodically at the frequency of the voltage source. The electric field will build up from zero to a maximum in one direction and then collapse back to zero. Next, the field will build up to maximum in the opposite direction and then collapse back to zero. This complete reversal occurs during a single cycle of the source voltage.

The half-wave dipole antenna (two separate rods in line as illustrated in Figure 3.4) is the fundamental element normally used as a starting point in any discussion concerning the radiation of electromagnetic energy into space. If RF (Radio Frequency) energy from the ac generator (or transmitter) is supplied to the element of an antenna, the voltage across the antenna lags the current by 90 degrees. The antenna acts as if it were a capacitor [38].

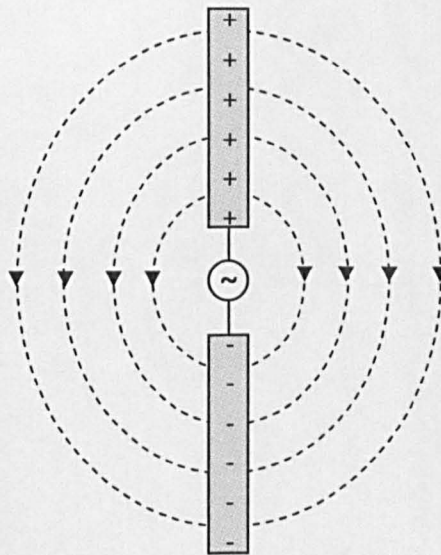


Figure 3.4. Electrical Fields of a Half-Wave Dipole Antenna.

3.1.2 The Magnetic Field

When current flows through a conductor, a magnetic field is set up in the area surrounding the conductor (i.e. any moving electric charge creates a magnetic field). The magnetic field is a region in space where a magnetic force can be detected and measured. There are two other fields involved—an induction field (or near field), which exists close to the conductor carrying the current, and the radiation field (or far field), which travels through space. To represent the magnetic field, lines of force are used to illustrate the energy. Magnetic lines are created by the flow of current rather than the change of voltage. The magnetic lines of force, therefore, are drawn at right angles to the direction of current flow. In Figure 3.5, the magnetic field shown in black are created by the current flow shown in red.

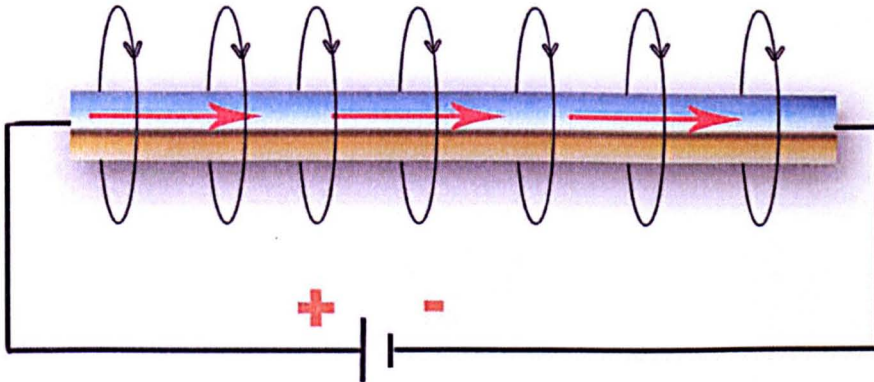


Figure 3.5. Magnetic fields created in a cable by current flow supplied by a DC power source[37].

There is a quick way to remember the direction of both fields. The method is called 'The Right Hand Rule' [37, 38].

3.1.3 Transmission System Properties

For every device shown on the electromagnetic spectrum, transmission of energy is necessary. Transmission systems are used to transfer energy from one point to another. The energy transferred may be electrical power, or digital/analogue/optical signals. The system may be a transmission line such as waveguide, a microstrip line, a coplanar waveguide, an optical fiber or a cable.

Historically the bifilar cables line is the first type of transmission line used for telegraphic communications and telephones. Two conductors are held using insulated holders regularly spaced approximately every 20cm, and having the air as the dielectric. Figure 3.6 shows the profile of bifilar cables.

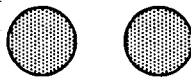


Figure 3.6. Bifilar cables.

The losses were very low and allowed communications over 20-30km without any intermediate amplification.

Coaxial lines have larger bandwidths which allow a few hundred telephone communications at once when the signal is modulated in frequency. Figure 3.7 displays the profile view of a coaxial cable.

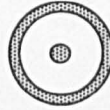


Figure 3.7. Coaxial line.

The exterior conductor cylinder protects the inner conductor against losses and interference. The distance between the outer and inner conductors is kept constant by adding a cylinder of dielectric between them.

Some other well known types of transmission lines are the microstrip (figure 3.8(a)), the slot line (figure 3.8(b)) and the coplanar waveguide (figure 3.8(c)). They have an essential part in laboratory testing and in passive component production.

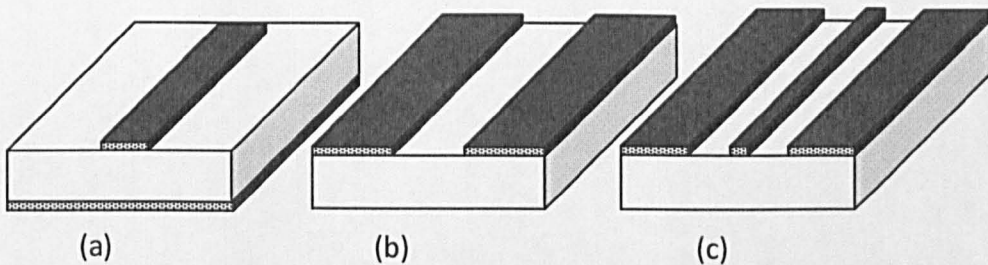


Figure 3.8. Microstrip line (a), Slot line (b) and coplanar waveguide (c).

The microstrip line composes a dielectric substrate completely metalised on one side (ground) and has a metallic line on the other side. The slot line does not have

a ground plane. The two conductors forming the transmission line are on the same side of the dielectric. The coplanar waveguide has three metallic strips on the same side of the dielectric, separated by two air slots.

Waveguides are perhaps the most used type of transmission line used for frequencies above 2GHz. Figure 3.9 shows the two most common kinds of electrical waveguide, rectangular and circular. They are usually made of copper or brass. As their length is usually a multiple of the wavelength, they are typically used for microwave frequencies (1GHz-300GHz rarely below).

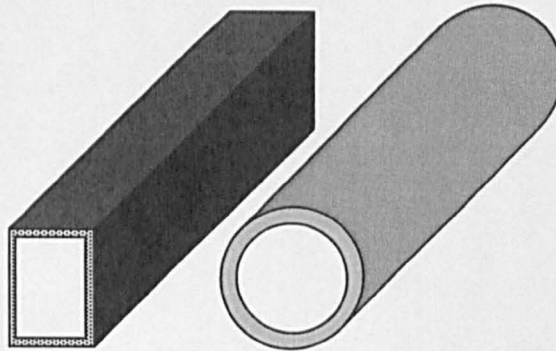


Figure 3.9. Rectangular and circular waveguides.

Their losses are very small because air is used as the dielectric, and their walls present very little Joule losses. They are easy to build and offer total protection against interference.

The last type of transmission line presented in this thesis is the dielectric waveguide. The core is a dielectric completely surrounded by another dielectric. The profile view is shown in figure 3.10.

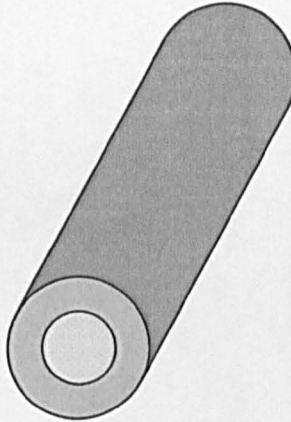


Figure 3.10. Dielectric waveguide.

The waves propagate by consecutive reflection at the interface between the two dielectrics similarly to the reflection between air and walls in a metallic waveguide. Fibre optics are dielectric waveguides [42].

3.1.4 Structure Transitions

When building microwave circuits, it is impossible to avoid transition between different type of structures (coaxial line to waveguide, coaxial line to microstrip, rectangular to circular waveguide, etc). The function of a microwave transition is to couple the electromagnetic wave from one type of transmission structure to another.

It transforms the electromagnetic field distribution of a transmission structure to conform to the boundary conditions of another transmission structure [39]. Figure 3.11 shows different structures and their fields. The solid lines represent the electric fields and the dashed lines represent the magnetic fields.

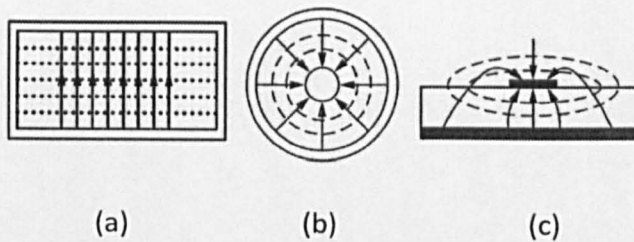


Figure 3.11. Field distribution of three types of transmission structure, rectangular waveguide (a), Coaxial line (b), Microstrip (c) [43].

The objective of a transition design is to make the transformation between different types of transmission structures as efficient as possible. To obtain good transformations, two requirements should be considered: impedance matching and field matching. The transition from one structure to another needs to be made gradually. To achieve both field matching and impedance matching, most of the transitions use step transition or continuous taper transition approaches.

3.2 Reflection, Transmission and Standing Waves

Microwaves or optical waves have a high probability of encountering obstacles along their transmission path (see Figure 3.12). An obstacle is a medium with finite

boundaries which causes perturbation/change in the direction of the waves. An incident plane travelling in the first medium hits the boundary of a second medium. If the second medium is a perfect conductor, then all the energy in the plane wave is reflected. If the second medium is a dielectric, part of the wave is reflected and part is transmitted (or refracted). The sum of the transmitted wave and the reflected wave is always equal to the incident wave, this is a fundamental equation.

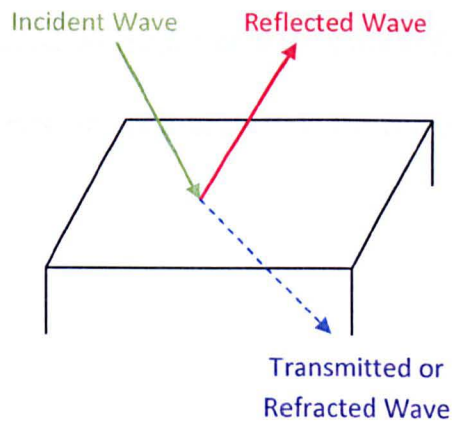


Figure 3.12. Wave properties.

3.2.1 Wave Normally Incident On a Conductor

In figure 3.13, medium 1 is a dielectric characterised by its permittivity ϵ and its permeability μ in which the incident wave (\vec{E}_i, \vec{H}_i) and reflected wave (\vec{E}_r, \vec{H}_r) propagate. Medium 2 is a perfect conductor, inside which the electromagnetic field is nil. Σ is the interface between these two media.

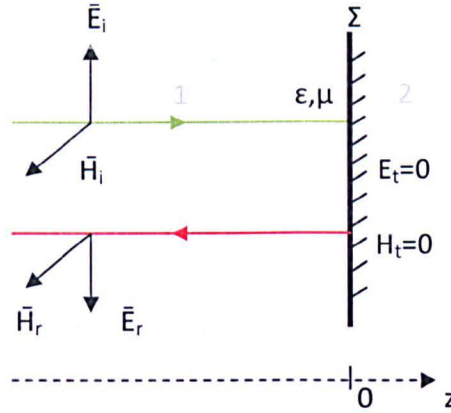


Figure 3.13. Plane wave normally incident on a conductor.

The incident wave is perpendicular with the surface Σ , as well as \vec{E}_i and \vec{H}_i . If the Oz axis is parallel with the direction of propagation, the complex instant value of \vec{E}_i and \vec{H}_i are given by:

$$\bar{e}_i(z,t) = \bar{E}_i e^{j(\omega t - kz)} \tag{3.5}$$

$$\bar{h}_i(z,t) = \bar{H}_i e^{j(\omega t - kz)} \tag{3.6}$$

$$k = \frac{2\pi}{\lambda} \text{ wave number}$$

At the conductor, the incident wave is reflected and the resulting reflected wave (\vec{E}_r, \vec{H}_r) propagates perpendicularly to Σ and in the reverse direction ($-\bar{z}$). The expressions for \vec{E}_r and \vec{H}_r in instant complex values are as follows:

$$\bar{e}_r(z,t) = \bar{E}_r e^{j(\omega t + kz)} \tag{3.7}$$

$$\bar{h}_r(z,t) = \bar{H}_r e^{j(\omega t + kz)} \tag{3.8}$$

We then obtain the ratios which define the intrinsic impedance (ζ):

$$\frac{E_i}{H_i} = -\frac{E_r}{H_r} = \zeta = \sqrt{\frac{\mu}{\epsilon}} \quad (3.9)$$

The three axes formed by vectors \vec{E} , \vec{H} , and \vec{z} must remain the same, as the reflected signal is travelling in the reverse direction, therefore, $\vec{E}_i = -\vec{E}_r$ and $H_i = H_r$. Figure 3.14 shows the change of direction of the fields of a electromagnetic wave normally incident on a perfect conductor.

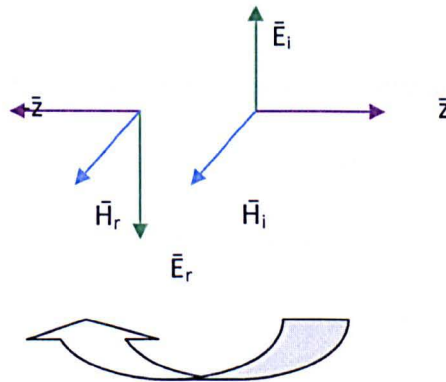


Figure 3.14. Change of direction of normally incident wave against a perfect conductor.

The overall electromagnetic field at a point z in the dielectric is the result of the superposition of the incident wave and the reflected wave:

$$\begin{aligned} \vec{e}(z,t) &= \vec{E}_i e^{j(\omega t - kz)} + \vec{E}_r e^{j(\omega t + kz)} \\ &= \vec{E}_i (e^{-jkz} - e^{jkz}) e^{j\omega t} \end{aligned} \quad (3.10)$$

$$= -2j \bar{E}_i \sin kz e^{j\omega t}$$

$$\begin{aligned} \bar{h}(z,t) &= \bar{H}_i e^{j(\omega t - kz)} + \bar{H}_r e^{j(\omega t + kz)} & (3.11) \\ &= \bar{H}_i (e^{-jkz} + e^{jkz}) e^{j\omega t} \\ &= 2 \bar{H}_i \cos kz e^{j\omega t} \end{aligned}$$

Another expression of $\bar{e}(z,t)$ is:

$$\bar{e}(z,t) = 2 \bar{E}_i \cos(kz - \pi/2) e^{j(\omega t - \pi/2)} \quad (3.12)$$

This means that the electric field and the magnetic field are always at a $-\pi/2$ angle in time and space. Therefore, a standing wave can be created:

- In the Σ plane, and in every plane situated at $n(\lambda/2)$ (n is an integer), the electrical field is nil and the magnetic field is maximal or minimal.
- In every plane situated at $(2n+1)\lambda/4$, it is the opposite, the electrical field is maximal or minimal and the magnetic field is nil.

Note that polarisation problems are not difficult in the case of normally incident waves because the electric and magnetic fields keep a uniform polarisation at any point in space.

3.2.2 Wave Obliquely Incident on a Conductor

In figure 3.15, the incident plane is defined by yOz . There are two fundamental polarisations:

- If the electrical field E is perpendicular to the incident plane (the magnetic field H is then parallel to the incident plane). This polarisation is called T.E. (Transverse Electric) mode.
- If the magnetic field H is perpendicular to the incident plane (the electric field E will also be parallel to the incident plane). This is called T.M. (Transverse Magnetic) mode.

If \vec{E} is perpendicular with the incident plane: T.E. mode

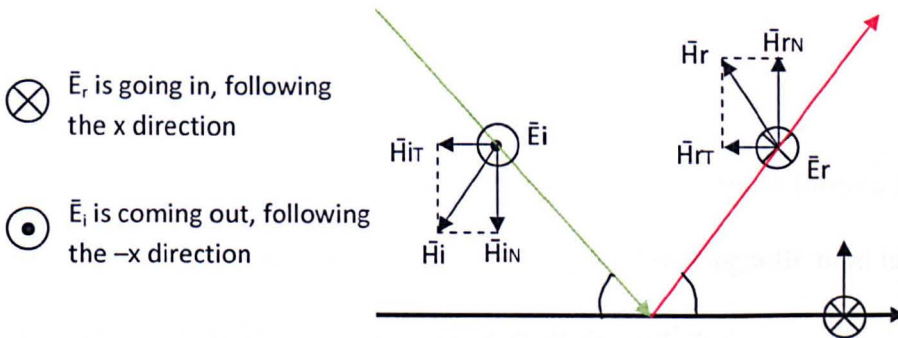


Figure 3.15. T.E. Reflection on Perfect Conductor at an angle.

The incident wave

By applying the rule of continuity of the vectors \vec{E} , \vec{H} and z and knowing the properties of the surface Σ ($E_{iT} + E_{rT} = 0$): $\vec{E}_i = -\vec{E}_r$. The magnetic field H can be decomposed into two vectors. The vectors H_{iN} being the vector perpendicular to the surface Σ , and the vector H_{iT} being the tangent (or parallel vector) to the surface Σ . The expressions of the \vec{E}_i and \vec{H}_i fields in complex amplitude are the following:

$$E_{ix} = -\vec{E} e^{jky \sin \Psi} e^{-jkz \cos \Psi} \quad (3.13)$$

$$H_{iy} = \vec{H} \cos \Psi e^{jky \sin \Psi} e^{-jkz \cos \Psi} \quad (3.14)$$

$$H_{iz} = -\vec{E} \sin \Psi e^{jky \sin \Psi} e^{-jkz \cos \Psi} \quad (3.15)$$

\vec{E} and \vec{H} are the amplitude at the origin of the electric field and magnetic field of the incident wave.

The reflected Wave

The electric field is still perpendicular to the incident plane formed by yOz and therefore has only one constituent in the x direction. The magnetic field is still in the incident plane and therefore, has two constituents in y and z .

$$\vec{E}_{rx} = \vec{E} e^{-jky \sin \Psi} e^{-jkz \cos \Psi} \quad (3.16)$$

$$\vec{H}_{ry} = \vec{H} \cos \Psi e^{-jky \sin \Psi} e^{-jkz \cos \Psi} \quad (3.17)$$

$$\vec{H}_{rz} = -\vec{E} \sin \Psi e^{-jky \sin \Psi} e^{-jkz \cos \Psi} \quad (3.18)$$

Total fields

On any point of the dielectric, the electromagnetic state is the superposition of the incident wave and the reflected wave. The complex amplitudes of the resulting fields are:

$$E_x = -2jE \sin(ky \sin \Psi) e^{-jkz \cos \Psi} \quad (3.19)$$

$$H_y = -2jH \cos \Psi \sin(ky \sin \Psi) e^{-jkz \cos \Psi} \quad (3.20)$$

$$H_z = -2H \sin \Psi \cos(ky \sin \Psi) e^{-jkz \cos \Psi} \quad (3.21)$$

It is now possible to know in which direction the energy is propagating by calculating the three Poynting's vector:

$$\bar{P}_x = \frac{1}{2} \bar{E}_x \bar{H}^* \quad (3.22)$$

$$\bar{P}_x = \frac{1}{2} (E_y H_z^* - E_z H_y^*) = 0 \quad (3.23)$$

Therefore there is no propagation of energy in the Ox direction.

$$\bar{P}_y = \frac{1}{2} (E_z H_x^* - E_x H_z^*) = -\frac{1}{2} E_x H_z^* \quad (3.24)$$

$$\bar{P}_y = -j2EH \sin \Psi \sin(ky \sin \Psi) \cos(ky \sin \Psi) \quad (3.25)$$

Note that \bar{P}_y is purely imaginary. The energy that propagates in the Oy direction is the reactive power.

$$\bar{P}_z = \frac{1}{2} (E_x H_y^* - E_y H_x^*) = -\frac{1}{2} E_x H_y^* \quad (3.26)$$

$$\bar{P}_z = 2EH \cos \Psi \sin^2 (ky \sin \Psi) \quad (3.27)$$

\bar{P}_z is a real number: The power propagating in the Oz direction is the real power. The propagation is characterised by a standing wave in the y direction perpendicular to the surface \mathcal{L} , and by a travelling wave in the Oz direction.

The wave impedance of propagation of the active power in the Oz direction is given by:

$$\zeta_z = -\frac{E_y}{H_x} = \frac{E}{H \cos \Psi} \quad (3.28)$$

$$\zeta_{TE} = \frac{\zeta}{\cos \Psi} \quad (3.29)$$

If \vec{H} is perpendicular with the incident plane: T.M. mode

Figure 3.16 shows the reflection of wave in TM mode on a perfect conductor at an angle.

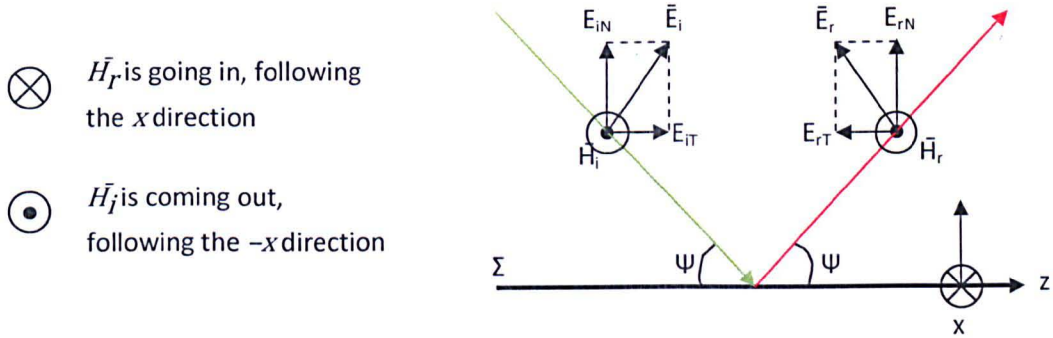


Figure 3.16. T.M. Reflection on Perfect Conductor at an angle.

Incident Wave

Again, the electric field \underline{E} being in the incident wave plane, can be decomposed in two vectors: The vectors E_{iN} being the vector perpendicular to the surface Σ , and the vector E_{iT} being the tangent (or parallel vector) to the surface Σ . The expressions of the \vec{E}_i and \vec{H}_i fields in complex amplitude are the following:

$$H_{iX} = -H e^{jky \sin \Psi} e^{-jkz \cos \Psi} \tag{3.30}$$

$$E_{iy} = E \cos \Psi e^{jky \sin \Psi} e^{-jkz \cos \Psi} \tag{3.31}$$

$$E_{iz} = E \sin \Psi e^{jky \sin \Psi} e^{-jkz \cos \Psi} \tag{3.32}$$

Reflected Wave

Considering that $\vec{E}_{iT} + \vec{E}_{rT} = 0$ at the surface Σ and by respecting the continuity and direction of vectors $\vec{E}, \vec{H}, \vec{z}$.

$$\vec{E}_i = -\vec{E}_r \quad (3.33)$$

$$\vec{H}_i = \vec{H}_r \quad (3.34)$$

The expressions of \vec{E}_r and \vec{H}_r then become:

$$H_{rx} = -H e^{-jky \sin \Psi} e^{-jkz \cos \Psi} \quad (3.35)$$

$$E_{ry} = E \cos \Psi e^{-jky \sin \Psi} e^{-jkz \cos \Psi} \quad (3.36)$$

$$E_{rz} = -E \sin \Psi e^{-jky \sin \Psi} e^{-jkz \cos \Psi} \quad (3.37)$$

Total fields

The complex amplitude of the superposition of both waves decomposed in x , y and z gives:

$$H_x = -2H \cos(ky \sin \Psi) e^{-jkz \cos \Psi} \quad (3.38)$$

$$E_y = 2E \cos \Psi \cos(ky \sin \Psi) e^{-jkz \cos \Psi} \quad (3.39)$$

$$E_z = 2jE \sin \Psi \sin(ky \sin \Psi) e^{-jkz \cos \Psi} \quad (3.40)$$

Calculating average Poynting's vectors again, one can demonstrate that \vec{P}_x is nil, \vec{P}_y is purely imaginary and \vec{P}_z is a real number. This means that there is only real

power propagated in the Oz direction. In the magnetic transverse mode, the wave impedance is given by:

$$\zeta_z = -\frac{E_y}{H_x} = \frac{E}{H} \cos \Psi \quad (3.41)$$

$$\zeta_{TM} = \zeta \cos \Psi \quad (3.42)$$

3.2.3 Reflection and Transmission between Two Dielectrics

If \vec{E} is perpendicular with the incident plane: T.E. mode

Figure 3.17 shows the reflection and transmission of a magnetic wave between two dielectrics.

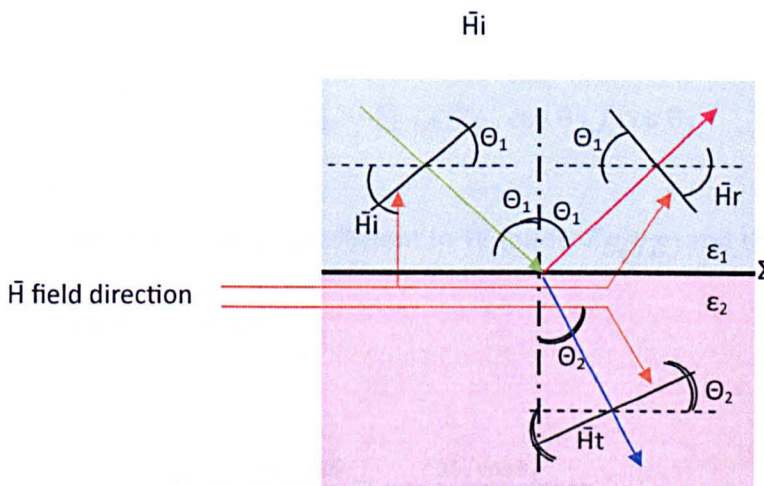


Figure 3.17. T.E. wave properties between two dielectrics.

To understand the propagation through dielectrics, we need to establish the fields \vec{E} and \vec{H} conditions of continuity between the both dielectrics first. As they are applicable to the tangential components of the fields, it is important to notice that, in the transverse electric:

- \vec{E} fields are tangential to Σ .
- The tangential components of the \vec{H} fields are in $\cos\theta$.

The complex amplitudes are then as follow:

$$\begin{cases} E_i + E_r = E_t & (3.43) \\ (H_i + H_r) \cos\theta_1 = H_t \cos\theta_2 & (3.44) \end{cases}$$

As $E_i/H_i = \zeta_1$, $E_r/H_r = -\zeta_1$ and $E_t/H_t = \zeta_2$

Therefore,
$$\begin{cases} E_i + E_r = E_t & (3.45) \\ E_i - E_r = E_t \zeta_1/\zeta_2 \cdot \cos\theta_2 / \cos\theta_1 & (3.46) \end{cases}$$

The \vec{E} field transmission coefficient in TE mode $T_{E(TE)}$ and the reflection coefficient $R_{E(TE)}$ are as follows :

$$T_{E(TE)} = \frac{|E_t|}{|E_i|} = \frac{2\zeta_2 \cos\theta_1}{\zeta_2 \cos\theta_1 + \zeta_1 \cos\theta_2} \quad (3.47)$$

$$R_E(\text{TE}) = \frac{|E_r|}{|E_i|} = \frac{\zeta_2 \cos \theta_1 - \zeta_1 \cos \theta_2}{\zeta_2 \cos \theta_1 + \zeta_1 \cos \theta_2} \quad (3.48)$$

Because $H_r/H_i = -(E_r/E_i)$ it is then only needed to change the sign of the E field reflection coefficient to get the reflection coefficient of the H field.

$$R_H(\text{TE}) = -R_E(\text{TE}) \quad (3.49)$$

Concerning the transmission coefficient,

$$\frac{H_t}{H_i} = \frac{E_t}{E_i} \frac{\zeta_1}{\zeta_2} \quad (3.50)$$

$$T_H(\text{TE}) = T_E(\text{TE}) \frac{\zeta_1}{\zeta_2} \quad (3.51)$$

Generally $\mu_1 = \mu_2 = \mu_0$, therefore,

$$\zeta_1 = \sqrt{\frac{\mu_0}{\epsilon_1}}, \zeta_2 = \sqrt{\frac{\mu_0}{\epsilon_2}} \quad (3.52)$$

After multiplying $R_E(\text{TE})$ and $T_E(\text{TE})$ by

$$\frac{\sqrt{\epsilon_1 \epsilon_2}}{\sqrt{\epsilon_1 \epsilon_2}}$$

and simplifying them, we obtain:

$$R_E(TE) = \frac{\sqrt{\epsilon_1} \cos \theta_1 - \sqrt{\epsilon_2} \cos \theta_2}{\sqrt{\epsilon_1} \cos \theta_1 + \sqrt{\epsilon_2} \cos \theta_2} \tag{3.53}$$

$$T_E(TE) = \frac{2\sqrt{\epsilon_1} \cos \theta_1}{\sqrt{\epsilon_1} \cos \theta_1 + \sqrt{\epsilon_2} \cos \theta_2} \tag{3.54}$$

One can see that $T_E(TE)$ is always positive, because $0^\circ \leq \theta_1 \leq 90^\circ$ and $0^\circ \leq \theta_2 \leq 90^\circ$, $R_E(TE)$, on the other hand can, depending of the values of $\sqrt{\epsilon_1} \cos \theta_1$ and $\sqrt{\epsilon_2} \cos \theta_2$ be positive or negative.

On figure 3.18 (left), $\epsilon_2 > \epsilon_1$ then $\theta_1 < \theta_2$ and $\cos \theta_1 > \cos \theta_2$. On figure 3.18(right), $\epsilon_2 > \epsilon_1$ then $\theta_1 < \theta_2$ and $\cos \theta_1 > \cos \theta_2$.

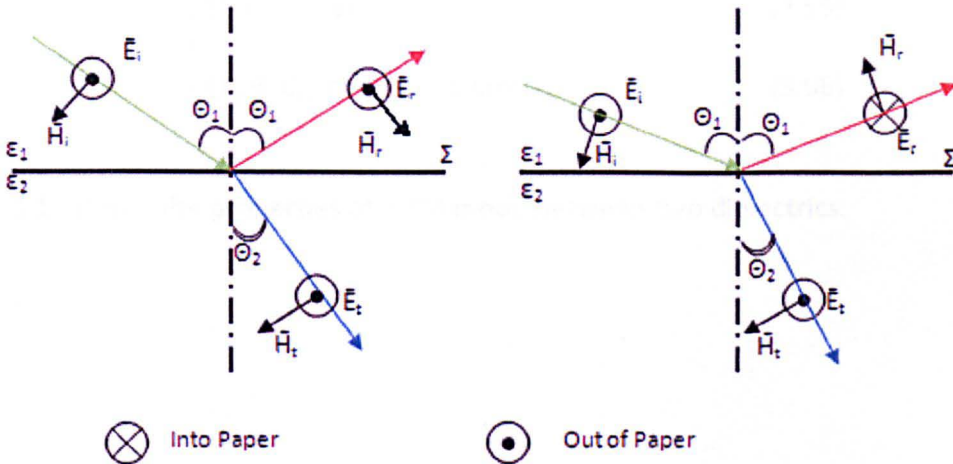


Figure 3.18. Reflection of a T.E. wave depending on the dielectrics ϵ_2 and ϵ_1 .

In other terms, if the permittivity ϵ_1 is greater than ϵ_2 , \vec{E}_r is in the direction as \vec{E}_i . If the permittivity ϵ_1 is less than ϵ_2 , \vec{E}_r is in the opposite direction \vec{E}_i . In both case \vec{E}_t is positive.

If \vec{H} is perpendicular with the incident plane: T.M. mode

Again to understand the propagation through dielectrics, we need to establish the fields \vec{E} and \vec{H} conditions of continuity between the both dielectrics first. As they are applicable to the tangential components of the fields, it is important to notice that, in the TE mode:

- \vec{H} fields are tangential to Σ .
- The tangential components of the \vec{E} fields are in $\cos\theta$.

The complex amplitudes are then as follow:

$$\begin{cases} H_i + H_r = H_t & (3.55) \\ (E_i + E_r) \cos \theta_1 = E_t \cos \theta_2 & (3.56) \end{cases}$$

Figure 3.19 shows the properties of a TM mode between two dielectrics.

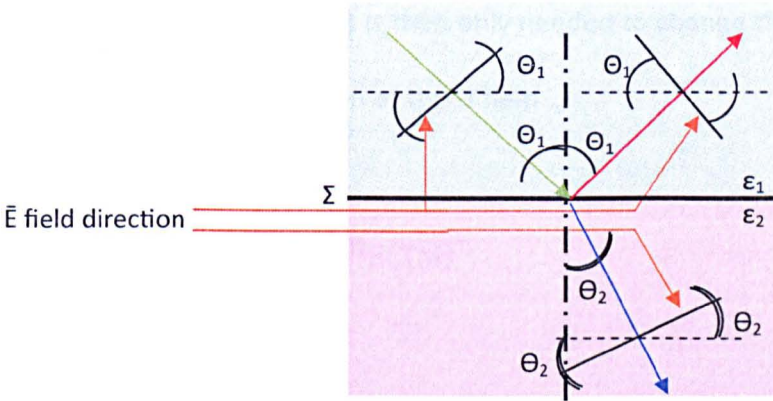


Figure 3.19. T.M. wave properties between two dielectrics.

As
$$E_i/H_i = \zeta_1, -E_r/H_r = \zeta_1 \text{ and } E_t/H_t = \zeta_2$$

Therefore,
$$\begin{cases} E_i - E_r = \zeta_1/\zeta_2 E_t & (3.57) \\ E_i + E_r = E_t \cos \theta_2 / \cos \theta_1 & (3.58) \end{cases}$$

The \vec{E} field transmission coefficient in TM mode $T_E(\text{TM})$ and the reflection coefficient $R_E(\text{TM})$ are as follows :

$$R_E(\text{TM}) = \frac{\zeta_2 \cos \theta_2 - \zeta_1 \cos \theta_1}{\zeta_1 \cos \theta_1 + \zeta_2 \cos \theta_2} \tag{3.59}$$

$$T_E(\text{TE}) = \frac{2 \zeta_2 \cos \theta_1}{\zeta_1 \cos \theta_1 + \zeta_2 \cos \theta_2} \tag{3.60}$$

Again, like for the TE mode, it is then only needed to change the sign of the E field reflection to get the reflection of the H field.

$$R_H(TM) = -R_E(TM) \quad (3.61)$$

The transmission coefficient,

$$T_H(TM) = T_E(TM) \frac{\zeta_1}{\zeta_2} \quad (3.62)$$

Generally $\mu_1 = \mu_2 = \mu_0$, therefore,

$$\zeta_1 = \sqrt{\frac{\mu_0}{\epsilon_1}} \quad (3.63)$$

and,

$$\zeta_2 = \sqrt{\frac{\mu_0}{\epsilon_2}} \quad (3.64)$$

After multiplying $R_E(TE)$ and $T_E(TE)$ by $\sqrt{\epsilon_1 \epsilon_2} / \sqrt{\epsilon_1 \epsilon_2}$ and simplifying them, we obtain:

$$R_E(TM) = \frac{\sqrt{\epsilon_1} \cos \theta_2 - \sqrt{\epsilon_2} \cos \theta_1}{\sqrt{\epsilon_2} \cos \theta_1 + \sqrt{\epsilon_1} \cos \theta_2} \quad (3.65)$$

$$T_{E(TM)} = \frac{2\sqrt{\epsilon_1} \cos \theta_1}{\sqrt{\epsilon_2} \cos \theta_1 + \sqrt{\epsilon_1} \cos \theta_2} \tag{3.66}$$

In the TM polarisation mode, the transmission of the electric field $T_{E(TM)}$ is constantly positive contrary to the reflection of the electric field $R_{E(TM)}$ that can be either positive or negative depending on the respective values of $\sqrt{\epsilon_1} \cos \theta_2$ and $\sqrt{\epsilon_2} \cos \theta_1$.

On figure 3.20 left, $\sqrt{\epsilon_1} \cos \theta_2 > \sqrt{\epsilon_2} \cos \theta_1$, on the right $\sqrt{\epsilon_1} \cos \theta_2 < \sqrt{\epsilon_2} \cos \theta_1$ [44].

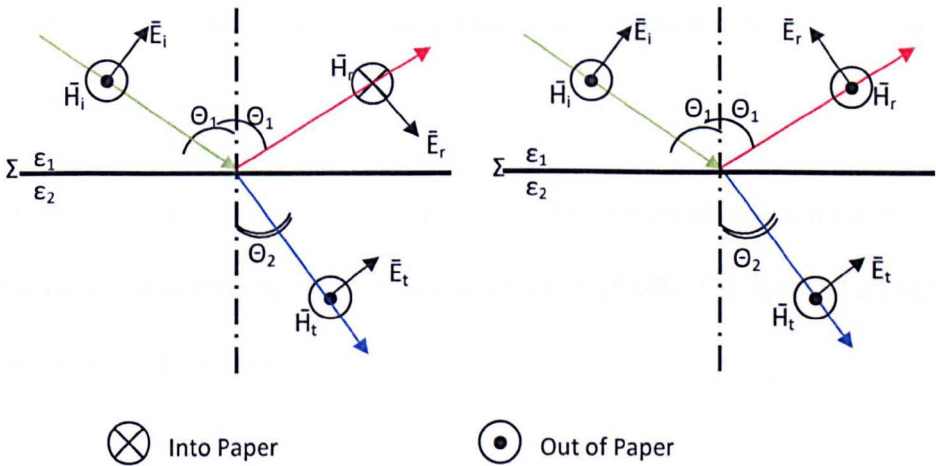


Figure 3.20. Reflection of a T.M. wave depending on the dielectrics ϵ_2 and ϵ_1 .

3.2.4 Standing Waves

A standing wave in a transmission line or in waveguides is a wave in which the distribution of current, voltage, or field strength is formed by the superposition of two waves of the same frequency propagating in opposite directions.

The effect is a series of nodes (zero displacement) and anti-nodes (maximum displacement) at fixed points along the transmission line.

Such a standing wave may be formed when a wave is transmitted into one end of a transmission line and is reflected from the other end by an impedance mismatch, discontinuity, such as an open circuit or a short. In practice, losses in the transmission line and other components mean that a perfect reflection and a pure standing wave are never achieved. The result is a partial standing wave, which is a superposition of a standing wave and a travelling wave.

The degree to which the wave resembles either a pure standing wave or a pure travelling wave is measured by the standing wave ratio (SWR). The figure 3.21 explains the formation of standing wave [45].

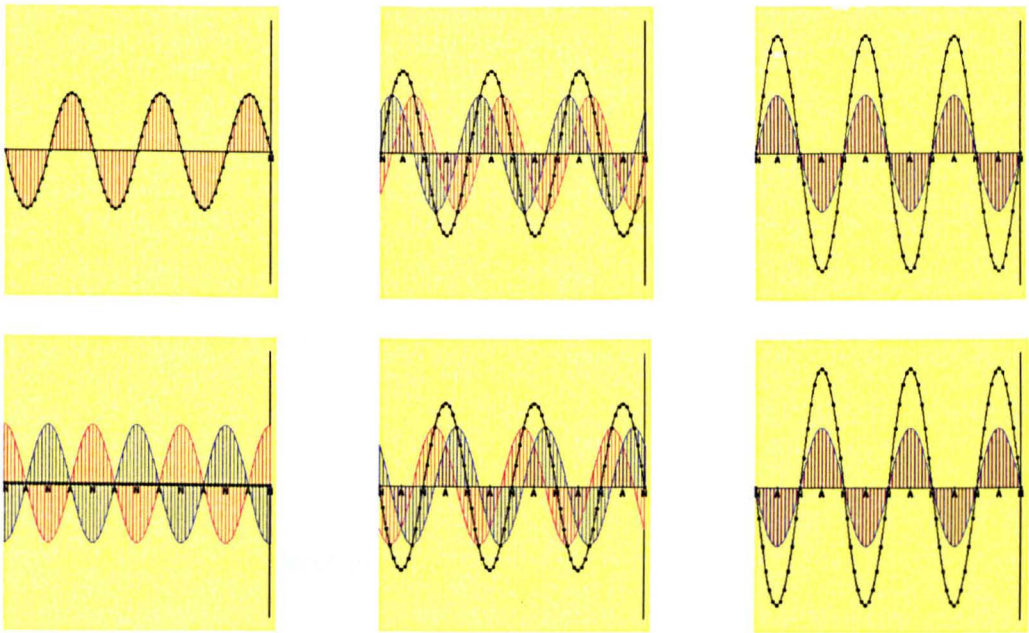


Figure 3.21. Creation of a standing wave.

Starting from the top left, a travelling wave (red) hits a conducting wall and forms a reflected wave (blue). The superposition of the travelling wave and the reflected wave is given by the black curve which is the standing wave. When the travelling wave and the reflected wave are in phase, the standing wave reaches its maximum values (top right and bottom right). When they are out of phase by 180° , the standing wave is completely null (bottom left). Because the travelling wave and the reflected wave are going in opposite directions, on an anti-node (noted A), the standing wave reaches its maximum before collapsing and then reaches its minimum; known as the maximum displacement for an anti-node. On the other hand, the nodes (noted N) have no displacement at all and are always equal to zero.

From a mathematical point of view, if y_1 is the travelling wave, y_2 the reflected wave and y the standing wave, we obtain:

$$y_1 = y_0 \sin(kx - \omega t) \quad (3.67)$$

$$y_2 = y_0 \sin(kx + \omega t) \quad (3.68)$$

where:

- y_0 is the amplitude of the waves,
- ω (called angular frequency, measured in *radians per second*) is 2π times the frequency (in *hertz*),
- k (called the wave number and measured in *radians per metre*) is 2π divided by the wavelength λ (in *metres*), and
- x and t are variables for longitudinal position and time, respectively.

So the resultant wave y equation will be the sum of y_1 and y_2 :

$$y = y_0 \sin(kx - \omega t) + y_0 \sin(kx + \omega t) \quad (3.69)$$

Using a trigonometric identity to simplify, the standing wave is described by:

$$y = 2y_0 \cos(\omega t) \sin(kx) \quad (3.70)$$

This describes a wave that oscillates in time, but has a dependence that is stationary: $\sin(kx)$. At locations $x = 0, \lambda/2, \lambda, 3\lambda/2...$ which are the nodes (the amplitude is always zero), whereas at locations $x = \lambda/4, 3\lambda/4, 5\lambda/4, ...$ which are the anti-nodes (the amplitude is maximum). The distance between two conjugative nodes or anti-nodes is $\lambda/2$ [46].

3.3 Microwave and Material Characterisation

3.3.1 Material Properties in the Microwave Region

Depending on their frequencies, electromagnetic waves have different behaviour with different materials. The behaviour of a material depends on the permittivity of the molecules. The permittivity is a physical quantity that describes how an electric field affects and is affected by a dielectric medium. The permittivity is determined by the ability of a material to polarize in response to the field, and thereby reduce the field inside the material. It is typically represented by the Greek letter ϵ . The permeability is the degree of magnetization of a material that responds linearly to an applied magnetic field. Magnetic permeability is typically represented by the Greek letter μ . In general, the absorption of electromagnetic energy by dielectrics is covered by a few different mechanisms that influence the shape of the permittivity as a function of frequency [47].

The first mechanism is the resonance effects which arise from the rotations or vibrations of atoms, ions, or electrons. These processes are observed in the neighbourhood of their characteristic absorption frequencies. Figure 3.22 presents how dielectric molecules will behave depending on the frequency.

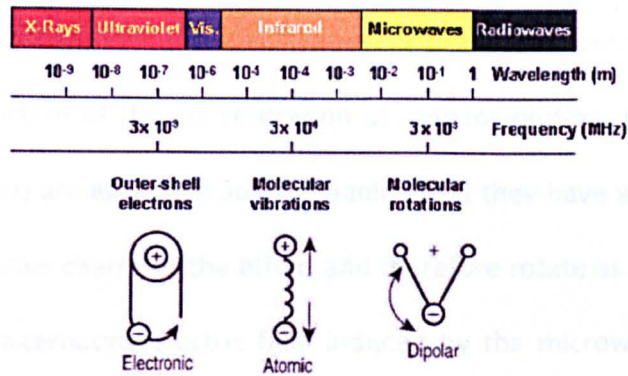


Figure 3.22. Molecular behaviour depending of the frequency.

Dipole interactions occur with polar molecules. To measure the rotational spectrum of a material, it requires that its molecules have a dipole moment. This is the difference between the centre of charge and the centre of mass, or equivalently a separation between two unlike charges. It is this dipole moment that enables the electric field of the electromagnetic wave to exercise a torque on the molecule causing it to rotate more quickly (in excitation) or slowly (in de-excitation). Diatomic molecules such as oxygen (O_2), hydrogen (H_2), etc. do not have a dipole moment and hence no pure-rotational spectrum [47,48]. When polar ends of a molecule tend to align themselves and oscillate in step with the oscillating electrical field of the microwaves,

collisions and friction between the moving molecules result in heating. Broadly, the more polar a molecule, the more effectively it will couple with (and be influenced by) the microwave field. Ionic conduction is only minimally different from dipole interactions. Ions in solution do not have a dipole moment. They are charged species that are randomly distributed and cannot therefore couple with the oscillating electrical field of the microwaves. The effectiveness or rate of microwave heating of an ionic solution is a function of the concentration of ions in solution. Many molecules (such as those of water) are electric dipoles, meaning that they have a positive charge at one end and a negative charge at the other, and therefore rotate as they try to align themselves with the alternating electric field induced by the microwave beam. This molecular movement creates heat as the rotating molecules hit other molecules and put them into motion. Microwave heating at the correct frequency is most efficient in the case of liquid water, and much less so on fats and sugars (which have less molecular dipole moment), and ice (where the molecules are not free to rotate) [49]. Figure 3.23 shows a water molecule (H_2O), which in many ways behaves like an electric dipole.

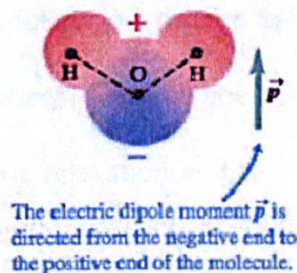


Figure 3.23. A water molecule showing positive charge in red and negative charge in blue.

The water molecule is electrically neutral. However the chemical bonds within the molecule cause a displacement of charge. The result is a net negative charge on the oxygen end of the molecule and a net positive charge on the hydrogen end, forming an electrical dipole [50]. Figure 3.24 shows the rotation of a dipolar molecule under the influence of an electromagnetic wave.

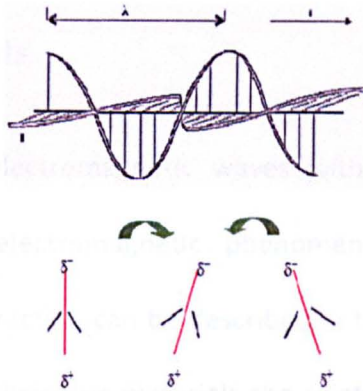


Figure 3.24. Molecular rotation of a dipole.

The second mechanism is the relaxation effects associated with permanent and induced molecular dipoles. At low frequencies the field changes slowly enough to allow dipoles to reach equilibrium before the field has measurably changed. For frequencies at which dipole orientations cannot follow the applied field due to the viscosity of the medium, absorption of the field's energy leads to energy dissipation. The mechanism of dipoles relaxing is called dielectric relaxation and for ideal dipoles is described by classic Debye relaxation [48].

Microwave interaction with matter is also characterized by a penetration depth. That is, microwaves can penetrate only a certain distance into a bulk material. Not only is the penetration depth a function of the material composition, it is a function of the frequency of the microwaves. Conductors strongly absorb microwaves and any lower frequencies because they cause electric currents which heat the material [51]. Both mechanisms require effective coupling between components of the target material and the rapidly oscillating electrical field of the microwaves [52].

3.3.2 Dielectric Materials

The interaction of electromagnetic waves with matter is governed by its complex permittivity. All electromagnetic phenomenon-transmission, diffraction, scattering, reflection and refraction can be described in terms of complex permittivity and permeability. For most dielectric materials the relative permeability is unity and permittivity is the only governing factor.

The relative complex permittivity or complex dielectric constant, $\epsilon^* = \epsilon' - j\epsilon''$, has two components, the real part, called the dielectric constant, and the imaginary part, called the dielectric loss factor [53]. The following three bullet point explains more about the dielectric constant, the loss factor, and the molecular relation time:

- **The dielectric constant**

The dielectric constant causes a reduction in the velocity of the microwaves across the microwave cavity. As an electromagnetic wave passes through the sample it causes an alternating polarisation within the material. The material stores some of the wave energy, and releases it back to the wave slowly, therefore reducing the wave's velocity.

- **The conductivity or loss factor**

This causes a reduction in the magnitude of the wave. The loss factor is a measure of how well a material absorbs the electromagnetic energy to which it is exposed. As molecules orientate in the electric field, energy is lost due to friction, reducing the magnitude of the wave. Both these parameters are usually represented by the dissipation factor, often called the loss tangent. The dissipation factor is a ratio of the dielectric loss (loss factor) to the dielectric constant. One other factor must be taken in consideration: the molecular relaxation time.

- **The molecular relaxation time**

This originates from permanent and induced dipoles aligning with an electric field. With no external influence, their orientation polarisation is disturbed by thermal noise (which de-aligns the dipole vectors from the direction of the field), and the time needed for dipoles to relax is determined by the local viscosity. These two facts make dipole relaxation heavily dependent on temperature and chemical surrounding [54].

3.3.3 Resonant and Non-Resonant Measurements

The microwave methods for material characterisation generally fall into two categories namely non resonant methods and resonant methods. Non resonant methods are often used to get a general knowledge of electromagnetic properties over a frequency range, while resonant methods are used to get an accurate knowledge of dielectric properties at a single frequency or at several discrete frequencies.

In non-resonant methods, the properties of materials are fundamentally deduced from their impedance and the wave velocities in the materials. As shown in Figure 3.25, when an electromagnetic wave propagates from one material to another (from free space to sample), both the characteristic wave impedance and the wave velocity change, resulting in a partial reflection of the electromagnetic wave from the interface between the two materials.

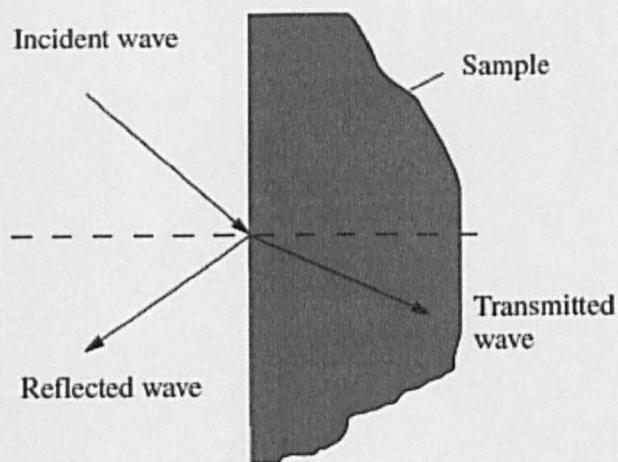


Figure 3.25. Effect of an incident wave on a sample.

Measurements of the reflection from such an interface and the transmission through the interface can provide information for the deduction of permittivity and permeability relationships between the two materials. Non-resonant methods mainly include reflection methods and transmission/reflection methods. In the reflection method, the materials properties are calculated on the basis of the reflected wave from the sample, and in a transmission/reflection method, the material properties are calculated on the basis of the reflection from the sample and the transmission through it. Non-resonant methods require a means of directing the electromagnetic energy toward a material, and then collecting what is reflected from the material, and/or what is transmitted through the material. In principle, all types of transmission lines can be used to carry the wave for non-resonant methods, such as coaxial line, hollow metallic waveguide, dielectric waveguide, planar transmission line, and free space.

The resonant method is also often called the *dielectric resonator method*. It can be used to measure the permittivity of dielectric materials and the surface resistance of conducting materials. In a resonator method for dielectric property measurement, the dielectric sample under measurement serves as a resonator in the measurement circuit, and the dielectric constant and loss tangent of the sample are determined from its resonant frequency and quality factor. Figure 3.26 shows the configuration often used in the dielectric resonator method. In this configuration, the sample is sandwiched between two conducting plates, and the resonant properties of this

configuration are mainly determined by the properties of the dielectric cylinder and two pieces of the conducting plates.

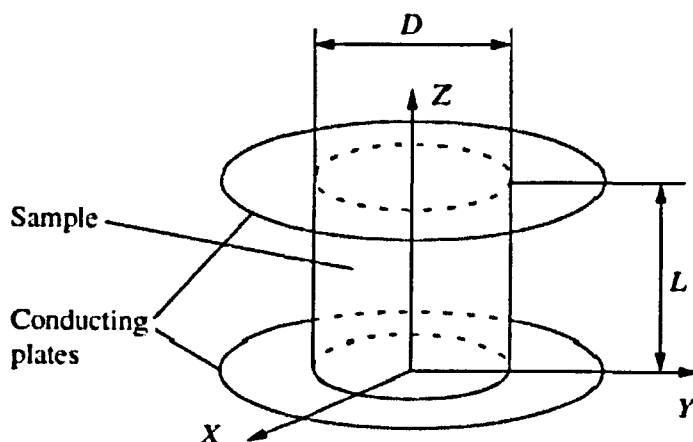


Figure 3.26. Simple Dielectric resonator.

In the measurement of the dielectric properties of the dielectric cylinder, it is assumed that the properties of the conducting plates are known [43].

3.3.4 One Port and Two Ports Measurement Methods

The one-port method is mainly used for reflection measurements. In this method, one port both transmits signals and receives the reflected signals from the sample under test. The S-parameter measured by one port is S_{11} or S_{22} . The dynamic range of reflection measurements is mainly limited by the directivity of the measurement port. To improve measurement accuracy and sensitivity, it is usually required to perform a one-port calibration. In reflection methods for material

characterisation, one-port reflection measurements are required. One-port calibration can measure and remove three systematic error terms in one-port measurements: directivity, source match and reflection tracking.

The two-port method is suitable for the transmission/reflection method for material property characterisation. In a two-port method, one port transmits the signal and the other port receives the signal from the sample under test. With two ports, the S-Parameters S_{11} , S_{12} and S_{21} , S_{22} can be measured. In a two-port method there are six types of systematic errors: directivity and cross talk errors relating to the signal leakage, source and load; impedance mismatches relating to the reflections; and frequency response errors caused by reflection and transmission tracking within the test receivers. The full two-port calibration error model includes all six of these terms for the forward direction and the same six terms for the reverse direction, for a total of twelve error corrections. To obtain the twelve terms of systematic errors, usually a TOSM (Through Open Short Match) calibration is made [44].

3.3.5 Scattering Parameters (S-Parameters)

The responses of a network to external circuits can be described by the input and output waves as shown in figure 3.27 and figure 3.28 [43]. The input waves at port 1 and port 2 and denoted a_1 and a_2 respectively. The output waves at port 1 and port 2

are denoted b_1 and b_2 respectively. These parameters (a_1 , a_2 , b_1 and b_2) could be voltage or current.

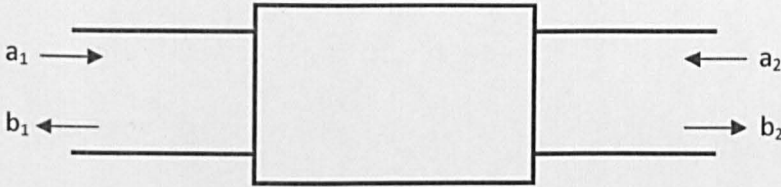


Figure 3.27. Representation of a two-port network.

The relationship between the input wave $[a]$ and the output wave $[b]$ can be described by scattering parameters $[S]$:

$$[b] = [S][a] \quad (3.71)$$

Where $[a] = [a_1, a_2]^T$, $[b] = [b_1, b_2]^T$, and the scattering matrix $[S]$ has the following form:

$$[S] = \begin{bmatrix} S_{11} & S_{12} \\ S_{21} & S_{22} \end{bmatrix} \quad (3.72)$$

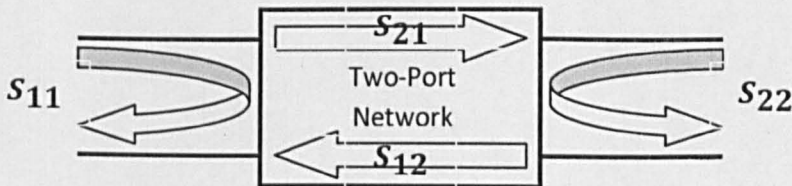


Figure 3.28. Visualisation of a two-port Network S-Parameters.

For a scattering parameter S_{ij} , if $a_i=0$ ($i \neq j$) we obtain,

$$S_{jj} = \frac{b_j}{a_j} \quad (j = 1,2) \quad (3.73)$$

$$S_{ij} = \frac{b_i}{a_j} \quad (i \neq j, j = 1,2, i = 1,2) \quad (3.74)$$

The equation (3.73) shows that when port j is connected to a source and the other port to a matching load, the reflection coefficient at port j is equal to S_{jj} :

$$\Gamma_j = S_{jj} = \frac{b_j}{a_j} \quad (3.75)$$

The equation (3.74) shows that when port j is connected to a source and port i is connected to a matched load, the transmission coefficient from port j to port i is equal to S_{ij} :

$$T_{j \rightarrow i} = S_{ij} = \frac{b_i}{a_j} \quad (3.76)$$

Note that the reverse voltage gain S_{12} and the output port voltage reflection coefficient S_{22} are very small compared to the input port voltage reflection coefficient S_{11} and to the forward voltage gain S_{21} . Therefore, they can be negligible when characterising samples with S-parameters and will not be measured in this project.

3.3.6 Quality Factor (Q-Factor)

In resonant material characterisation methods, the resonant frequency and the quality factor is measured. The quality factor can be calculated according to:

$$Q = \frac{f_0}{\Delta f} \quad (3.77)$$

Where f_0 is the resonant frequency and Δf is the half power bandwidth.

The quality factor of the reflected signal S_{11} is determined by using the half power width ($S_{11}, \Delta f$) as:

$$S_{11, \Delta f} = 10 \cdot \log_{10} \left(\frac{10^{S_{11,b}/10} + 10^{S_{11,f_0}/10}}{2} \right) \quad (3.78)$$

Where $S_{11,b}$ is the S_{11} value of the base line of the resonance, and S_{11,f_0} is the S_{11} value at the resonant frequency as shown figure 3.29.

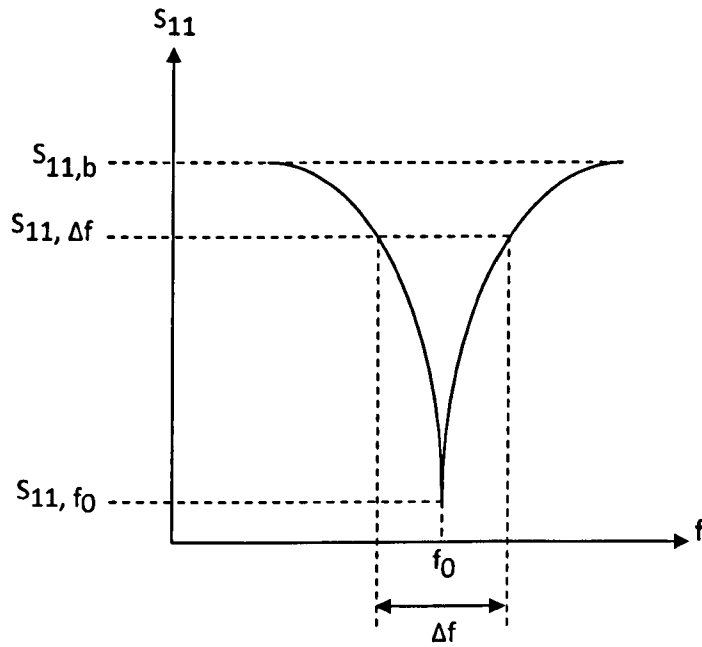


Figure 3.29. Method to find S_{11} Q-Factor.

In a two-port method, the Q-factor is obtained by the transmission scattering parameter (S_{21}):

$$S_{21, \Delta f} = S_{21, f_0} - 3\text{dB} \quad (3.79)$$

Where S_{21, f_0} is the S_{21} value at the resonant frequency as displayed on figure 3.30.

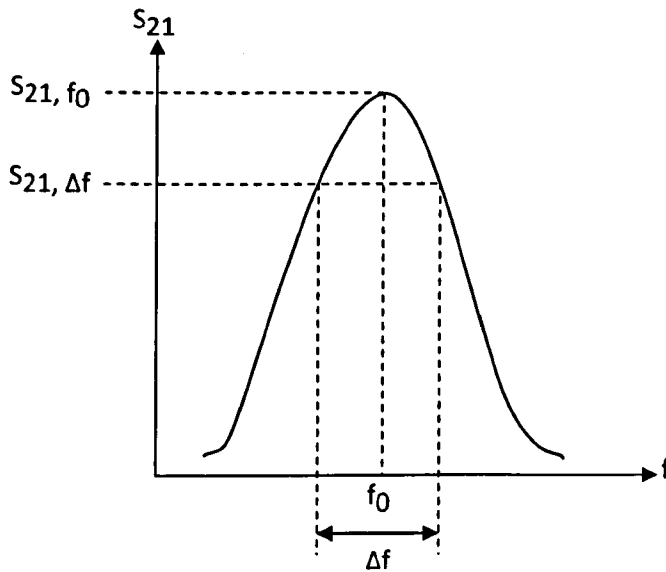


Figure 3.30. Method to find S_{21} Q-Factor [39].

3.3.7 Expected Response of a Sample

As described previously, microwaves operate at a frequency low enough to be very sensitive to presence of polar molecules (such as water and ethanol) and to DC conductivity changes (such as ion/salt concentrations). Microwaves have also the advantage penetrating the entire mixture instead of just the surface. As the microwaves go through the material present in the cavity, the waves rotate molecules into or out of polar alignment.

When a microwave signal is sent through the cavity, the electromagnetic waves pass through the sample in the resonator providing a representative measurement of the bulk product under test. In the presence of microwave energy, the polar molecules

in the sample (water and ethanol) rotate and align with the electromagnetic field, similar to aligning poles on a magnet. The movement of the molecules causes the microwave signal to be attenuated and the velocity of the wave decreases as it passes through the sample. The resonance occurs in a cavity when the electric and magnetic fields, satisfying Maxwell's equations, form a standing wave. From the Maxwell's equation, is possible to derive the electromagnetic wave equation.

The electromagnetic wave equation is a second-order partial differential equation that describes the propagation of electromagnetic waves through a medium or in a vacuum. The homogeneous form of the equation, written in terms of either the electric field E or the magnetic field H , takes the form [55]:

$$\nabla^2 E - \frac{1}{c^2} \frac{\partial^2 E}{\partial t^2} = 0 \quad (3.80)$$

$$\nabla^2 H - \frac{1}{c^2} \frac{\partial^2 H}{\partial t^2} = 0 \quad (3.81)$$

Where c is the speed of light in the medium. In a vacuum, $v = c = 2.998 \times 10^8 \text{ m/s}$, which is the speed of light in free space.

From Maxwell's equations, it is possible to extrapolate the first order shift in frequency of the response in the cavity. As described earlier, the movement of the

molecules causes the microwave signal to be attenuated and the velocity of the wave to decrease as it passes through the sample [54]. The dielectric constant of the ethanol is 24.3 (25°C) and that the dielectric constant of the water is 81 (25°C).

$$\varepsilon' = \frac{c^2}{v^2} \quad (3.82)$$

Therefore, from the equation presented above, the change in velocity (represented as a change in frequency) can be quantified with the dielectric constant, c the velocity of light in vacuum and v the velocity through the sample.

As a result, if the permittivity inside the cavity increases, then the velocity and the wavelength of the electromagnetic wave inside the cavity are reduced by the square root of the permittivity (see Figure 3.31)[56].

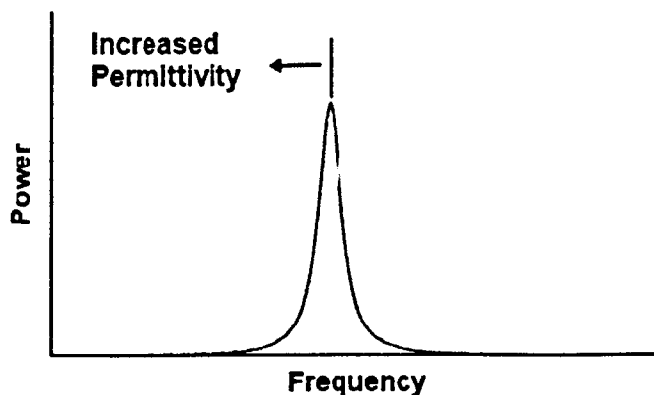


Figure 3.31. Frequency shift depending of the permittivity.

Two other parameters, described earlier also affect the scalar response of the tube under test in the cavity: the loss factor and the molecular relaxation time. In the same way, the molecular relaxation time cannot be approximated as a function of external parameters. However, the loss factor can be extrapolated from the response of the sample in the cavity. The loss factor is a measure of how well a material absorbs the electromagnetic energy to which it is exposed. The dissipation factor is a ratio of the dielectric loss (loss factor) to the dielectric constant.

Summary

Chapter 3 discusses the properties of electromagnetic waves and how they can be used in order to characterise the dielectric properties of materials. Different methods, such as the resonant and non-resonant methods were treated, and measurement techniques were shown. The definitions of the scattering parameters are also given.

4 CAVITY RESONATOR DESIGN AND SIMULATIONS

4.1 Cavity Resonator Properties

4.1.1 Cavity Resonator Definition

A microwave cavity resonator is used to restrict the three dimensional "free space" propagation of the electromagnetic wave to a guided dimension. At the same time, the use of a waveguide avoids some attenuations of the signal (in the bandwidth of the microwave cavity resonator) [57]. By definition, a resonant cavity is any space that is completely enclosed by conducting walls that can contain oscillating electromagnetic fields and possess resonant properties [58]. Cavity resonators are constructed from sections of waveguide. If a hollow rectangular waveguide is sealed with conductive walls perpendicular to the direction of propagation, the incident and reflected waves are superimposed to generate a standing wave. The tangential electric and normal magnetic field components are equal to zero at this wall and at distances of integral half wavelengths from it. If the resonator is excited through a coupling mechanism, the field intensity builds up to a maximum when the length of the resonator is an integral multiple of half wavelengths. Due to the different field modes that can possibly exist in the waveguide, an infinite number of resonant frequencies can occur [59]. Good resonant cavities have a very high Q factor (Quality factor) and can be built to handle relatively large amounts of power. The high Q gives these devices a narrow pass band

and allows very accurate tuning. Simple, rugged construction is an additional advantage.

4.1.2 Cavity Coupling

Probes in waveguides, supplied with microwave energy, act as a quarter-wave antenna. Current flows in the probe and sets up an E field such as the one shown in figure 4.1. The E lines detach themselves from the probe. When the probe is located at the point of highest efficiency, the E lines set up an E field of considerable intensity.

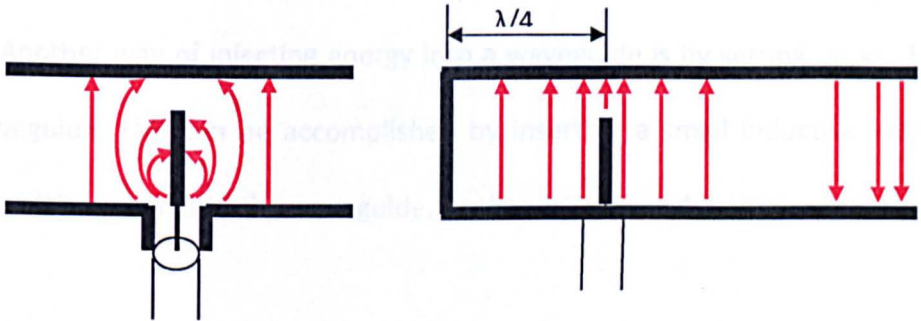


Figure 4.1. Probe coupling/E coupling for cavities.

The most efficient location for the probe is at a quarter-wavelength from the short end of the waveguide. This is the point at which the E field is a maximum in the dominant mode. Therefore, energy transfer (coupling) is a maximum at this point. Note that the quarter-wavelength spacing is at the frequency required to propagate the dominant mode.

In many applications a lesser degree of energy transfer, called loose coupling, is desirable. The amount of energy transfer can be reduced by decreasing the length of the probe, by moving it out of the centre of the E field, or by shielding it. Where the degree of coupling must be varied frequently, the probe is made retractable so the length can be easily changed. The size and shape of the probe determines its frequency, bandwidth, and power-handling capability. As the diameter of a probe increases, the bandwidth also increases. The greater power-handling capability is directly related to the increased surface area.

Another way of injecting energy into a waveguide is by setting up an H field in the waveguide. This can be accomplished by inserting a small inductive loop which carries a high current into the waveguide, as shown in figure 4.2.

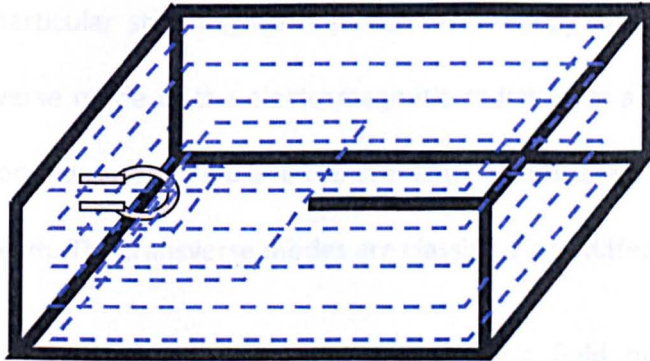


Figure 4.2. Loop antenna/H coupling for cavities.

A magnetic field builds up around the loop and expands to fit the waveguide. If the frequency of the current in the loop is within the bandwidth of the waveguide, energy will be transferred to the waveguide.

When the diameter of the loop is increased, its power-handling capability also increases. The bandwidth can be increased by increasing the size of the wire used to make the loop. When a loop is introduced into a waveguide in which an H field is present, a current is induced in the loop [60].

4.1.3 Cavity Propagation Modes

The whole field pattern inside the cavity resonator is called a "Mode". The waveguide propagation of modes depends on the operating wavelength and polarization, and the shape and size of the guide. The longitudinal mode of a waveguide is a particular standing wave pattern formed by waves confined in the cavity. The transverse mode of the electromagnetic radiation is a particular intensity pattern of radiation measured in a plane transverse (perpendicular) to the propagation direction of the beam. The transverse modes are classified into different types [58]:

- *TE* modes (Transverse Electric) have no electric field in the direction of propagation.
- *TM* modes (Transverse Magnetic) have no magnetic field in the direction of propagation.

- TEM modes (Transverse Electromagnetic) have no electric or magnetic field in the direction of propagation.

A rectangular waveguide supports TM and TE modes but not TEM waves because it is not possible to define a unique voltage since there is only one conductor in a rectangular waveguide. A rectangular waveguide cannot propagate waves below a certain frequency. This frequency is called the cut-off frequency. [60]

Figure 4.3 shows a cavity resonator made from a rectangular waveguide by shorting the two ends using conducting plates. Its structural dimensions include the width a , the height b and the length c .

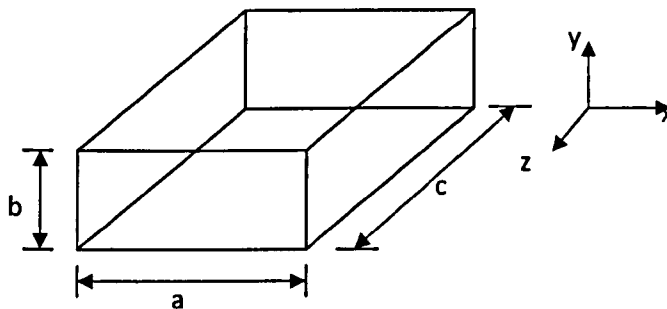


Figure 4.3. Structure of a rectangular cavity resonator.

A rectangular cavity resonator has only two transmission modes (TE_{mnp} and TM_{mnp}) which correspond to the TE_{mn} and TM_{mn} propagation modes in a rectangular waveguide respectively. The two subscripts m and n correspond to the

changing cycle in the x and y directions respectively. The subscript p represents the changing cycles along the z direction.

TE Resonant modes

According to the TE propagation mode of rectangular waveguides and the boundary conditions, the field distributions of the TE_{mnp} resonating mode are as follow:

$$H_x = j \frac{2A}{k_c^2} \cdot \frac{p\pi}{c} \cdot \frac{m\pi}{a} \sin\left(\frac{m\pi}{a} x\right) \cos\left(\frac{n\pi}{b} y\right) \cos\left(\frac{p\pi}{c} z\right) \quad (4.1)$$

$$H_y = j \frac{2A}{k_c^2} \cdot \frac{p\pi}{c} \cdot \frac{m\pi}{b} \cos\left(\frac{m\pi}{a} x\right) \sin\left(\frac{n\pi}{b} y\right) \cos\left(\frac{p\pi}{c} z\right) \quad (4.2)$$

$$H_z = -j2A \cos\left(\frac{m\pi}{a} x\right) \cos\left(\frac{n\pi}{b} y\right) \sin\left(\frac{p\pi}{c} z\right) \quad (4.3)$$

$$E_x = 2A \frac{\omega\mu}{k_c^2} \cdot \frac{n\pi}{b} \cos\left(\frac{m\pi}{a} x\right) \sin\left(\frac{n\pi}{b} y\right) \sin\left(\frac{p\pi}{c} z\right) \quad (4.4)$$

$$E_y = -2A \frac{\omega\mu}{k_c^2} \cdot \frac{m\pi}{a} \sin\left(\frac{m\pi}{a} x\right) \cos\left(\frac{n\pi}{b} y\right) \sin\left(\frac{p\pi}{c} z\right) \quad (4.5)$$

$$E_z = 0 \quad (4.5)$$

With,

$$k_c^2 = \left(\frac{m\pi}{a}\right)^2 + \left(\frac{n\pi}{b}\right)^2 \quad (4.6)$$

And A being the amplitude of the generated signal.

The resonant mode TE_{101} is the most widely used in the characterisation of electromagnetic materials. The fields components of the TE_{101} modes would be:

$$H_x = j \frac{2Aa}{c} \sin\left(\frac{\pi}{a} x\right) \cos\left(\frac{\pi}{c} z\right) \quad (4.7)$$

$$H_z = -j2A \cos\left(\frac{\pi}{a} x\right) \sin\left(\frac{\pi}{c} z\right) \quad (4.8)$$

$$E_y = -2 \frac{A\omega\mu a}{\pi} \sin\left(\frac{\pi}{a} x\right) \sin\left(\frac{\pi}{c} z\right) \quad (4.9)$$

$$E_z = E_x = H_y = 0 \quad (4.10)$$

Figure 4.4 illustrates the field distribution of the TE_{101} mode.

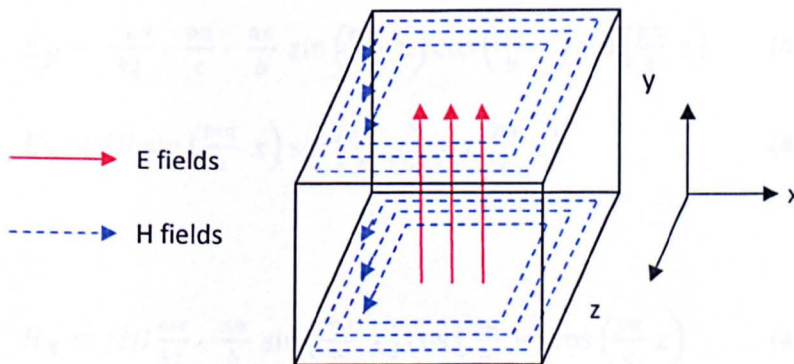


Figure 4.4. TE_{101} distributions fields.

The resonant wavelength for TE_{mnp} mode is given by:

$$\lambda_0 = \frac{2}{\sqrt{\left(\frac{m}{a}\right)^2 + \left(\frac{n}{b}\right)^2 + \left(\frac{p}{c}\right)^2}} \quad (4.11)$$

So the resonant wavelength for the TE_{101} mode is given by:

$$\lambda_0 = \frac{2ac}{\sqrt{a^2+c^2}} \quad (4.12)$$

That indicates that if b is the shortest among the three sides (a, b and c), the TE_{101} mode has the largest resonant wavelength, so it is the lowest mode.

TM Resonant modes

According to the properties of TM wave propagation modes and the boundary conditions, the fields components of the TM_{mnp} mode are as follow [43,44]:

$$E_x = \frac{-2B}{k_c^2} \cdot \frac{p\pi}{c} \cdot \frac{m\pi}{a} \cos\left(\frac{m\pi}{a} x\right) \sin\left(\frac{n\pi}{b} y\right) \sin\left(\frac{p\pi}{c} z\right) \quad (4.13)$$

$$E_y = \frac{-2B}{k_c^2} \cdot \frac{p\pi}{c} \cdot \frac{n\pi}{b} \sin\left(\frac{m\pi}{a} x\right) \cos\left(\frac{n\pi}{b} y\right) \sin\left(\frac{p\pi}{c} z\right) \quad (4.14)$$

$$E_z = 2B \sin\left(\frac{m\pi}{a} x\right) \sin\left(\frac{n\pi}{b} y\right) \cos\left(\frac{p\pi}{c} z\right) \quad (4.15)$$

$$H_x = j2B \frac{\omega\epsilon}{k_c^2} \cdot \frac{n\pi}{b} \sin\left(\frac{m\pi}{a} x\right) \cos\left(\frac{n\pi}{b} y\right) \cos\left(\frac{p\pi}{c} z\right) \quad (4.16)$$

$$H_y = -j2B \frac{\omega\epsilon}{k_c^2} \cdot \frac{m\pi}{a} \cos\left(\frac{m\pi}{a} x\right) \sin\left(\frac{n\pi}{b} y\right) \cos\left(\frac{p\pi}{c} z\right) \quad (4.17)$$

$$H_z = 0 \quad (4.18)$$

Where

$$k_c^2 = \left(\frac{m\pi}{a}\right)^2 + \left(\frac{n\pi}{b}\right)^2 \quad (4.19)$$

And the resonant wavelength λ_0 for the TM_{mnp} mode for vacuum is:

$$\lambda_0 = \frac{2}{\sqrt{\left(\frac{m}{a}\right)^2 + \left(\frac{n}{b}\right)^2 + \left(\frac{p}{c}\right)^2}} \quad (4.20)$$

Figure 4.5 summarises the main TE and TM modes usually used with rectangular cavity, and figure 4.6 shows the modes for a circular waveguide.

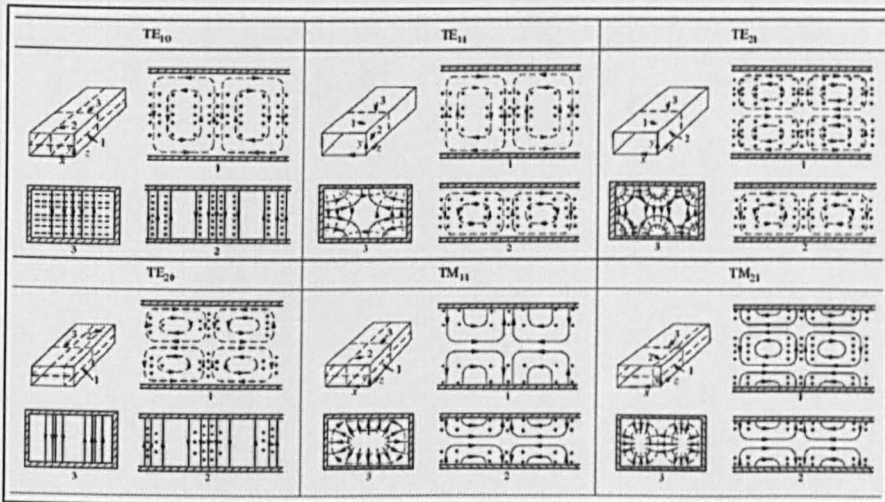


Figure 4.5. Fields distribution of a rectangular cavity's TE and TM main modes [42].

The magnetic fields are represented by dashed lines and the electric fields are drawn as solid lines.

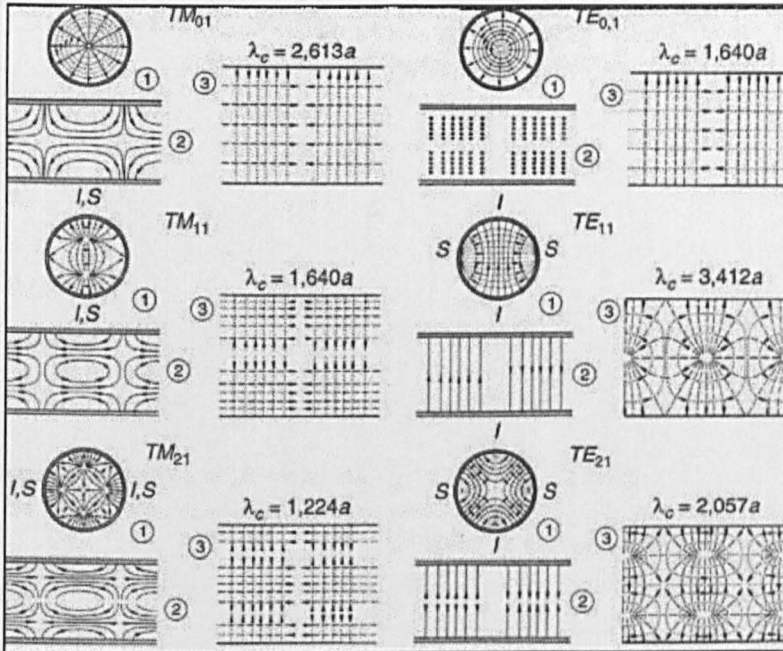


Figure 4.6. Circular cavity modes for TE and TM main modes [42].

The cylindrical cavities have not been used for this project and therefore will not be explained in detail.

4.2 Cavity Resonator Design

4.2.1 Cavity Resonator construction

The cavity used in this investigation has been built for a previous Master project using a standard WG9A cavity section. It was designed according to the cavity mode and Maxwell's equations. It is made of 1mm thick copper. Its internal size is 43mm by 86mm. Flanges are soldered on both sides of the cavity section to allow connections

with the loop antenna end plates and a tuning section. The tuning section is 150mm long and comprises a WG9A cavity section and four adjustable tuning stubs. A 16mm diameter hole has been drilled on the top of the resonator to introduce the sample and another hole of 6mm diameter has been drilled on the bottom, opposite to the insertion hole, to take the sample temperature using the Infra-Red (IR) thermometer [61]. Thermocouples were not an option because the samples would have to be opened for every measurement, allowing ethanol to evaporate.

Loop antennas were chosen to transmit and receive the electromagnetic signals in the cavity resonator because they are cheap and easy to build. They are connected via two coaxial cables to the Vector Network Analyser (VNA) [62]. Figure 4.7 is a 3D model showing the different parts forming the cavity with a sample introduced.

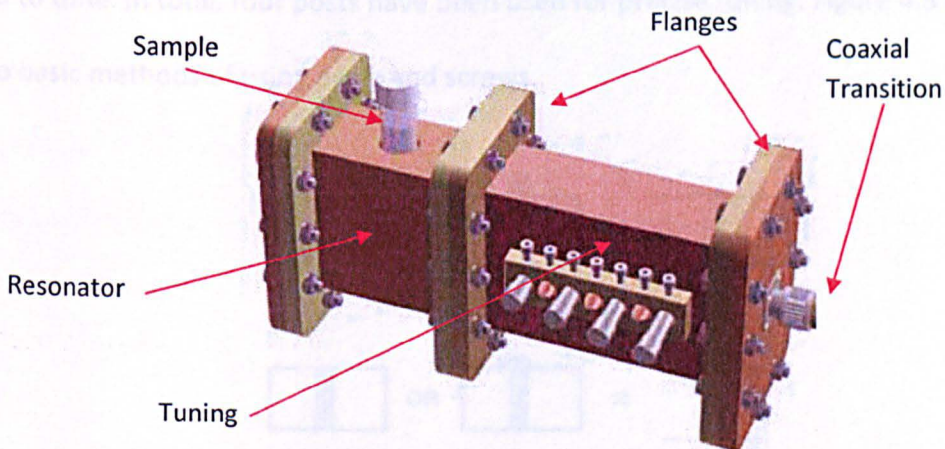


Figure 4.7. 3D Model of the Cavity Resonator.

A similar cavity, without the tuning section, was used for the measurement of the dielectric constant and loss tangent of epoxy resin. It was built using a WG9A (WR340) waveguide section and was designed to work at 2.45GHz [63].

4.2.2 The Tuning Section

Waveguide transmission systems are not always perfectly impedance matched to their load devices. The standing waves that result from a mismatch cause a power loss, a reduction in power-handling capability, and an increase in frequency sensitivity. Impedance-changing devices are therefore placed in the waveguide to match the waveguide to the load. These devices are placed near the source of the standing waves and could be irises (horizontal, vertical or both) or posts and screws. Irises require opening the cavity for tuning by changing their sizes and shapes. For this experiment, adjustable posts similar to the screws shown are used because they are easier to build and to tune. In total, four posts have been used for precise tuning. Figure 4.8 illustrates two basic methods of using posts and screws.

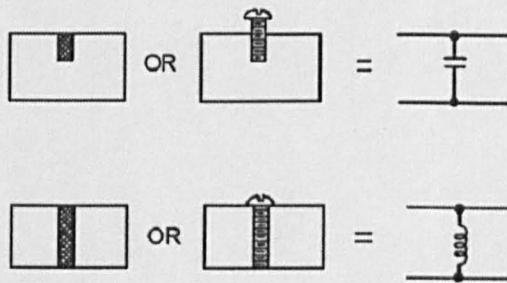


Figure 4.8. Post and screws electrical equivalents.

A post or screw which only partially penetrates into the waveguide acts as a shunt capacitive reactance. When the post or screw extends completely through the waveguide, making contact with the top and bottom walls, it acts as an inductive reactance. Note that when screws are used the amount of capacitive reactance can be varied [60].

4.3 Cavity Resonator Simulations

4.3.1 HFSS Model Simulations

The cavity has been modelled, as shown in figure 4.9 using HFSS [64]. HFSS utilizes a 3D full-wave Finite Element Method (FEM) to compute the electrical behaviour of high-frequency and high-speed components. The model reproduces the conditions of the real cavity resonator. The screws and antennas materials are assigned to PEC (Perfect Electrical Conductor), the test tube is made of polypropylene and filled with distilled water. The cavity is represented by a vacuum. The antennas are set to be the excitation ports of the system. The HFSS files are available in appendix A (CD-Rom). HFSS applies the equations presented in section 3.2 and 3.3.

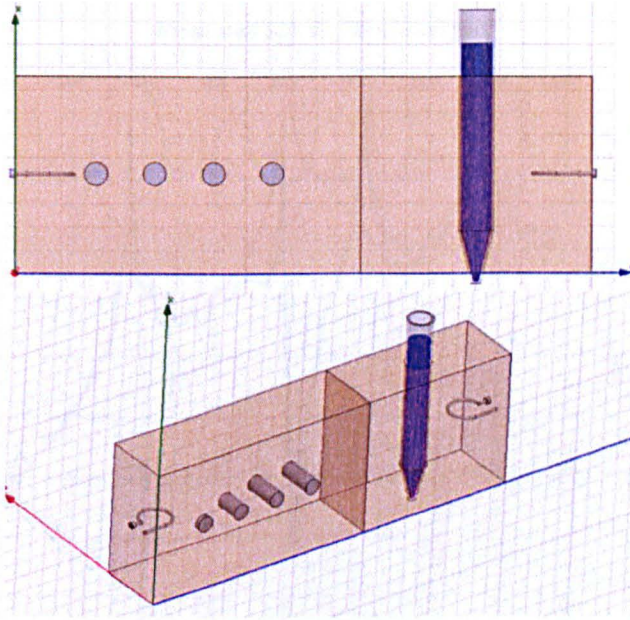
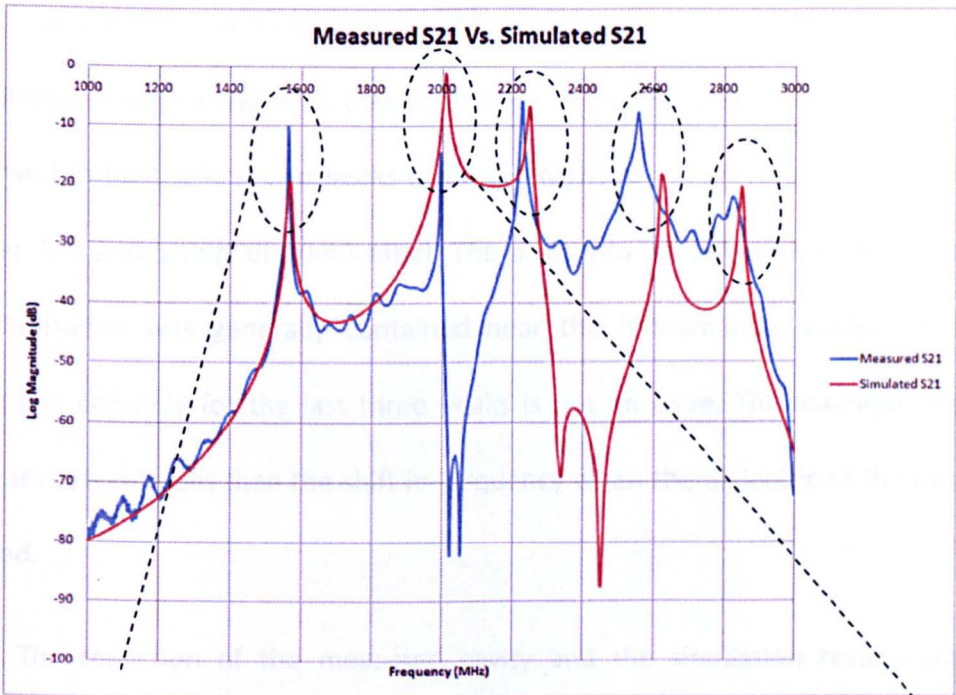


Figure 4.9. 3D Cavity Resonator Model in HFSS.

The cavity resonator had been built before the project started but had never previously been modelled and simulated with such precision.

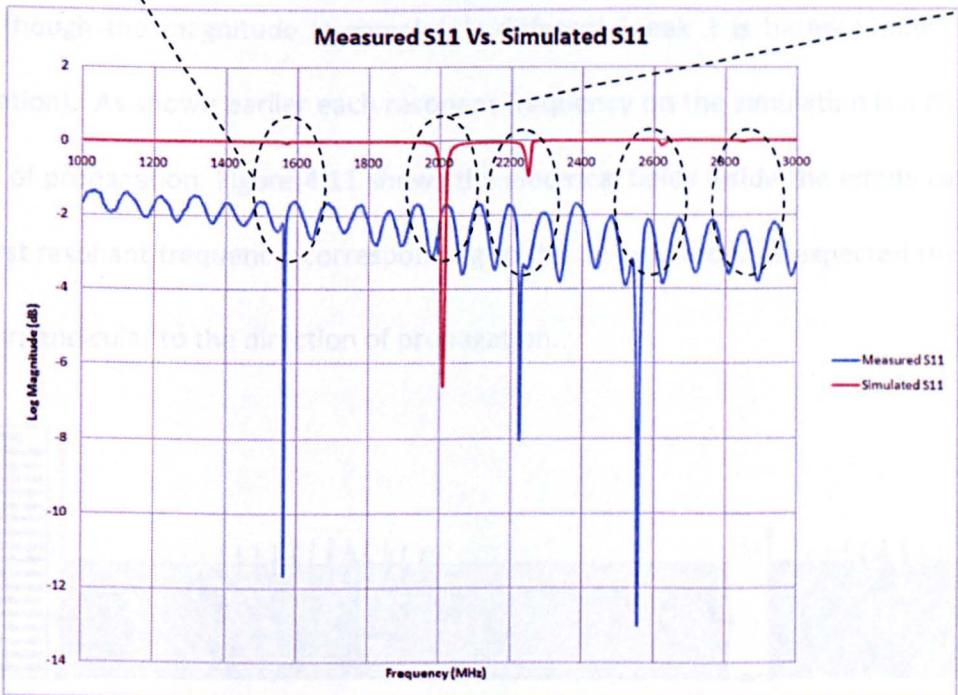
The first simulation carried out for an empty cavity with a frequency sweep starting at 1GHz and finishing at 3GHz. The RF output power was set to 0dBm. The results are compared to the actual cavity response to the same range of frequency, Figure 4.10 show this comparison.



1st Resonance; Mode TE₁₀₁

(a)

2nd Resonance; Mode TE₁₀₂



(b)

Figure 4.10. Measured and simulated transmission S21 (a), Measured and simulated reflection S11 (b).

The transmission parameters of the simulation and the measured signal have very similar shapes at the peak points. Looking at the frequencies of the peaks, they are close too for the first two peaks (shift <10 MHz), but a bit less accurate for peak number 3, 4 and 5 (shift of 20-40 MHz). The most information retrievable in material characterisation was generally contained near the fundamental modes. Therefore having less accuracy for the last three peaks is not an issue. The magnitudes of the peaks are less relevant than the shift in frequency when the dielectric of the sample is changed.

The reflection of the measured cavity and the simulation results are very accurate too if we look at the frequency. The first 3 trough frequencies are very close even though the magnitude is completely different (peak 1 is barely visible on the simulation). As shown earlier each resonant frequency on the simulation is a different mode of propagation. Figure 4.11 shows the electrical fields inside the empty cavity at the first resonant frequency, corresponding to the TE_{101} mode. As expected the fields are perpendicular to the direction of propagation.

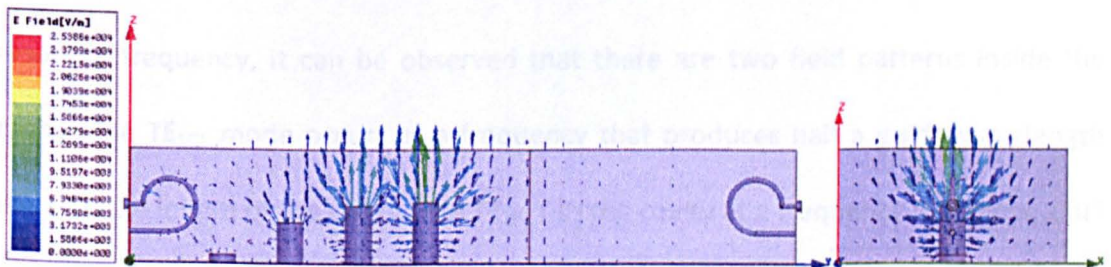


Figure 4.11. TE_{101} Electrical fields.

Figure 4.12 represents the magnetic fields at the same frequency. As expected in the fundamental TE_{101} mode, the magnetic fields have a component in the direction of propagation.

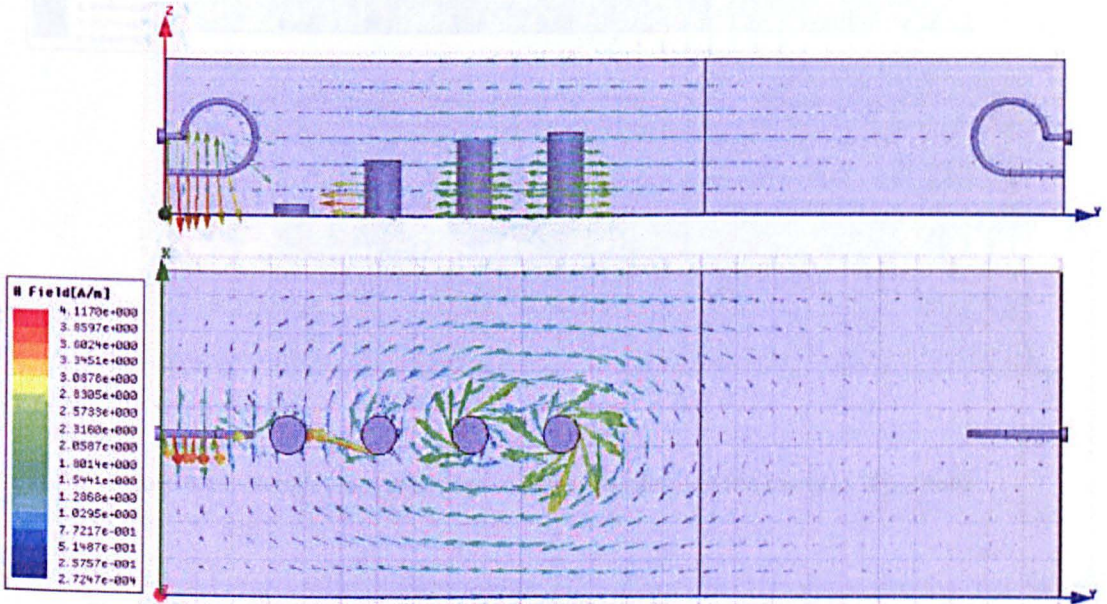


Figure 4.12. TE_{101} magnetic fields.

The magnetic fields at the sample location will be shown in details later in the thesis when the cavity is simulated with different samples. Looking closer at the second resonant frequency, it can be observed that there are two field patterns inside the cavity. The TE_{101} mode occurs at a frequency that produces half a guide wavelength equal to the length of the cavity. The TE_{102} fills the cavity at a frequency that gives a full guide wavelength. Figure 4.13 shows how the E field (top) and H field (bottom) appear for TE_{102} .

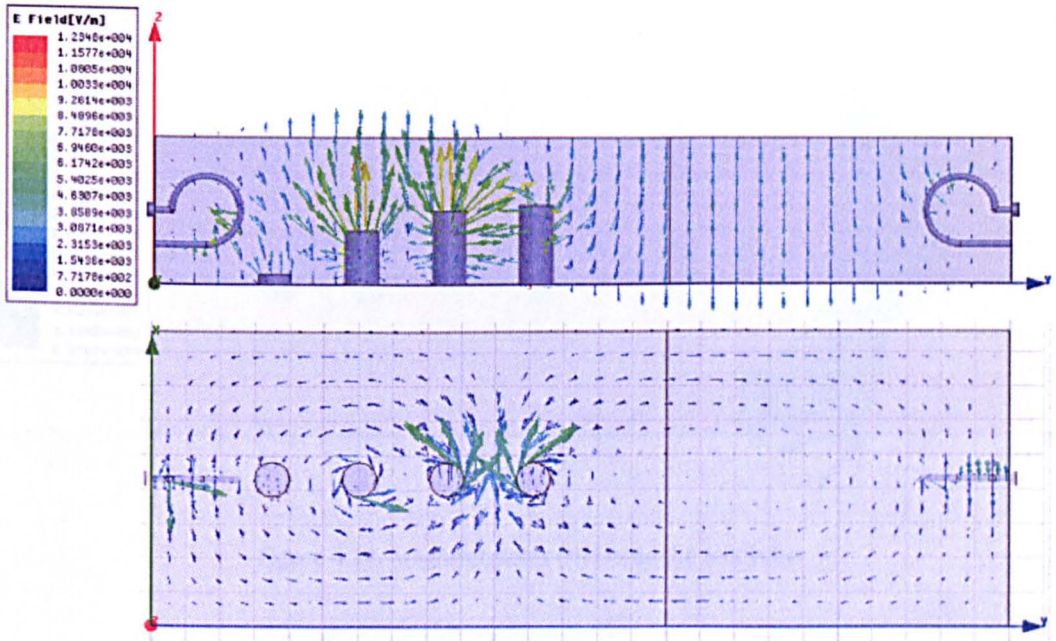


Figure 4.13. Electric (top) and magnetic fields (bottom) of the cavity in TE_{102} mode.

Figure 4.14 shows the H field inside the test tube. The intensity of the vectors has decreased due to the change of permittivity of water. In this picture, it is easier to understand how the reflected and transmitted fields are measured.

4.3.3 Diagnostic Simulations

The vectors going backward (from right to left) represent the reflection, and will be measured by the loop antenna used to emit the signal too (left). The vectors going forward (from left to right) are transmitted and will be measured by the antenna on the right (receiver).

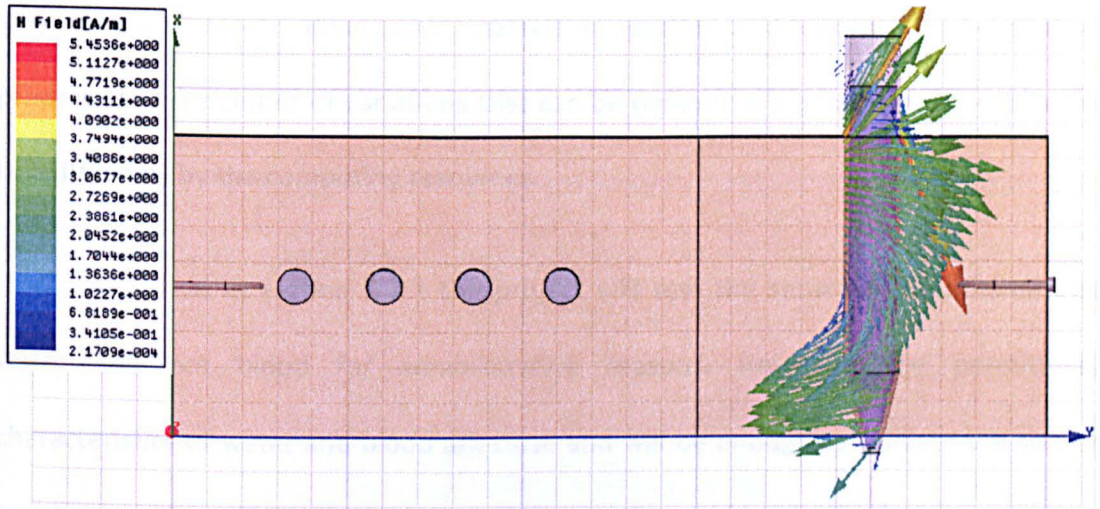


Figure 4.14. Magnetic fields (H) inside the test tube.

Notice that the vectors at the top and bottom (inside the cavity) have intensities greater than the field vectors in the middle of the sample. This is due to the properties of the TE_{10} mode. When the loop antenna emits the electromagnetic wave, it expands inside the cavity, and reaches its highest intensity near the cavity walls.

4.3.2 Parametric Simulations

The cavity has been simulated with the help of a parametric analysis of the liquid inside the test tube. Running a parametric analysis enables the user to simulate several design variations using a single model. If a series of variable values within a range is defined, or a *variable sweep definition*, HFSS generates a solution for each design variation. The user can then compare the results to determine how each design variation affects the performance. Design parameters that are assigned a quantity can

vary, such as geometry dimensions, material properties, and boundary and excitation properties. The number of variations that can be defined in a parametric sweep setup is limited only by the computing resources.

As stated in section 5.2.1 the project will test the sensor using ethanol and water and not blood for administrative reasons. However, the permittivity characteristics of water and blood are close and will be enough to validate the sensor capabilities. Figure 5.15 shows the permittivity values of blood cells depending on the frequency.

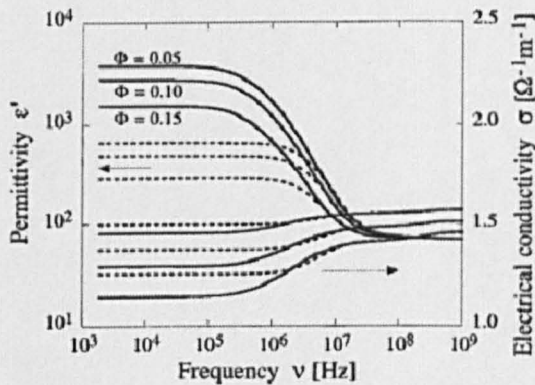
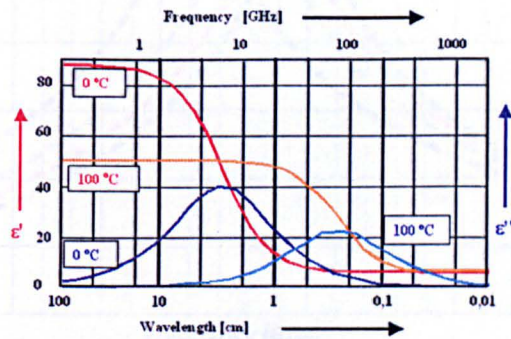


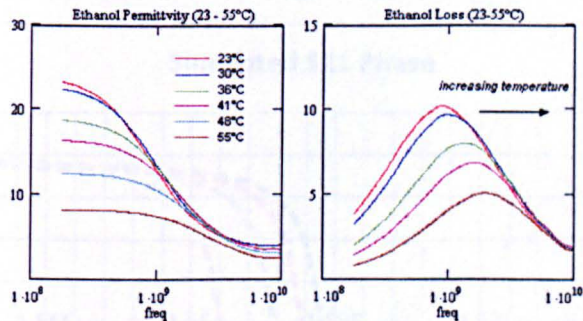
Figure 4.15. Permittivity values of blood cells over the frequency [65].

The dielectric values of water and ethanol depend on the frequency and temperature as shown in figure 4.16. Figure 4.17 shows the different results obtained by applying a parametric analysis inside the test tube for permittivity constants ranging

from 20 to 80, in increments of 20. Those values cover the dielectric value for water ($78 < \epsilon_r < 82$) as well as the dielectric value for ethanol ($14 < \epsilon_r < 24$) for frequencies between 100MHz to 3GHz. All those characteristics are known as relaxation parameters of a material.



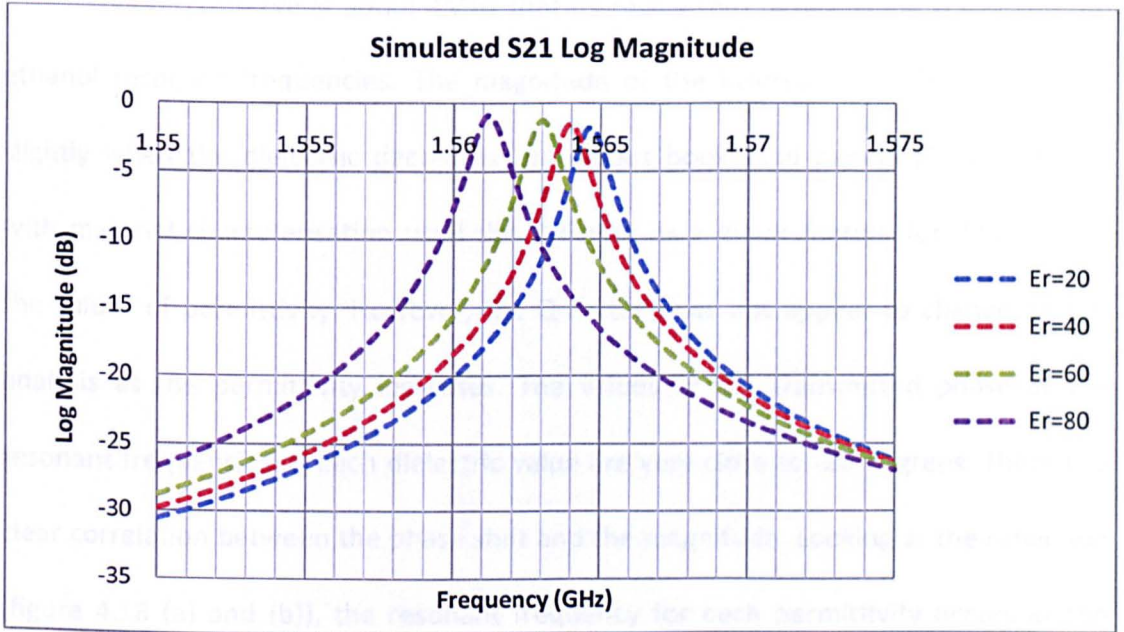
(a)



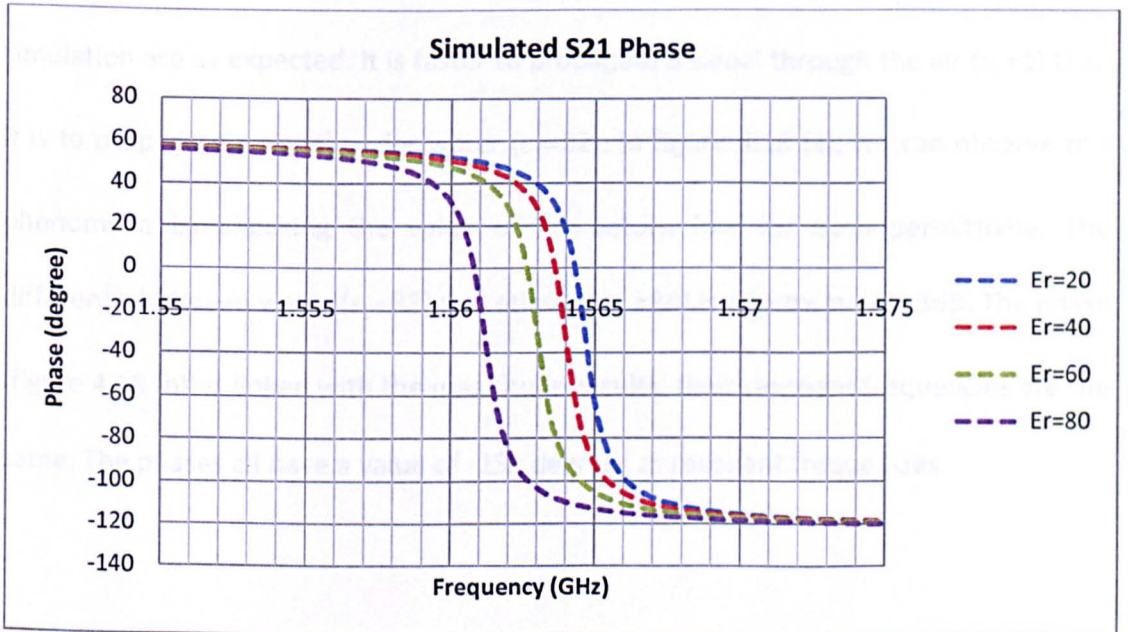
(b)

Figure 4.16. Relaxation properties of water (a) [66], relaxation properties of ethanol (b) [67].

The results of the parametric analysis made on the transmission confirm the results obtained by Wylie and Al-Shamma'a [7], who concluded that an increase of dielectric in a material would decrease its resonant frequency.



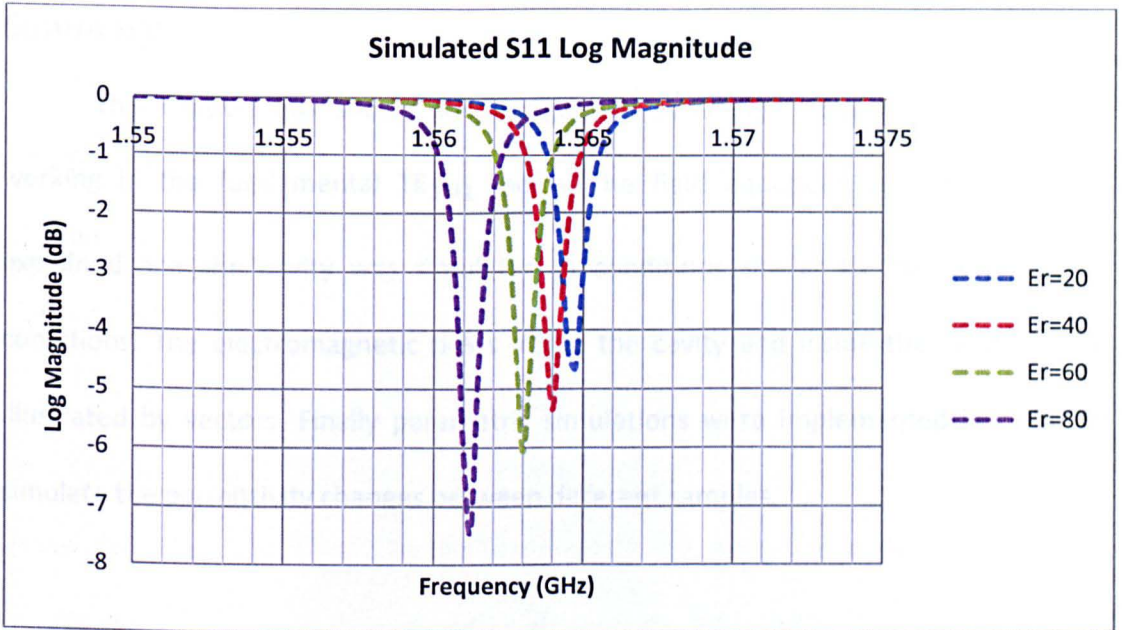
(a)



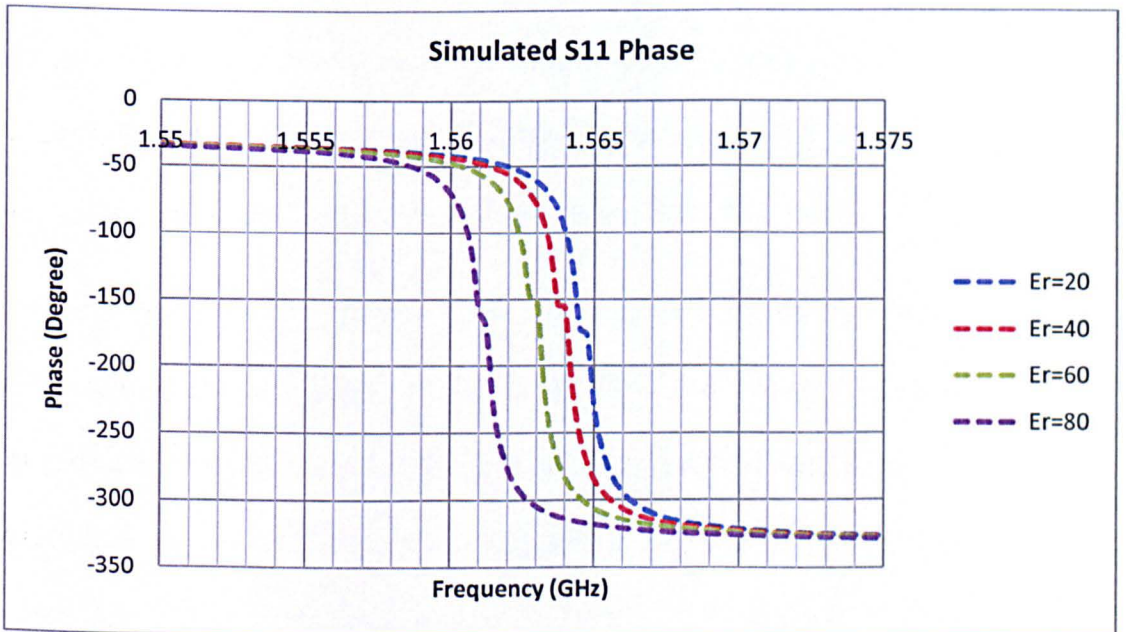
(b)

Figure 4.17. S21 (transmission S-parameter) magnitude (a) and phase (b) simulations for the test tube filled with dielectric permittivity of 20,40,60,and 80.

We can observe at about 4MHz that there is a shift between the water and the ethanol resonant frequencies. The magnitude of the Insertion Loss (S21) increases slightly when the dielectric decreases. Numerous books and papers [42-44] dealing with material characterisation used the Q-Factor as a major feature for determining the values of permittivity. However, the Q-Factor does not appear to change on the analysis as the permittivity increases. The values of the transmitted phase at the resonant frequencies of each dielectric value are very close to -20 degrees. There is a clear correlation between the phase shift and the magnitude. Looking at the reflection (figure 4.18 (a) and (b)), the resonant frequency for each permittivity occurs at the same frequencies as for the transmission. The reflection magnitudes from the simulation are as expected. It is faster to propagate a signal through the air ($\epsilon_r=1$) than it is to propagate a signal under water ($\epsilon_r=82$). In figure 4.18 (a), we can observe this phenomena by checking the value of the return loss for each permittivity. The difference between water ($\epsilon_r=82$) and ethanol ($\epsilon_r=24$) is approximately 3dB. The phase (figure 4.18 (b)) is linked with the magnitude results, their resonant frequencies are the same. The phases all have a value of -150 degrees at resonant frequencies.



(a)



(b)

Figure 4.18. S11 (reflection S-parameter) magnitude (a) and phase (b) simulations for the test tube filled with dielectric permittivity of 20,40,60,and 80.

Summary

This chapter has shown the design and simulation of a rectangular cavity working in the fundamental TE_{101} mode. The field equations used by HFSS are explained and the cavity was simulated in conditions similar to the experimental conditions. The electromagnetic fields inside the cavity and inside the sample were illustrated by vectors. Finally parametric simulations were implemented in order to simulate the permittivity changes between different samples.

5 CAVITY RESONATORS EXPERIMENT RESULTS

5.1 System Setup

5.1.1 Hardware

The non-invasive system (figure 5.1) is based on a WG9A (also called WR340) cavity resonator, under which an infrared thermometer measures the temperatures of the samples through a small hole. A vector network analyser (VNA) sends and receives electromagnetic waves from the cavity by coaxial cables and SMA ports, and is connected to a computer via an Ethernet RJ-45 network cable and is fully controllable remotely by using TCP/IP sessions. The VNA extracts the S-Parameters of the loaded cavity and sends it to the software especially created for this system.

It can deliver a frequency sweep ranging from 9kHz to 3GHz with up to 4001 points and a gain of up to +27dBm. The Optris CT InfraRed (IR) thermometer is connected by USB to the computer but uses a HyperTerminal session to access the data. It has a precision of a tenth of a degree Celsius. It is possible to focus the IR beam by adding different lenses to the sensor.

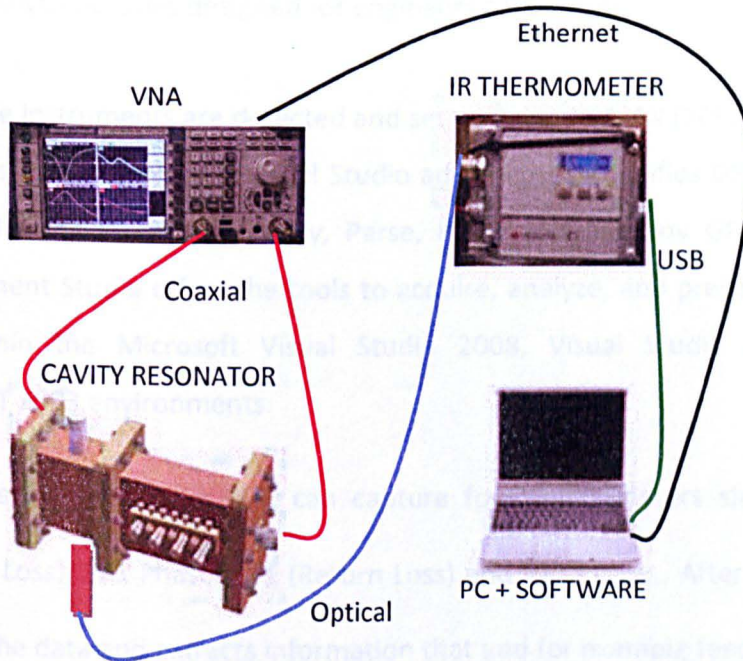


Figure 5.1. Microwave non-invasive testing system setup.

5.1.2 Software

The system is controlled by software created using Visual Studio 2008 C# [68] to which the National Instruments Measurement Studio has been added. This add-on is an integrated suite of managed classes and controls designed especially for test, measurement, automation applications and instrument drivers. Measurement Studio [69] for Visual C# .NET provides:

- Managed .NET controls for creating rich Web and Windows GUIs.
- Multithreaded API for data acquisition.
- Instrument control APIs.

- Analysis libraries designed for engineers and scientists.

The instruments are detected and set up using NI MAX [70] and some TCP/IP NI VisaNS sessions. VisaNS is a Visual Studio add-on that simplifies GPIB machines to be controlled using VisaTasks (Query, Parse, Read) just like any GPIB based controls. Measurement Studio offers the tools to acquire, analyze, and present real-world data from within the Microsoft Visual Studio 2008, Visual Studio 2005, and Visual Studio.NET 2003 environments.

The Software and VNA can capture four S-parameters simultaneously, S_{21} (Insertion Loss), S_{21} Phase, S_{11} (Return Loss) and S_{11} Phase. After the acquisition, it analyses the data and extracts information that and for example feed a neural network for a prediction.

In terms of capabilities, the software is very powerful. It acquires the measurements from the VNA in less than two seconds using the VisaNS protocols, whereas the previous software, made without Measurement Studio needed between 10 and 20 seconds to perform this task. Within the two seconds, it displays the S-Parameters and extracts useful additional parameters such as Q-Factors, S-Parameter magnitudes and phases (as well as minima, maxima and gradients), reflection coefficient, VSWR and the temperature of the sample. Figure 5.2 shows the layout of the main tab of the software, and figure 5.3 illustrates all the extracted values displayed on gauges and meters. The C# code for the software is provided in appendix B.

The software also offers the possibility to export the graphs, parameters and temperature to CSV files (Comma Separated Values) for further data manipulation and analysis (e.g. Microsoft Excel). Another important feature of the software is the VNA control capability. It is possible to recall the calibrations previously made, apply smoothing and change its aperture, autoscale, setting the input power as well as changing the start and stop frequencies as shown in Figure 5.4.

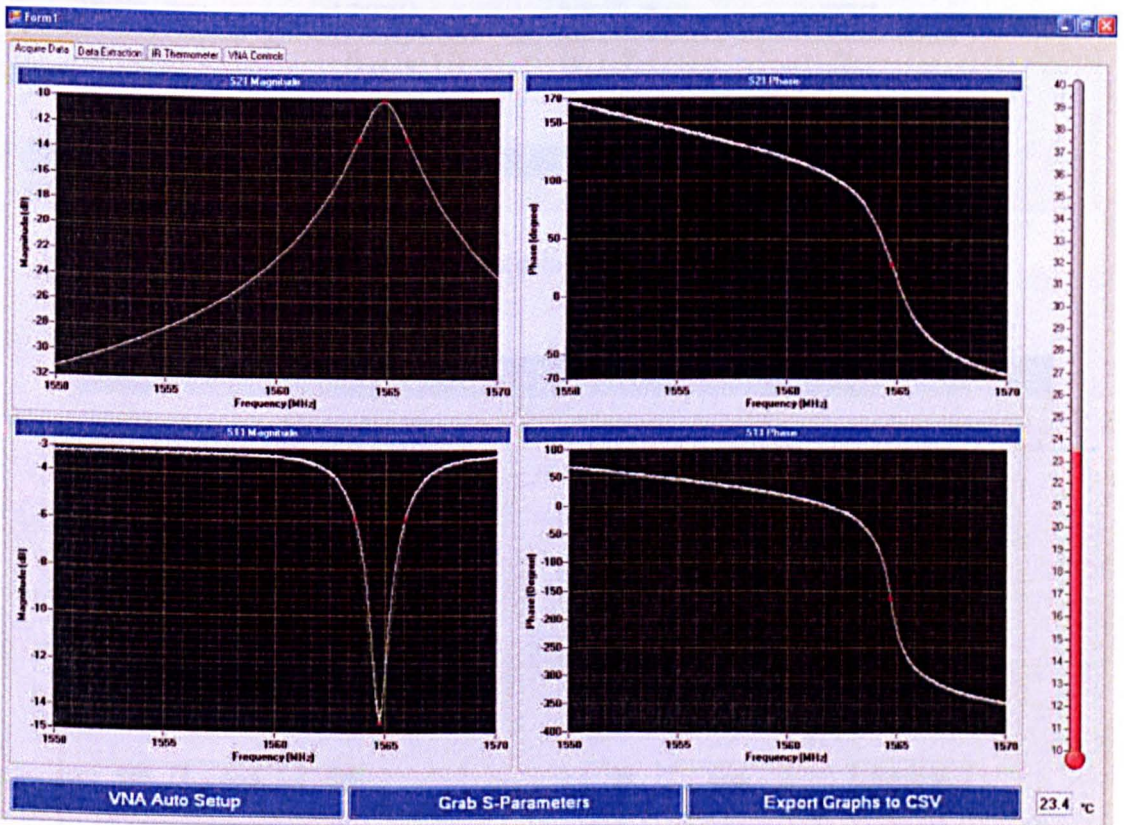


Figure 5.2. Main tab displaying the S-Parameters and the temperature of the sample under test.

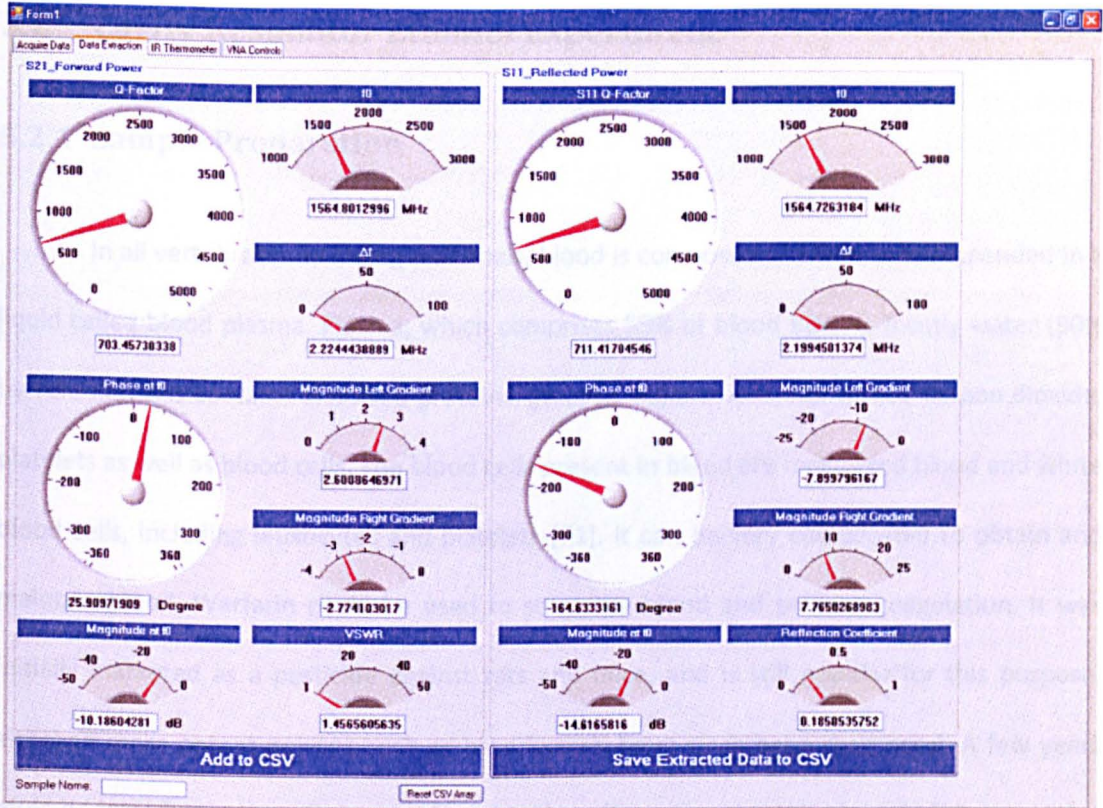


Figure 5.3. Extracted data from the S-Parameters.

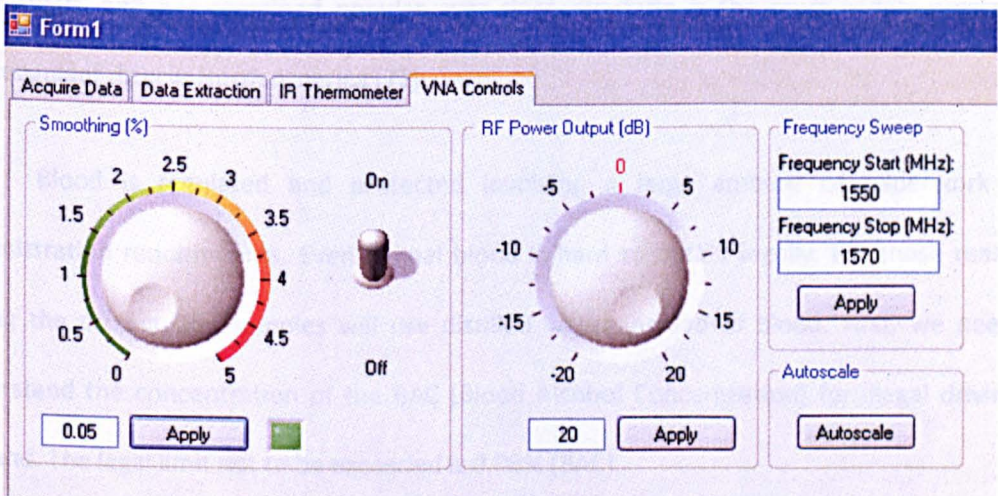


Figure 5.4. Software VNA Controls.

5.2 Cavity Resonator Ethanol Experiment

5.2.1 Sample Preparation

In all vertebrates including mammals, blood is composed of blood cells suspended in a liquid called blood plasma. Plasma, which comprises 55% of blood fluid, is mostly water (90% by volume), and contains dissolved proteins, glucose, mineral ions, hormones, carbon dioxide, platelets as well as blood cells. The blood cells present in blood are mainly red blood and white blood cells, including leukocytes and platelets [71]. It can be very complicated to obtain and maintain blood. Warfarin could be used to store the blood and prevent coagulation. It was initially marketed as a pesticide against rats and mice, and is still popular for this purpose, although more potent poisons such as brodifacoum have since been developed. A few years after its introduction, warfarin was found to be effective and relatively safe for preventing thrombosis and embolism in many disorders. It was approved for use as a medication in the early 1950s, and has remained popular ever since; warfarin is the most widely prescribed anticoagulant drug in North America [72].

Blood is regulated and protected involving a large amount of paperwork and administration requirements. Even animal blood is hard to obtain legally. For those reasons, during the project, the samples will use distilled water instead of blood. First, we need to understand the concentration of the BAC (Blood Alcohol Concentration) for illegal driving in England. The legal limit not to be exceeded is 0.08% (BAC).

The table 5.1 shows the conversion of the BAC to different mass per volume and volume by volume concentrations as well as its equivalent in a 15ml sample by volume. The density of ethanol is $0.789\text{g/cm}^3 = 0.789\text{g/mL} = 789\text{g/l}$.

Concentration of ethanol in blood (Mass/volume & volume/volume)						
% BAC	g / l	mg/dl	ml / l	ml / ml	concentration % (v/v)	concentration ml /15ml sample
0.08	0.8	80	1.01394	0.00101394	0.101394	0.01521

Table 5.1. BAC conversion to 15ml samples.

The samples were prepared using a 200 μl -1000 μl pipette, some pure ethanol and distilled water were kindly donated by the biology department of Liverpool John Moores University (see Figure 5.5).

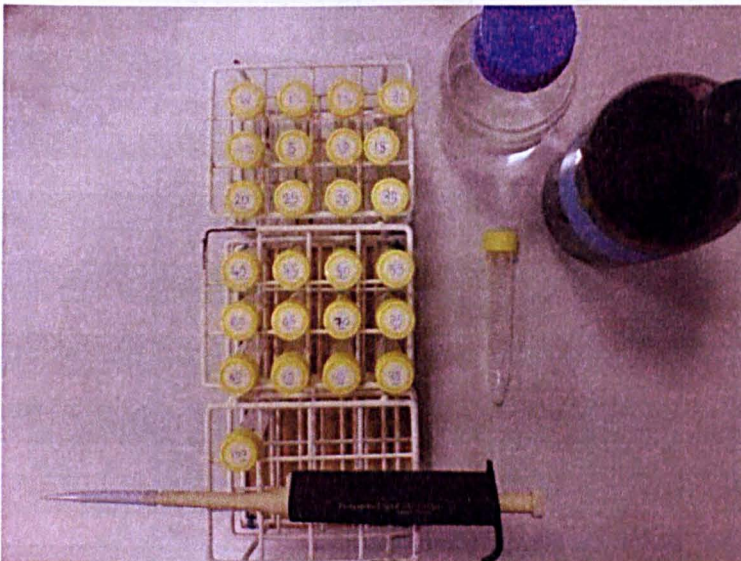


Figure 5.5. Samples, pipette, water and ethanol.

The ethanol increment between each sample, for preliminary tests and to check how the cavity would react was set to 5%. However as the interest is based on low percentages, 1% ethanol increments were used from pure water to 5% ethanol. This range of samples should provide a representative test response over the whole water/ethanol mixture range. As shown in the table 5.2, the samples were named depending on percentage of ethanol.

Sample Concentrations				
Sample's Name	Ethanol (%)	Water (%)	Ethanol (ml)	Water (ml)
0 or 'w'	0	100	0	15
1	1	99	0.15	14.85
2	2	98	0.3	14.7
3	3	97	0.45	14.55
4	4	96	0.6	14.4
5	5	95	0.75	14.25
10	10	90	1.5	13.5
15	15	85	2.25	12.75
20	20	80	3	12
25	25	75	3.75	11.25
30	30	70	4.5	10.5
35	35	65	5.25	9.75
40	40	60	6	9
45	45	55	6.75	8.25
50	50	50	7.5	7.5
55	55	45	8.25	6.75
60	60	40	9	6
65	65	35	9.75	5.25
70	70	30	10.5	4.5
75	75	25	11.25	3.75
80	80	20	12	3
85	85	15	12.75	2.25
90	90	10	13.5	1.5
95	95	5	14.25	0.75
100 or 'e'	100	0	15	0

Table 5.2. Sample concentrations in percentage (%) and millilitres (ml).

Five more samples were used to approach the BAC level, 0.8%, 0.6%, 0.4%, 0.2% and finally 0.1%. This means that with 0.1% , it is lower than the BAC (0.101394% by volume). Table 5.3 shows the concentrations inferior to 1%. 0.1% ethanol by volume is equal to 0.015ml of pure ethanol per 15ml samples. The former volume is too small to achieve accurately using the pipette.

Sample Concentrations					Sample Concentrations using Ethanol 1%		
Sample's Name	Ethanol (%)	Water (%)	Ethanol (ml)	Water (ml)		ethanol 1% (ml)	water (ml)
0.1	0.1	99.9	0.015	14.985	=	1.5ml	13.5ml
0.2	0.2	99.8	0.03	14.97	=	3ml	12ml
0.4	0.4	99.6	0.06	14.94	=	6ml	9ml
0.6	0.6	99.4	0.09	14.91	=	9ml	6ml
0.8	0.8	99.2	0.12	14.88	=	12ml	3ml

Table 5.3. Samples Under 1%.

To solve this problem, water and a solution of 1% ethanol was used to fill the samples. The 'Sample Concentration using Ethanol 1%' columns of table 5.3 shows that, a 0.1% sample can be realised using 1.5ml of 1% ethanol instead of 0.015ml of 100% ethanol. The same preparation procedure was used for the other concentrations.

5.2.2 Ethanol Results- 0% (Water) to 100% (Ethanol) by 5%

Increments

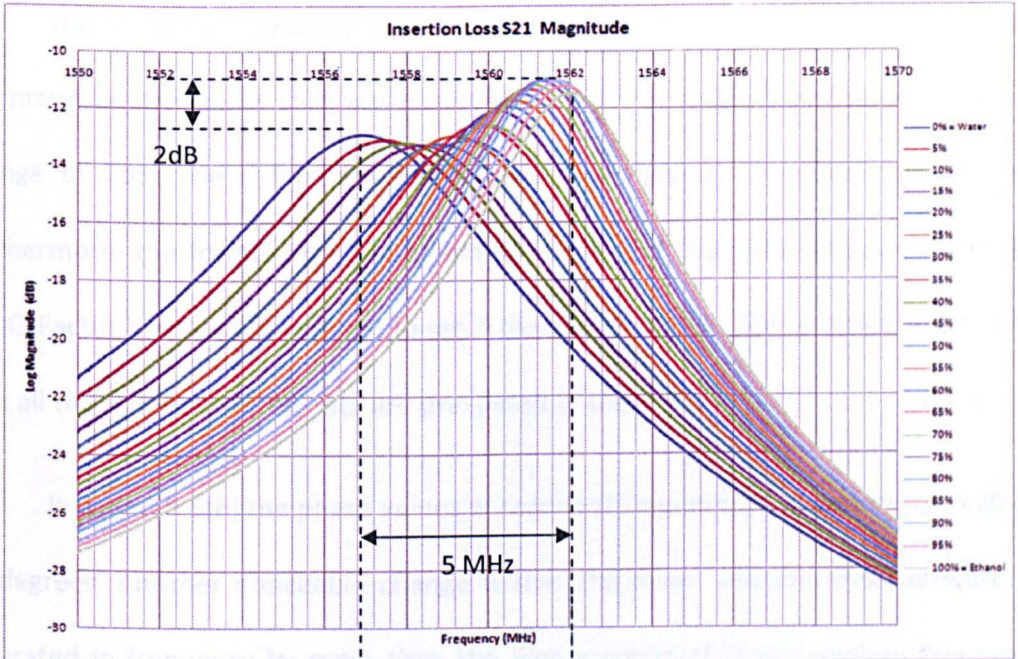
The experiments shown in this section were conducted at room temperature ($21.4 \pm 0.5^\circ\text{C}$). A 2-port TOSM (Through Open Short Match) calibration was performed for the 1.55GHz-1.57GHz frequency window for each of the four graphs on the VNA.

It is known that temperature has a huge effect on the resonant frequency and therefore was closely monitored during testing. To obtain results without temperature sensitivity, the temperature should not change by more than half a degree Celsius between the samples. Therefore, in order to achieve accurate results, the experiment should be performed in a room monitored with thermostats or automatic air conditioning to keep the temperature within $\pm 0.5^{\circ}\text{C}$.

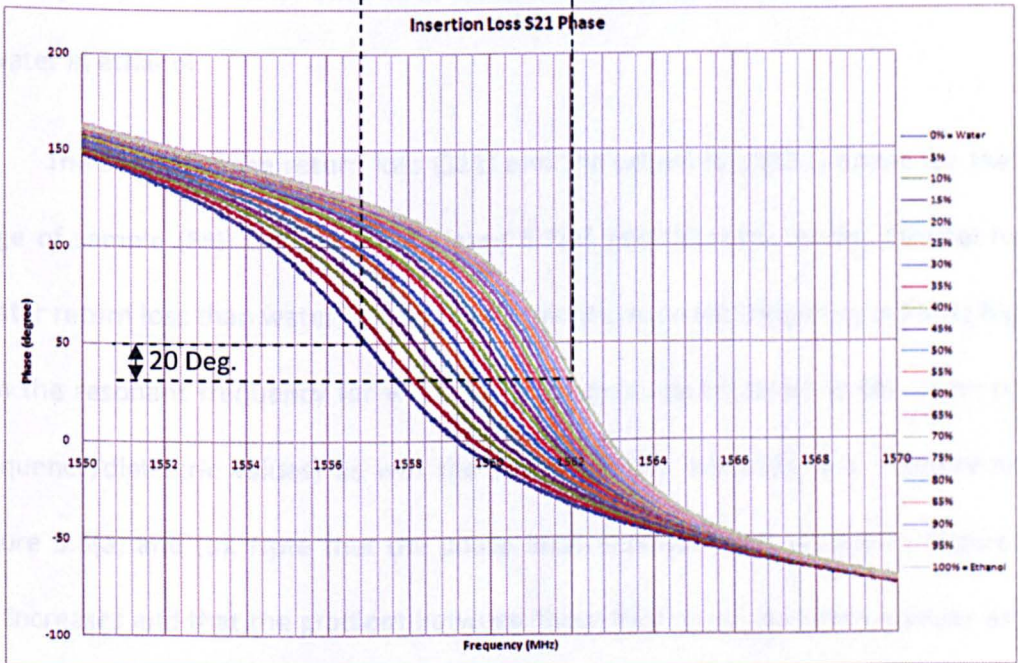
The samples were placed one by one into the cavity and tests were performed. The software captures the 4 graphs representing the transmission and reflection S-Parameters and their phases. All the data was saved to a .CSV file and subsequently exported to Excel to be analysed.

With a few algorithms running inside the acquisition software, useful data was extracted from the 4001 points in each graph, such as the resonant frequencies, magnitudes and phase and the Q-factors.

Figure 5.6 (a) and (b), are the results of the insertion loss of the samples. The average frequency shift for the 5% increments is excellent; none of the concentrations are too close to each other and every sample is clearly distinguishable. Water has more insertion loss than ethanol.



(a)



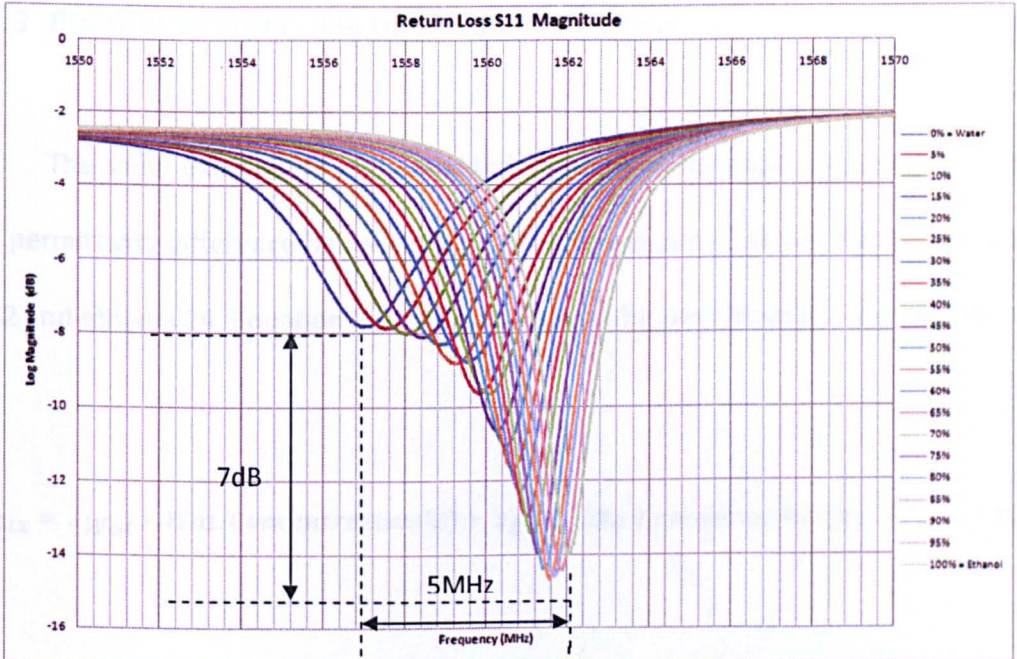
(b)

Figure 5.6. Experimental results of the insertion loss (a), and the insertion loss phase (b) for the full range of samples (5%).

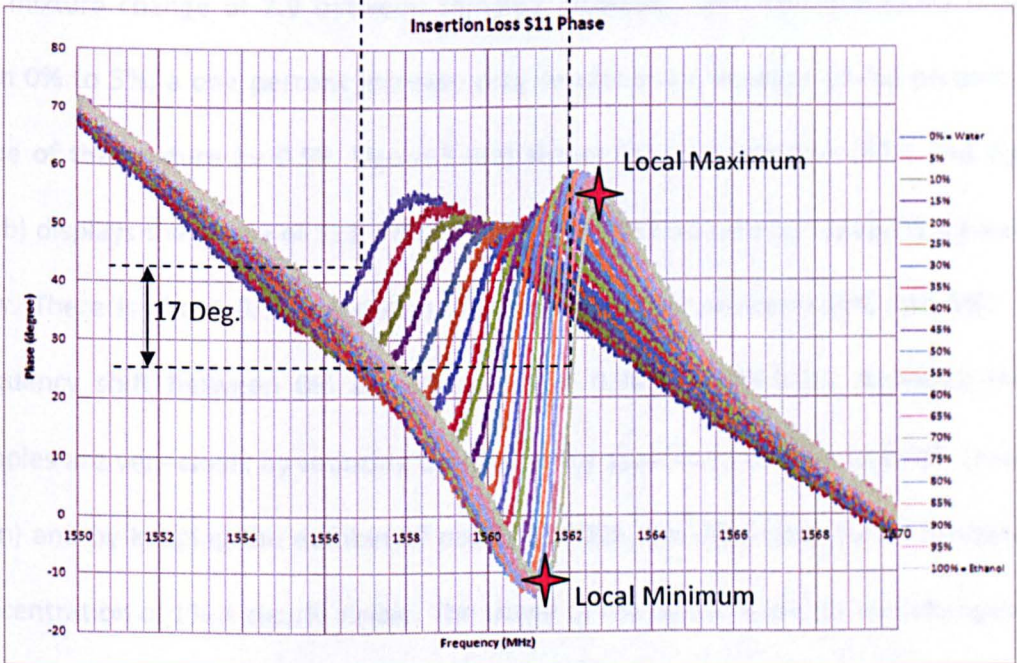
The resonant frequency increases as the permittivity decreases as anticipated. The maximum frequency shift was observed as 5MHz as well as a maximum magnitude change of 2dB. The Q-factor displayed significant changes between the samples. Furthermore, the formula for S21 Q-factor is different than the formula to calculate S11 Q-Factor, so it was of interest to see if the curves match. The Q-factor results along with all the other extracted data are presented in section 3.3.6.

In Figure 5.6(b) the phase values at resonant frequencies occur between 20 and 50 degrees. Another noticeable change is that the lower concentration samples are separated in frequency by more than the higher concentration samples. This means that very small amounts of ethanol in water are more detectable than small amounts of water in ethanol.

The results of the return loss (S11) and the return loss (S11) phase for the full range of sample (5%) are shown in Figure 5.7(a) and (b) respectively. Ethanol has a greater return loss than water by about 7dB, and its resonant frequency is 5MHz higher than the resonant frequency for water. The samples appear to be in the same order (frequency/dielectric values) as was the case with the insertion loss measurements (Figure 5.6(a) and (b)). Note that the phase local minimum and maximum (Figure 5.7 (b)) increases and that the gradient between those two points becomes steeper as the sample's dielectric constant increases.



(a)



(b)

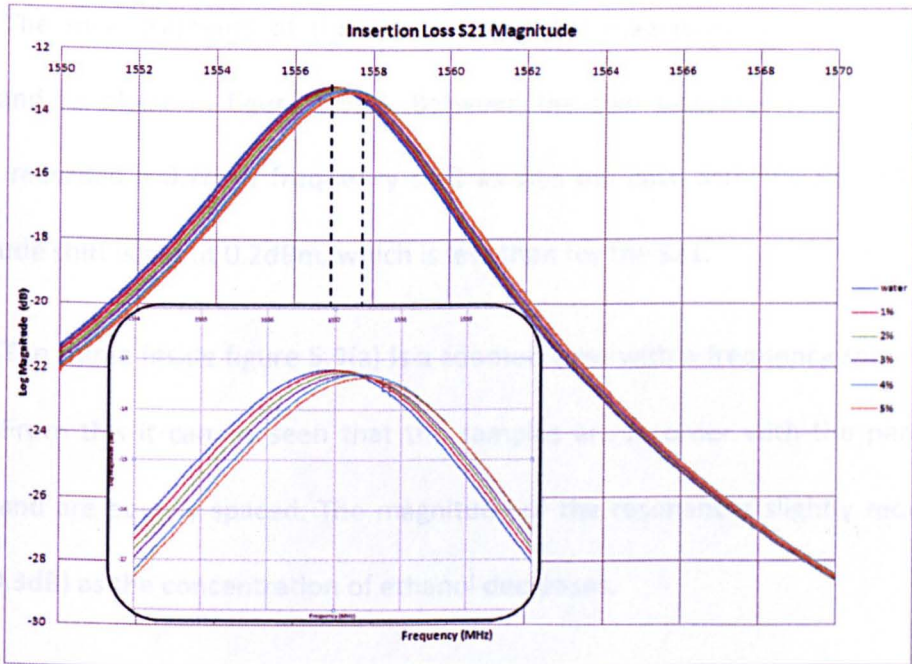
Figure 5.7. Experimental results of the return loss (a), and return loss phase (b) for the full range of samples (5%).

5.2.3 Ethanol Results- 0% to 5% by 1% Increments

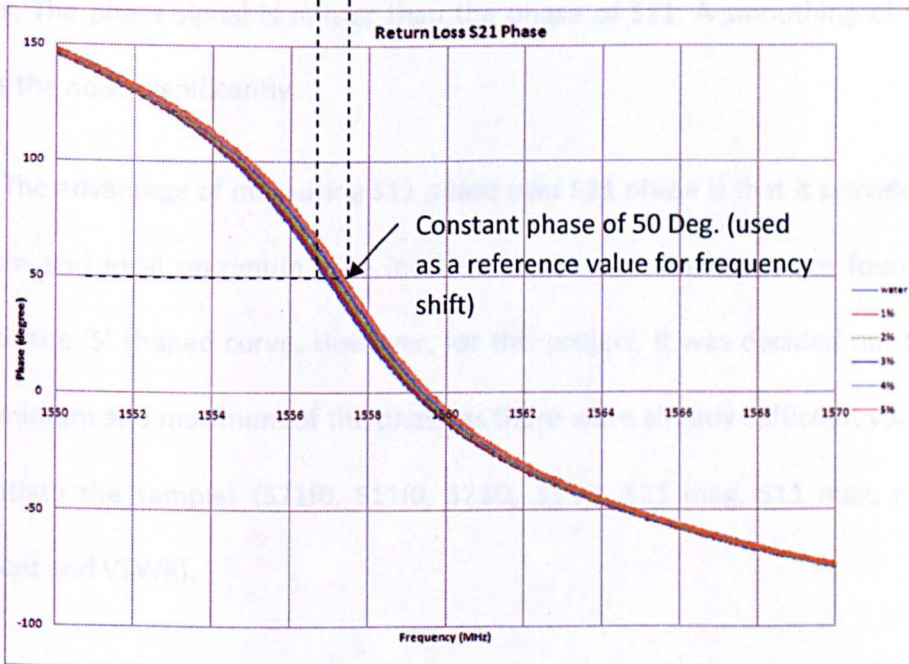
The same experiment was repeated with low percentage samples (0% to 5%). The permittivity difference between 0% and 5% is very small. Water has a permittivity of 82 and ethanol 24. Equation 5.1 is used calculate the permittivity of any samples.

$$\epsilon_{Mix} = \epsilon_{Wat} * Wat.Concentration(\%) + \epsilon_{Eth} * Eth.Concentration(\%) \quad (5.1)$$

A change of 5% as in the previous experiment corresponds to a permittivity of the mixture change of 2.9 between samples. However, with concentrations ranging from 0% to 5%, a one percent increase only results in an increase of the permittivity value of the mixture by 0.58. Figure 5.8(a) shows the insertion loss (S21) and figure 5.8(b) displays the phase of S21. The frame inside the insertion loss graph is a zoomed view. There is about 0.35-0.40dB loss between the two extremes (0% and 5%). The frequency shift between 0% and 5% is about 0.7MHz (700 KHz). Although the 6 samples are very close, by reducing the frequency span from 20MHz to 6MHz (zoom's span) and by keeping the number of points to 4001, the difference for an increase in concentration of 1% is clearly visible. The shape of the phase response also changes. To use the phase as an indication for ethanol concentration, the largest shift in frequency at constant phase values (for 50 degree) was measured.



(a)



(b)

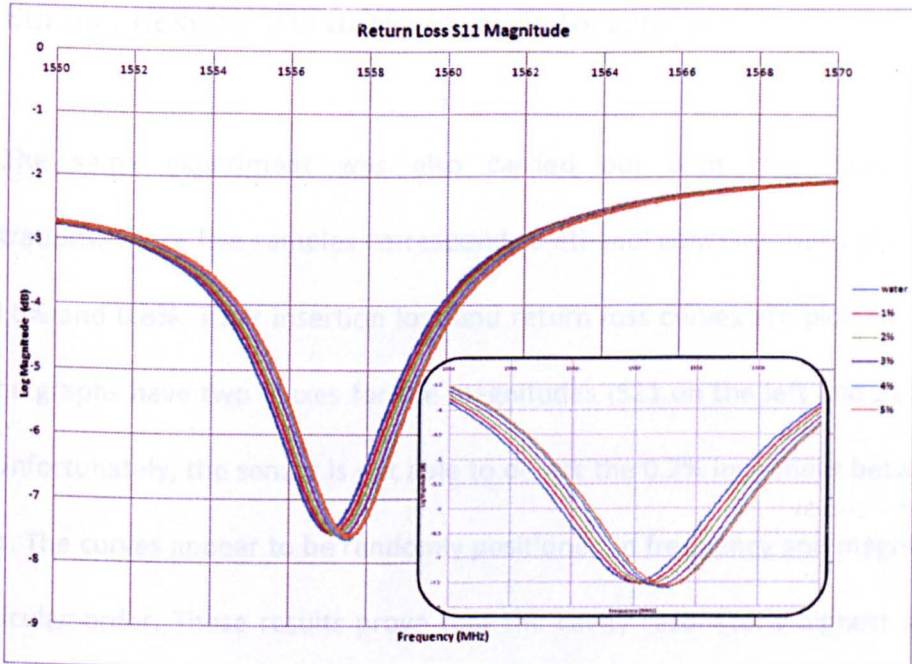
Figure 5.8. S21 measurements, (a) insertion loss, (b) phase.

The measurements of the return loss (S_{11}) magnitude are shown in figure 5.9(a) and its phase in figure 5.9(b). Between the two extremes (0% and 5%), the system recorded a 0.7MHz frequency shift as was the case with the S_{21} values. The magnitude shift is about 0.2dBm, which is less than for the S_{21} .

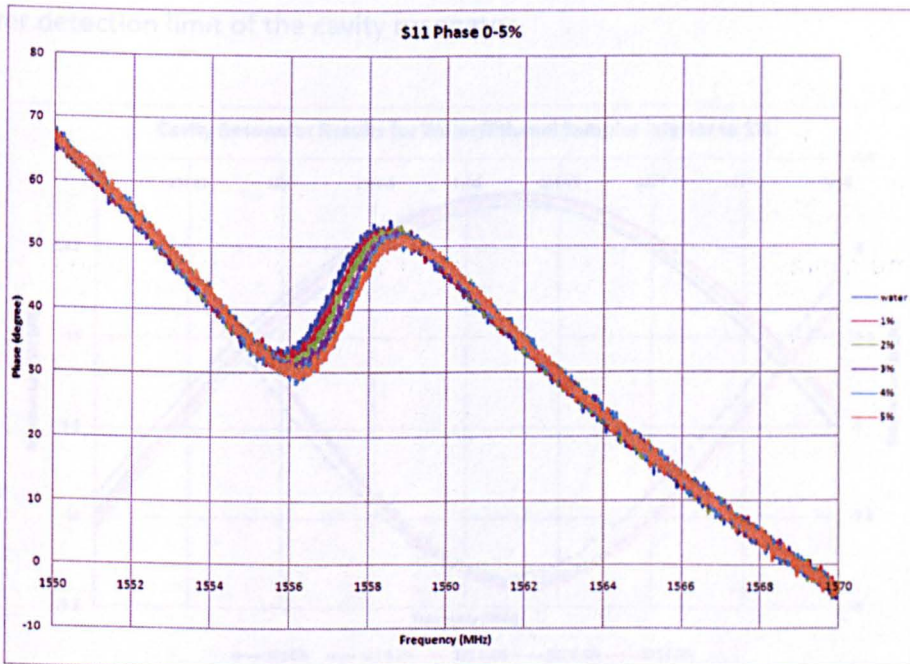
The frame inside figure 5.9(a) is a zoomed view with a frequency span equal to 6MHz. From this it can be seen that the samples are in order with the permittivity values and are equally spaced. The magnitude of the resonances slightly reduces (by about 0.3dB) as the concentration of ethanol decreases.

In figure 5.9(b), one can observe the reaction of the phase for the different samples. The phase signal is noisier than the phase of S_{21} . A smoothing of 0.5-2.5% reduces the noise significantly.

The advantage of measuring S_{11} phase over S_{21} phase is that it provides a local minimum and local maximum. The local minimum and maximum are found in the bends of the 'S' shaped curve. However, for this project, it was decided not to retain local minimum and maximum of the phase as there were already sufficient variables to differentiate the samples ($S_{21}f_0$, $S_{11}f_0$, $S_{21}Q$, $S_{11}Q$, S_{21} mag, S_{11} mag, reflection coefficient and VSWR).



(a)



(b)

Figure 5.9. S11 measurements, (a) return loss magnitude, (b) phase.

5.2.4 Ethanol Results- 0% to 1% by 0.2% Increments

The same experiment was also carried out with the lowest sample concentrations. These five samples correspond to ethanol concentrations of 0%, 0.2%, 0.4%, 0.6% and 0.8%. Their insertion loss and return loss curves are plotted in figure 5.10. The graphs have two Y-axes for the magnitudes (S_{21} on the left and S_{11} on the right). Unfortunately, the sensor is not able to detect the 0.2% increment between the samples. The curves appear to be randomly positioned in frequency and magnitude, in no particular order. Those results prove that the cavity resonator's highest accuracy allows concentration change of 1% for water/ethanol mixtures to be detected. This is the lower detection limit of the cavity resonator.

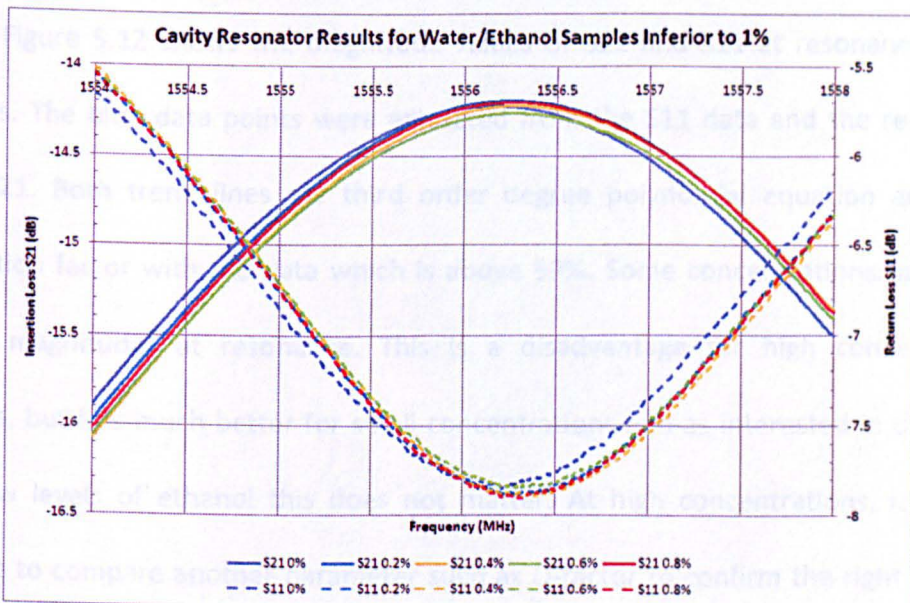


Figure 5.10. Cavity Results for Sample Inferior to 1% (0%-0.8%).

5.2.5 Ethanol Extracted Data

From the S-parameters acquired from the VNA, the software extracts information, analyses and stores it in a comma separated file which is readable by Microsoft Excel. This information can then easily be plotted against the concentration in order to characterise the full range of samples. Figure 5.11 shows the resonant frequencies of S21 and S11 for each sample from 0% to 5% by 1% increments and from 5% to 100% by 5% increments of ethanol per sample, a total of 25 samples. Because resonance of insertion loss and return loss are literally the same, only one trend line was used. The trend line is a third order degree polynomial equation and has a correlation factor with the data points greater than 99%.

Figure 5.12 shows the magnitude values of S21 and S11 at resonance for all samples. The blue data points were extracted from the S11 data and the red points from S21. Both trend lines are third order degree polynomial equation and have correlation factor with the data which is above 99%. Some concentrations have very similar magnitudes at resonance. This is a disadvantage for high concentration samples, but it is much better for small concentrations and as interested in detecting very low levels of ethanol this does not matter. At high concentrations, it can be possible to compare another parameter such as Q-factor to confirm the right amount of ethanol present in the sample.

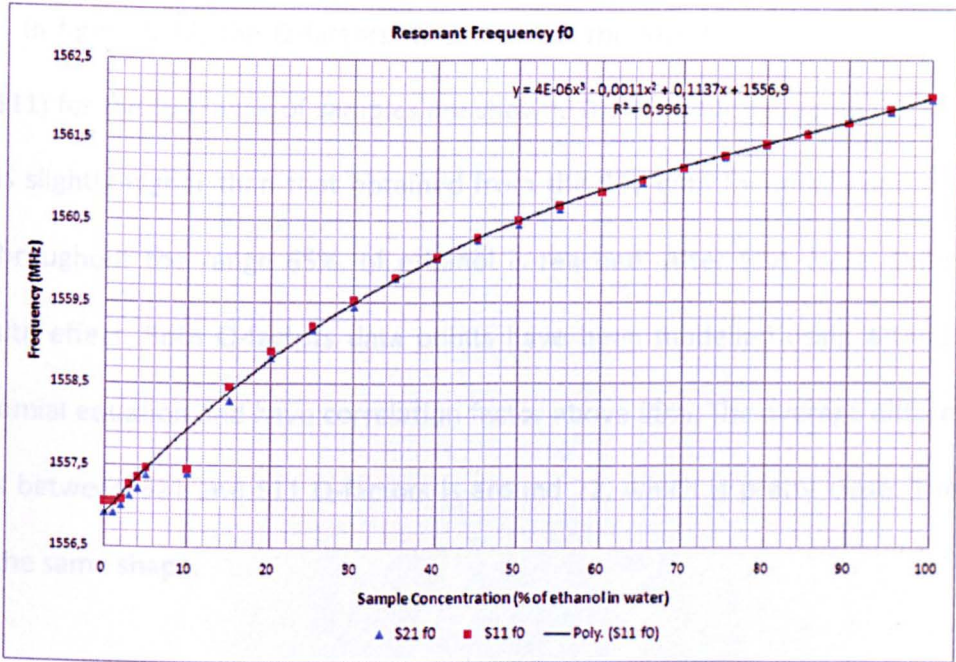


Figure 5.11. Resonant Frequency for different ethanol/water concentration.

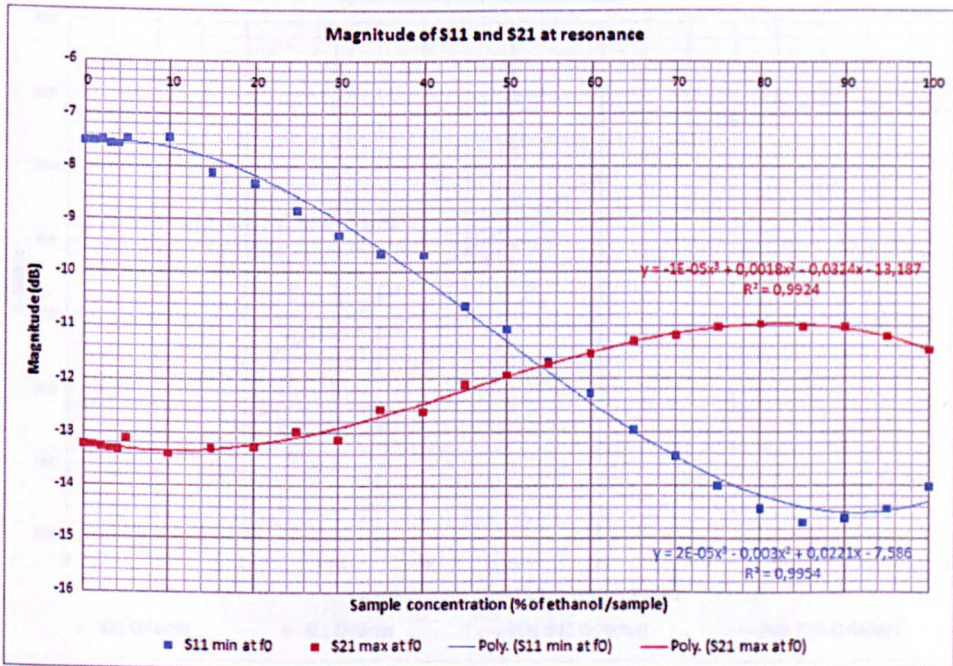


Figure 5.12. Magnitude of S21 and S11 at resonance.

In figure 5.13, the Q-factors measured on the insertion loss (S21) and return loss (S11) for the full range of samples are shown. The Q-factor extracted from the S21 data is slightly higher than that obtained from the S11 data for small concentrations and throughout the range 65%, of ethanol is reached. After that value, there is an opposite effect. Both Q-factors data points have been modelled using a third order polynomial equation and have correlation factor above 99%. The average difference of values between S21 and S11 Q-factors is around 22, which is pretty close. They also have the same shape.

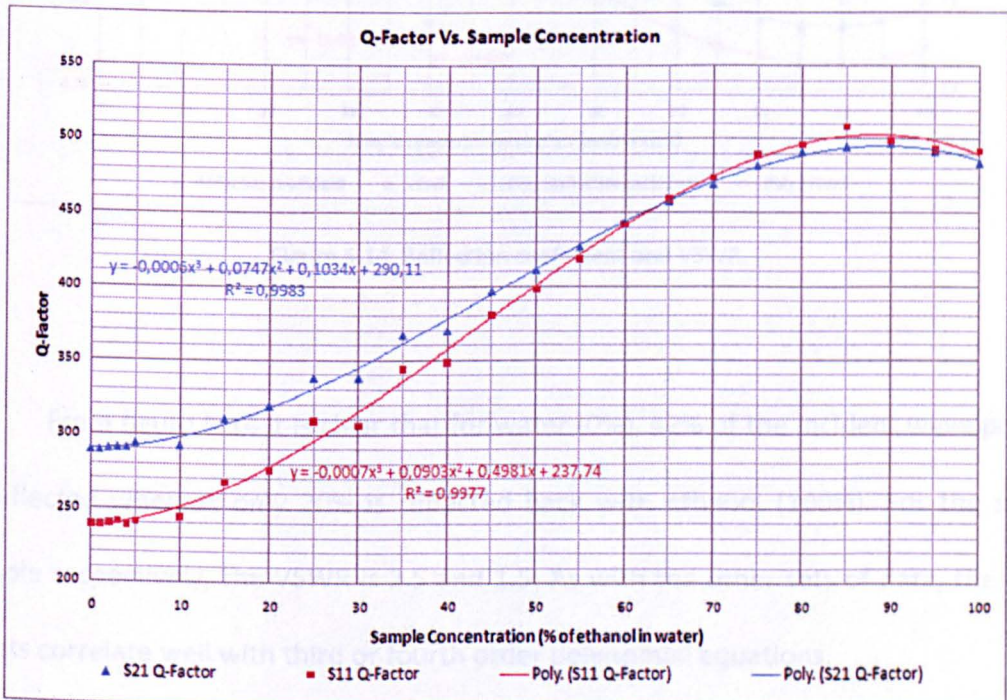


Figure 5.13. S21 and S11 Q-factors.

The last sets of extracted data to be presented are the reflection coefficient and the VSWR which are shown in figure 5.14. Note that graph has two Y-axes, one to read the reflection coefficient (left) and one to read the VSWR (right).

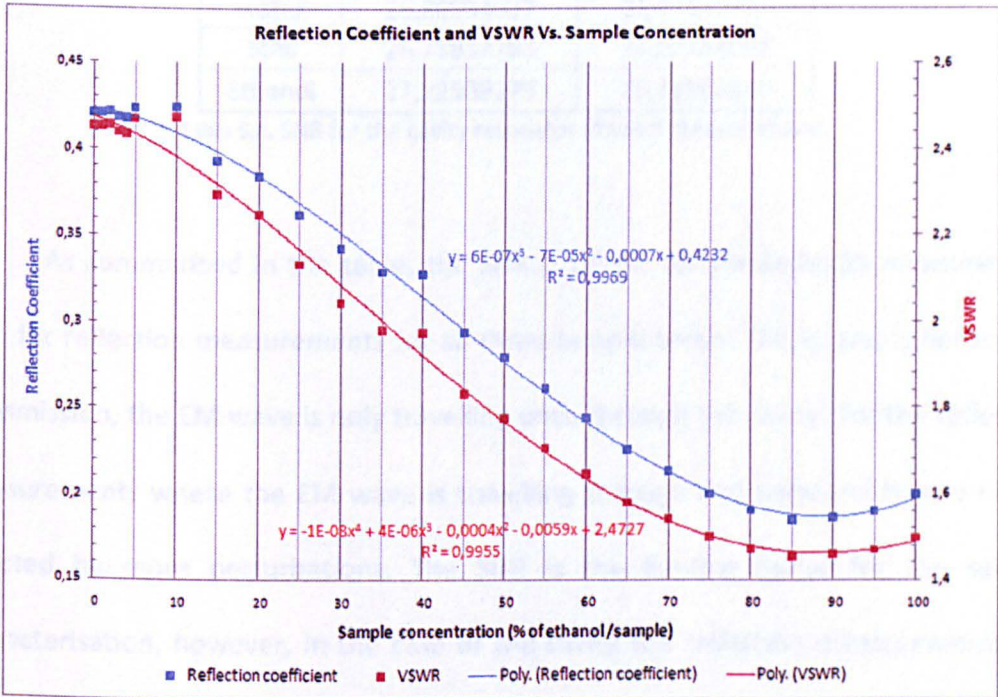


Figure 5.14. Reflection coefficient and VSWR.

From figure 5.14 it is clear that for water (0%), 42% of the incident wave power is reflected whereas only 20% is reflected back with ethanol (100%). For the same sample respectively, the VSWR is 2.5 and 1.5. As with the other sets of data, the data points correlate well with third or fourth order polynomial equations.

Table 5.4 describe the Signal to Noise Ratio (SNR) for S21 and S11 for 3 samples (water, 50% and ethanol). Their value has been calculated according to equation 5.1.

$$SNR = 10 \cdot \log_{10} \left(\frac{\text{signal in dB}}{\text{noise in dB}} \right)$$

5.1

Rectangular Cavity Signal to Noise Ratio for Ethanol Measurements		
	S21	S11
water	26,86934037	21,87349772
50%	26,71817758	24,02131062
Ethanol	27,22509279	25,31865816

Table 5.4. SNR for the cavity resonator ethanol measurements.

As summarised in the table, the SNR is better for transmission measurement than for reflection measurements for all three sample taken. This is simply because in transmission, the EM wave is only travelling once through the cavity. For the reflection measurements where the EM wave is travelling through and back and is as a result, affected by more perturbations. The SNR is the limiting factor for the sample characterisation, however, in the case of the cavity the reflection measurements are still acceptable.

Figure 5.15 show the repeatability of the system, done for four measurements of water for a temperature equal to 22°C at 1 hour of interval each time. The maximum frequency shift is equal to 50kHz and the maximum magnitude shift is equal to 0.045dB.

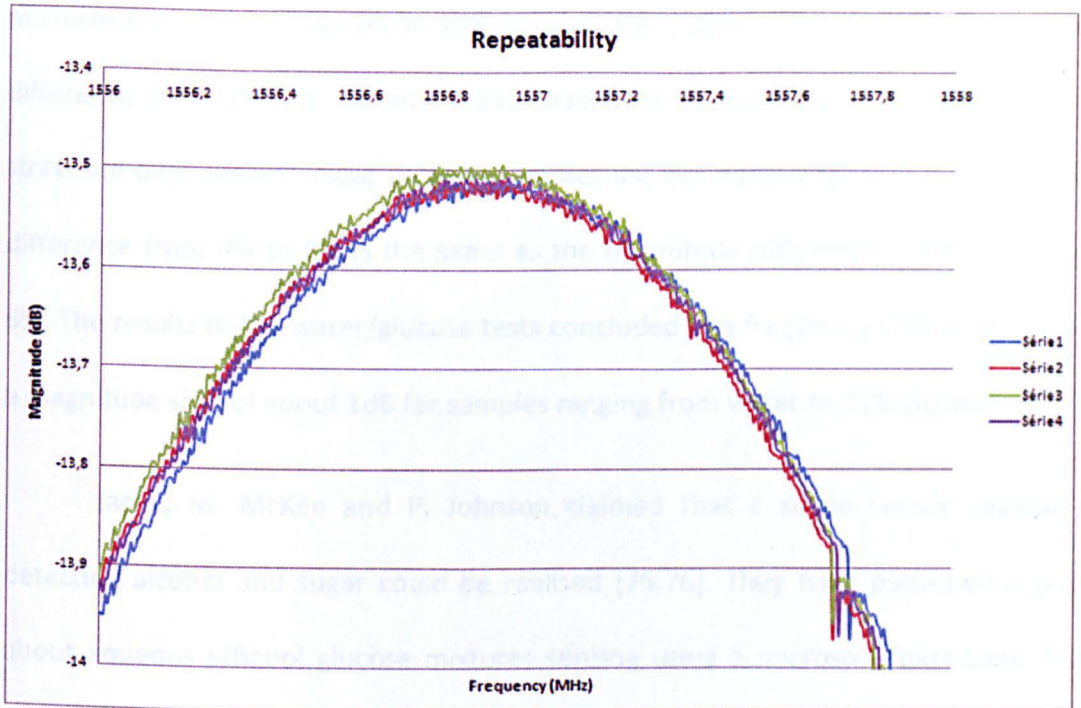


Figure 5.15. Repeatability of the system.

Comparing the results with other studies, in the paper called 'Measurement of Liquid Composition Percent using Coaxial Cavity Resonator' [73], the authors used a circular cavity with an inside section that can be filled with a liquid solution to be tested. Their cavity works in the TE_{11} mode at 140MHz. It was tested for the full range of sample from water to ethanol. They only reported the resonant frequencies versus the sample concentrations and found 18MHz shift between the water sample and the ethanol sample.

Another paper [74], based on a circular cavity working in the TM_{010} mode have done some tests on water/ethanol and water/sugar mixtures. Their water/ethanol

mixtures were tested from 0% to 10% ethanol. They observed about 5db of magnitude difference between the minimum and maximum concentration but they are only stretched over 100kHz. Note that the samples are not equally spaced; the magnitude difference from 0% to 5% is the same as the magnitude difference between 5% and 6%. The results of the water/glucose tests concluded in a frequency shift of 50kHz and a magnitude shift of about 1dB for samples ranging from water to 11% glucose.

James M. McKee and P. Johnson claimed that a single sensor capable of detecting alcohol and sugar could be realised [75,76]. They have published a paper about aqueous ethanol glucose mixtures sensing using a microstrip pass-band filter. They claim that after calibrations, the volume percentage of an n-component(s) solution can be uniquely determined by measuring the real part of the permittivity at n-1 distinct frequencies.

5.3 Cavity Resonator Glucose Results

5.3.1 Sample Preparation

The samples used to check whether glucose quantities are detectable with the cavity resonator and the suspended ring resonators ranged from water (0 mol/l) to 1 mol/l of glucose solution.

Samples were prepared and tested for 0.1 mole increments. The mole (symbol: mol) is a unit of amount of substance, it is an SI base unit, and one of the few units used to measure this physical quantity. The mole is defined as the amount of substance of a system that contains as many "elementary entities" (e.g. atoms, molecules, ions, electrons) as there are atoms in 12 g of carbon-12 (^{12}C) [77]. A mole has 6.0221415×10^{23} atoms or molecules of the pure substance being measured. A mole will possess a mass exactly equal to the substance's molecular/atomic weight in grams. Because of this, one can measure the number of moles in a pure substance by weighing it and comparing the result to its molecular/atomic weight.

Figure 5.16 presents a molecule of Glucose. The molecular equation is $\text{C}_6\text{H}_{12}\text{O}_6$, where C is carbon (black), H is hydrogen (red) and O is oxygen (white).

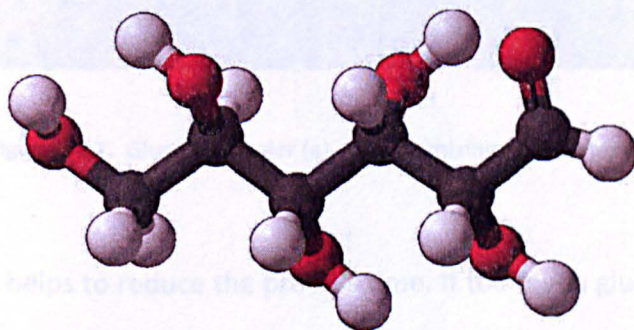


Figure 5.16. Glucose Molecule [78].

The molar mass of glucose is 180.16g. Therefore 1 mole of glucose is made by dissolving 180.16g of glucose in 1 litre of water. The glucose samples have been made

in the biological department of Liverpool John Moores University. First, 180.16g of glucose (Figure 5.17 (a)) was weighed on an electronic scale capable of measuring to an accuracy of 1 milligram. Then, de-ionized water was poured (about 500ml) into a pyrex glass container and placed on a stirring/hot plate device as shown on Figure 5.17(b).



Figure 5.17. Glucose powder (a), glucose mixing with water (b).

The device helps to reduce the process time. If too much glucose is poured into cold water it crystallises and becomes hard. To avoid that, the hot plate has also a magnetic field rotating inside the plate, and when a magnet stirrer was placed inside the container, it rotated and mixed the glucose powder with water efficiently. Once the water had reached about 50°C, glucose was added slowly until all the 180.16g was completely mixed with water. When the solution was clear of crystals and fully mixed,

the remaining water was added to top up the solution to 1 litre. The jar then contains a solution of 1 mol/l of glucose. This was then used to make the samples as table 5.5 shows. The glucose samples were made by mixing glucose in solution and water with 2 pipettes (0.1-1ml and 1-5ml).

Glucose Concent. (mole/l)	Glucose Water Ratio g/l = mg/ml	15 ml sample (Cavity)		55ml sample (Ring)	
		water (ml)	1 mole sol. (ml)	Water (ml)	1 mole sol. (ml)
0	0	15	0	55	0
0.1	18.016	13.5	1.5	49.5	5.5
0.2	36.032	12	3	44	11
0.3	54.048	10.5	4.5	38.5	16.5
0.4	72.064	9	6	33	22
0.5	90.08	7.5	7.5	27.5	27.5
0.6	108.096	6	9	22	33
0.7	126.112	4.5	10.5	16.5	38.5
0.8	144.128	3	12	11	44
0.9	162.144	1.5	13.5	5.5	49.5
1	180.16	0	15	0	55

Table 5.5. Glucose Sample Concentration.

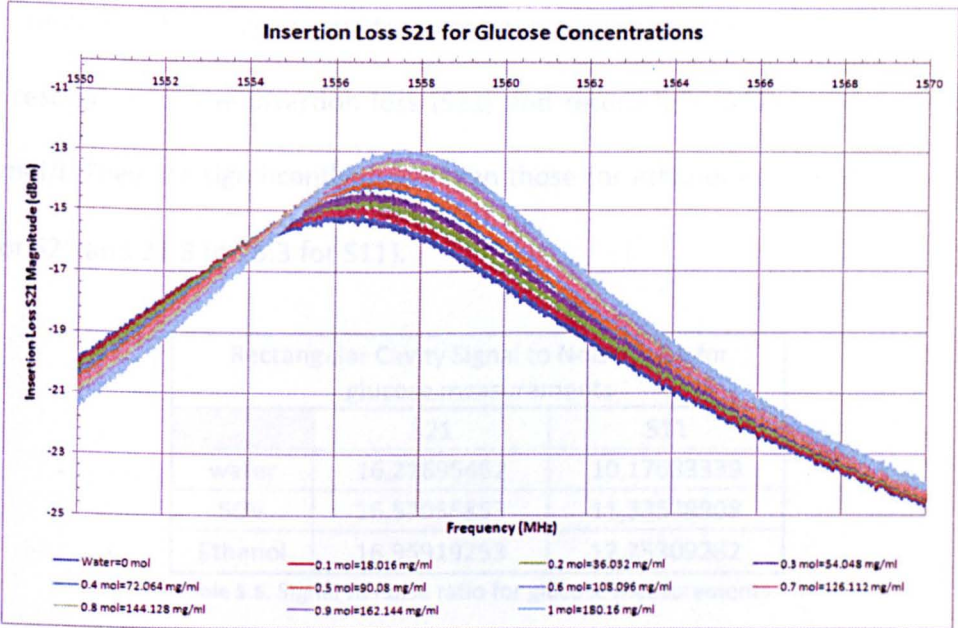
Two sets of samples were made, one for the cavity resonator (15ml) and one for the suspended ring resonator (55ml). The smallest sample apart from water (0.1mol/l = 100mmol/l) is 18.016mg/ml. Humans have a normal blood sugar level of 4.4-6.1mmol/l. A value of 5mmol/l converts to 0.95mg/ml. Shortly after consumption of food the blood sugar level increases temporarily to reach up to 7.8mmol/l (1.4mg/ml) [89].

5.3.2 Glucose Results - 0mol/l of glucose to 1mol/l by 0.1mol/l

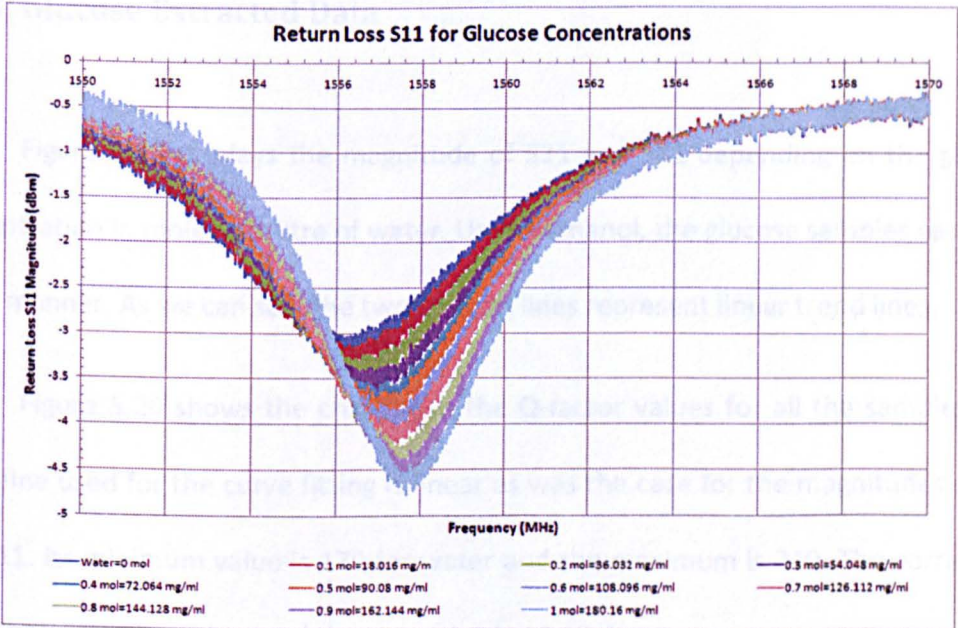
Increments

The samples were prepared a day in advance and were stored in a fridge overnight at a temperature of 6.5°C. Their temperatures were monitored and recorded between 6.9°C to 7.6°C when the tests were carried out. This was done to insure that the samples were measured exactly at the same temperature. The software was able to record up to 5-6 measurements per minute. The 11 samples were analysed by the cavity resonator in about 2 minutes allowing their temperatures only to rise by 0.7°C. This is acceptable for measurement comparison.

The insertion loss (S21) for each concentration is shown in Figure 5.18(a), and the return loss (S11) in Figure 5.18(b). The magnitude changed by 2.2dB between water and the 1mol/l solution. The return loss magnitude difference between the same samples was only 1.6dB. Their resonant frequencies were separated by 1.5MHz at peak value.



(a)



(b)

Figure 5.18. Responses for glucose concentration, insertion loss S21 (a) and the return loss S11 (b).

Table 5.6 shows the signal to noise ratio for the glucose measurements of the cavity resonator for the insertion loss (S21) and return loss (S11) for water, 0.5mol/l and 1mol/l. They are significantly lower than those for ethanol measurements (26.8 to 27.2 for S21 and 21.8 to 25.3 for S11).

Rectangular Cavity Signal to Noise Ratio for glucose measurements		
	S21	S11
water	16,21695462	10,17033339
50%	16,57055853	11,33538908
Ethanol	16,95919253	12,25309282

Table 5.6. Signal to noise ratio for glucose measurements.

5.3.3 Glucose Extracted Data

Figure 5.19 displays the magnitude of S21 and S11 depending on the glucose concentration in moles per litre of water. Unlike ethanol, the glucose samples react in a linear manner. As we can see, the two straight lines represent linear trend lines.

Figure 5.20 shows the changes in the Q-factor values for all the samples. The trend line used for the curve fitting is linear as was the case for the magnitudes of S21 and S11. Its minimum value is 179 for water and the maximum is 240. The correlation factor between the points and the trend line is 98.85%.

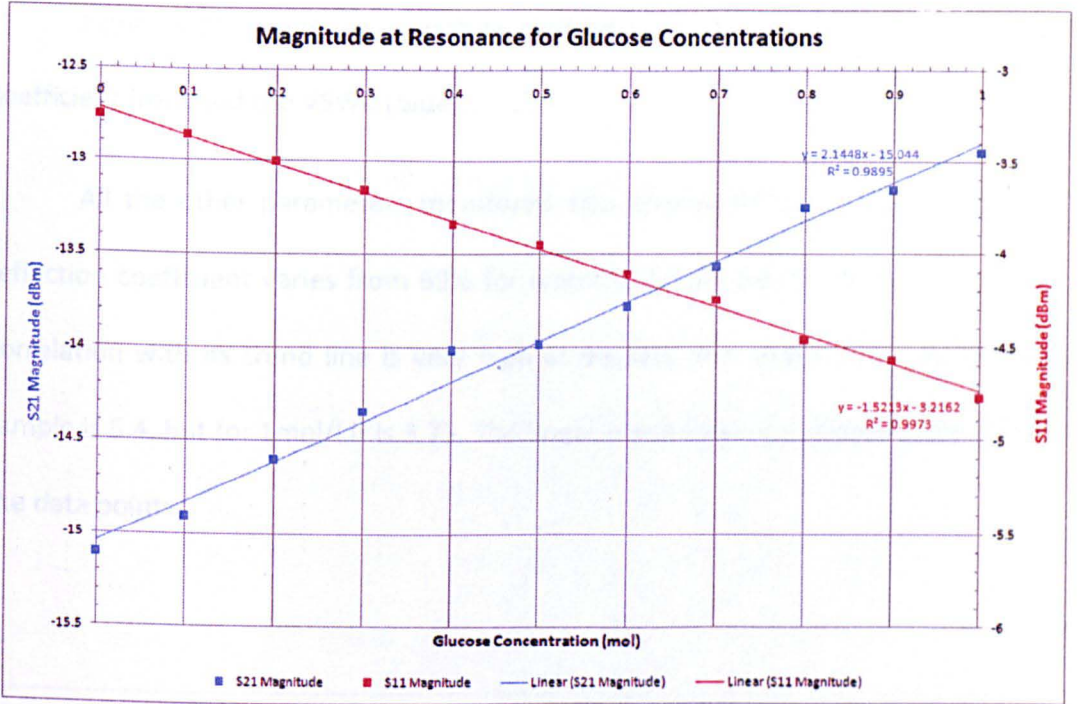


Figure 5.19. Magnitude of S21 and S11 at resonance for water/glucose concentration.

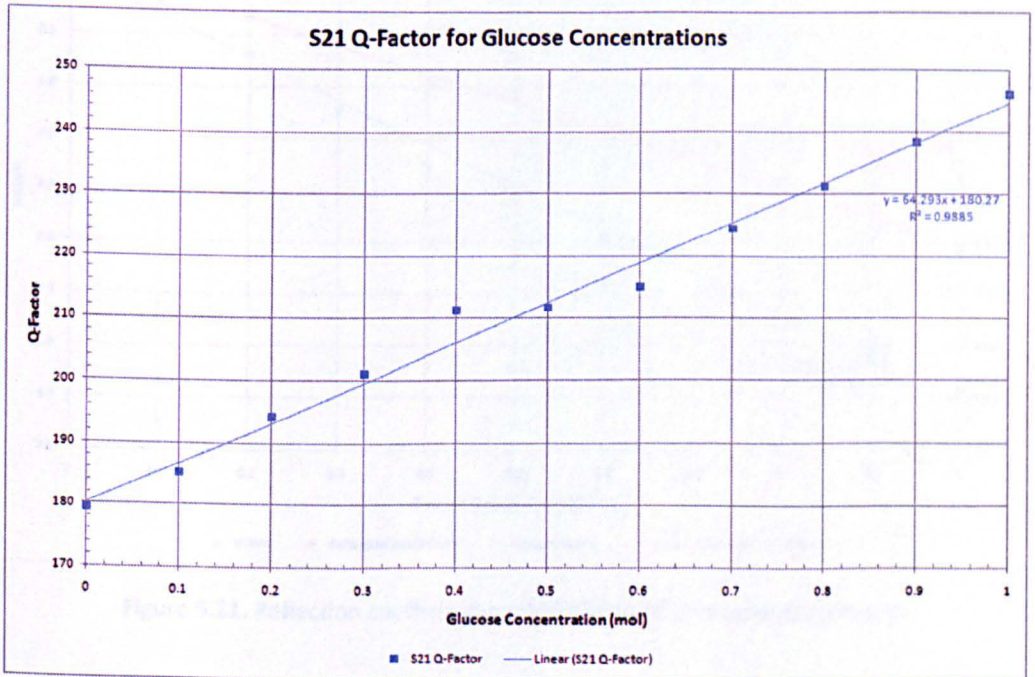


Figure 5.20. Q-Factor for glucose concentrations.

Figure 5.21 shows two variables derived from the return loss, the reflection coefficient (red) and the VSWR (blue).

All the other parameters monitored also displayed linear characteristics. The reflection coefficient varies from 69% for water to 57.5% for the 1mol/l mixture. The correlation with its trend line is very high at 99.84%. The VSWR value for the water sample is 5.4, but for 1mol/l it is 3.75. The linear trend line is correlated at 99.29% with the data points.

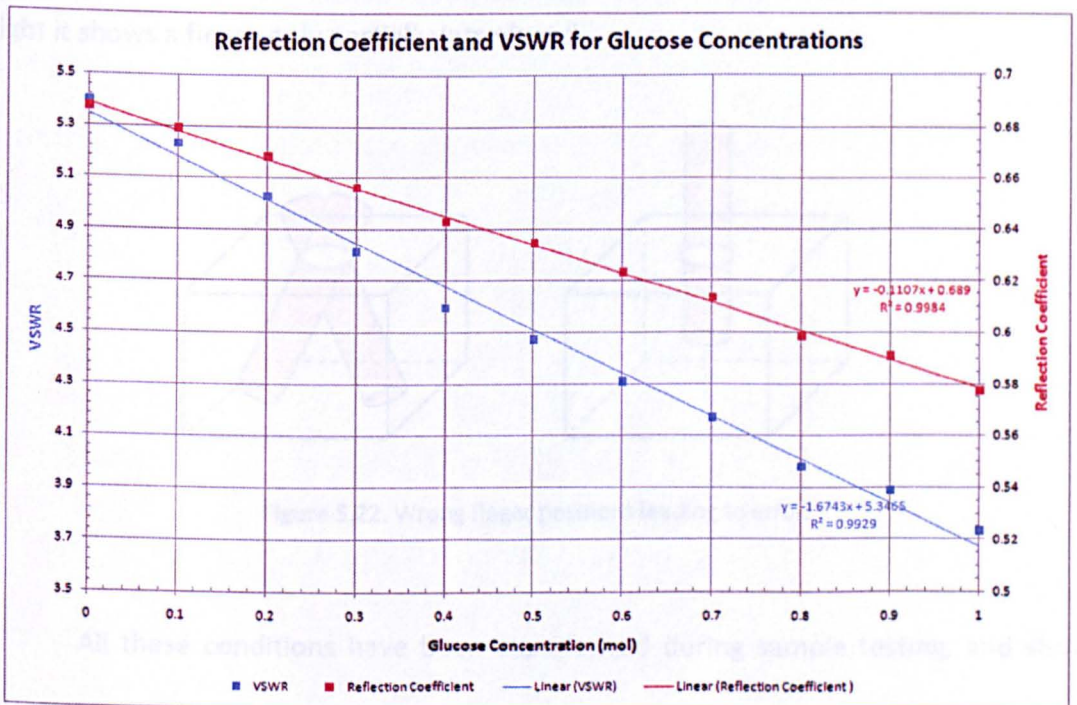


Figure 5.21. Reflection coefficient and VSWR for different glucose samples.

The main disadvantage of this cavity is that the insertion hole will only accommodate a specific size of finger. If the diameter of the insertion hole is bigger than the diameter of the finger, microwaves will escape or leak from the cavity, introducing errors in readings. If the insertion hole is too small, the finger cannot be introduced and no measurements can be taken. Furthermore, the finger has to be long enough to touch the opposite wall of the cavity (8.6cm away). If the finger is only partially introduced the reading would be wrong. Also, if the finger is not perfectly perpendicular to the insertion hole plane, results would be false. Figure 5.22 shows on the left, fingers introduced that are not perpendicular to the hole plane, and on the right it shows a finger only partially introduced.

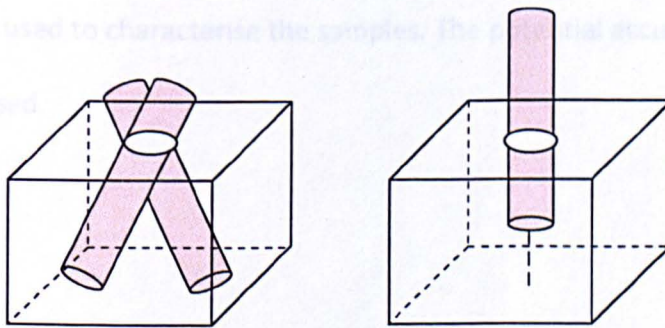


Figure 5.22. Wrong finger positions leading to errors

All these conditions have been experienced during sample testing, and show that a cavity resonator with an insertion hole is not the best for this kind of measurement. The irregularities between everybody's fingers are also very challenging. This resonator has proven that measuring water/ethanol concentration of up to 1% is

feasible, but the geometrical parameters of the resonator are not suitable for finger tests. For this reason, in chapter 6, a novel microwave sensor for alcohol detection is explained and its design illustrated. This sensor is based on a suspended ring resonator, derived from a microwave sensor used for a completely different application. Parametric simulations are shown for the same permittivity values as those that were used for the rectangular cavity, allowing simulation comparisons between the two designs.

Summary

In this chapter, the design of a rectangular cavity sensor was discussed and results for both water/ethanol mixtures and water/glucose mixtures are given, followed by the extracted data used to characterise the samples. The potential accuracy and drawbacks are also discussed.

6 SUSPENDED RING RESONATOR DESIGN AND SIMULATIONS

6.1 Microstrip Ring Resonator Background

The microstrip ring resonator was first proposed by P. Troughton in 1969 for measurements of the phase velocity and dispersive characteristics of a microstrip line. In the first 10 years most investigations were concentrated on the measurements of characteristics of discontinuities of micro-strip lines. Figure 6.1 shows a portion of a microstrip line. It consists of a copper track of width w and height b , glued on a PCB of thickness h and with a dielectric constant ϵ_r . A copper ground plane is present on the other side.

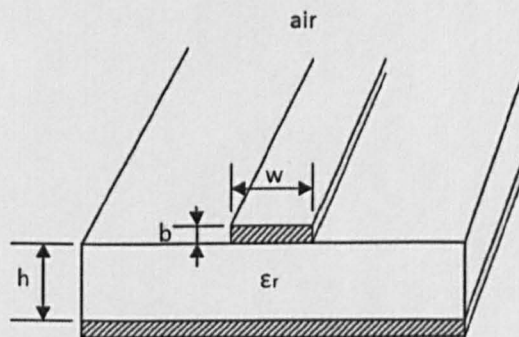


Figure 6.1. Microstrip Line Characteristics.

In the 1980s, applications using ring circuits as antennas, and frequency-selective surfaces emerged. Microwave circuits using rings for filters, oscillators,

mixers, and couplers were also reported. Sophisticated field analyses were developed to give accurate modelling and prediction of a ring resonator. Some unique properties and excellent performances have been demonstrated using ring circuits built in coplanar waveguides and slot lines. Integration with various solid-state devices was also realized to perform tuning, switching, amplification, oscillation, and optoelectronic functions [79].

6.2 Microstrip Ring Resonator Design Properties

6.2.1 General Properties

The ring resonator is a simple circuit. The structure only supports waves that have an integral multiple of the guided wavelength equal to the mean circumference. The circuit is also easy to fabricate. However, more complicated circuits can be created by cutting a slit, adding a notch, cascading two or more rings, implementing some solid state devices, integrating with multiple input and output lines, and so on. These circuits are best suited to particular applications. It is believed that the variations and applications of ring circuits have not yet been exhausted and many new circuits will certainly come out in the future [80].

The ring resonator is a transmission line formed in a closed loop (figure 6.2). The basic circuit consists of the feed lines, coupling gaps, and the resonator. The feed lines are separated from the resonator by a distance called the coupling gap. The feed lines couple power into and out of the resonator. The size of the gap should be large

enough such that the fields in the resonator are not appreciably perturbed, yet small enough to allow adequate coupling of power. If the distance between the feed lines and the resonator is large, then the coupling gaps do not affect the resonant frequencies of the ring. This type of coupling is also called “loose coupling.” Loose coupling is a manifestation of the negligibly small capacitance of the coupling gap. If the feed lines are moved closer to the resonator, however, the coupling becomes tight and the gap capacitances become appreciable. This causes the resonant frequencies of the circuit to deviate from the intrinsic resonant frequencies of the ring. Hence, to accurately model the ring resonator, the capacitances of the coupling gaps should be considered [44,80].

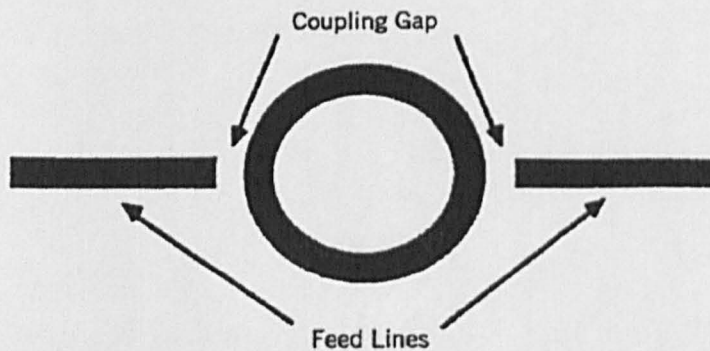


Figure 6.2. Composition of a ring resonator.

When the mean circumference of the ring resonator is equal to an integral multiple of a guided wavelength, resonance is established. This may be expressed as:

$$2\pi r = n\lambda_g \quad \text{for } n = 1, 2, 3, \dots \quad (6.1)$$

$$f_0 = \frac{nc}{2\pi r \sqrt{\epsilon_{\text{eff}}}} \quad (6.2)$$

Where r is the mean radius of the ring that equals the average of the outer and inner radius, λ_g is the guided wavelength, n is the mode number, and f_0 is the resonant frequency. This relationship is valid for the loose coupling case, as it does not take into account the coupling gap effects. From this equation, the resonant frequencies for different modes can be calculated since λ_g is frequency dependent.

There exists a linear relationship in a non-dispersive medium between the frequency and the phase constant or wave-number, β , where:

$$\beta = 2\pi/\lambda_g \quad (6.3)$$

If the frequency doubles, then likewise the wave-number doubles. In a dispersive medium this is not true. The microstrip line is a dispersive medium. The dispersion in a microstrip line can be explained by examining the effective permittivity, ϵ_{eff} . In the case of a microstrip the effective permittivity is a measure of the fields confined in the region beneath the strip. In the case of very narrow lines (feed lines and ring width) or a very low frequency the field is almost equally shared by the air ($\epsilon_r = 1$) and the substrate so that, at this extreme,

$$\epsilon_{\text{eff}} = \frac{1}{2} (\epsilon_r + 1) \quad \text{as } f \rightarrow 0 \quad (6.4)$$

Where ϵ_r is the relative dielectric of the substrate. For very wide lines or a very high frequency nearly all of the field is confined to the substrate dielectric, and therefore at this extreme,

$$\epsilon_{\text{eff}} = \epsilon_r \quad \text{as } f \rightarrow \infty \quad (6.5)$$

It is therefore clear that the effective permittivity is frequency dependent, increasing as the frequency increases. The effective permittivity is defined in equation 6.6 where c is the velocity in free space, f the frequency, and λ_g the guided wavelength:

$$\epsilon_{\text{eff}}(f) = \left(\frac{c}{f\lambda_g} \right)^2 \quad (6.6)$$

If we assume that, as in Equation (6.6), any microstrip resonator will only support wavelengths that are an integral multiple of the total length, then

$$l_t = n\lambda_g \quad (6.7)$$

Where l_T is the total length of the resonator. Substituting for λ_g in Equation (6.8) yields the following equation:

$$\epsilon_{\text{eff}}(f) = \left(\frac{nc}{fl_T}\right)^2 \quad (6.8)$$

If the total length of a resonator, the resonance order, n , and the resonant frequency are known, then ϵ_{eff} can be calculated from Equation (6.8) [42].

6.2.2 Coupling Gap

The coupling gap is an essential element of the ring resonator. It is the electrical discontinuity of the feed lines from the ring that allows the structure to only support selective frequencies. Coupling efficiency between the microstrip feed lines and the annular microstrip ring element will affect the resonant frequency and the Q -factor of the circuit. Choosing the correct coupling for the proper application is important. The size of the coupling gap also affects the performance of the resonator. If a very small gap is used, the losses will be lower but the fields in the resonant structure will also be more greatly affected. A larger gap results in less field perturbation but greater losses. The coupling gap between the feed line and the ring is represented by an L network of capacitance C_g (*gap*) and C_f (*feed lines*). The lossless ring resonator can be represented by a shunt circuit of L_r and C_r . In addition, comparing C_g and C_f , the

coupling gap is significantly dominated by C_g . To simplify the calculation of the input impedance, the fringe capacitance C_f is neglected as shown on the right of Figure 6.3

(b). The total input impedance obtained from the simple equivalent circuit is given by:

$$Z_{in} = \frac{j[\omega^2 L_r (C_r + C_g) - 1]}{\omega C_g (1 - \omega^2 L_r C_r)} \quad (6.9)$$

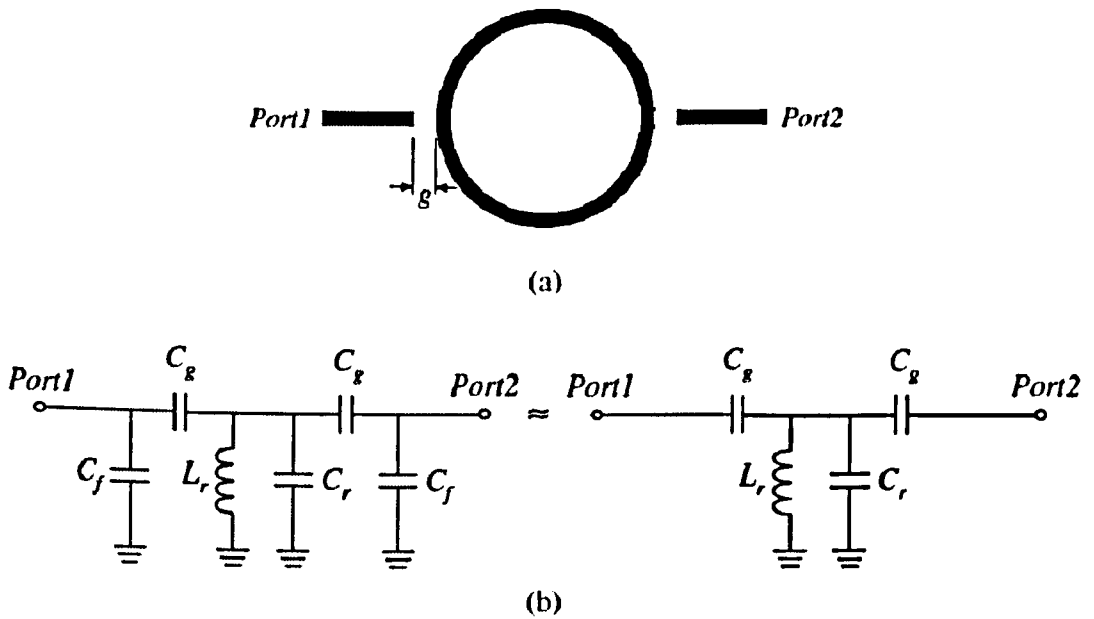


Figure 6.3. Ring resonator (a); equivalent electrical schematic (b).

Where ω is the angular frequency. At resonance, $Z_{in} = 0$ and the resonant angular frequency (ω_0) can be found using equation 6.10:

$$\omega_0 = \frac{1}{\sqrt{L_r (C_r + C_g)}} \quad (6.10)$$

The equation shows that if the coupling gap size g is decreased (C_g increases), the resonant frequencies are reduced. The coupling gap size effect on the insertion loss can be observed from the two-port ring circuit shown in Figure 6.3. The insertion loss S_{21} of the simplified equivalent circuit on Figure 6.3(b) is given by

$$S_{21}(\omega = \omega_0) = \frac{2}{2(1+Z_g Y) + Z_g(2+Z_g Y)/Z_0 + Y Z_0} \quad (6.11)$$

Where,

$$Z_g = \frac{1}{j(\omega_0 C_g)} \quad (6.12)$$

$$Y = \frac{j((\omega_0)^2 L_r C_r - 1)}{\omega_0 L_r} \quad (6.13)$$

and Z_0 is the characteristic impedance.

It can be found that a smaller (larger) gap size g has a lower (higher) insertion loss and a more (less) significant effect on resonant frequency. In many of the ring's applications, the resonant frequency is measured in order to determine another quantity. For example, the resonant frequency is used to determine the effective permittivity (ϵ_{eff}) of a substrate and its dispersion characteristics. It is important in this measurement that the coupling gap does not affect the resonant frequency of the ring and introduces errors in the calculation of ϵ_{eff} . Troughton [43] realised this and took

steps to minimize any error that was introduced. He initially used a small gap. The resonant frequency was measured and then the gap was etched back. Through repeated etching and frequency measurements the optimum point was determined at which the feed lines were not seriously disturbing the fields of the resonator. However, this is a very tedious and time-consuming process [42, 43, 80].

6.2.3 Ring Width

As the normalized ring width/ring radius, (w/R_m) is increased, higher modes are excited. This occurs when the ring width reaches half the guided wavelength and is similar to the transverse resonance on a micro-strip line. Figure 6.4 shows the characteristic parameters of the ring physical dimensions.

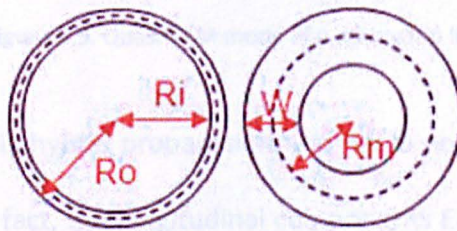


Figure 6.4. Ring Properties.

To avoid excitation of higher order modes, a design criteria of $w/R_m < 0.2$ should be observed [42]. Another characterisation of ring width is the increase of dispersion on narrow rings. If rings for which $w/R_m < 0.2$ are used, then dispersion becomes

important for the modes of $n > 4$. Wide rings do not suffer the effect of dispersion as much as narrow rings [43].

6.2.4 Ring Propagation Modes and Dielectric Determination

The difficulty in the study of a micro-strip propagation mode is that the propagation occurs in the substrate of permittivity ϵ_r , and as well as in the surrounding air which has a permittivity equal to 1 as shown in Figure 6.5.

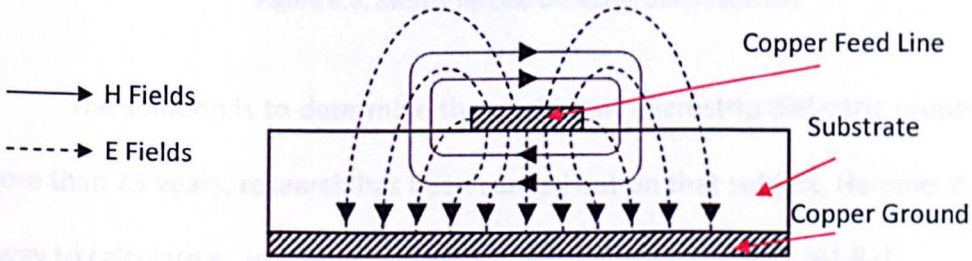


Figure 6.5. Quasi-TEM mode of a microstrip line.

The propagation is hybrid propagation and has 6 non-zero components of the electromagnetic field. In fact, the longitudinal components E_z and H_z are small and the propagation mode can be considered as quasi-T.E.M. Even in this case, it is very difficult to define a propagation velocity (v). For a TEM wave the propagation velocity is given by equation 6.14 :

$$v = c/\sqrt{\epsilon_r} \quad (6.14)$$

ϵ_r being the dielectric constant of the medium of propagation.

However in this case, the propagation occurs in 2 different media with different dielectric constants ϵ_r . The problem would be easier if there is a single medium around the microstrip line as shown in figure 6.6.

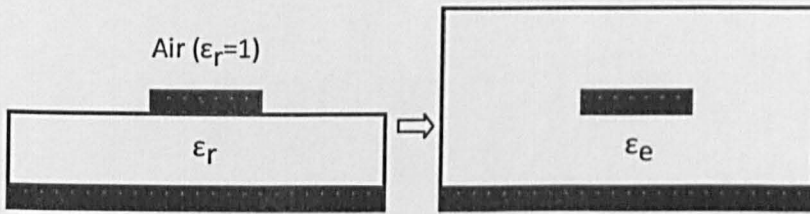


Figure 6.6. Microstrip Line Dielectric Determination.

The solution is to determine the equivalent microstrip dielectric properties. For more than 25 years, research has been carried out on that subject, Hammerstad found a way to calculate ϵ_e using equations that depend on w , h and ϵ_r [81,82].

For micro-strip lines with a ratio $w/h \geq 1$:

$$\epsilon_e = \frac{1}{2} (\epsilon_r + 1) + \frac{1}{2} (\epsilon_r - 1) \left(1 + 12 \frac{h}{w}\right)^{-1} \quad (6.15)$$

and for micro-strip lines with a ratio $w/h \leq 1$:

$$\epsilon_e = \frac{1}{2} (\epsilon_r + 1) + \frac{1}{2} (\epsilon_r - 1) \left[\left(1 + 12 \frac{h}{w}\right)^{-1} + 0.04 \left(1 - \frac{w}{h}\right)^2 \right] \quad (6.16)$$

However, for liquid detection, a plastic pipe or sample holder is needed to contain the liquid, adding two more dielectric values to the problem. Figure 6.7 is a cross-sectional view of the liquid detection model. The micro-strip resonator is indicated in bold with the plastic tube filled with liquid on top.

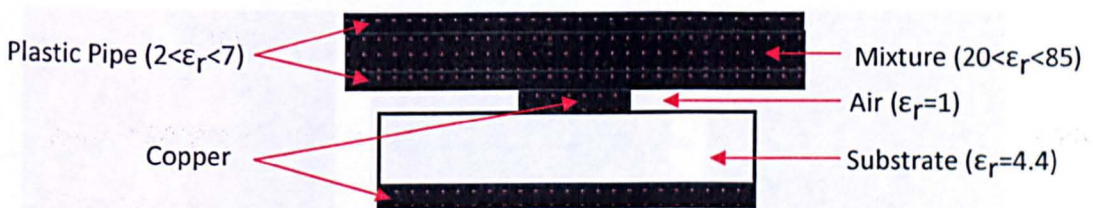


Figure 6.7. Principle of liquid testing using microstrip circuits.

The equation to determine ϵ_e is totally different than the Hammerstad equation, and very difficult to define. For this reason for this investigation dielectric variations are simulated and not calculated [44].

6.3 HFSS Design and Simulations

6.3.1 HFSS Models of Microstrip Ring Resonator

Before reaching the final design, several intermediary designs were simulated and tested. Different coupling methods were adopted from a paper by Park and Lee

[83] and tested for water/ethanol detection. The first design is a simple microstrip ring resonator (RR) with loose coupling, as is the second but this differs in that it has feed lines that are curved to increase the coupling (Arc1). The third design has two curved feed lines and a split ring (Arc2) also called a 'two line with a slit ring'. Figure 6.8 shows respectively the top view of the different designs.

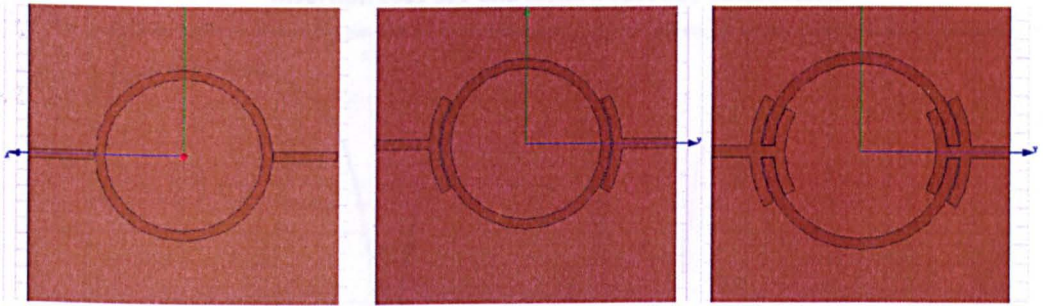


Figure 6.8. Evolution of the ring design (RR, Arc1 and Arc2 from left to right).

The simulation results are shown in figure 6.9. The simple ring (RR) reflects almost all the power and as a result the reflected signal S_{11} is nearly flat. The transmitted signal S_{21} is too weak to measure any dielectric changes or Q-factor. It was tested with water/ethanol mixture and shown to be inaccurate and unstable.

The second design (Arc1) presented some high quality-factor peaks, at resonance, the insertion loss S_{11} drops to -25dB meaning that the transmission is very good. The transmission signal S_{21} is very strong reaching -1dB. After the tests were carried out, the ring was able to detect up to 10% changes between the samples. The observed frequency shift was 4MHz.

The simulation for the last ring design (Arc2) showed that the coupling was very good but weak peaks mean very low Q-factors. This is not suitable for material characterisation. Note that the mean radius of Arc2 is slightly larger which results in a first resonance at 1.5GHz where Arc1 and RR resonate at about 1GHz. The split ring suppresses the third resonance peak on S21.

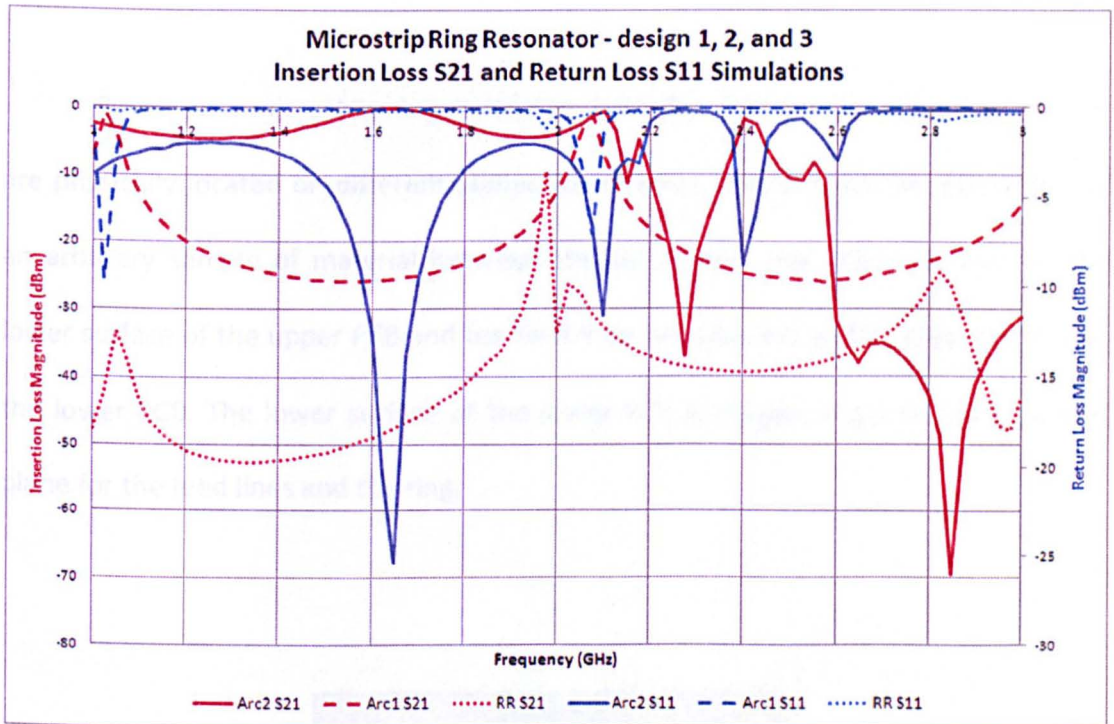


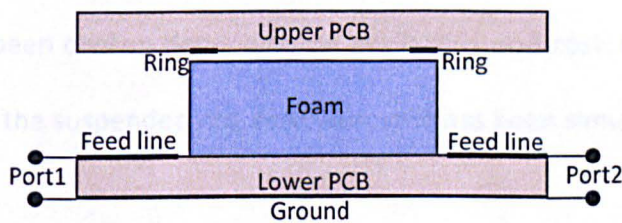
Figure 6.9. S-parameter simulation results for RR, Arc1 and Arc2.

The final design for the ring was inspired by Gopalakrishnan and Chang [84] and is called suspended ring resonator. The model relating to this design is considered in the following section.

6.3.2 HFSS Model of the Suspended Microstrip Ring Resonator

The final design, a suspended ring resonator for liquid detection, has been derived from a similar system used to measure the dielectric value of foams [85] (figure 6.10). The sizes of the ring and feed line have been changed to match the frequency and the purpose of the ethanol detection project [85].

Based on a microstrip ring resonator, here the ring and the feed line network are physically located on different planes (substrates). This enables the placement of an arbitrary sample of material between the substrates. The ring is located on the lower surface of the upper PCB and the feed lines are situated on the upper surface of the lower PCB. The lower surface of the lower PCB is copper and provides a ground plane for the feed lines and the ring.



(a)

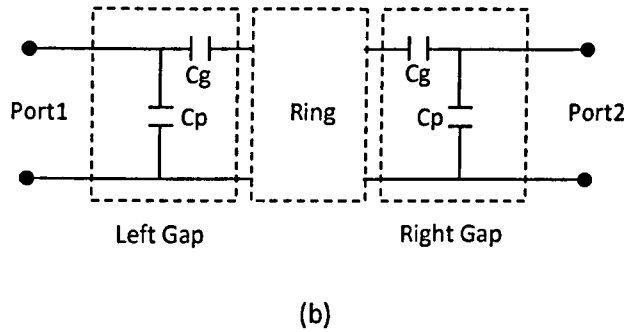


Figure 6.10. Structure of suspended ring resonator: cross section view (a), equivalent network parameter

The feed lines were designed to be 50 Ohm lossless transmission lines. Each coupling gap can be modelled as an L-network of two capacitors whose values depend on the physical geometry of the gaps. Their values can be estimated, but in this project they were simulated to obtain the best transmission. The effect of the ring width, the height between the two planes and the effect of permittivity changes when a sample is introduced were simulated.

The PCB used to build the circuit was a double-sided FR-4 substrate (permittivity = 4.4) and was 1.6mm thick. The copper layers were 35 μm thick. Those parameters have been chosen depending on availability and cost. Figure (6.11) shows the HFSS model of the suspended ring resonator as it has been simulated.

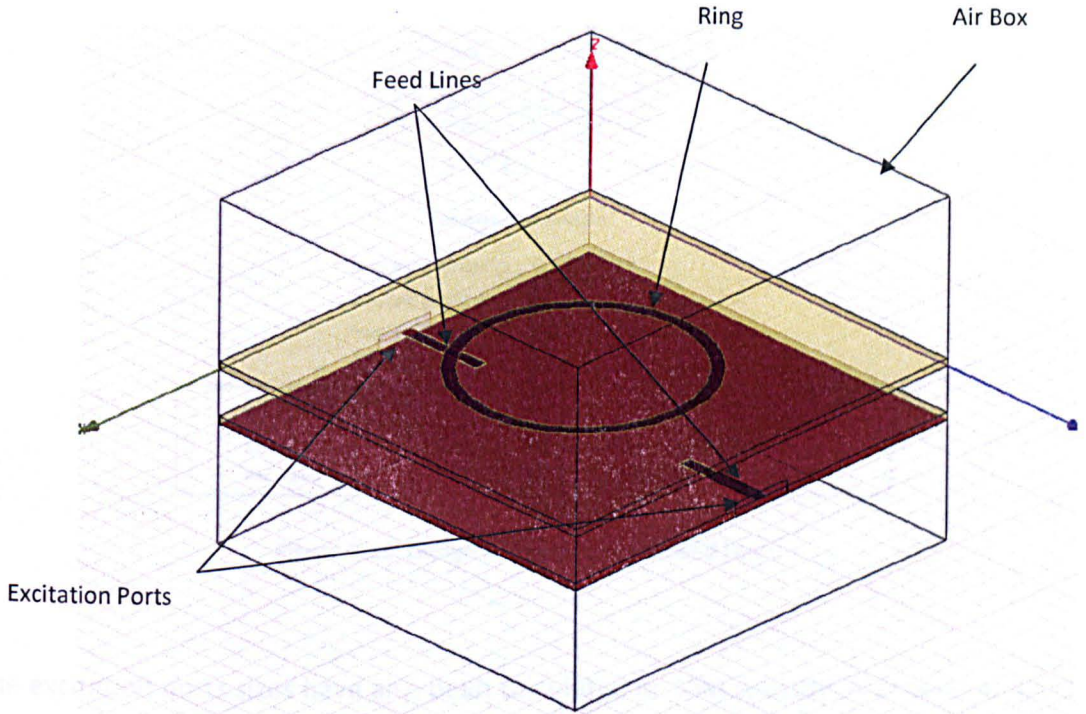


Figure 6.11. HFSS 3D Model of the Suspended Ring Resonator.

The feed lines, the ring and the ground were assigned as copper, the substrate as FR-4 dielectric. The air box was necessary to show the E and H fields, its height was equal to $\lambda/4$.

The mesh resolution was set to $\lambda/10$ as this is the minimum requirement to get accurate results. The width and length of the feed lines was calculated to have an impedance of 50 Ohm using an HFSS tutorial found on the EMTalk website [39]. Figure 6.12 shows the web application used to calculate the physical dimension of the feed lines.

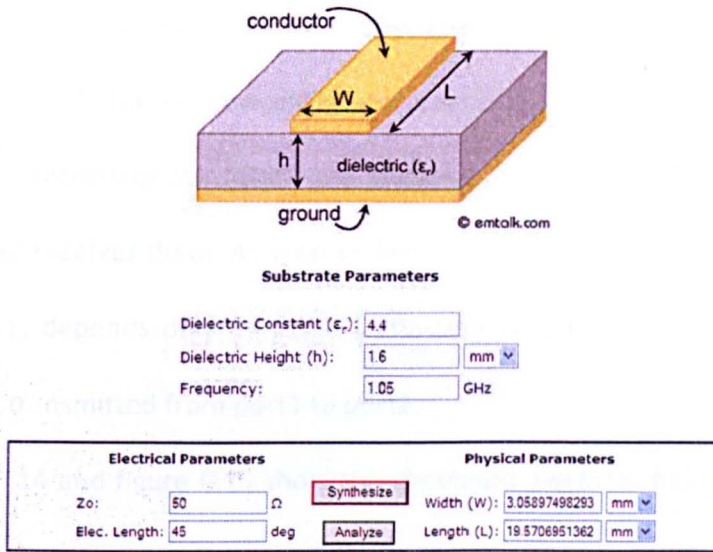


Figure 6.12. Design Properties of the Feed Lines.

The excitation ports sizes have also been calculated on that website as shown on figure 6.13. Their size only depends on the track width and the substrate height.

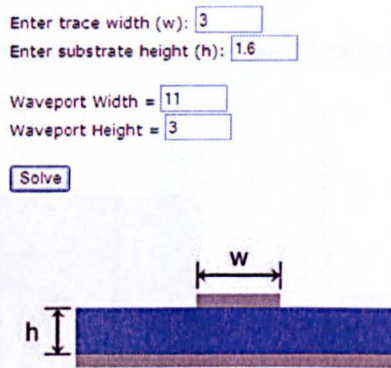


Figure 6.13. Excitation Port Size Calculator.

The ports are made of two 2D sheets then assigned to excitation wave ports. The direction of the electrical field is defined by an arrow pointing down (TEM Mode),

going from the copper feed-lines to the copper ground. The excitation ports position is shown in figure 6.13. The ports were in fact placed at the exact position where the SMA coaxial to microstrip transitions are situated. Port1 sends the electromagnetic waves and port2 receives them. As seen earlier in the section 3.3.5 'S-Parameters', the return loss (S_{11}) depends only on port1 (reflection on port1) and the insertion loss (S_{21}) is what is transmitted from port1 to port2.

Figure 6.14 and figure 6.15 show the simulated electrical field vectors and the magnetic field vectors respectively. They form the characteristic pattern of the fundamental Quasi-TEM modes for ring resonator. The electric field is measured in V/m (Volts per metre) and the magnetic field is measured in A/m (Amperes per metre). The electric fields are stronger in the immediate proximity of the coupling gaps and nil on the top and bottom of the ring. Note that on the side view of both the magnetic and electric fields, the energy transferred from the feed lines to the ring is shown.

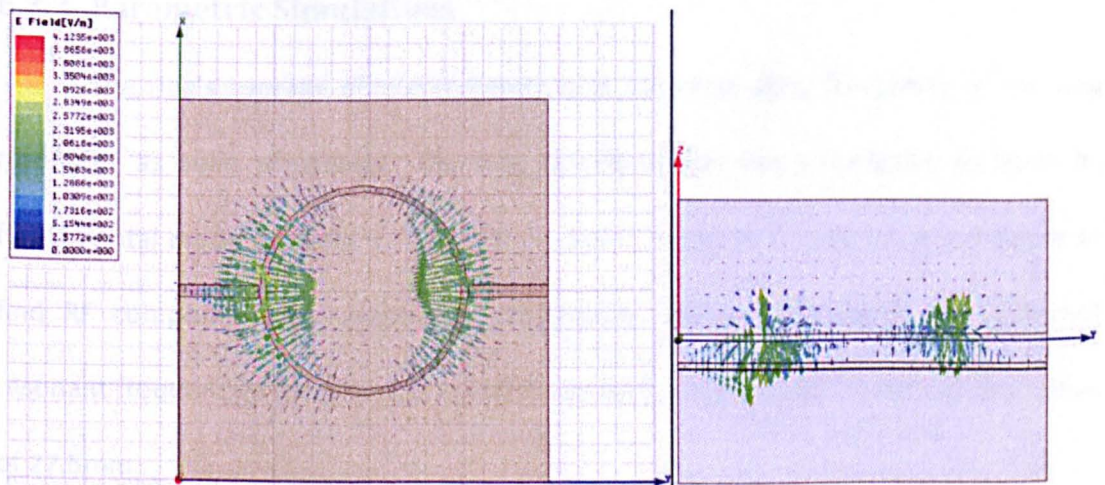


Figure 6.14. Suspended Ring Resonator Electric Field Vectors.

The magnetic fields are stronger where the electrical fields are not present. The directions of the magnetic vectors are perpendicular to the directions of the electric vectors, as seen in section 3.1.

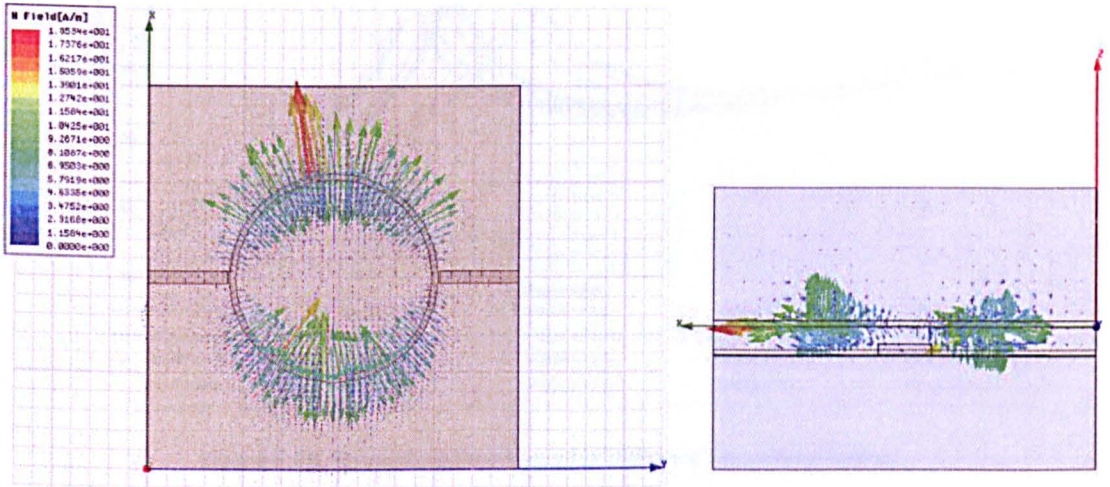


Figure 6.15. Suspended Ring Resonator Magnetic Field Vectors.

6.3.3 Parametric Simulations

The ring's average diameter determines the resonating frequency of the ring resonator as seen previously. The ring resonator has been designed to have its fundamental mode at about 1.5GHz. This is purely because it is easier and cheaper to find RF components for electronic prototyping. Figure 6.16 shows the different resonant frequencies for different internal ring radius at a constant external ring radius of 27.5mm.

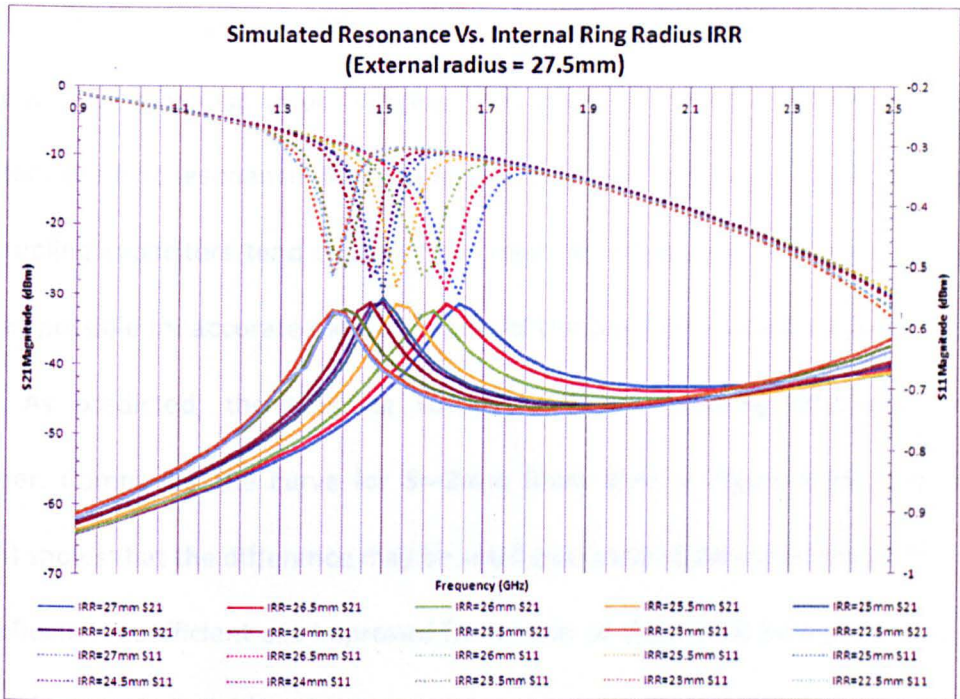


Figure 6.16. Resonating Frequency for Different Mean Ring Radius.

The coupling gap S for a normal ring resonator must be greater than zero and is generally in the range of 0.1mm to 0.5mm [84]. As the suspended ring resonator has two different planes (one for the feed lines and one for the ring), it is possible to introduce negative values for the coupling gap S in order to increase the coupling. Figure 6.17 shows the principle of a normal coupling (left), coupling for $S=0$ (middle) and a negative coupling gap (right).

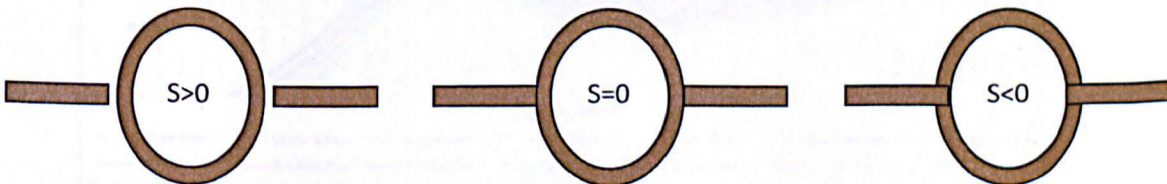


Figure 6.17. Introduction to negative coupling gap ($S < 0$) for suspended ring resonator.

Figure 6.18 shows the HFSS parametric simulation results (S_{21} , S_{11}) for the 3D model with coupling gap values ranging from 1mm to -2mm by variations of 0.5mm. Note that the first resonance does not appear exactly at 1.5GHz as predicted, because the coupling capacitors tend to lower the resonant frequency and these must be as small as possible for accurate measurements of the resonant frequency [86].

As predicted, the coupling surface and the coupling efficiency increase together. Comparing the curve for $S=-2\text{mm}$ (dark blue in Figure 6.18) and $s=1\text{mm}$ (green) shows that the difference may be small but is still significant because the VSWR and reflection coefficient are improved (reduction of the VSWR by a value of 9 and Γ improved by 1.6%, see Table 6.1.).

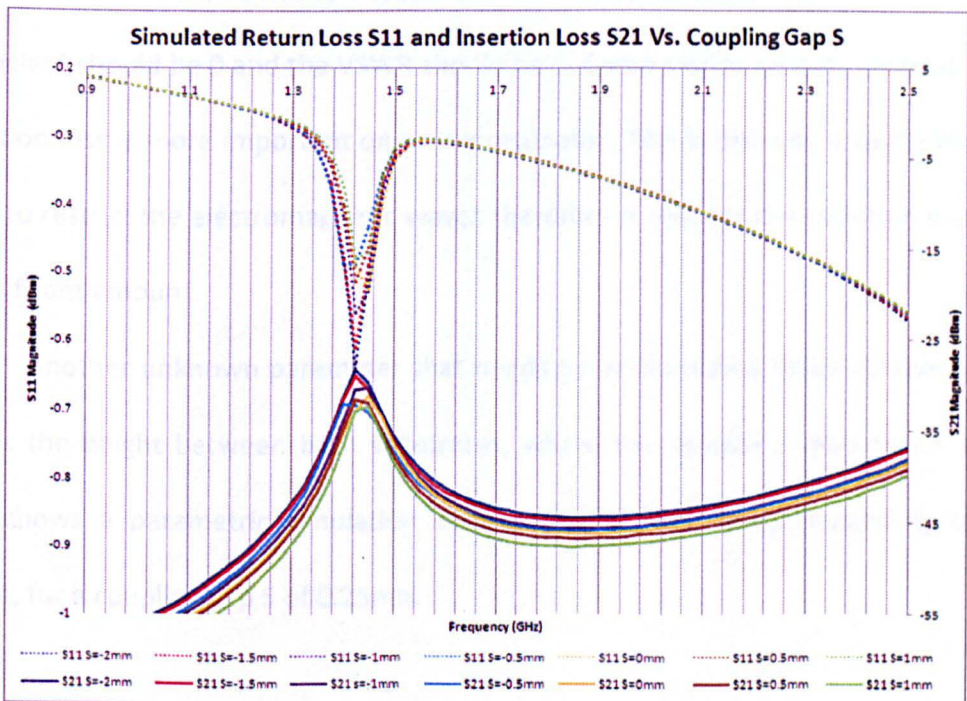


Figure 6.18. Coupling Gap Effect on S-Parameters.

Influence of the Coupling Gap on the Reflection Coefficient and VSWR

s	IL	RL	Γ	VSWR
-2	-28.2772	-0.6403679	92.8927	27.140098
-1.5	-28.9755	-0.6113911	93.20312	28.425258
-1	-30.2057	-0.5600035	93.75616	31.031587
-0.5	-31.9784	-0.4900671	94.51411	35.45716
0	-31.2037	-0.5246972	94.13804	33.118264
0.5	-31.5607	-0.514274	94.25107	33.789097
1	-32.2205	-0.4810097	94.61272	36.124467

s = Coupling Gap (mm)
 IL = Insertion Loss (dB)
 RL = Return Loss (dB)
 Γ = Reflection Coefficient (%)
 VSWR = Voltage Standing Wave Ratio

Table 6.1. Coupling Gap Effect on VSWR and Reflection Coefficient.

By increasing the coupling surface the reflection coefficient has been improved by almost 2% and the VSWR by a factor of 9. For a perfect transmission, the reflection coefficient should be 0 and the VSWR should be 1. Compared to a cavity resonator, the reflection loss is more important on a ring resonator. This is because a cavity has four walls to restrict the electromagnetic waves therefore it reduces the radiation losses by a significant amount.

Another unknown parameter that needs to be simulated is the sample height. This is the height between both substrates, where the sample is introduced. Figure 6.19 shows a parametric simulation showing the S-parameters depending on the height, for a coupling gap S of 0.25mm.

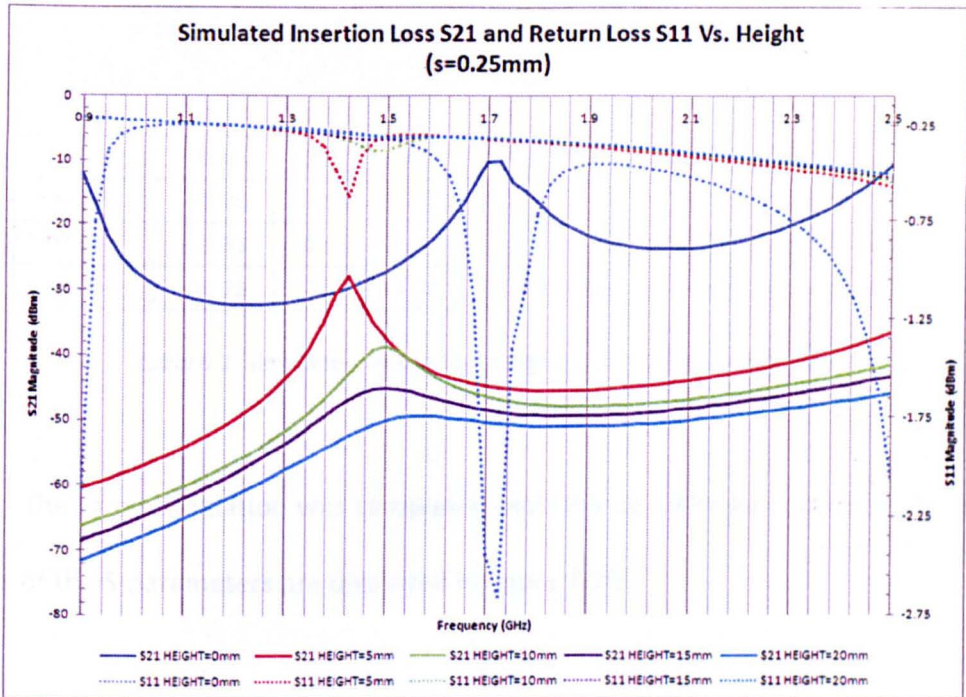


Figure 6.19. S-Parameter Results for Different Sample Height at S=0.25mm.

It is clear from Figure 6.19 that the closer the two boards, the better the transmission. Table 6.2 summarises the reflection coefficient and the VSWR for different height values and for a coupling gap of 0.25mm. The best reflection coefficient is clearly when the height is equal to 0mm which means both boards are in electrical contact. The reflection coefficient difference for height values going from 5mm to 20mm, does not show significant changes (93.1% for s=5mm to 94.33% for s=20mm). However, the magnitude and Q-factor is decreases rapidly as the height increases.

S=0.25mm	Peak1			
Height	IL	RL	Γ	VSWR
0mm	-10.14	-2.66	73.63	6.585
5mm	-28.06	-0.62	93.1	27.97
10mm	-38.89	-0.54	93.97	32.19
15mm	-43.53	-0.53	94.12	33.02
20mm	-46.23	-0.51	94.33	34.28

IL = Insertion Loss S21 (dB)
 RL = Return Loss (dB)
 Γ = Reflection Coefficient (%)
 VSWR = Voltage Standing Wave Ratio

Table 6.2. Simulation results for changing height when S=0.25mm.

The same simulation was completed with the coupling gap equal to -2mm. The results of the S-parameters are displayed in figure 6.20.

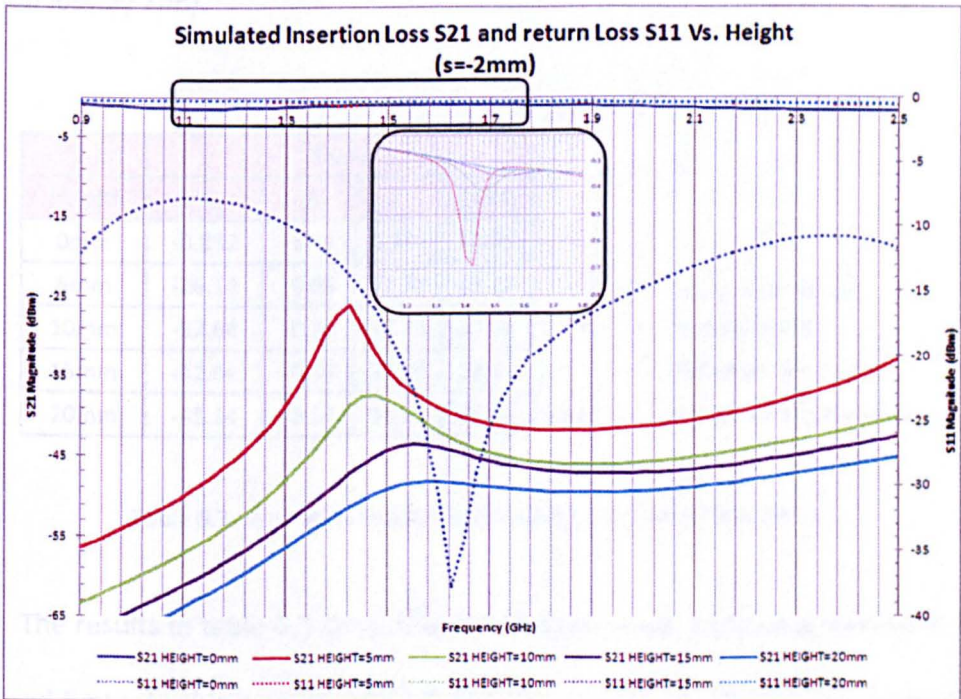


Figure 6.20. S-Parameter Results for Different Sample Height at S=-2mm.

When the height is zero, not only do the boards make contact but the feed lines and the ring also make contact (S being negative). As a result, the insertion loss is -0.83 dB and the return loss is -37.7 dB. Those calculations show that the transmission is very good. It is easily verified with the help of table 6.3, the reflection coefficient is only 1.3% and the VSWR is 1.026. As the height increases, as with the previous simulation, the reflection coefficient and VSWR increase rapidly. For a sample height of 5mm, the reflection coefficient is 92.3% and the VSWR is 25.2. This means that the design for which $S=-2$ mm responds slightly better than the design for which $S=0.25$ mm. (i.e. the reflection coefficient has improved by 0.7%, the VSWR by approximately 2.8, and the insertion loss by 2dB).

S=-2mm Height	Peak1			
	IL	RL	Γ	VSWR
0mm	-0.832	-37.7	1.306	1.026
5mm	-26.14	-0.69	92.38	25.24
10mm	-37.64	-0.56	93.76	31.06
15mm	-42.64	-0.54	94.02	32.44
20mm	-45.24	-0.52	94.21	33.55

IL = Insertion Loss S21 (dB)
 RL = Return Loss (dB)
 Γ = Reflection Coefficient (%)
 VSWR = Voltage Standing Wave Ratio

Table 6.3. Simulation results for changing height when $S=0.25$ mm.

The results in table 6.3 show that the sample needs to have a maximum height of around 5mm. In this project, soft silicone pipes with an external diameter of 6mm were used. However, in order to detect a low level of alcohol, the inner diameter of the pipe needs to be as close as possible to its external diameter. This allows more volume

of liquid to be tested and therefore improve the accuracy of the system. To improve the sensitivity further, the pipes were made to pass through the detector four times as shown in figure 6.21. The four pipes were equally distributed on the ring resonator, and were perpendicular to the feed lines. In figure 6.21 the pipes are shown in silver with blue used to represent the liquid under test. Its permittivity can be changed to different values. The cylindrical form representing the liquid has a diameter of 4.8mm, which is the internal diameter of the pipes. The volume of a cylinder is $\pi r^2 h$ with r =radius and h =height of cylinder.

The width of the substrate is 100mm. The total sample volume being tested is therefore $4 * \pi * 2.4^2 * 100 = 7238.22 \text{mm}^3 = 7.238 \text{ml}$ of liquid.

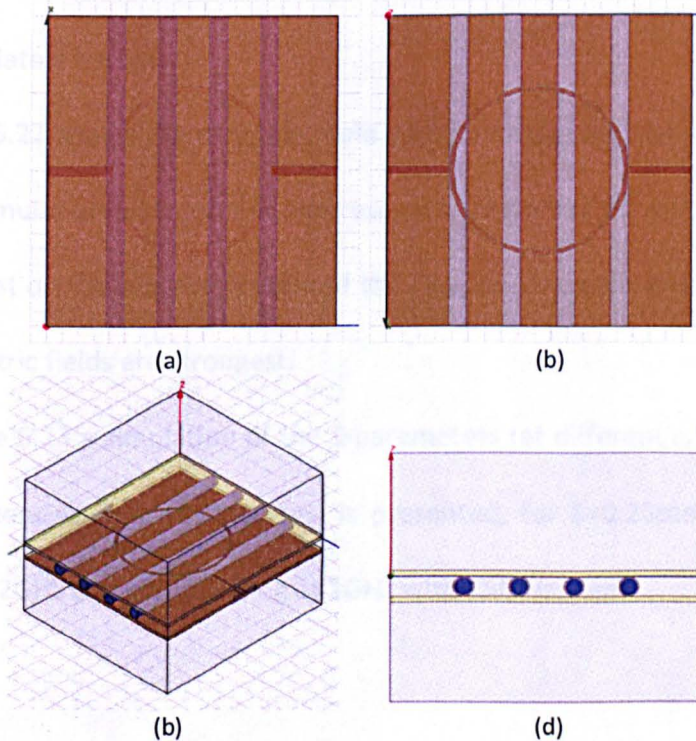


Figure 6.21. HFSS 3D model of the Ring Resonator with Sample Pipes, View from Below (a), View from Above (b), 3D Model (c), Side View (d).

Once the 3D model was completed it was possible to simulate a change of permittivity for the liquid sample inside the pipes. This was done using a parametric analysis for five key permittivity values ($\epsilon_r = 1, 20, 40, 60, 80$) for coupling gaps $S=0.25$ and $S=2$ mm.

These values were chosen because 1 is the permittivity of air (empty pipes), 20 is close to the permittivity of pure ethanol (22-24), 80 is close to the permittivity of water (78-82), and 40 and 60 are two arbitrary values in between.

Furthermore, the time required for one parametric simulation performed on the 3D model with the pipes filled with liquid (for 5 different permittivity values) was approximately 72 hours. Therefore, it was necessary that five values were enough to be able to validate a design.

Figure 6.22 shows the magnetic field vectors inside the pipes filled with water ($\epsilon_r=80$). The simulation was done at the resonant frequency for water. The magnetic field is strongest on the top and bottom of the ring, and is weakest near the feed lines, where the electric fields are strongest.

In figure 6.23 a simulation of the S-parameters (at different ϵ_r) for the first two resonant frequencies (two first modes) is presented, for $S=0.25$ mm. The frequency span used was 2GHz and commencing at 1GHz with 25MHz steps.

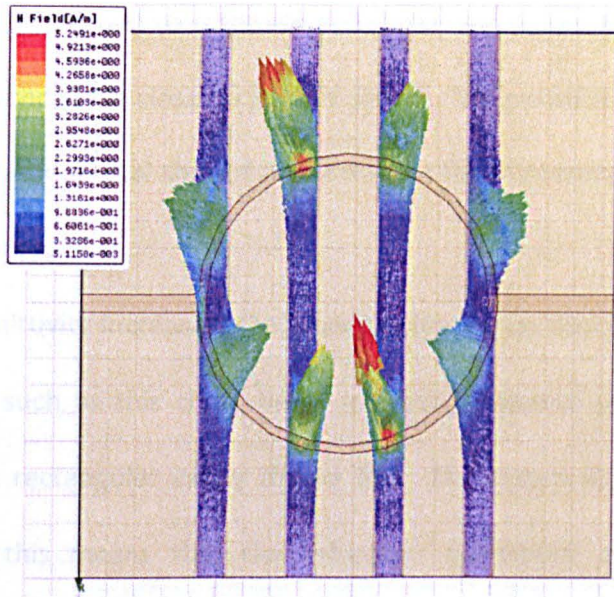


Figure 6.22. Magnetic fields inside the pipes.

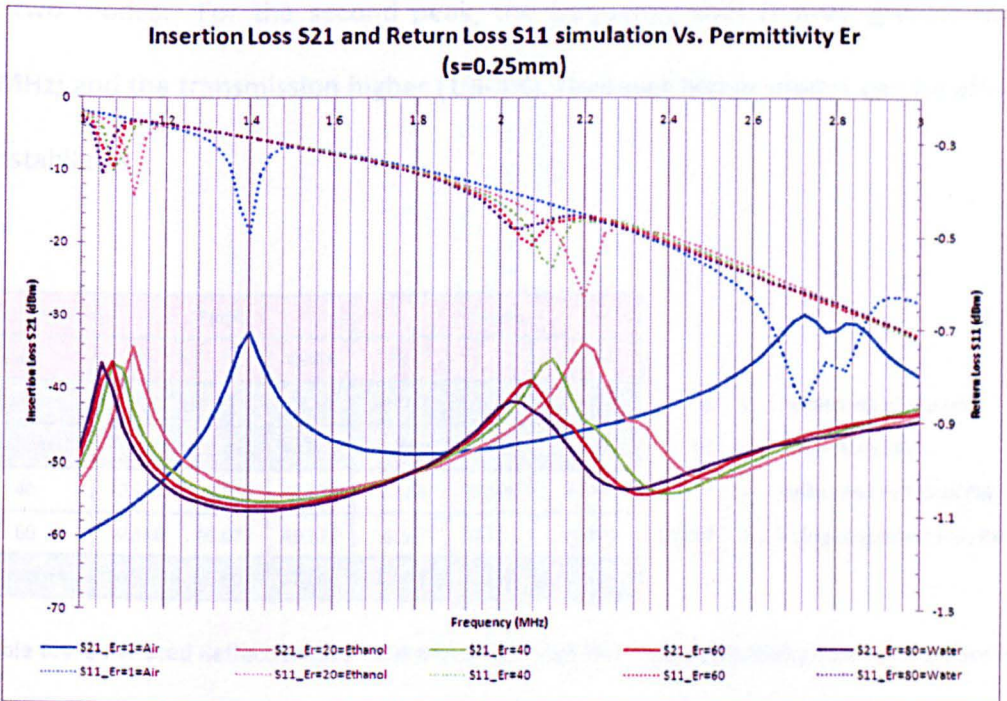


Figure 6.23. Parametric Simulation for Permittivity Changes ($S=0.25\text{mm}$)

The ring was designed to resonate at 1.5GHz. When the pipes are introduced the resonant frequency falls close to 1.4GHz ($\epsilon_r=1$). The permittivity values between $\epsilon_r=20$ and $\epsilon_r=80$ create a total shift of about 80MHz for the resonant frequencies (for the fundamental mode).

As the permittivity increases, the resonant frequency decreases. An important shift in frequency such as this could be of interest compared with the 5MHz shift observed with the rectangular cavity (figure 5.7). The return loss is relatively high (around -10dB), this means that the reflection coefficient and the VSWR are correspondingly high.

Table 6.4 presents the simulated reflection coefficient and the VSWR for the first two modes. For the second peak, the frequency shift is even greater (about 180MHz) and the transmission higher (1.5-4%). However higher modes can be affected by instabilities.

S=0.25mm	Peak1			Peak2		
ϵ_r	RL	Γ	VSWR	RL	Γ	VSWR
1= Air	-0.491	94.507	35.41	-0.863	90.538	20.137
20=Ethanol	-0.411	95.381	42.301	-0.631	92.995	27.55
40	-0.357	95.974	48.676	-0.565	93.699	30.74
60	-0.348	96.077	49.978	-0.52	94.191	33.429
80=Water	-0.363	95.902	47.805	-0.484	94.58	35.901

- ϵ_r = Permittivity of Material
- RL = Return Loss (dB)
- Γ = Reflection Coefficient (%)
- VSWR = Voltage Standing Wave Ratio

Table 6.4. Simulated Reflection Coefficient and VSWR for Different Permittivity Values (S=0.25mm).

The same experiment was repeated with the coupling gap $S=-2\text{mm}$. Figure 6.24 shows the parametric simulation performed on HFSS.

The results of figure 6.24 indicate that the negative coupling gap is capable working well. The return loss is smaller, therefore the reflection coefficient and the VSWR are smaller too. This mean less insertion loss and higher Q-factors.

Table 6.5 shows quantitatively the reflection coefficient and VSWR of the parametric simulation for the different permittivity values. When compared to the results when the coupling gap S equals 0.25mm , the reflection coefficient has been lowered by an average of 4% and the VSWR has been increased from 42.3 to 20.9 for water and from 47.8 to 22.5 for ethanol.

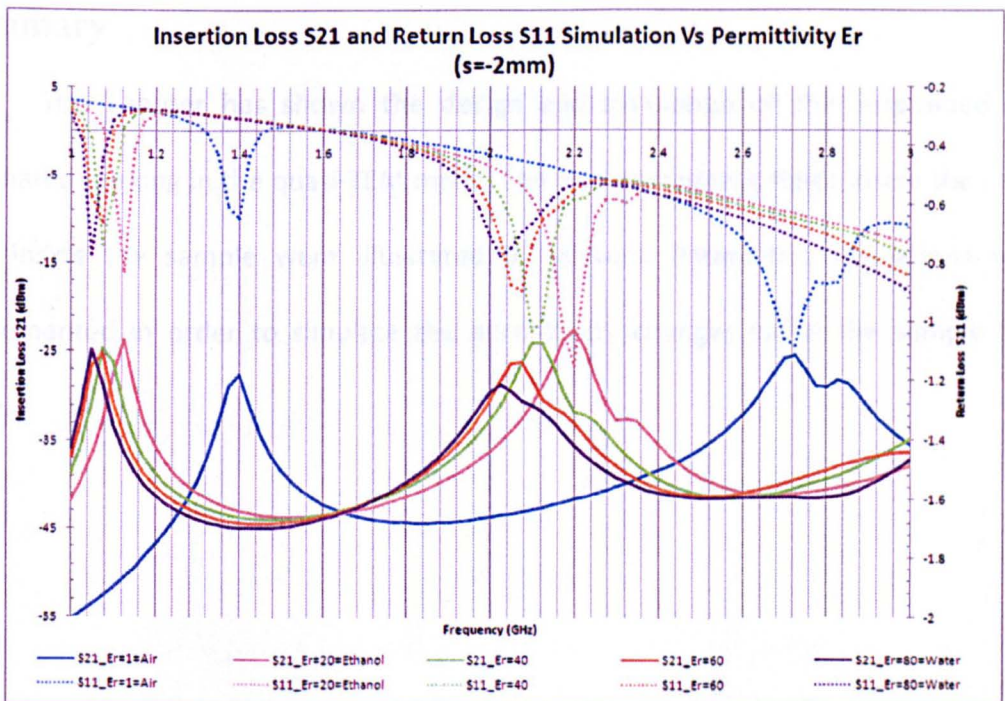


Figure 6.24. Parametric Simulation for Permittivity Changes ($S=-2\text{mm}$).

S=-2mm	Peak1			Peak2		
ϵ_r	RL	Γ	VSWR	RL	Γ	VSWR
1= Air	-0.648	92.813	26.829	-1.084	88.267	16.046
20=Ethanol	-0.83	90.883	20.937	-1.151	87.59	15.116
40	-0.735	91.883	23.638	-1.033	88.788	16.837
60	-0.661	92.669	26.281	-0.896	90.199	19.406
80=Water	-0.772	91.501	22.531	-0.899	90.162	19.33

ϵ_r = Permittivity of Material
 RL = Return Loss (dB)
 Γ = Reflection Coefficient (%)
 VSWR = Voltage Standing Wave Ratio

Table 6.5. Simulated Reflection Coefficient and VSWR for Different Permittivity Values (S=-2mm).

The results of the simulation have indicated that the suspended ring resonator is capable of detecting 5 different permittivity values in the permittivity range of 1 to 80. The negative coupling gap has been simulated and validated for the final design.

Summary

This chapter has shown the design and simulation of the suspended ring resonator working in the quasi-TEM mode. The electromagnetic fields inside the cavity and inside the sample were illustrated by vectors. Parametric simulations were implemented in order to simulate the permittivity changes inside the sample feed tube.

7 MICROSTRIP RING RESONATORS EXPERIMENT RESULTS

7.1 Microstrip Ring Resonator Construction

Creating a microstrip ring resonator is a relatively simple fabrication process. A sheet of double sided FR-4 Printed Circuit Board (PCB) of 1.6mm thickness and with a 35 μ m copper layer deposited on each side. The bottom side being the ground and no processing is required on that side. A PCB 3D model was created using a design suite of software called Percival. The PCB prototyping software in that suite is called Galaad [88]. Galaad produces 3D designs for a 3 axis milling machine. The shape of a ring resonator is designed using major shapes such as lines, rectangles, circles and arcs.

Figure 7.1 shows a screen capture of Galaad, for the test design of a split ring resonator with enhanced feed line. The height of the dielectric is important and affects the impedance of the feed lines and ring, therefore, it is essential to take as small amount of dielectric as possible during machining.

The accuracy of the milling machine is approximately 50 μ m. Such errors would change the impedance of the circuit so it was decided to only mill the contours of the ring and feed lines and perform the remaining clearance of copper manually.

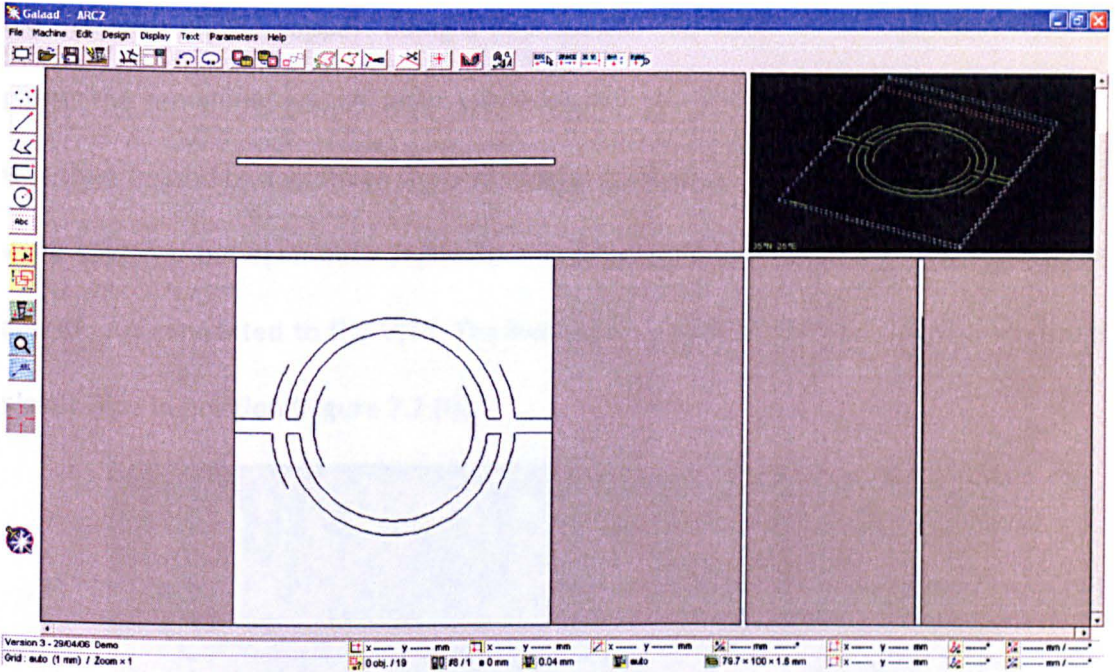


Figure 7.1. Galaad Graphical User Interface (GUI).

The positions and sizes of the shapes forming the pattern of the ring and feed lines were sent to the milling machine (Figure 7.2 (a)).

The PCB was attached to a wooden board and clamped on the milling machine table. The origin was set using the X,Y and Z axis to align the tool with the bottom left corner of the PCB (Figure 7.2 (b)).

At this stage the machine was ready to cut the pattern into the PCB. The 0.25mm \varnothing tool rotates at 20000rpm and start machining (Figure 7.2 (c)). Figure 7.2 (d) shows the finished ring.

As stated previously, to avoid losing too much dielectric material, the machine did not clear all the copper. Using a heat gun at 250-300°C and a flat ended pair of pliers, the remaining copper layer was manually peeled off (Figure 7.2 (e)). The PCB was then resized to a width at the end of both feed lines. Two SMA coaxial connectors were soldered between each feed line and ground. Those connectors were the RF in and RF out connected to the VNA. The two green plastic loops were used to keep the plastic pipe in position (Figure 7.2 (f)).

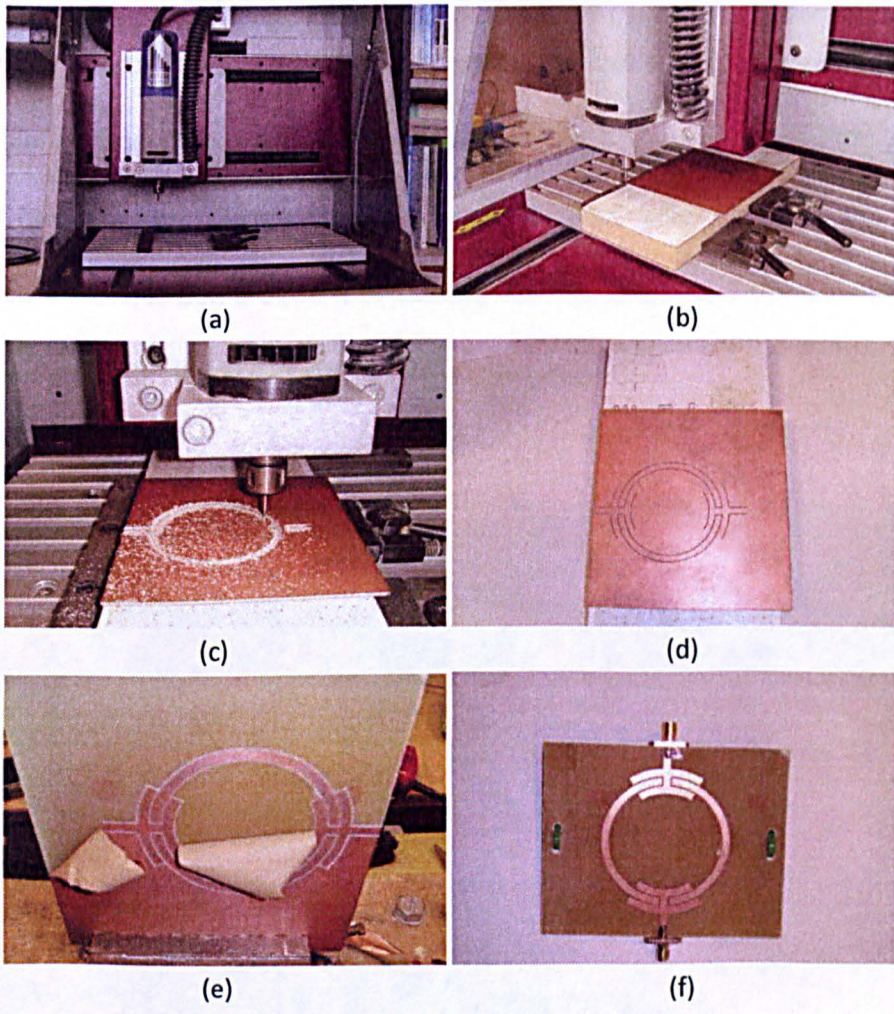


Figure 7.2. Construction Cycle of a Microstrip Ring Resonator.

7.2 Suspended Ring Resonator Ethanol Experiment

7.2.1 Experimental Setup

The microstrip suspended ring resonator was created using the same technique. After the resonator was milled, the two boards were superimposed and four holes were drilled in the corners. Four plastic screws were placed in the holes to allow the height of the upper PCB to be adjusted. Nylon screws were used instead of metal screws to avoid any unwanted electrical coupling between both dielectrics. After a few primary tests, it was determined that the ring was working normally. However some radiation above the ring was detected. By simply passing a hand above it, the resonant frequency and Q-factor were changed. A simple option to solve this problem was to use a metallic box around it to contain the radiation. i.e. form a Faraday cage. Figure 7.3 shows the ring in its Faraday cage.

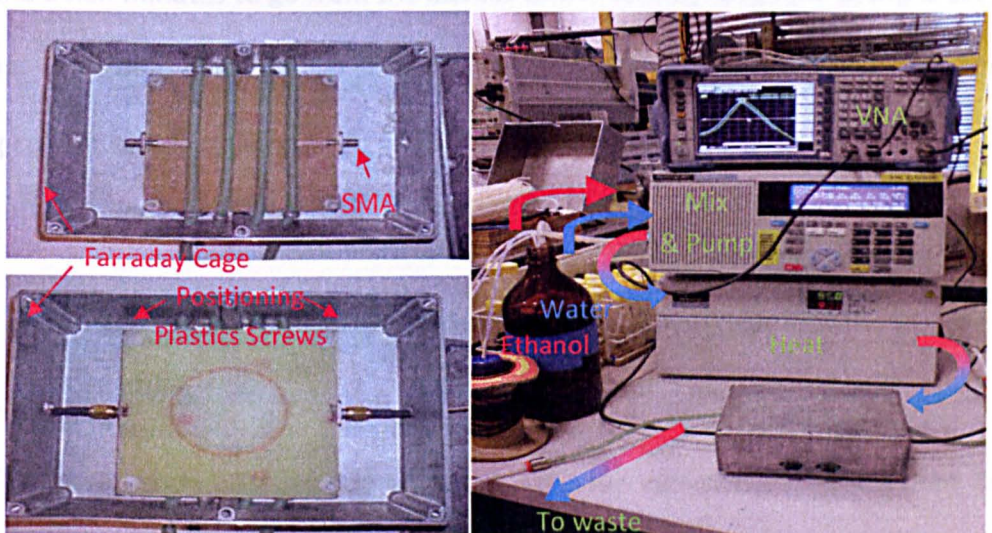


Figure 7.3. Ring Configuration (left), Experimental Setup (right).

Figure 7.3 (right) shows the experimental setup. The VNA sends and receives electromagnetic waves to and from the ring and analyses the S-parameters. The concentrations of the samples were made using a Perkin Elmer [89] mixing pump. The device pumps in ethanol and/or water from external bottles depending on the concentration needed. It can mix up to four different liquids at a time with an accuracy of 0.1%.

When the mixture was prepared, it was sent to the Perkin Elmer [89] heat column. The heat column is used to regulate the temperature of the samples between 10°C and 90°C. Generally in scientific papers and journals, the temperature is set to ambient temperature (25°C). The temperature regulated sample was then sent to the sensor to be measured.

After being measured the mixture flows into a waste jar. The mixture takes three and a half minutes to go from the bottles to the sensor, when the pump is set to 5ml/min. The pump could be set to a maximum of 10ml/min, but the effect of the heating column was greatly reduced at this value.

7.2.2 Ethanol Results-0% (Water) to 100% (Ethanol) by 5% Increments

Figure 7.4 shows the experimentally determined variation of the insertion loss (S₂₁) for the full range (water to ethanol) of samples in 5% concentration steps. The

resonant frequencies are higher by about 100-150MHz compared with the simulations. The frequency shift between the resonating peaks of water and ethanol is 44MHz whereas on the simulation they were separated by about 80MHz. The frequency shift from water to a 50% mixture was about 11MHz, when the shift from 50% ethanol to 100% is about 33MHz.

Figure 7.5 shows that the phase of S21 is significant for sample determination too. As with the insertion loss, lower concentration samples are more closely bounded than higher concentration values. The values of the phase at resonant frequencies are all in the region of -170 degree.

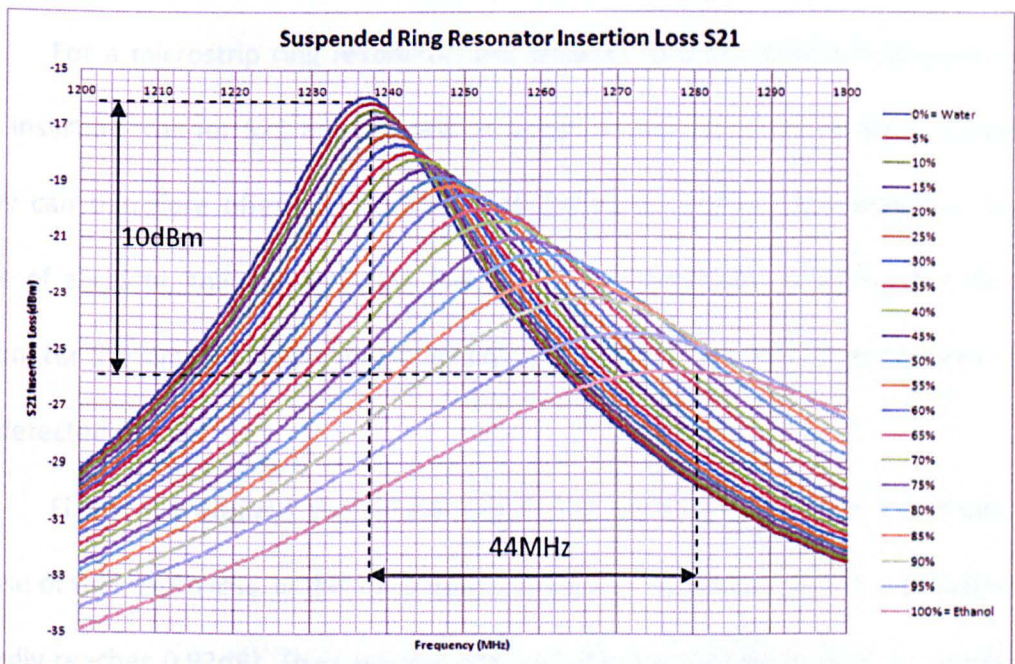


Figure 7.4. Insertion Loss (S21) for the Full Range of Samples.

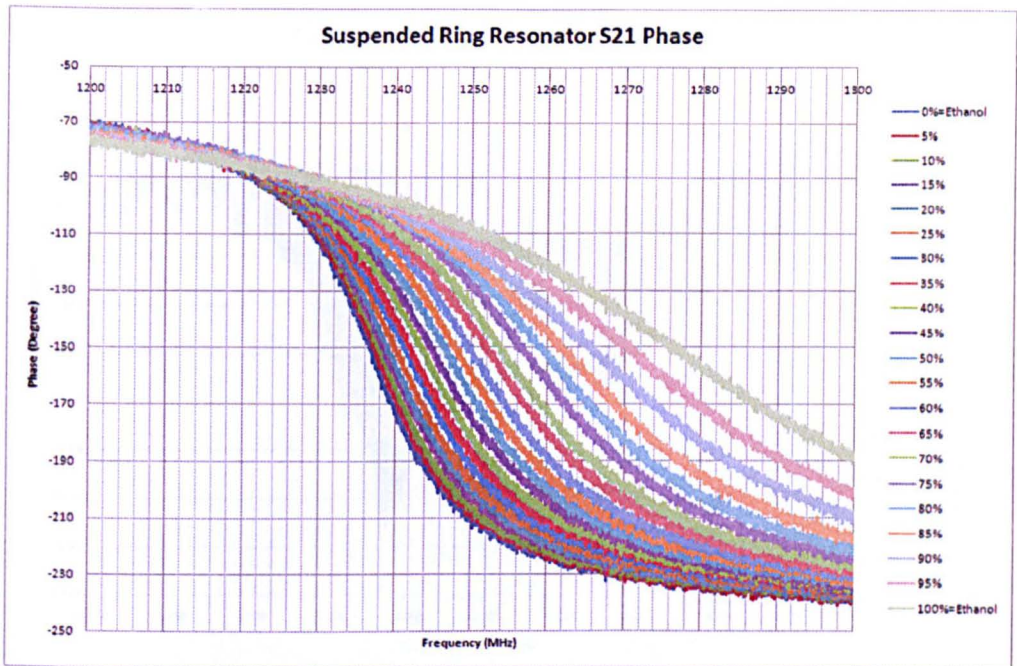


Figure 7.5. S21 Phase for the Full Range of Samples.

For a microstrip ring resonator, the Q-factor and the resonant frequencies of the insertion loss for S21 are essential in order to accurately characterise materials. They can therefore offer a good prediction for concentration determination. In the case of a cavity, the insertion loss and return loss are used, however, for the ring resonator the simulation has shown that the return loss is so small that sample cannot be detected.

Figure 7.6 displays the return loss of the samples and figure 7.7 shows the phase of the return loss. In the simulations, the return losses are very low in magnitude (hardly reaches 0.92dB). They are that low that interference and noise are significant. In this case finding an equation to fit the Q-factors or resonance would be almost impossible.

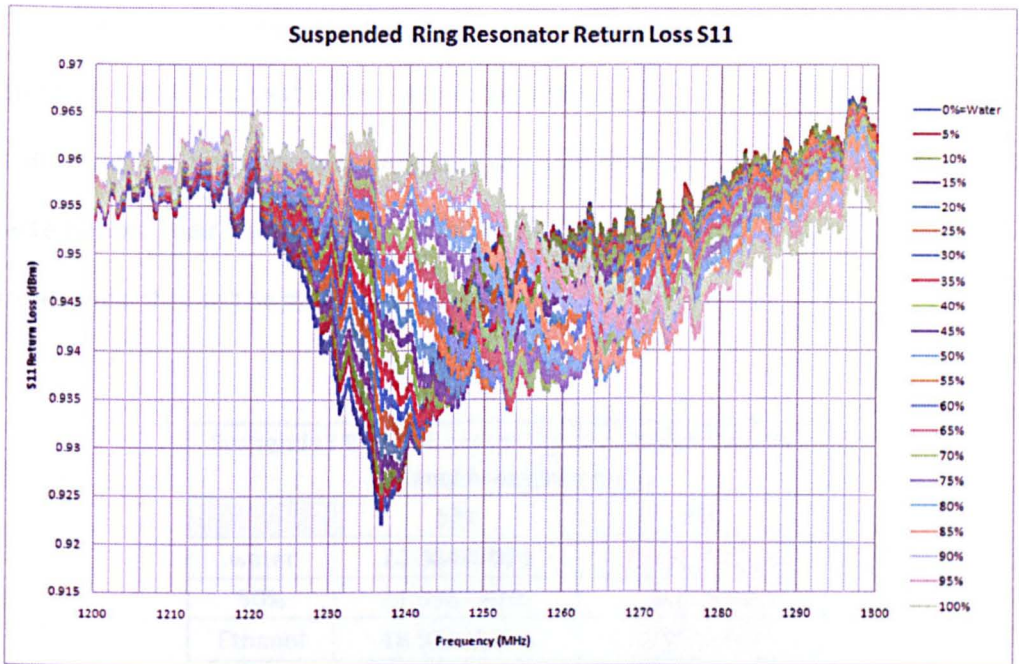


Figure 7.6. Return Loss (S11) for the Full Range of Samples.

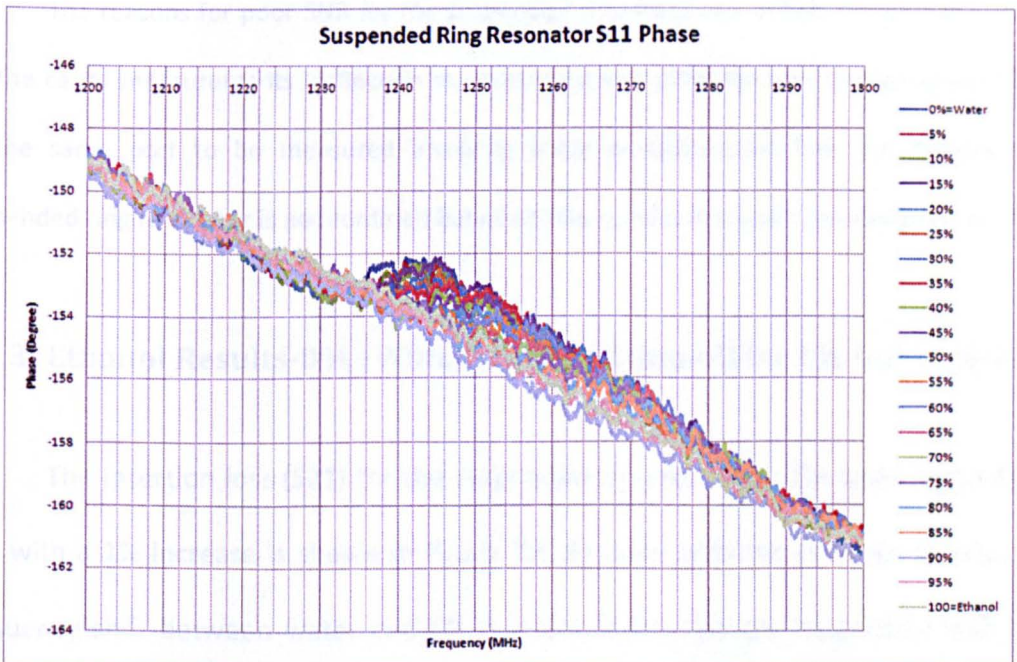


Figure 7.7. Return Loss (S11) Phase for the Full Range Of Samples.

Table 7.1 show the signal to noise ratio (SNR) for water, 50% and ethanol. The transmission SNR is acceptable for sample characterisation with value ranging from 18.5 to 22.3. However, the reflection measurements are very poor and could not be used for sample characterisation. Their values are shown in table 7.1 in red. For this reason, in the next sets of measurements, they will be measured or displayed.

Suspended Ring Resonator Signal to Noise Ratio for Ethanol Measurements		
	S21	S11
water	22,30448921	4,398587926
50%	21,39879086	2,438644894
Ethanol	18,57332496	1,026623419

Table 7.1. Signal to noise ratio for the suspended ring resonator for ethanol measurements.

The reasons for poor SNR for the suspended ring resonator reflection are the same as for the cavity measurements (reflection measurement are going through the sensor and back to the same port to be measured involving more perturbations) but also because the suspended ring resonator is not confined between four conduction walls (meaning less loss).

7.2.3 Ethanol Results-0% (Water) to 5% (Ethanol) by 1% Increments

The insertion loss (S21) for the suspended ring resonator for small samples (0-5%) with a 1% increase is shown in figure 7.8. As seen with the previous results, the frequency shift between water and 5% is about 2MHz and the magnitude shift was approximately 0.3dB. Here, the results are plotted in millivolts but the shift between 0% and 5% is the same as the shift shown in figure 7.4 in dB, only the scale is different.

We can clearly determine the difference in frequency and magnitude between each sample. The curves are not as smooth as those of the cavity, but more frequency span and more amplitude changes have been observed.

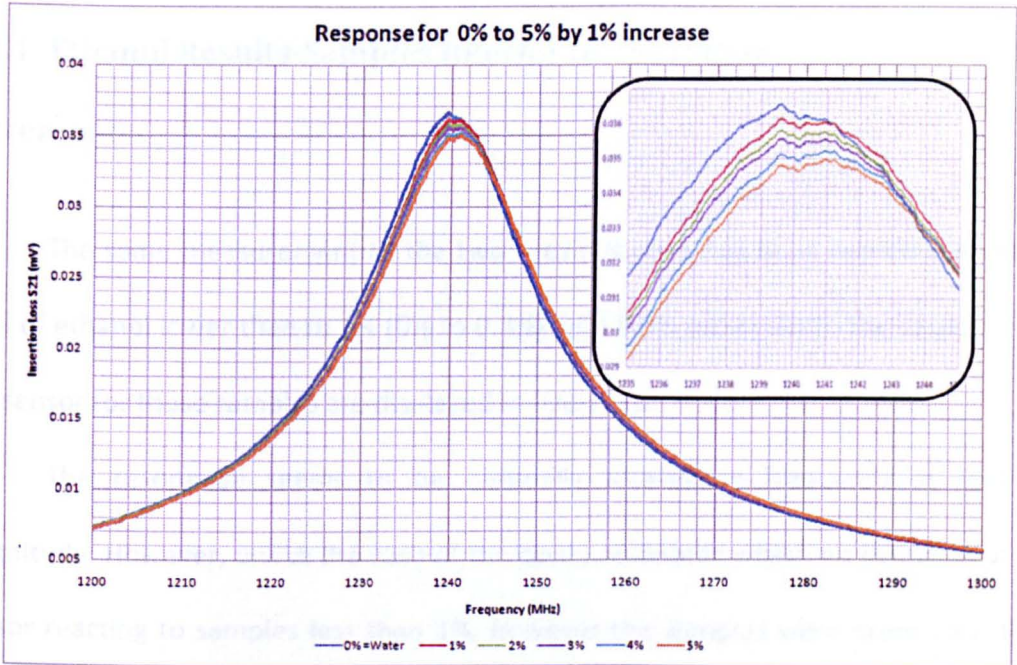


Figure 7.8. Water to 5% ethanol sample insertion loss S21 by increment of 1%.

The insertion loss for the samples (0% to 5%) correspond with the permittivity values, the magnitude is decreasing as the concentration of ethanol increases. The resonant frequencies extracted by the software were almost all the same for the simple reasons that an imperfection (in the manufacture of the ring) created a small peak in the magnitude close to the resonance. For this reason, the software took each maximum at the same frequency even though the real magnitude and frequency at resonance should be situated on the symmetric line separating the insertion loss peak in two. On the zoomed image in figure 7.8, the little peak (at the same frequency) is

not the natural maximum. Applying a smoothing of 0.05%-to 1% suppresses the imperfection and reveals the magnitude and frequency as it should be.

7.2.4 Ethanol Results-Samples Inferior to 1% (Ethanol) by 0.2%

Increments

The same measurement as the two previous ones has been carried out with a level of ethanol lower than to 1% (0% to 0.8%) with 0.2% increments. The responses of the sensor for those samples are displayed in figure 7.9.

The resonance seems to be randomly located in frequency as well as magnitude. However, unlike the case of the cavity resonator where no evidence of the sensor reacting to samples less than 1%, however the samples were order with their permittivity values looking at the positive gradient (left) of the peak (zoomed image in figure 7.9). Indeed, for a single and fixed frequency point (dashed line inside the zoomed image), the sample magnitudes can be used to determine the concentration.

The difference between water and the 0.8% sample is $1\mu\text{V}$ meaning that the average magnitude difference for a 0.2% change is around $0.2\mu\text{V}$. Note that if any difficulties in measuring that difference is experienced, a solution would be to increase the incident wave power. For all the experiments made in this thesis the output power of the VNA was set to 0dBm (1mW).

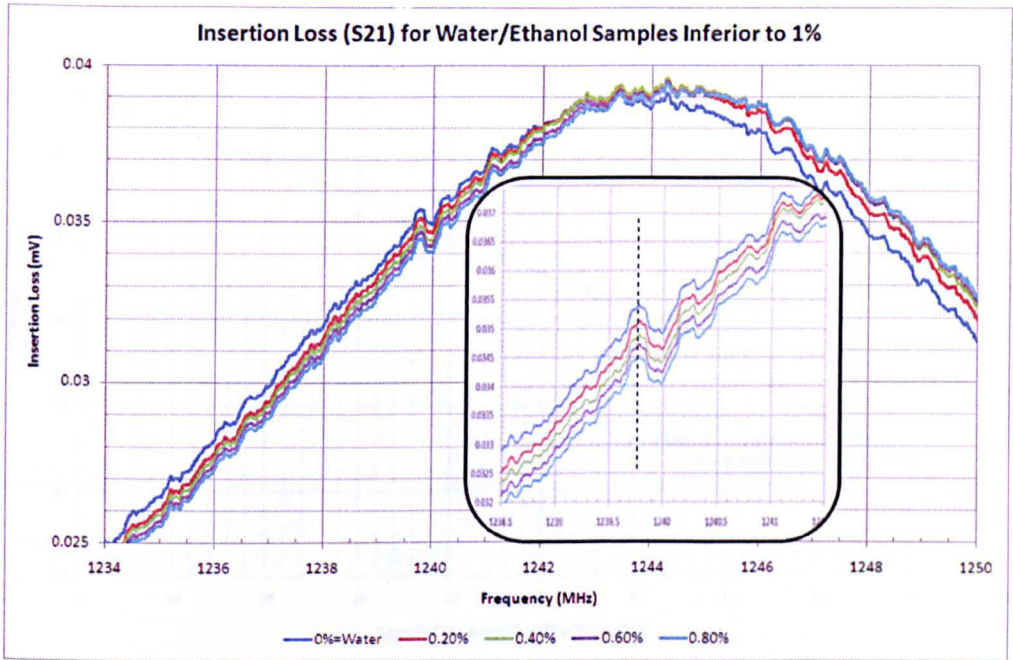


Figure 7.9. Insertion Loss for Sample Inferior to 1% of Ethanol.

7.2.5 Ethanol Extracted Data

Figure 7.10 displays the Q-factor values against the ethanol concentrations. The Q-factors of the simulation were almost identical to the measured Q-factors.

In the experiment, the Q-factor reduces significantly as the concentration of ethanol increases. For low levels of ethanol, the peak is sharp and high, this results in a higher Q-factor. High levels of ethanol lead to a low Q-factor because their peaks are stretched over more frequencies and are weaker in magnitude. The resonant frequencies are plotted against the concentration of the samples in figure 7.11.

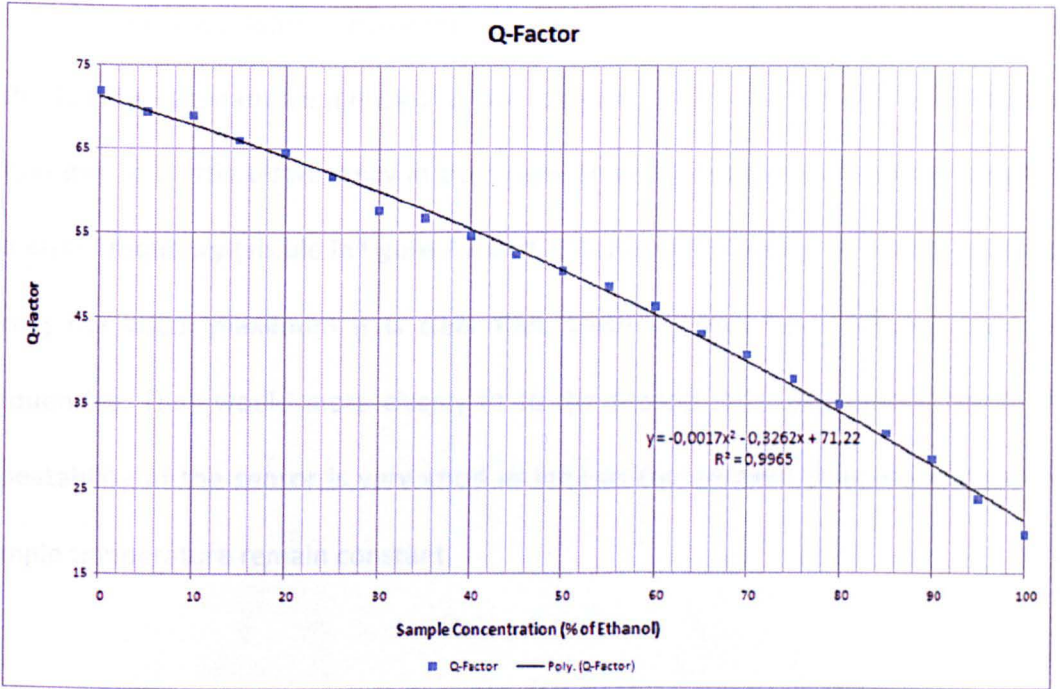


Figure 7.10. Q-Factor for the full range of samples.

7.2.5 Temperature Effect

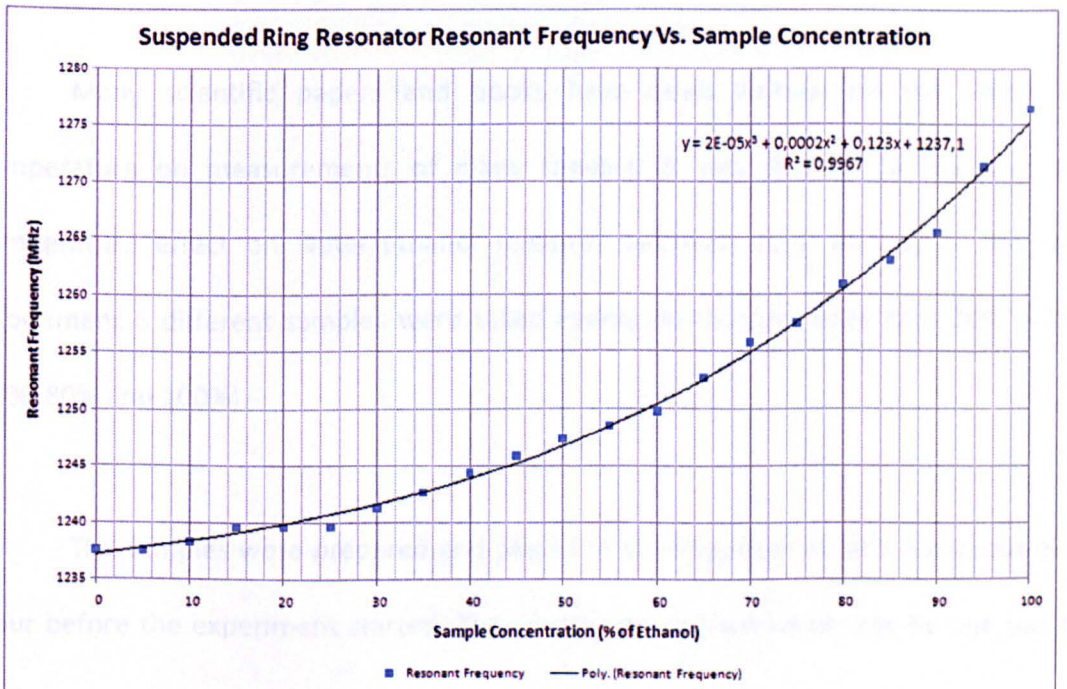


Figure 7.11. Resonant Frequencies of the samples.

The characteristic of resonant frequencies versus concentration is not linear. Note that the resonant frequencies for the samples 15%, 20%, and 25% are the same. This is due to a little discrepancy in the shape of S21 that appears on every sample at the same frequency (visible in figure 7.8 and 7.9). However looking at the S21 plots and taking the visual maximum it is clear that those samples have different resonant frequencies. They would more closely fit to the second order polynomial trend. The repeatability of the sensor is very good as long as the ambient temperature and the sample temperature remain constant.

7.2.6 Temperature Effect

Many scientific papers and books have been written on the effect of temperature on measurements of many sensors. It was decided to monitor the temperature effect on water/ethanol mixtures between 20°C and 40°C. For this experiment 6 different samples were taken evenly on the full range (0%, 20%, 40%, 60%, 80% and 100%).

The samples were prepared and placed in a refrigerator at 10°C for about one hour before the experiment started. The samples were then taken one by one out of

the fridge and tested. The heat column was set to 90°C, because the pump speed only allows samples to reach a maximum of 45-50°C.

Once the samples reached 20°C the measurements started. With the help of the acquisition software, the s-parameters were captured every 2.5°C until the samples reach 40°C. Figure 7.12 shows those results for the three major temperatures (20°C, 30°C and 40°C). The temperature increases exponentially with time, so the liquid heats up very fast at the beginning but slows afterwards.

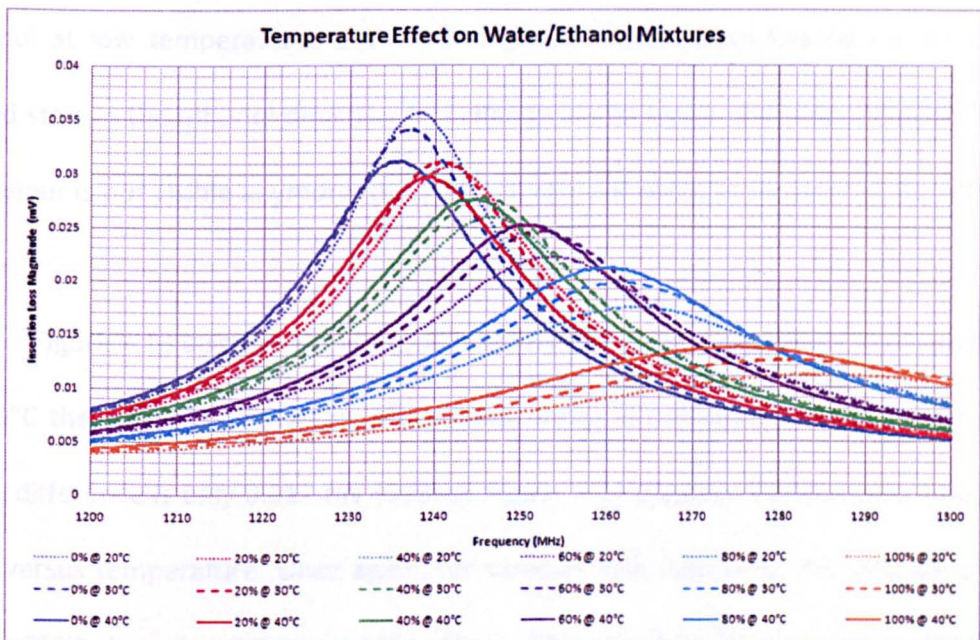


Figure 7.12. Temperature effect on S21 for Water/Ethanol mixtures.

An interesting behaviour was noticed during the tests. The water sample resonant frequency and magnitude decreased as the temperatures increased. Contrary

to water, the magnitude of ethanol's resonant frequency increased as the temperature increased, but like water its resonant frequency decreased when heated.

A simple directional vector was used to characterise both frequency and magnitude at different temperature as: right/left being the frequency, up/down being the magnitude and the direction of the arrow being the Temperature increasing. The vector for pure water would be ↙, and the vector for pure ethanol would be ↖. For a sample made of a mix of the two and inferior to 60%, the vector points differently depending on the concentration. For example at 20% it seems to be affected by ethanol at low temperatures but increasingly by water when heated up. Its vector would start in the ethanol direction and change to the water direction. After 60% that behaviour is not visible anymore, the effect of ethanol being stronger than the effect of water.

Figure 7.13 displays the effect of temperature on the magnitude of the samples. At 20°C the difference between ethanol and water is 0.035mV (10dBm), at 40°C the same difference is only 0.017 mV (5dBm). Figure 7.14 displays the resonant frequency shift versus temperature. Once again, for samples less than 60%, the average shift is about 2MHz between 20°C and 40°C. Above 60% the shift increases up to 10MHz as the ethanol concentration reaches 100%. Like the magnitude, the frequency shift is bigger at low temperatures. In 2000, Petong, Pottle and Kaatz were studying the relaxation of water/ethanol mixtures at different temperatures [82]. Their results show

the permittivity values of five different samples for temperatures ranging from 0°C to 60°C.

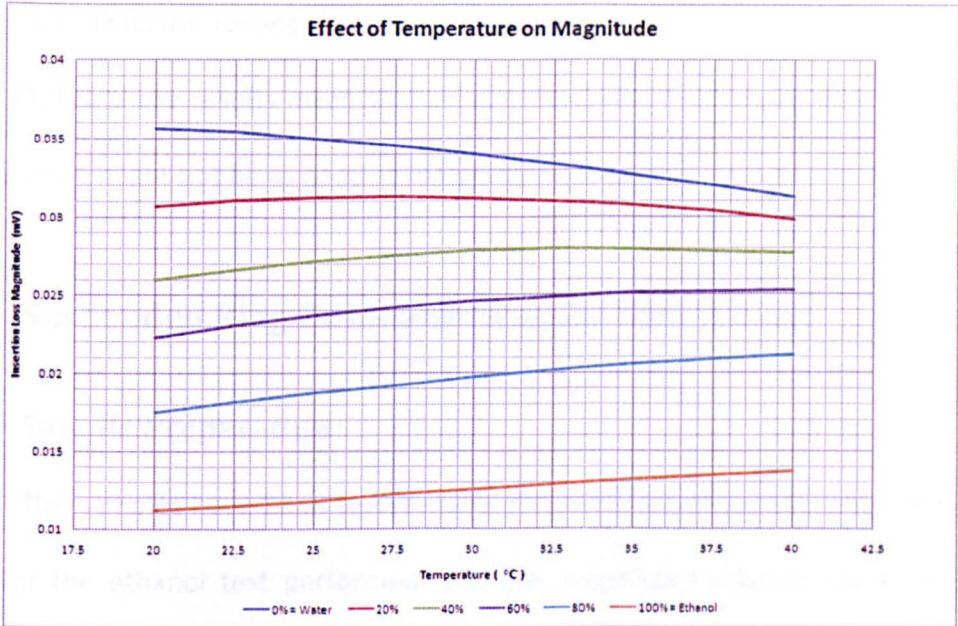


Figure 7.13. Temperature Effect on Magnitude.

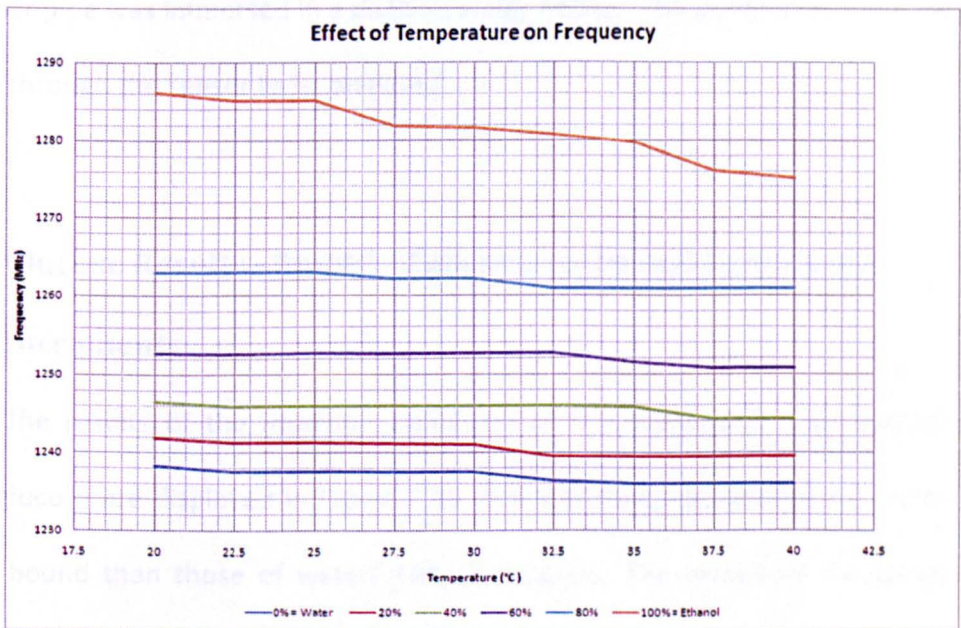


Figure 7.14. Temperature Effect on Resonant frequency.

The ambient room temperature was 22.4°C ($\pm 1.0^{\circ}\text{C}$) when the experiment was carried out. It has been shown that the temperature must be considered when performing dielectric testing. However, with the human blood average temperature being 37.5°C , these results mean that good measurement of liquids at ambient room temperature might not be as good at temperatures between 30°C and 40°C .

7.3 Suspended Ring Resonator Glucose Experiment

7.3.1 Sample Preparation

The samples have been tested using the same experimental setup as the one used for the ethanol test performed with the suspended ring resonator. A 1 litre solution of 1mol/l glucose was made and input to one of the pipes of the mixing pump. The other pipe was immersed in a distilled water bottle. The pump mixed and sent the sample through the sensor to be analysed.

7.3.2 Glucose Results - 0mol/l of glucose to 1mol/l by 0.1mol/l

Increments

The results of the insertion loss (S21) of the suspended ring resonator for water/glucose are displayed in Figure 7.15. The resonant frequencies are much more closely bound than those of water/ethanol mixtures. The maximum frequency shift between water and the 1mol/l sample is 4MHz. The maximum difference in magnitude is 1.6dB.

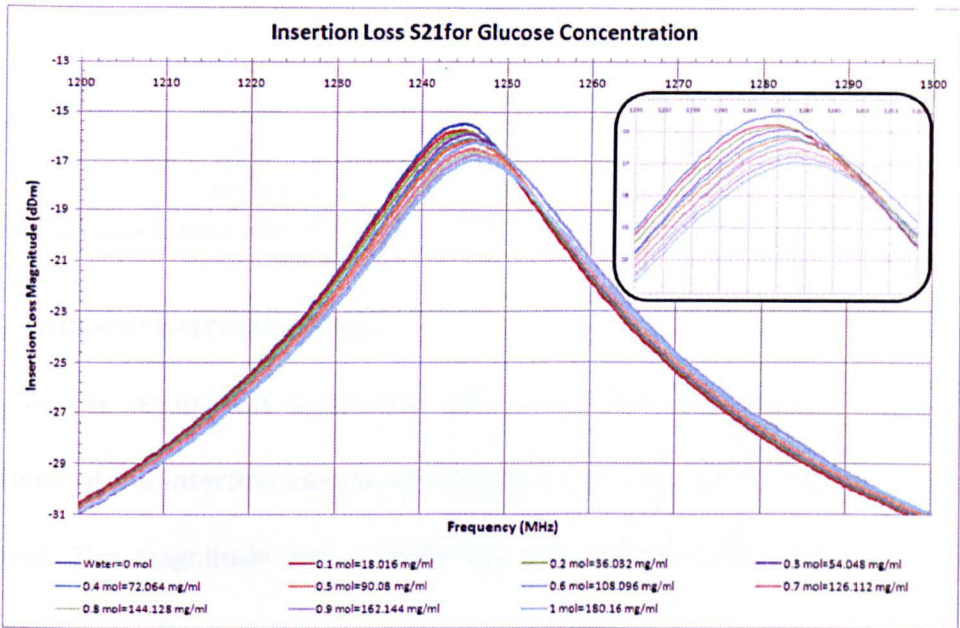


Figure 7.15. Glucose Results from the Suspended Ring Resonator.

The resonant frequencies are in order according to the glucose concentrations. An increase of 0.1mol/l (100mmol/l) is detectable using the suspended ring resonator. However, this is still far from the 5mmol/l level usually found in the human body. The glucose results shown in figure 7.15 are displayed with a smoothing equal to 0.25%.

The signal to noise ratio is shown in table 7.2. As for the suspended ring resonator results for ethanol measurements, the return loss has too much perturbation to be used for sample characterisation. The SNR values are also lower than those measured for the ethanol measurements (22.3 to 18.5 for S21 and 4.4 to 1 for S11).

Suspended Ring Resonator Signal to Noise Ratio		
	S21	S11
water	17,63427994	2,671717284
50%	17,45595216	2,430380487
Ethanol	17,26998728	2,174839442

Table 7.2. Signal to noise ratio (SNR) for the suspended ring resonator for glucose measurements.

7.3.3 Glucose Extracted Data

As the return loss signal was too weak, only the resonant frequency and magnitude of the insertion loss could be used. As a result, only the Q-factor could be extracted. The magnitude and Q-factor are displayed as a function of the glucose concentrations in Figure 7.16.

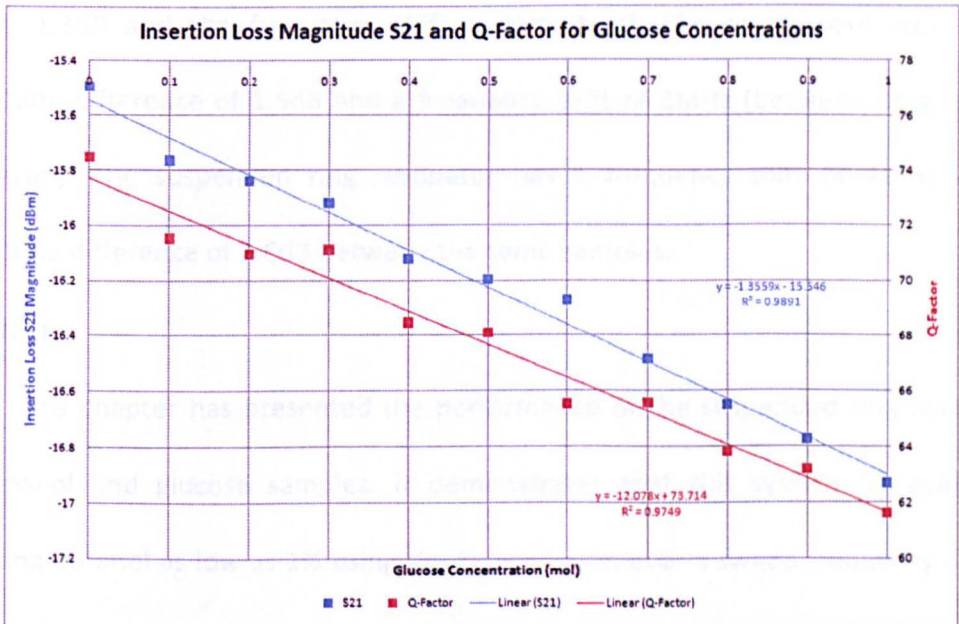


Figure 7.16. Insertion loss and Q-factor for glucose measurement.

The blue data points represent the magnitude of the insertion loss at resonance and the blue line is the trend line used to calculate the equation in blue. The red points represent the Q-factor depending on the concentration of glucose.

The preliminary test for water/glucose samples were conclusive and shown that ring resonators could also be used. Tests were made from 0 to 1mol/l of glucose by increments of 0.1mol/l (100mmol/l). This is still relatively high compared to the glucose level in the human body (0.9 mg/ml to 1.4mg/ml). The samples were in order but relatively close to each other. Lower levels of glucose could be measured with a purpose built sensor. Nevertheless, if we compare the results with those of S. Kim et al. [92], their results show that between 0mg/ml and 200mg/ml the magnitude difference is only 1.3dB and the frequency shift is almost nil. The cavity resonator has a magnitude difference of 1.5dB and a frequency shift of 2MHz (between 0mg/ml and 180mg/ml). The suspended ring resonator has a frequency shift of 4MHz and a magnitude difference of 1.6dB between the same samples.

Summary

This chapter has presented the performance of the suspended ring resonator for ethanol and glucose samples. It demonstrates that this system is capable of detecting ethanol as low as 1% using the transmission over a sweep frequency and up to 0.2% using the transmission at a single frequency. The suspended ring resonator was also able to detect glucose samples down to 0.1mol.

8 ELECTRONIC CIRCUIT FOR MICROWAVE MEASUREMENTS

8.1 Mini-Circuits Modules

The first stage of design development consists of using RF (Radio Frequency) modules to determine the feasibility and limits of the system. Those components are more expensive than surface-mounted technology but allow the user to switch and test different components until the final design is agreed. The final device needs to be small and reproduce the same characteristics as the VNA using surface-mounted components if possible.

The possibilities of making this system mobile and portable are real. The price of a VNA operating up to 3GHz is around £2000-£5000, this is high for a transportable system. Furthermore its weight and the size are not suitable for that kind of application. In order to reduce the cost, size and weight of the system, it was decided to replace the VNA by electronic components that can be bought separately and assembled.

Mini-Circuits [91] is an RF component manufacturer producing voltage controlled oscillators (VCOs), couplers, power detectors, and phase detector modules. The components are boxed modules with SMA connections. Quotations have been

sent to the manufacturer for a system that could measure exactly the same parameters as the VNA. A few key modules have been ordered, assembled and tested. Mini-Circuits quotes and data sheets are available in appendix C.

8.1.1 S-Parameters and Phase Measurements

The equivalent of the VNA using RF modules is shown Figure 8.1. The different components needed and their applications are as follows:

- **VCO** can be tuned over a range of frequencies by applying a voltage (tuning voltage) to it. Used in many applications such as radio tuners and telecommunications, VCOs are less costly than crystal oscillators, but not as stable. They are active components that need a power supply higher than the tuning voltage, usually 25V-30V [92].
- **Couplers** couple part of the transmission power in a transmission line by a known amount out through another port, often using two transmission lines set close enough together such that energy passing through one is coupled to the other. A **directional coupler** couples only to waves traveling in a particular direction in a primary transmission system to the secondary system, while zero coupling waves traveling in the opposite direction. They are passive components that do not require a power supply. They can be used as either a

forward coupler or a reverse coupler as the RF in and RF out pins can be reversed [93].

- **Splitters** are used to divide a signal into two quasi-equal signals. They can be used as combiners when their pins are swapped. They are passive circuits and do not require a power supply.
- **Power detectors** detect the active power of a transmission line and output a proportional voltage. Linear or logarithmic power detectors are available, with different detection ranges. They are active components and need a 5V power supply.
- **Phase detectors** measure the phase difference between two inputs, and create a DC voltage output that reflects this difference. They are passive component and do not require a power supply.

The following modules have been tested: the ZX95-1700w+ VCO creates a frequency sweep output ranging from 770MHz to 1.70GHz when a 1-24V DC sweep is applied to its input. The forward coupler and power detector monitors the VCO's performance. The power detector provides a 0.5V-2.1V DC output that represents the power of the VCO in dB (-60dB to 10dB).

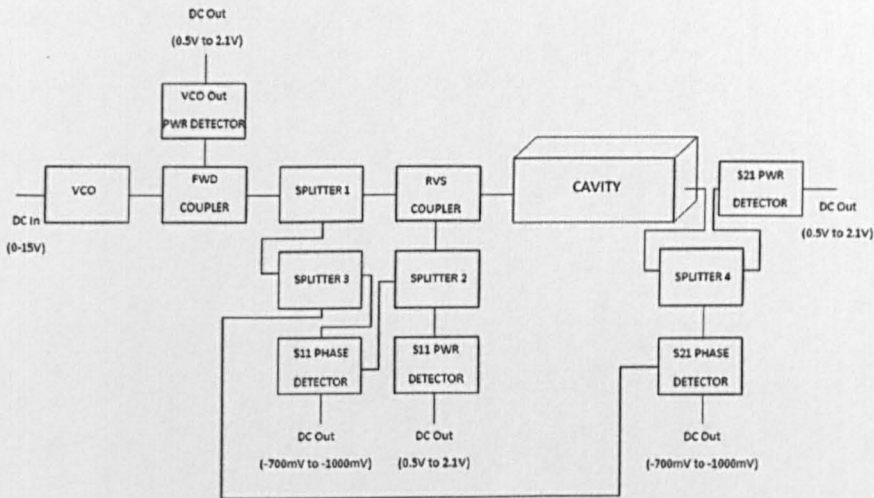


Figure 8.1. Function Diagram of the VNA-like Microwave System.

All the power detectors used for the project are the same and therefore have the same characteristics. The splitter 1 module splits the forward power from the VCO into two signals; one for the S11 detector and one that will supply the cavity with power. Between splitter 1 and the cavity, a reverse coupler is inserted to provide the reflected signal to splitter 2. Splitter 2 divides the signal between the S11 phase detector and the S11 power detector input. The phase detector provides a measure of the phase difference between the forward power and the reflected power. The S11 power detector measures the power reflected (S11) from the cavity and/or sample. At the other end of the cavity, the S21 power detector measures the power output from the cavity (S21).

Figure 8.2 shows photographically the complete system with two phase detectors. The two phase detectors are not appropriate for 1.5GHz but they have been placed there to show how the full system would look. Note that the ring resonator is placed where the cavity is on the function diagram.

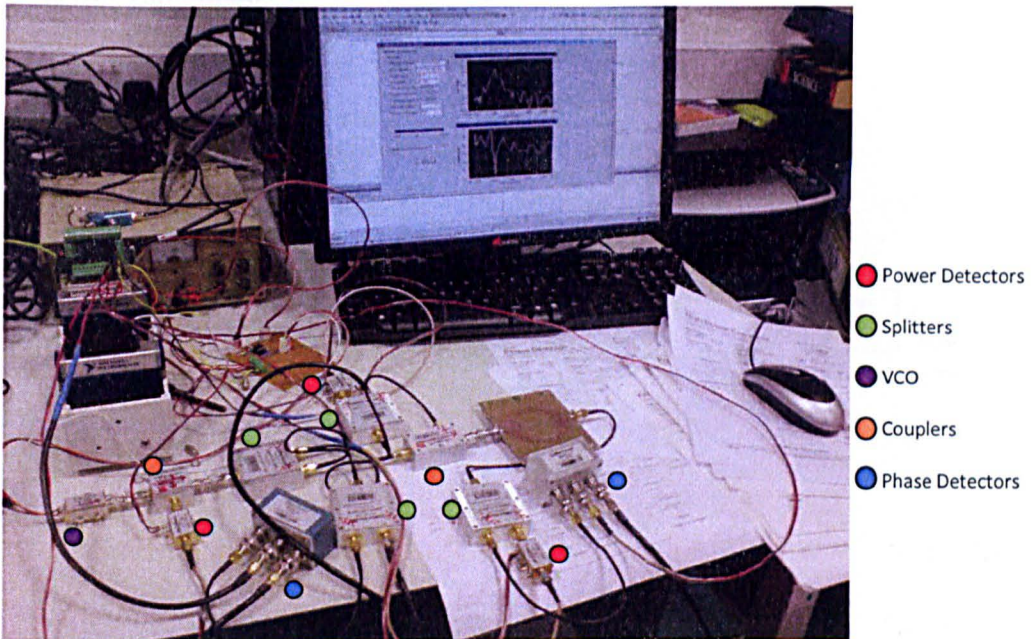


Figure 8.2. Complete System replacement for the VNA using RF modules.

8.1.3 Experimental Setup

8.1.2 Measurements of S-Parameters only

As described in chapters 5 and 7, the phase is not the main signature for material characterisation. The most important measurements are the insertion loss S_{21} and the return loss S_{11} . This is how the Q-factors, the reflection coefficient and the VSWR are determined. It will also reduce the size and cost without any loss in

accuracy. In addition the four splitters were only required if the phases were to be measured. Figure 8.3 shows how simple the function diagram becomes without the phase detectors. The system could be further simplified by not monitoring the output power of the VCO; this would make the forward coupler and one of the power detectors redundant.

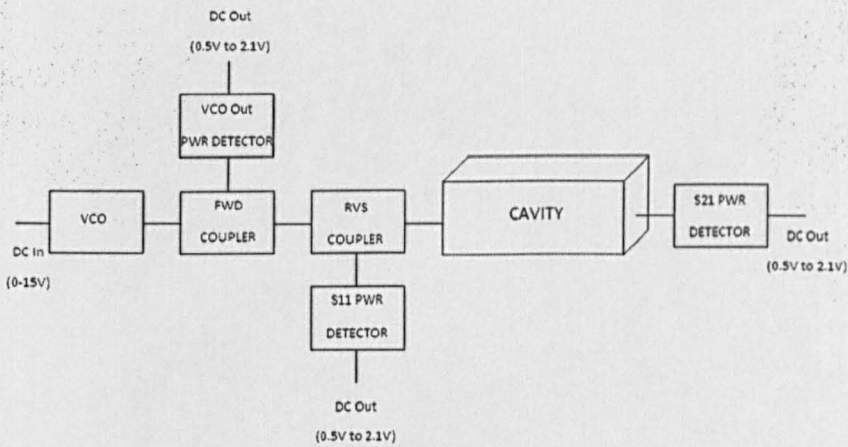


Figure 8.3. Function Diagram to measure S11 & S21.

8.1.3 Experimental Setup

In order to conduct the experiment efficiently, a software application was created that controlled a National Instruments DAQmx rack which was used to generate and acquire signals. The National Instruments rack communicates with the computer via USB, and allows the user to select a frequency sweep and capture S11 and S21 data. A wide range of modules can be used with this rack. For this project, all

that was required was an analogue out module and an analogue in module (to measure voltages). They can be seen in figure 8.4, with the rest of the system setup.

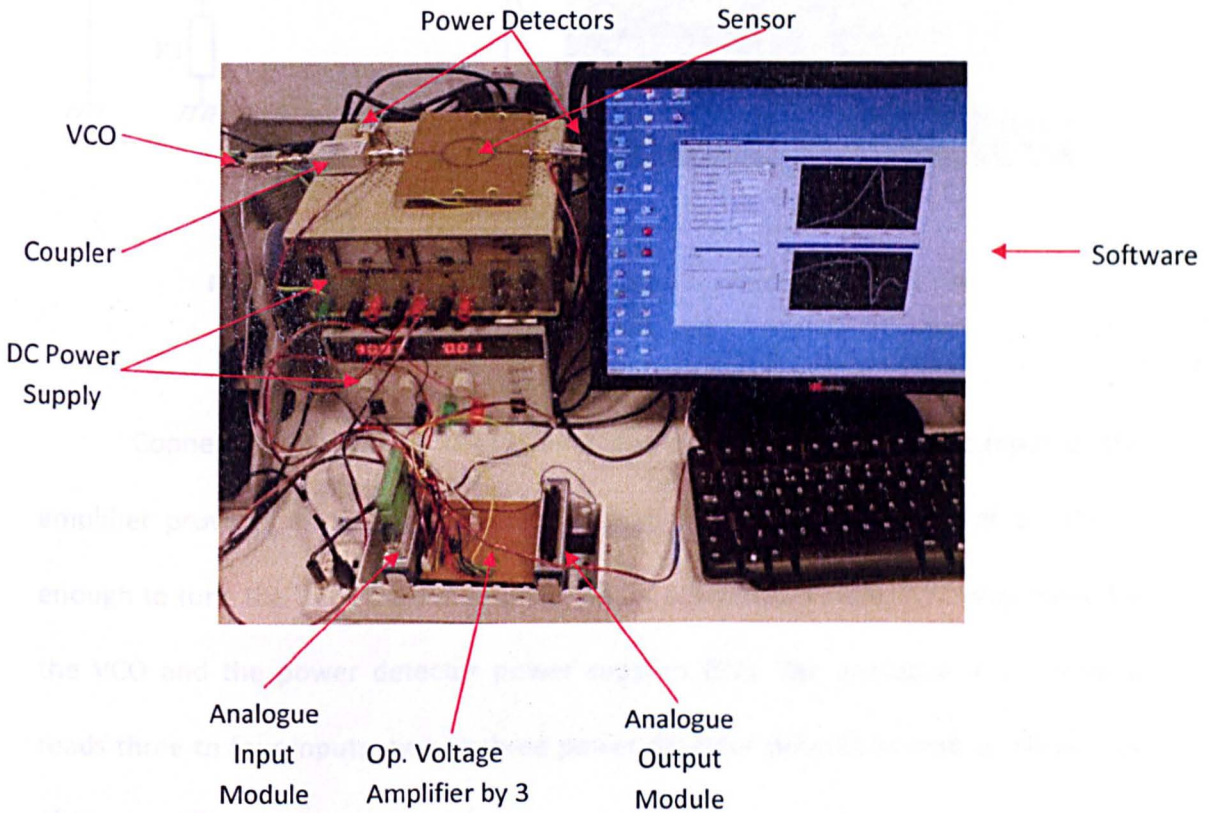


Figure 8.4. Test Bench.

8.1.4 Power Supply Issues

The National Instruments analogue output module (NI9263) only generates a maximum output of 10V, but the VCO needs a tuning voltage ranging from 1V to 24V. For this reason an operational amplifier circuit was used. Figure 8.5 shows a non-inverting amplifier, and if the resistor $R2=2 \cdot R1$, the gain of the amplifier is 3.

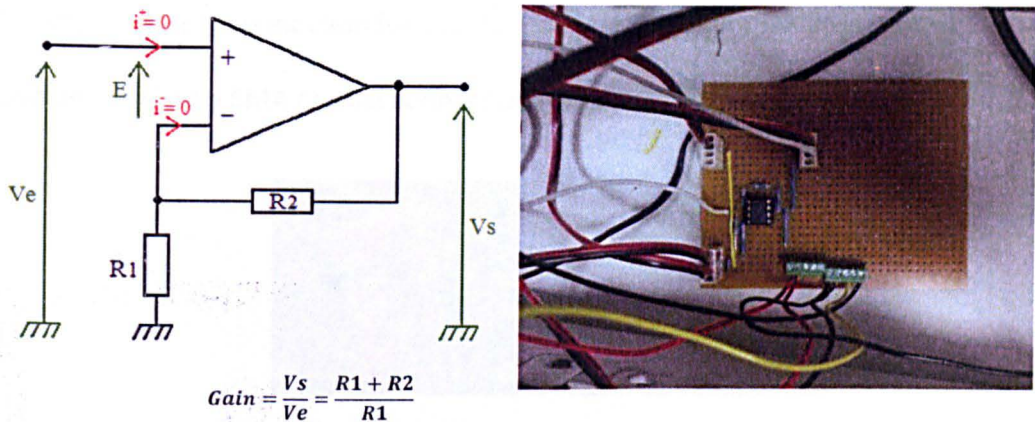


Figure 8.5. Schematic (left) and circuit (right) of a Non-Inverter Amplifier.

Connecting the NI9263 output analogue voltage (0V-10V) to the input of the amplifier provides an analogue output ranging from 0V to 30V (Gain of 3). This is enough to tune the VCO. On the amplifier board connections have also been made for the VCO and the power detector power supplies (5V). The analogue input module reads three to four inputs; two or three power detector outputs as well as the output of the amplifier.

8.1.5 VCO Calibration

The VCO calibration was performed by applying a DC voltage on the VTune pin and by verifying the output frequency (RF Out pin) on a spectrum analyser. Even though the data sheets are given by the manufacturer, it is important to ensure that the data provided is accurate because individual components may differ slightly. Figure

8.6 shows the pin connection for the VCO, red for 5V, white for Vtune, black for ground and on the right a SMA coaxial connection for the output.



Figure 8.6. VCO connections.

The peaks visible in figure 8.7 show the response of the VCO for a tuning voltage of 5V on the left and 20V on the right. On the y-axis the magnitude can be seen, and on the x-axis the frequency. The peaks represent the frequency emitted by the VCO. It is clear that the frequency increases when the tuning voltage increases. Thus, by applying a voltage sweep a frequency sweep can be obtained as an output. This recreates the frequency sweep of the VNA.

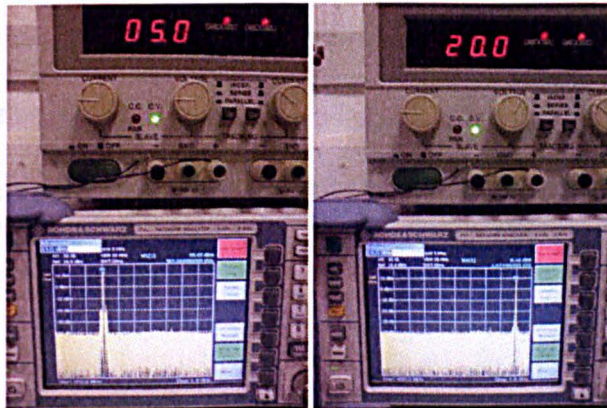


Figure 8.7. Spectral response of the VCO for a DC voltage equal to 5V (left), 20V (right)

To calibrate the VCO, its emitted frequencies were measured as the tuning voltage was changed from 1V to 24V, the results are displayed in figure 8.8. Those data points were input into a curve-fitting software called CurveExpert [94] in order to create a characteristic equation.

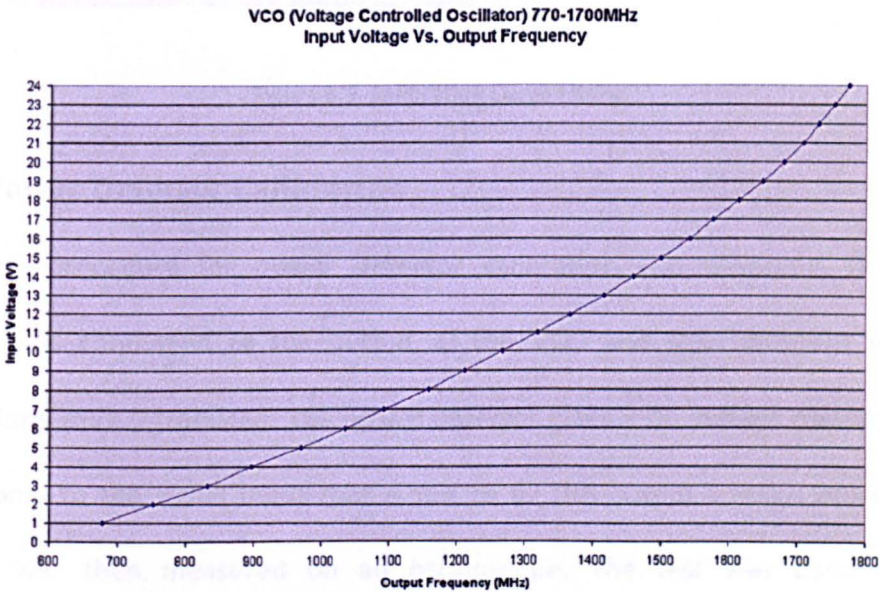


Figure 8.8. VCO Calibration Graph.

Figure 8.9 shows the software application generating the best fit equation. The best fit has a correlation factor of 99.99% using a 4th order polynomial equation. The equation coefficients are shown on the right of the equation form (figure 8.9).

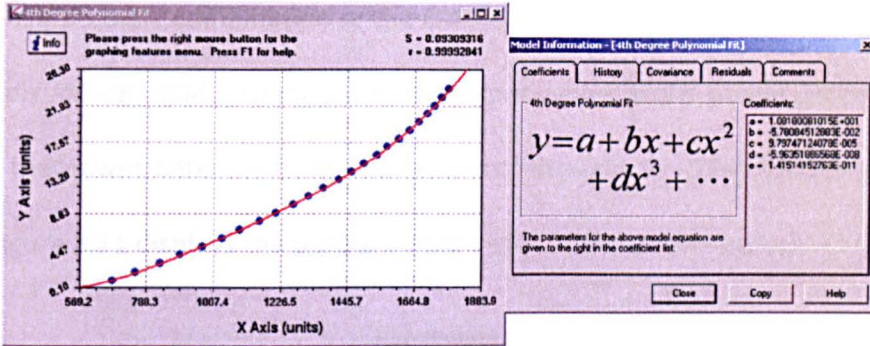


Figure 8.9. Calibration Curve Fitting.

8.1.6 Power Detector Calibration

The procedure for power detector calibration was different. The power detector was connected to the output of the VCO and then different values of attenuations were introduced. The power detector gives a DC voltage output which is proportional to the signal input that is fed to it. The output voltage of the power detector was then measured on an oscilloscope. The test was done at room temperature (21°C). Figure 8.10 shows the VCO on the left, the power detector on the right and an attenuator in blue in the middle.

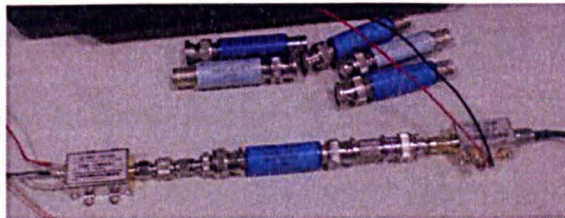


Figure 8.10. Test of the power detector using various attenuation values.

Every possible combination of the 6 different attenuators was used (-1dB, -2dB, -3dB, -12db, -15 dB, -20dB) to measure the output values of the power detector and to calibrate the power detector from 0dB (straight through) to -53dB (all attenuators in series). Figure 8.11 displays the output voltage against the power input.

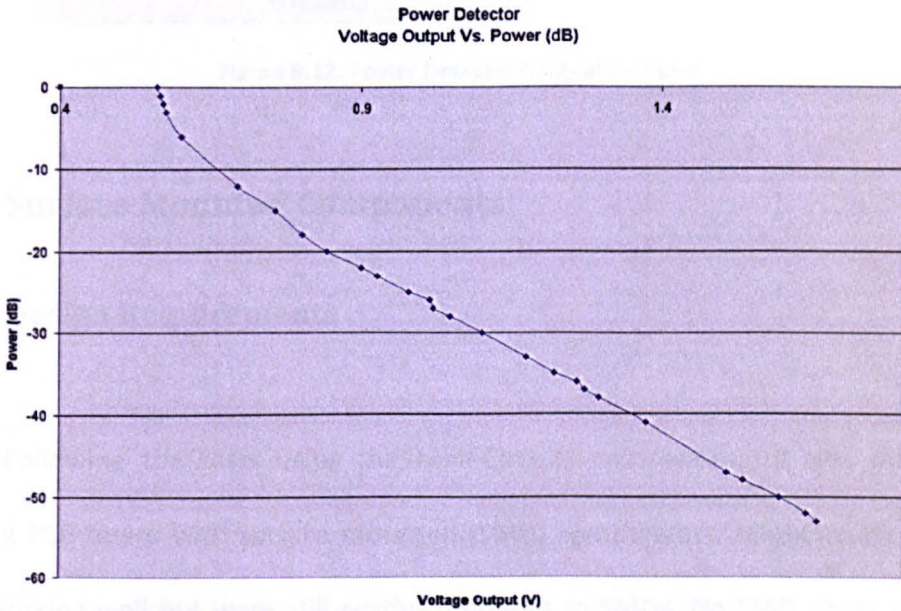


Figure 8.11. Power Detector Output Voltage depending on the Power Attenuation in dB.

These data points were input to the curve fitting software. The power detector output voltage is shown on the x-axis of figure 8.11. This value was put in the equation so the acquisition software displayed the graph in dB. Figure 8.12 shows the data points and their best fit. The correlation factor of this 4th order polynomial equation is 99.96%. The equation coefficients are shown on the right of the equation form (figure 8.12).

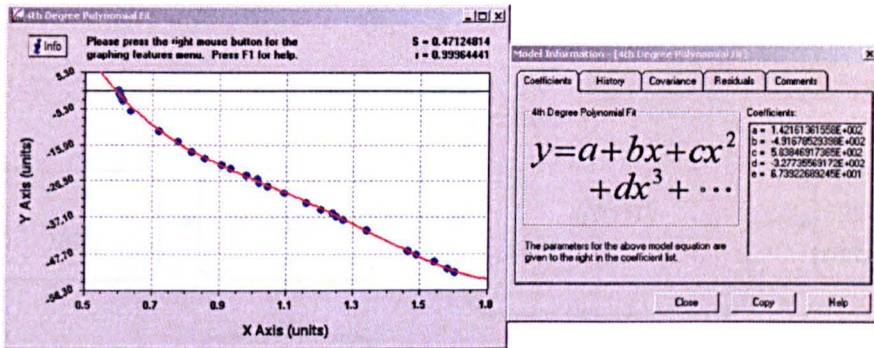


Figure 8.12. Power Detector Calibration Curve.

8.2 Surface Mounted Components

8.2.1 Design Requirements

Following the tests using the Mini-Circuits components, it was decided to create a PCB board with surface mounted (SMD) components. Mini-Circuits modules were working well but were still costly compared to SMDs. No SMD phase detectors are available from the main suppliers such as Farnell or CPC so the design was limited a device that can read the return loss power (S11) and the insertion loss power (S21) only. The Crystek VCO [95] was controlled using a 0V to 5V tuning voltage and powered from a 5V power supply. The MAX 2015 power detectors also use a 5V power supply. This means that if embedded with the software on a micro-controller, the whole system could be powered by a 9V battery or four 1.5V batteries. Figure 8.13 shows the connection schematic diagram of the parts and the National Instruments Data Acquisition rack.

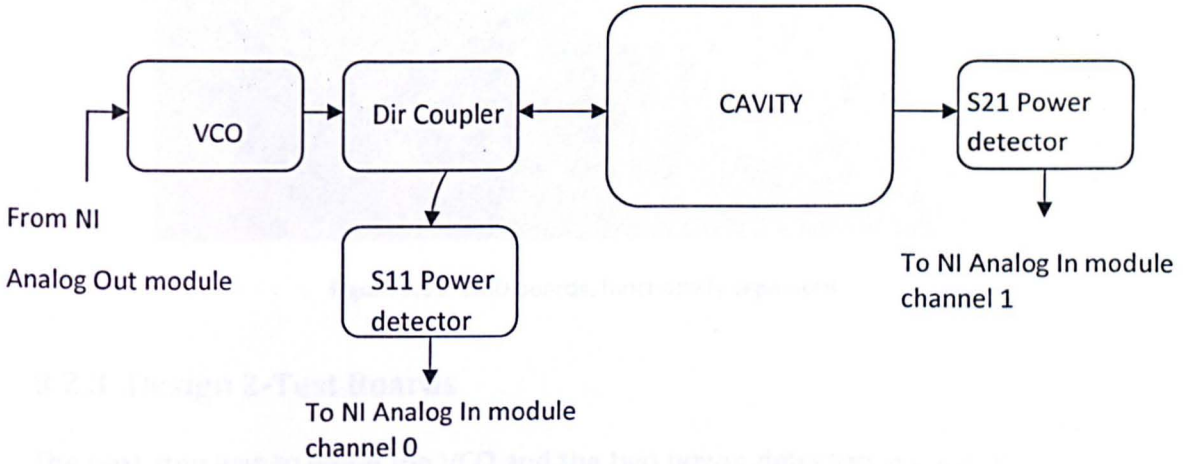


Figure 8.13. Connection between components.

8.2.2 Design 1-Test Boards

To ensure that the full circuit worked, each component was designed on its own PCB board. Figure 8.14 shows the PCB layout of the VCO (left), and the power detectors (right).

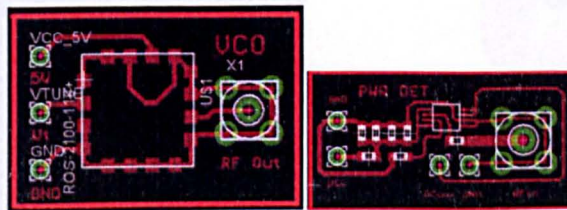


Figure 8.14. PCB layout : VCO (right), Power Detector (left).

Figure 8.15 shows the finished VCO (left), the two power detectors (middle), and the Mini-Circuit coupler (right).

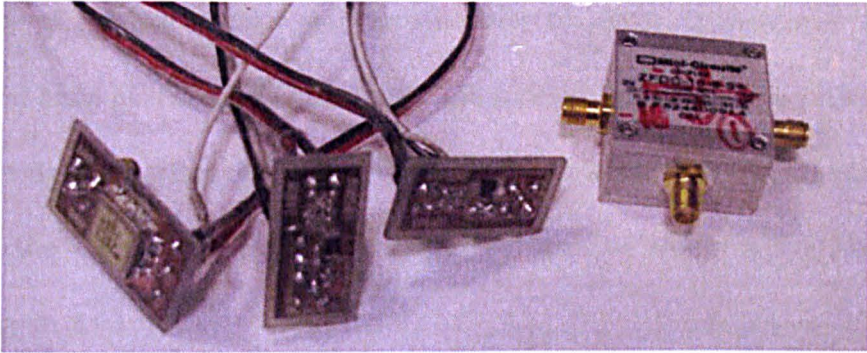


Figure 8.15. SMD boards, functionally separated.

8.2.3 Design 2-Test Boards

The next step was to group the VCO and the two power detectors on one board and a directional coupler on another board (Picture 8.16).

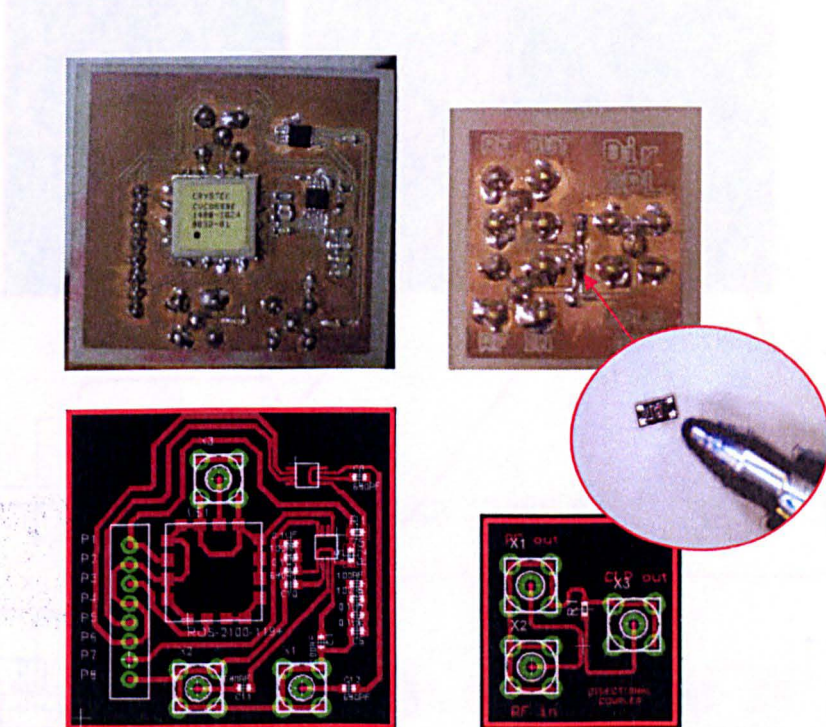


Figure 8.16. Two separate boards (VCO + power detectors and directional coupler).

The directional coupler was very difficult to solder, it measures 1.6mm by 0.8mm and has 4 pins located underneath. The zoomed image in figure 8.16 shows the size of the directional coupler compared to the tip of a pen. The boards worked well including the directional coupler. The last goal was to create a full board, with everything on it.

8.2.4 Design 3-Single Board

Figure 8.17 shows the final board (layout and PCB) compared to the size of a penny as well as the schematics used to design it in Eagle PCB Software.

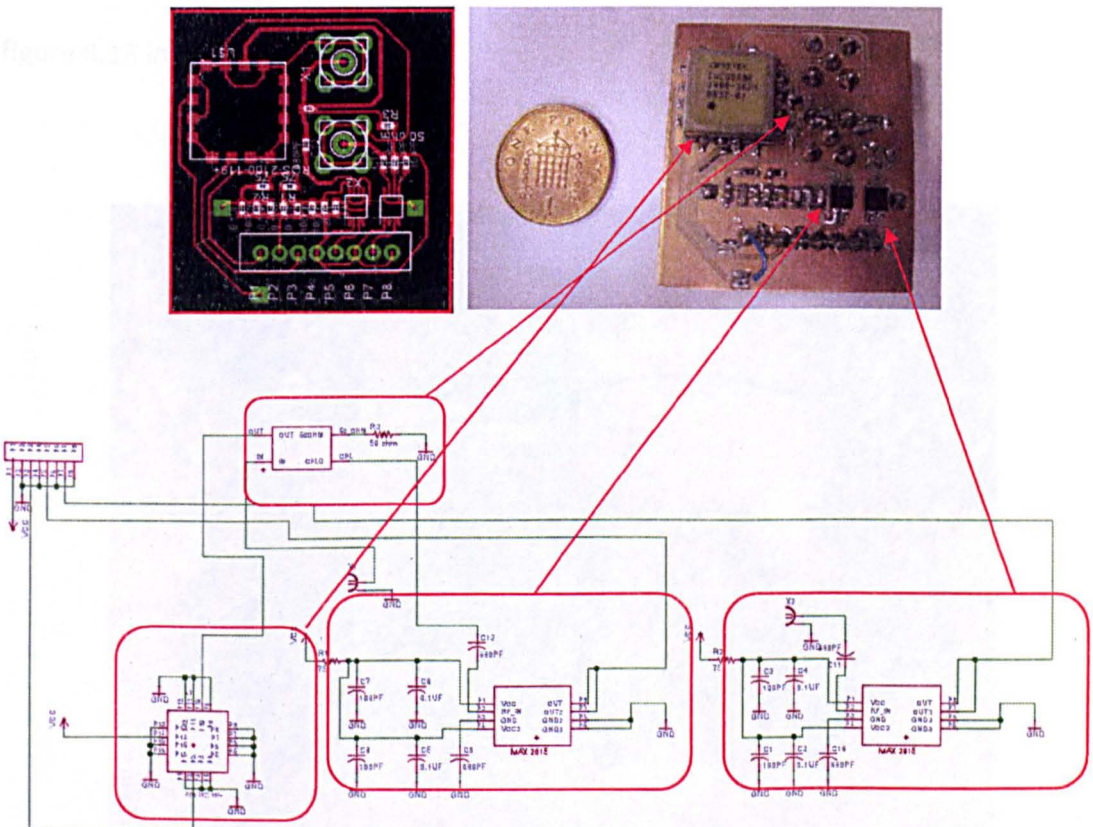


Figure 8.17. Full board Final Design.

8.2.5 Experimental Setup

This board has two SMA coaxial plugs to connect it to the cavity. An 8 way connector is used to connect the board to the power supply (5V, ground pin 1 and 2), the tuning voltage of the VCO (Vtune, ground pin 3 and 4) and the DC output of the two power detectors (DC out pin 5 and 7 and ground pin 6 and 8). The tuning voltage used for the VCO was from the analogue output of the National Instruments module. Because the surface mounted VCO only required a 5V power supply, there is no need for the operational amplifier. The two DC outputs from the power detectors were connected to the analogue inputs of the National Instrument module as shown in figure 8.18 in the red circles.

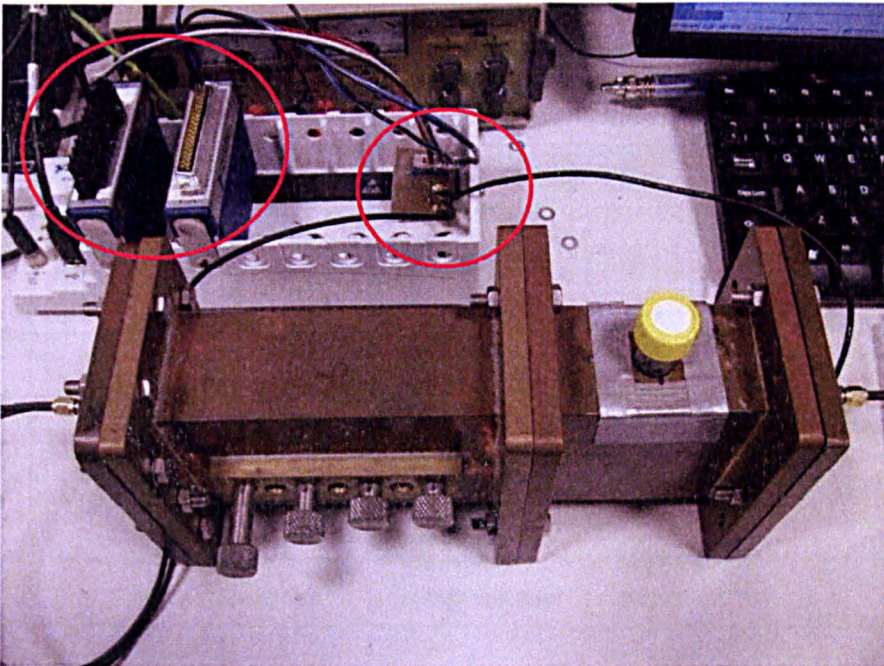


Figure 8.18. Connection of the board between the cavity and the National Instruments modules.

8.2.6 Calibrations and Experimental Results

The two power detector voltage outputs have been calibrated against power in dB using the Curve Expert software. However, a double calibration was required against frequency. This leads to a 3D surface equation. The surface equation is very complex and has not been done, however for proof of concept a test of the calibration was done at a fixed centre frequency of 1.56GHz (the resonant frequency for the water sample for the cavity). The VCO was calibrated using the same software; the output equation gave the input voltage necessary to provide the required frequency. A comparison between the VNA measurements and the SMD board measurements is given for the reflected power in Figure 8.19, and for the transmitted power in Figure 8.20.

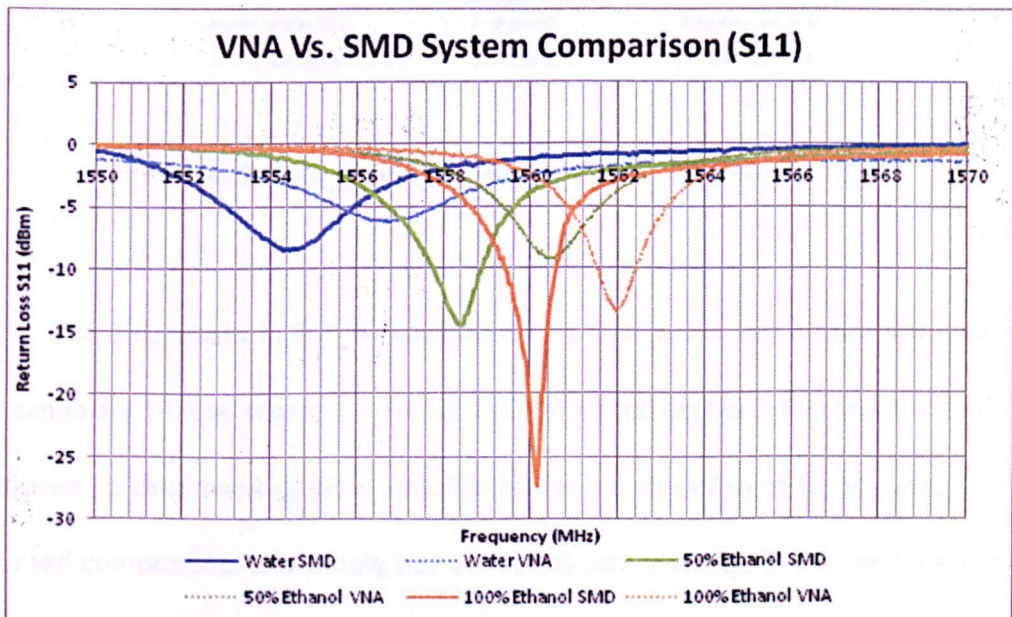


Figure 8.19. Comparison between the return VNA and SMD systems.

The tests were performed using different amounts of ethanol. The absolute resonant frequencies differ by about 2MHz but the frequency shifts between the samples remain the same. There is also a distortion that appears in the transmitted power for the highest concentration of ethanol.

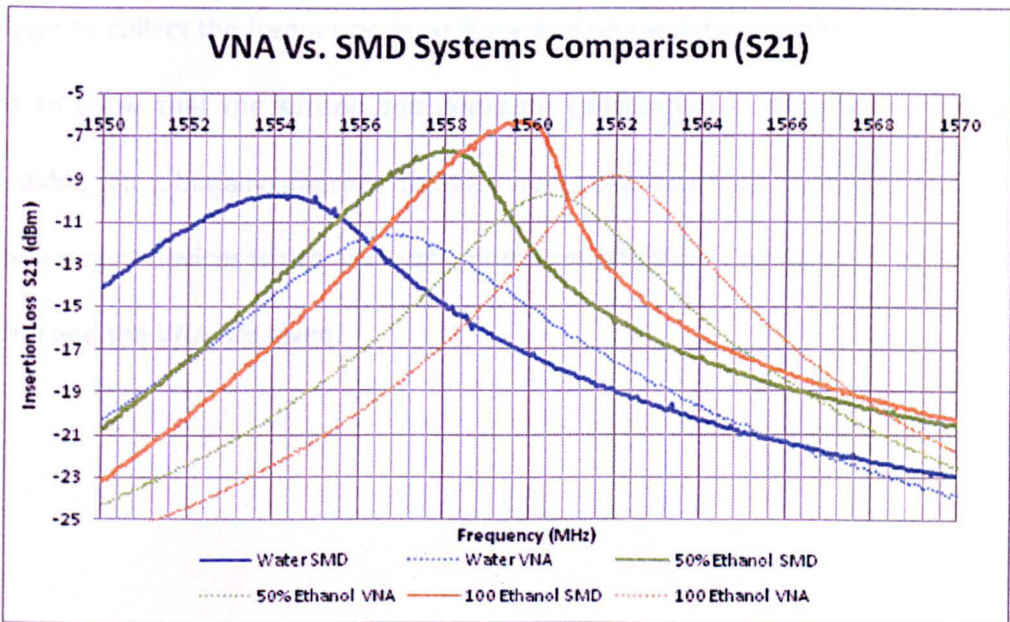


Figure 8.20. Comparison between the S21 VNA and SMD systems.

The differences in the measurements are noticeable but do not interfere with the capability of the sensor to detect alcohol concentration. The method was also employed to determine glucose concentrations but at different frequencies. Surface mounted components can simply be connected with a soldering iron and a voltmeter (to test connections). The main advantage at that time in the laboratory was the

milling machine, although the same results would be possible using etching techniques.

Summary

This chapter discusses the hardware that has been used in place of a vector network analyser to collect the frequency, magnitude and phase data from the sensor. This was done to show that the sensor unit could be constructed in a portable form at an affordable price. Initially, discrete modules were used but these were later replaced by surface mount devices which are much more cost effective. Comparisons between this system and the VNA are given.

9 CONCLUSION AND FURTHER WORK

9.1 Conclusion

This thesis demonstrated the potential use of non-invasive testing of the alcohol level in the blood stream using a microwave sensor. The study detailed the rectangular cavity resonator including its design characteristics and application. Also, the thesis introduced for the first time a novel non-invasive measurement technique using a microstrip suspended ring resonator. The designs have been modified in order to fulfill the targets stated in the first chapter. They have been simulated, tested, studied and their results were compared. Both methods have strengths and weaknesses mainly due to their physical properties.

Data acquisition and analysis software was created for this project in order to simplify the extraction of the data from the different devices. It was able to display both graphically and numerically the details of each sample and its extracted data. The data was exported to Excel files via .CSV files and the characterisation of a full range of samples generated by curve fitting software.

An electronic device was also created with the intention of replacing the vector network analyser. It was designed based on a voltage control oscillator, directional couplers and power detectors. The following sections will discuss the capabilities and limits of each measurement technique as well as possible evolutions.

9.1.1 Cavity Resonator

The cavity resonator is relatively simple to make, it has a robust construction and provides low-loss/attenuation due to its design properties. The measurements of both insertion loss (S_{21}) and return loss (S_{11}) provided much useful information to characterise the samples (S_{21} resonant frequency, S_{11} resonant frequency, S_{21} mag, S_{11} mag, S_{21} Q-factor, S_{11} Q-factor, Phases at F_0 , reflection coefficient and VSWR). At constant room and sample temperature, the reproducibility of the sensor was good, the peaks only shift by a few kilohertz. The rectangular cavity design was able to detect a percentage of ethanol in water equal to 1% inside the polypropylene test tubes. The disadvantage is that it is very sensitive to the position of the sample tube meaning that it is not particularly suitable for non-invasive measurement via a finger.

9.1.2 Microstrip Ring Resonator

The weaknesses of the cavity resonator led to the study of microstrip ring resonators. The main reason for using a microstrip ring resonator is that the resonator is on one plane, allowing a finger or wrist to just make contact with the ring to be analysed. Unfortunately, the different ring resonators (RR, Arc1 and Arc2) that were tested appeared to have a too small accuracy to be considered as a solution for alcohol sensing. The best results were made with Arc1 which was able to detect 10%

increment between the water/ethanol samples (100 times the BAC). Other solutions should then to be studied.

9.1.3 Suspended Microstrip Ring Resonator

A novel suspended ring resonator was designed especially for alcohol detection in the blood stream. It is based on a design derived from a dielectric foam sensor. The ring and feed line sizes have been changed and the air gap between the sample and the ring/upper dielectric has been removed. The design was simulated on HFSS. They are very easy to build using to a milling machine. Etching techniques work too, but the definition of the pattern is not as clear making the resonator less accurate. The suspended ring resonator has a very weak return loss (S_{11}), on which data cannot be extracted, leaving only the insertion loss (S_{21}) for measurements. However, the sensor is easily able to detect 1% difference between the samples using the resonant peak magnitude, frequency and Q-factor. In fact, the sensor was able to detect 0.2% increments of ethanol between the samples. This measurement was achieved using the transmission magnitude at a single frequency. That point is situated on the positive gradient (left) of the resonant peak. Those results mean that the level of the BAC (0.1%) for drink driving is very close indeed, and certainly achievable with improvements on the design. This level of sensitivity has not been found in any other scientific paper or books. This appears to be the first suspended ring resonator for alcohol detection, so the RFM (Radio Frequency and Microwave) laboratory and the GERI (General Engineering Research Institute) have decided to protect the design with

a patent, and the suspended ring resonator for alcohol detection is currently patent pending. This confirms that detecting a very low level of alcohol in the blood stream is feasible using non-invasive microwave sensors.

9.1.4 Glucose testing

The preliminary test for water/glucose mixtures were conclusive and have shown that ring resonators could also be used for that purpose. Test samples were made from 1mol/l glucose solutions in increments of 0.1mol/l (100mmol/l). This level of glucose is comparable with the glucose level in the human body (0.9 mg/ml to 1.4mg/ml). The measurements of samples were in order of concentration but relatively close to each other. The ring was designed for alcohol detection not glucose detection, so lower levels of glucose could be measured with a purpose built sensor. The cavity resonator has a magnitude difference of 1.5dB and a frequency shift of 2MHz (between 0mg/ml and 180mg/ml). The suspended ring resonator has a frequency shift of 4MHz and a magnitude difference of 1.6dB between the same samples.

9.1.5 Handheld Device Design

Concerning the feasibility of a portable device for alcohol/glucose detection, it has been shown that a simple circuit (VCO, coupler and power detectors) was able to measure the S-parameters (S21 and S11) of the sample under test with good accuracy.

That system still needs a computer to capture and analyse the data. It could incorporate a microprocessor instead, together with memory, DAC (Digital to Analogue Converter), ADC (Analogue to Digital Converter) and a screen to display the results. As we saw, only 5V is needed to power VCO and power detectors, this mean that four AA or AAA 1.5V batteries could power the whole system.

9.2 Further Work

9.2.1 Suspended Ring Resonator

The ring resonator has still to be tested with Ethanol/blood samples. Also some work should be carried out on improving the height between the two boards. Note that the dielectric characteristics of blood are different than those of water. Even though blood is mainly water (90%), the permittivity of water at 1GHz is situated between 78 and 82, whereas the permittivity of blood is about 64 (close to 70 for red blood cells). This means that there is less permittivity difference than for a water/ethanol mixture, thus there will be less frequency span between samples and it will be a little more challenging to detect the BAC level. Blood also has a higher conductivity than water, so it would be interesting to see how the sensor reacts. Some small changes in the design are likely to be needed. Many papers have carried out tests with calf blood because it has almost the same dielectric characteristics as human blood.

If the BAC is achieved again using the models, clinical tests should be carried out with volunteer patients such as people with alcohol related problems.

9.2.2 Glucose Testing

The blood sugar level tests are still at an early stage. The principle has been proven to work for samples in increments of 0.1mol/l between 100% water and 1mol/l of glucose. However, the sensor used was designed to detect ethanol and a new blood/sugar sensor should be designed using HFSS in order to achieve the typical blood-glucose level present in the average human blood stream.

9.2.3 Human Tissues Characterisation

Some further tests should be performed in relation to human tissues in order to see if the sensor is still able to detect the permittivity changes inside blood vessels. This is valid for alcohol and glucose tests. A skinny person will have a slightly different overall permittivity than an obese person because of the difference in fat layer size. If that difference is a problem, the sensor should be calibrated against a size/weight curve too. If the BAC level is achieved, an arm or finger can be replicated using gelatine models. Human tissues such as muscle, tendons, veins, and even bones can be tested using different concentrations of gelatine. The permittivity value for fat is 11.6, muscle is 58.8, skin is 46.7 and the permittivity for bones is 13.1. It would be judicious to realize a single model with an average gelatine permittivity equal to the percentage of

each component present in a human hand. The soft plastic pipes have the same permittivity as veins and can therefore be kept.

TABLE OF ABBREVIATION

BAC	Blood Alcohol Content
DAQ	Data Acquisition
dB	decibel
dl	deciliter
EHF	Extremely High Frequency
EMF	Electromotive Force
FEM	Finite Element Model
GHz	Giga Hertz
GMS	Guided Microwave Spectroscopy
IR	Infrared
KSI	Killed or Seriously Injured
l	liter
mg	milligram
MHz	Megahertz
ml	milliliter
mmol	milli-mole
mW	milli-Watt
NIFTS	Near Infrared Fourier Transform Spectrometer
NIRS	Near Infrared Fourier Spectrometer
PCB	Printed Circuit Board
PEC	Perfect Electrical Conductor
PLS	Partial Least Square
RF	Radio Frequency
RPM	Revolution Per Minute
SAC	Saliva Alcohol Concentration
SCRAM	Secure Continuous Remote Alcohol Monitor
SHF	Super High Frequency
SMA	connector SubMiniature version A
SMD	Surface Mounted Device
SNR	Signal to Noise Ratio
SWR	Standing Wave Ratio
TAC	Transdermal Alcohol Content
TE	Transverse Electric
TEM	Transverse Electromagnetic
TM	Transverse Magnetic
TOSM	Through Open Short Match
UHF	Ultra High Frequency
USB	Universal Serial Bus

UV	Ultra-Violet
VCO	Voltage Controlled Oscillator
VNA	Vector Network Analyzer
VSWR	Voltage Standing Wave Ratio
WRR	Weighed Ridge Regression

Bibliography

- [1] Department for Transport (2008). *Road Casualties in Great Britain: Main Results: 2007. DFT*. <http://www.dft.gov.uk/pgr/statistics/datatablespublications/accidents/casualtiesmr/rcgbmainresults2007>, Accessed 17 October 2008.
- [2] Department for Transport (2000). *Tomorrow's roads: safer for everyone*. <http://www.dft.gov.uk/pgr/roadsafety/strategytargetsperformance/tomorrowsroadsaferforeverone>, Accessed 20 October 2008.
- [3] E.N. Lee, L.H. Kidder (2004), *Combining Imaging and Spectroscopy:solving problems with near-infrared chemical imaging*, *Microscopy Today*, volume 16, No.6, pp1-4.
- [4] R. Wellock, A.D. Walmsley (2004). *Application of microwave spectroscopy in process analysis*. Department of Chemistry, University of Hull, <http://www.clairret.co.uk/downloads/PSC09.pdf>, *Process Spectroscopy, Process Colum*, pp.23-26, Accessed 21 October 2008.
- [5] M. Lazebnik, M.C. Converse, J.H. Booske, S.C. Hagness (2006). *Ultrawideband temperature-dependent dielectric properties of animal liver tissue in the microwave frequency range*. Institute of Physics Publishing – Physics in Medicine and Biology Volume 51, pp. 1941–1955.
- [6] J.Lucas, A.I. Al'Shamma'a (2002). *EM Wave Sensor for Wet Gas Metering, Multiphase Technology*, 3rd North American Conference, ISBN 1 85598 041 X, Banff,Canada, pp. 391-398.
- [7]S. Wylie, A.Shaw, A.I Al-Shamma'a (2005). *On Line RF- Microwave Sensor for Monitoring the Constituents of an Oil Pipe Line*. - *Journal of Physics - Conference Series* ISSN:1742-6588, Volume 15, pp. 342-347.
- [8] J. Zente (2000). *Laboratory and in-line moisture and composition measurements. Cereal Foods World*. – *Cereal foods world – New Technologies in Grain*, volume 45, Issue1 (dissem.), pp. 5-6.
- [9] B.R. Jean (2006). *Process Composition Monitoring at Microwave Frequencies: A Waveguide Cutoff Method and Calibration Procedure*. *IEEE Transactions on Instrumentation and Measurement*, Volume 55, Issue 1, pp. 180-186.
- [10] J.L. Smith (2006). *The Pursuit Of Non Invasive Glucose:"Hunting the Deceifful Turkey"*, http://www.mendosa.com/noninvasive_glucose.pdf, Accessed 1 November 2008.
- [11] US Department of Health and Human Services (2008). *Your Guide To Diabetes*. National Diabetes Information Clearinghouse . <http://diabetes.niddk.nih.gov/DM/pubs/type1and2/YourGuide2Diabetes.pdf>, Accessed 3 November 2008.

-
- [12] R. L. Myers (2007). *The 100 most important chemical compounds: a reference guide*. Westport, Greenwood Press, pp. 120-124.
- [13] J. Brick (2003). *Characteristics of Alcohol: Chemistry, Use and Abuse*. Handbook of the Medical Consequences of Alcohol and Drug Abuse. New York; Haworth Medical Press; 1-11.
- [14] C. R. Carroll, L.H. Durrant (2000). *Drugs in Modern Society*. Boston: McGraw-Hill College, fifth edition.
- [15] R. Breakspeare, P. Williams (1995). *Breath Alcohol Instrumentation: A Proposal in Commercial Taxonomy*. Central Queensland University, Rockhampton, Queensland 4702, Australia.
- [16] J.M. Holas (2004). *Modern Spectroscopy*. John Wiley & Sons, ISBN 0 470 84416 7, pp. 27-34.
- [17] F. McLennan, and B. R. Kowalski (1995). *Process Analytical Chemistry*, Blackie Academic and Professional, Chapman and Hall, London, UK, pp. 378.
- [18] C.N. Banwell (1983). *Fundamentals of Molecular Spectroscopy (Third Edition)*. McGrawhill, , pp. 124-129.
- [19] I.W. Campbell (2008), *Blood Glucose Levels- What should glucose levels be?* Health advice , diabetes blood sugar, Net Doctor, http://www.netdoctor.co.uk/health_advice/facts/diabetesbloodsugar.htm, Accessed on 12 november 2008.
- [20] J.J. Workman (1999). Review of Process and Non-Invasive Near Infrared and Infrared Spectroscopy. In *Applied Spectroscopy Review*, volume 33, issue 1, pp. 1-89.
- [21] M. Miyake, S. Diccini, A. Rita de Cassia Bettencourt (2003). *Interface of nail polish and time on pulse oximetry in healthy volunteers*. J. Pneumologia, volume 29, Issue 6, São Paulo. http://www.scielo.br/scielo.php?pid=S0102-35862003000600011&script=sci_arttext&tlng=en , Accessed 9 November 2008.
- [22] J. McNally (2005). *A Revolutionary System Noninvasive Alcohol Testing with Identity Verification*. International Technology Symposium –A Nation Without Drink Driving, Technology development challenges.
- [23] TruTouch (2006). TruTouch develops and markets Noninvasive Intoxication Measurement Systems , TruTouch Technology Inc.: <http://www.trutouchtechnologies.com> , Accessed 15 November 2008.
- [24] R. J. Bell (1972). *Introductory Fourier Transform Spectroscopy*. New York: Academic Press.
- [25] K. Sakai (1972). *Michelson-Type Fourier Spectrometer for the Far Infrared*, Applied Optics, Volume 11, Issue 12, pp. 2894-2901.

-
- [26] **B. Ver Steeg, T. Ridder (2005).** "A New Eye on Law Enforcement: Photonics Technology Enables. Accurate Noninvasive Alcohol Testing". *oeMagazine*, Volume 5, Issue 6, pp. 26–28.
- [27] **J.Zente (2000).** *Laboratory and In-Line Moisture and Composition Measurement*. In *Cereal Foods World*, New Technologies in Grain, Volume 45, pp. 5-6.
- [28] **A.Walmsley, V. Loades (2001).** *Determination of acetonitrile and ethanol in water by guided microwave spectroscopy with multivariate calibration*, *Analyst*, Volume 126, Issue 4, pp. 417-420.
- [29] **C. Rayment, S.Sherwin (2003).** *Introduction to Fuel Cell Technology*, Department of Aerospace and Mechanical Engineering, University of Notre Dame, Notre Dame, Academic Press, IN 46556, U.S.A.
- [30] **FuelCells2000 (2000).** *Fuel Cells Basics*, from Fuel Cells 2000: <http://www.fuelcells.org/basics/how.html> , Accessed 5 November 2008.
- [31] **Intoximeters Incorporated (2005).** *Fuel Cell Technology-The need for blood alcohol testing*. White Paper, Intox.com, <http://www.intox.com/fuelcell.asp> , Accessed 10 November 2008.
- [32] **SCRAM AMS (2008).** *SCRAM Product Information: The Facts on Continuous Alcohol Monitoring*, Alcohol Monitoring, http://alcoholmonitoring.com/ams_files/resources/SCRAMdatasheet.pdf, Accessed 11 November 2008.
- [33] **Dräger Safety (2008).** *Alco-check for Measurement of Breath Alcohol Concentration*, Dräger. <http://www.draeger.co.uk/ST/internet/pdf/Master/En/gt/Alcodrug/Alco-checkPI.pdf> , Accessed 7 November 2008.
- [34] **Chematics (2007).** *Alco Screen*, Saliva Test for the Presence Of Alcohol in the Blood, Chematics, <http://www.chematics.com/alcoscreen.php> , Accessed 21 November 2008.
- [35] **E. W. Weisstein (2007).** *Maxwell's equations-Dielectric*, Wolfram Research, Electromagnetism, Maxwell's Equations <http://scienceworld.wolfram.com/physics/MaxwellEquationsDielectric.html> , Accessed 23 November 2008.
- [36] **S. B. Miles, S.E. Sarma, J.R. Williams (2008).** *RFID Technology and Applications*. Cambridge University Press, pp. 48-61.
- [37] **National High Magnetic Field Laborator.** *The Magnetic Field Around a Wire*, Electromagnetism. (n.d.). Florida State University, University of Florida, <http://www.magnet.fsu.edu/education/tutorials/java/magwire/index.html> , Accessed 5 December 2008.
- [38] **B.Crowell (2002).** *Electricity and Magnetism*. Book 4 in the Light and Matter series of introductory physics textbooks, second edition, Arnold Arons.
- [39] **Antenna Theory.** (n.d.). *Microwave Theory 101, Antenna Theory Part1*, EM Talk Electromatics and Microwave Engineering. <http://www.emtalk.com/tutorials.htm> , Accessed 1 December 2008.

-
- [40] S. R. Howard (1998). *Module 10: Introduction to Wave Propagation, Transmission Lines and Antennas*. Navy Electricity and Electronic Training Series (NEETS): Naval education and training professional development and technology center.
- [41] SURA. *Electromagnetic Spectrum*. Retrieved from Southern University Research Association: [http://depts.washington.edu/cmditr/mediawiki/index.php?title=Terahertz Radiation](http://depts.washington.edu/cmditr/mediawiki/index.php?title=Terahertz_Radiation) , Accessed 29 November 2008.
- [42] E. Da Silva, (2001). *High Frequency and Microwave Engineering*. Butterworth Heinmann, pp. 43-50.
- [43] L. F. Chen, C. K. Ong, C. P. Neo, V. V. Varadan, V. K. Varadan (2004). *Microwave electronics: Measurements and materials characterization*. John Wiley and Sons inc.
- [44] P. F. Combes (1996). *Micro-Ondes: lignes, guides et cavites*, Cours et Exercices, Dunod, Volume 1, pp. 177-201.
- [45] W. Fendt. *Standing wave applet*. walter fendt de: <http://www.walter-fendt.de/ph14e/stwaverefl.htm> , Accessed 16 December 2008.
- [46] D. T. Blackstock (2000). *Fundamentals of physics acoustics*. Wiley Interscience Publication-IEEE, pp.1-55.
- [47] R.Bansal(2006). *Fundamentals of Engineering Electromagnetics*, Tailor and Francis Group CRC Press, edition 1, pp.53-89.
- [48] P.Y. Yu, M. Cardona (2001). *Fundamentals of semiconductors: Physics and Material Properties*. Berlin-Springer, Edition 4, pp.107-158.
- [49] C. Townes, A.L. Schawlow (1975). *Microwave Spectroscopy*. McGraw Hill Books dover.
- [50] H. D. Young, R.A. Freedman (2007). *University Physics with Modern Physics with Mastering Physics*, Addison Wesley, 12th Edition.
- [51] S. Gabirel, C. Gabriel (1996). *Compilation of the dielectric properties of body tissues at RF microwave frequencies*. Report AL/OE-TR-1996-0037, Brooks Air Force Base (USA), <http://www.brooks.af.mil/AFRL/HED/hedr/reports/dielectric/Report/Report.html> , Accessed 28 December 2008.
- [52] D. Butler (2002). *Guided microwave spectroscopy: A proven method of in-line analysis and considerations for in-line method*. http://ift.confex.com/ift/2000/techprogram/paper_5332.htm , Accessed 12 December 2008.

-
- [53] R.N. Karekar, R.C. Aiyer, R. K. Abegaonkar (1998). *A microwave microstrip ring resonator as a moisture sensor for biomaterials: application to wheat grains*. IOP Publishing , Measurement science & technology , volume 10, Issue 3, pp. 195-200.
- [54] V.Loades, A.D. Walmsey (2001), *Determination of acetonitrile and ethanol water by guided microwave spectroscopy with multivibrate calibration*, Analyst, volume 126, Issue 4, pp. 417-420.
- [55] J. C. Maxwell, T. F. Torrance (1865). *A Dynamical Theory of the Electromagnetic Field*. Philosophical Transactions of the Royal Society of London 155, Wipf and Stock.
- [56] A.I. Al-shamma'a, J. Lucas (2000). *Apparatus and method for determining dielectric properties of an electrically conductive fluid*, 9901304.7(WO00/43759).
- [57] G.A. Cristian (2005). *On-line, real-time, detection of alcohol in a blood stream using advanced microwave spectroscopy*. John Moores University Masters Project 2005.
- [58] Fast Neuron Research Facility, *Waveguide Theory*. Plasma and Beam Physics Research Facility, Chiang May University , Department of Physics and Materials Science, Faculty of Science. <http://www.fnrf.science.cmu.ac.th/waveguide/index.html>, Accessed 3 January 2009.
- [59] K.T. Mathew, U.Raveendranath (2001). *Cavity Perturbation Techniques for Measureing the Dielectric Parameters of Water and Other Allied Liquids*. Wiley Interscience, Sensor Update Vol. 7, p185-210.
- [60] S. R. Howard (1998). Module 11:. *Microwave Principles*. Navy Electricity and Electronic Training Series (NEETS): Naval education and training professional development and technology center.
- [61] Optris CT, *The new Optris Infrared Thermometers CHot , CTglass and CTlaser bring the heat under control, IR Thermometer*, Optris, Content Press Information, http://www.optris.de/en/content_press_information_2008_01_18.htm , Accessed 15 January 2009.
- [62] Rohde & Schwartz, Vector Network Analyser ZVL series, R&S, <http://www.rohde-schwarz.co.uk/uk/> , Accessed 16 January 2009.
- [63] M.J. Akhtar, L.Feher, M.Thumm (2006). *Measurement of Dielectric Constant and Loss Tangent of Epoxy Resins Using a Waveguide Approach*. IEEE Antennas and Propagation Society International Symposium 2006, USA, pp.3179-3182.
- [64] HFSS v.11, 3D-Finite Element Methodl for HF simulations, 3D Full-wave Electromagnetic Field Simulation, Ansoft, <http://www.ansoft.com/products/hf/hfss/> , Accessed 15 January 2009.
- [65] F. Bordi a, C. Cametti b, T. Gill (2002). *Dielectric spectroscopy of erythrocyte cell suspensions.A comparison between Looyenga andMaxwell–Wagner–Hanai effective medium theory formulations* ,Journal of Non-Crystalline Solids, volume 305, pp. 278–284.

-
- [66] Kiel University website, *Dielectric Characteristics of Ethanol at different temperature*, http://www.tf.uni-kiel.de/matwis/amai/elmat_en/kap_3/illustr/dk_water.gif, Accessed 14 November 2008.
- [67] Material Sensing and Instrumentation, *Dielectric Characteristics of Water at different Temperature*, http://www.msi-sensing.com/dielectric_images/ethanol_temperature.gif, Accessed 14 November 2008.
- [68] Microsoft Visual Studio 2008, Software Development, The Official Site of Visual Studio <http://www.microsoft.com/visualstudio/en-gb/default.aspx>, Accessed 18 March 2009.
- [69] Measurement Studio v8.6, Support for Engineering Applications, National Instruments, <http://www.ni.com/mstudio/>, Accessed 17 March 2009.
- [70] Measurement & Automation Explorer, Data Acquisition, National Instruments, <http://search.ni.com/>, Accessed 12 March 2009.
- [71] A. Maton, J. Hopkins, C. W. McLaughlin, S. Johnson, M. Q. Warner, D. LaHart, J. D. Wright (1993). *Human Biology and Health*. Englewood Cliffs, New Jersey, USA: Prentice Hall.
- [72] M.J. Kovacs, M. Rodger, D.R. Anderson, B. Morrow, G. Kells, J. Kovacs, E. Boyle (2003). *Comparison of 10-mg and 5-mg warfarin initiation nomograms together with low-molecular-weight heparin for outpatient treatment of acute venous thromboembolism. A randomized, double-blind, controlled trial*. *Annals of Internal Medicine*, Volume 138, Issue 9, pp. 714–719.
- [73] A. Guo, J. Fu, E. Fong (2000). *Measurement of Liquid Composition Percent Using Coaxial Cavity Resonator*, International Conference on Microwave and Millimeter Wave Technology Proceedings. 2nd International Conference on. ICMMT 2000, pp. 541 – 544.
- [74] B. Kapilevich, B. Litvak (2007). *Measurement Sensor for Accurate Measurements of Water Solution Concentrations*. Proceedings of Asia-Pacific Microwave Conference. APMC 2007, pp.1 - 4.
- [75] M. McKee, B.P. Johnson (2000). *Real-Time Chemical Sensing of Aqueous Ethanol Glucose Mixtures*, IEEE Transactions on Instrumentation and Measurements, Volume 49, Issue 1, pp. 114 - 119.
- [76] S. Kim, J. Kim, A. Babajanyan, K. Lee (2009). *Noncontact Characterisation of Glucose by a Waveguide Microwave Probe*. *Current Applied Physics*, volume 9, issue 4, pp. 856-860.
- [77] International Bureau of Weights and Measures (2007). SI Brochure, Appendix 2: *Realising the mol*, http://www.bipm.org/utis/en/pdf/SIApp2_mol_en.pdf, Accessed 26 February 2009.
- [78] R. Hopkins (2006). *The Microstrip Ring Resonator for Characterising Microwave Materials*. Advanced Technology Institute, School of Electronics and Physical Sciences University of Surrey.
- [79] K. Chang, L.H. Hsieh (2004). *Microwave Ring Circuits and Related Structures*, 2nd Edition, Wiley, ISBN: 978-0-471-44474-9.

-
- [80] E. Hammerstad (1975). *Equations for microstrip circuit design*, Proceedings of the 5th European Microwave Conference, Hamburg, September, pp. 268-72.
- [81] E. Hammerstad, O. Jensen (1980). *Accurate models for microstrip computer-aided design*, IEEE Transactions on Microwave Theory and Techniques, MTT-S, Volume 28, pp. 407-409.
- [82] J.Y. Park, J.C. Lee (1998). *A new enhanced coupling structure of microstrip ring resonator with two coupled lines and a slit*. IEEE Transaction on Microwave Theory and Techniques, Volume 50, Issue 5, pp. 1340-1345.
- [83] G.K.Gopalakrishnan, K.Chang (1994). *Novel excitation schemes for the microstrip ring resonator with lower insertion loss*, Electronic letters IEEE, Volume 30, Issue 2, pp.148-149.
- [84] I. Waldron, S.N. Makrov (2006). *Suspended Ring Resonator for Dielectric Constant Measurement of Foam*. Microwave and Wireless Components Letters IEEE, Volume 16, Issue 9, pp.496-498.
- [85] R.K.Hoffmann (1987). *Handbook of Microwave Integrated Circuits*. Norwood, Artech House.
- [86] K.Sarabandi, E.S. Li (1997). *Microstrip Ring Resonator for Soil Moisture Measurements*. Transactions on Geoscience and Remote Sensing IEEE. Volume 35, Issue 5, pp. 1223-1231.
- [87] Galaad Software, Integrated CAM-CAD-CNC for Windows, <http://www.galaad.net/drive-eng.html>. Accessed on 16 March 2009.
- [88] Perkins & Elmer, Mixer/Pump S200 Series, <http://las.perkinelmer.com/Catalog/ProductInfoPage.htm?ProductID=LCPUMP3> , Accessed on 18 March 2009.
- [89] Perkins & Elmer, Series 200 HPLC Column Ovens, http://las.perkinelmer.com/content/relatedmaterials/productnotes/prd_series200columnovensproductnote.pdf, Accessed on 17 March 2009.
- [90] P.Petong, R.Pottle, U.Kaatze (2000). *Water-Ethanol Mixtures at Different Compositions and Temperatures*. A Dielectric Relaxation Study, Journal of Physics and Chemistry, American Chemical Society, Volume 104, Issue 32, pp 7420–7428.
- [91] Mini-Circuits, RF/IF Designer's Guide, Components Retailer, <http://www.minicircuits.com/> , Accessed 23 July 2009.
- [92] Electronics Tutorials, *Voltage Controlled Oscillator*, <http://www.electronics-tutorials.com/oscillators/voltage-controlled-oscillators.htm> , Accessed 20 July 2009.
- [93] Microwave Encyclopedia, *Directional Couplers*, <http://www.microwaves101.com/encyclopedia/directionalcouplers.cfm> , Accessed 29 July 2009.

[94] **Curve Expert**, *Overview*, Free Curve Fitting Software,
<http://s91928265.onlinehome.us/curveexpert/> , Accessed 15 May 2009.

[95] **Crystek Microwave**, *Crystals and Microwave Component Manufacturer*.
<http://www.crystek.com/microwave/index.php> , Accessed 1 July 2009.

[96] **World of Molecules**, *Molecule of Glucose*, <http://www.worldofmolecules.com/foods/glucose.htm> ,
Accessed 24 May 2009.